広島大学学位請求論文

Energy Loss of Charm and Bottom Quarks in Quark-Gluon Plasma Created in Au+Au Collisions at $\sqrt{s_{NN}} = 200$ GeV

($\sqrt{s_{NN}} = 200$ GeV Au+Au 衝突で生成される
クォーク・グルーオン・プラズマ中における
チャーム/ボトムクォークのエネルギー損失)

2019年

広島大学大学院理学研究科
物理科学専攻

永嶋　和也

目次

1. 主論文
   Energy Loss of Charm and Bottom Quarks in Quark-Gluon Plasma. Created in Au+Au Collisions at $\sqrt{s_{NN}}$ = 200 GeV
   ($\sqrt{s_{NN}}$ = 200 GeV Au+Au 衝突で生成されるクォーク・グルーオン・プラズマ中におけるチャーム/ボトムクォークのエネルギー損失)
   永嶋　和也

2. 公表論文
   PHENIX measurements of single electrons from charm and bottom decays at midrapidity in Au+Au collisions.
   K. Nagashima for the PHENIX collaboration.
   Nuclear Physics A, **967**, 644-647 (2017).

3. 参考論文
   Single electron yields from semileptonic charm and bottom hadron decays in Au+Au collisions at $\sqrt{s_{NN}}$ = 200 GeV.
   A. Adare, K. Nagashima, *et al.*
   Physical Review C, **93**, 034904 (2016).

主論文

Energy Loss of Charm and Bottom Quarks in Quark-Gluon Plasma Created in Au+Au Collisions at $\sqrt{s_{NN}} = 200$ GeV

Kazuya Nagashima

A Dissertation submitted
in partial fulfillment of the requirements
for the degree of Doctor of Science

Department of Physical Science, Graduate School of Science, Hiroshima University

March, 2019

Abstract

A new state of matter composed of deconfined quarks and gluons, quark-gluon plasma (QGP), was predicted in 1973 immediately after the discovery of the asymptotic freedom of the QCD coupling constant. The QGP is believed to exist in 5 microseconds after the Big Bang. It was discovered with high-energy heavy-ion collisions at Relativistic Heavy Ion Collider (RHIC) and shows the unexpected nearly perfect fluid property. This emergent phenomenon in QCD is studied with high-energy heavy-ion collisions at RHIC and Large Hadron Collider (LHC).

Heavy quarks (charm and bottom) provide important information on the nature of the QGP such as a shear viscosity to entropy density ratio η/s. They are produced by gluon scatterings in an initial stage of heavy-ion collisions and propagate through the QGP. Since heavy quarks are hardly disappeared via pair annihilation and interact with the QGP via elastic and inelastic scatterings, the modification of their phase space distributio between initial and final state in heavy ion collisions strongly reflects the QGP dynamics. The nuclear modification factor $R_{\rm AA}$ which represents the modification of momentum distribution in the QGP is a key measurement to understand the quark dynamics in the QGP. Comparison between measured data and theoretical models provides η/s and gluon density of the QGP. However, the energy loss mechanism theoretically is not well understood. An understanding of quark mass dependence of energy loss is key to understand the energy loss mechanism in the QGP.

The PHENIX silicon vertex detector installed in 2011 enables the measurement of separated electrons from charm and bottom hadron decays with displaced vertex analysis. The nuclear modification factor $R_{\rm AA}$ and the fractional momentum loss $\rm S_{loss}$ are measured in Au+Au collisions at $\sqrt{s_{_{NN}}} = 200$ GeV by comparing results in $p + p$ collisions which assumed no QGP creation. Charm (bottom) quarks lose momentum in the QGP by 25% (20%) in case of most central Au+Au collisions. Both measured centrality dependence of $R_{\rm AA}$ and $\rm S_{loss}$ shows that charm quarks lose energy larger than bottom quarks. In other words, the quark mass dependence of energy loss in the QGP is found. It provides important knowledge to the energy loss mechanism for understanding the nature of the QGP.

Contents

List of Figures

List of Tables

Chapter 1

Introduction

1.1 Overview

After the appearance of Quantum Chromo Dynamics (QCD) and the discovery of the asymptotic freedom of the QCD coupling constant [1, 2], a new state of matter composed of deconfined quarks and gluons, called "quark-gluon plasma (QGP)" was predicted in the late 1970s [3, 4]. The QGP is believed to exist in 5 microseconds after the Big Bang. It was found by high-energy heavy-ion collisions at Relativistic Heavy Ion Collider (RHIC) in 2004 [5, 6, 7, 8] and shows the unexpected nearly perfect fluid property, strongly coupled QCD medium. Before the discovery, the QGP was predicted to be composed of weakly coupled quarks and gluons, like a free gas, based on the asymptotic freedom of the QCD coupling constant. This emergent phenomenon in QCD is studied with high-energy heavy-ion collisions at RHIC and Large Hadron Collider (LHC).

Heavy quarks (charm and bottom) are a sensitive probe of a QGP dynamics such as a shear viscosity to entropy density ratio (η/s) in high-energy heavy collisions. They are mostly produced by gluon scatterings in an initial stage of heavy-ion collisions and propagate through the QGP while preserving of the number of heavy quarks. Heavy quarks lose energy via elastic and inelastic scatterings in the QGP. The modification of their momentum distribution between initial and final state in heavy-ion collisions strongly reflects the QGP dynamics. Conversely, the QGP dynamics can be studied by the modification of a momentum distribution such as a nuclear modification factor. The nuclear modification factor $R_{\rm AA}$ is calculated by comparing heavy-ion (Au+Au) collisions and proton-proton ($p + p$) collisions which assumed no QGP creation. Comparison between measured $R_{\rm AA}$ and theoretical models provides η/s and gluon density of the QGP. However, the energy loss mechanism theoretically is still not well understood. Current theoretical models expect a mass ordering of quark energy loss in the QGP, $\Delta E_{\text{light quark}} > \Delta E_{\text{c quark}} > \Delta E_{\text{b quark}}$, because of a mass dependent collisional energy loss and the suppression of small-angle gluon radiation called Dead-Cone effect [9]. Experimental verification of the quark mass dependence of the energy loss leads to understanding of the energy loss mechanism and the QGP dynamics.

The PHENIX collaboration at RHIC has installed the silicon vertex detector for a precise measurement of displaced vertices, which allows separation of bottom

and charm contributions in the single electron spectrum. PHENIX has measured $R_{\rm AA}$ of separated $c \rightarrow e$ and $b \rightarrow e$ in minimum bias Au+Au collisions collected in 2011 [11]. It shows likely quark mass dependence of $R_{\rm AA}$, $R_{\rm AA}{}^{b \rightarrow e} > R_{\rm AA}{}^{c \rightarrow e}$. However, there is no enough significance of quark mass dependence. In 2014-2016, PHENIX has collected dataset for 200 GeV Au+Au (and $p+p$) collisions which are ∼20 times larger than the 2011 dataset. It allows a precise measurement of collision centrality dependence of $R_{\rm AA}$ to systematic study energy loss of charm and bottom quark as a function of QGP size.

This dissertation details the measurement of separated electrons from charm and bottom hadron decays in Au+Au ($p+p$) collisions at $\sqrt{s_{_{NN}}} = 200$ GeV collected in 2014 (2015). The nuclear modification factor $R_{\rm AA}$ and the fractional momentum loss $\rm S_{loss}$ are calculated by comparing results in $p+p$ collisions which assumed no QGP creation. $\rm S_{loss}$ is a more direct measurement of energy loss in the QGP because momentum loss can be regarded as energy loss in case of high-$p_{\rm T}$ region, quark-mass $<< p_{\rm T}$. Measured $\rm S_{loss}$ show that charm (bottom) quarks lose momentum by 25% (20%) in the QGP in case of most central Au+Au collisions. Both measured centrality dependence of $R_{\rm AA}$ and $\rm S_{loss}$ shows that charm quarks lose energy larger than bottom quarks. In other words, the quark mass dependence of energy loss in the QGP is found. It provides important knowledge to the energy loss mechanism for understanding the nature of the QGP.

1.2 Quantum Chromo Dynamics

Quantum Chromodynamics (QCD) is the gauge theory of the interaction between quarks and gluons and part of the Standard model. QCD assumes that a quark (gluon) has 3 (8) types of colors which are a source of the force. The color force is carried by a gluon as with a photon carrying the electromagnetic force. The new degree of freedom, color, was expected after the discovery of Λ^{++} composed of same quarks having the same spin ($\rm u^{\uparrow}u^{\uparrow}u^{\uparrow}$), $\rm J^P = \frac{3}{2}$ which violates Pauli Principle without a new degree of freedom. The electron-positron annihilation measurement provides evidence of three colors for quarks [13, 14]. Fig. 1.1 shows the ratio of the number of hadron events to the number of muon events in $\rm e^+e^-$ collisions, described as

$$R = \frac{\sigma_{hadron}}{\sigma_{muons}} = \frac{\sum \sigma_{q\bar{q}}}{\sigma_{muons}} = \sum (\frac{q_q}{e})^2, \tag{1.1}$$

where $\rm q_q$ and e are a charge of quarks and muons. If we assume only one color for u, d, c, s, and b quarks, the R is approximately calculated as

$$R = \left(\frac{2}{3}\right)_u^2 + \left(\frac{1}{3}\right)_d^2 + \left(\frac{1}{3}\right)_s^2 + \left(\frac{2}{3}\right)_c^2 + \left(\frac{1}{3}\right)_b^2 = \frac{11}{9}. \tag{1.2}$$

The single color model can not describe the measured data. On the other hand, if we assume three colors, R is approximately calculated as

$$R = 3\left[\left(\frac{2}{3}\right)_u^2 + \left(\frac{1}{3}\right)_d^2 + \left(\frac{1}{3}\right)_s^2 + \left(\frac{2}{3}\right)_c^2 + \left(\frac{1}{3}\right)_b^2\right] = \frac{33}{9}. \tag{1.3}$$

The three colors model shows reasonable agreement with the measured data, which is evidence of three colors for quarks.

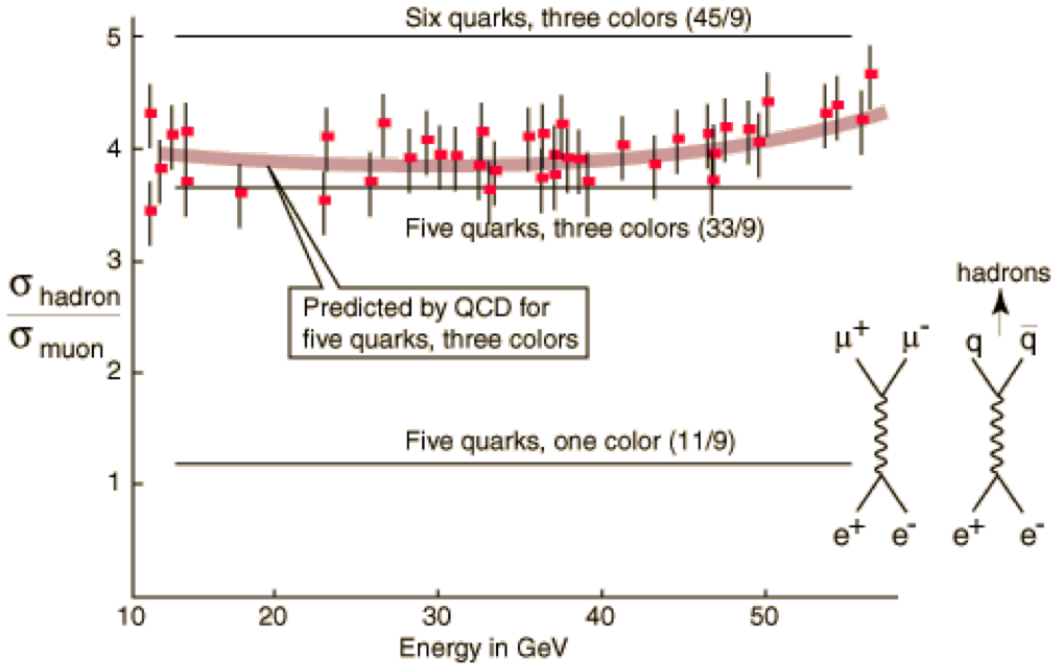

Figure 1.1: the ratio of the number of hadron events to the number of muon events in e^+e^- collisions [13, 14]. The three colors model reproduces the measured data well.

QCD was constructed by the three colors SU(3) gauge symmetry with reference to Quantum Electrodynamics (QED), U(1) gauge theory, which constitutes a part of the Standard Model. The Standard Model based on SU(3)×SU(2)×U(1) gauge symmetry describes interactions of 17 elemental particles with fundamental forces, the electromagnetic, weak, and strong interactions. The Lagrangian of QED part in Standard Model is described as

$$\mathcal{L}_{QED} = \sum_f \bar{\phi}_f (i\gamma^\mu \partial_\mu - m_\mu)\phi_f + e\sum_f Q_f \bar{\phi}_f \gamma^\mu \phi_f A_\mu - \frac{1}{4} F_{\mu\nu}F^{\mu\nu}, \tag{1.4}$$

where e is the electromagnetic coupling, Q_f is a charge of a fermion, $\bar{\phi}_f$ is probability of emission or absorption of fermions, and A_μ is the probability of emission or absorption of photons. The integrated loop calculation of intermediate state, next leading order diagrams as shown in Fig. 1.2, gives infinity in the QED Lagrangian. Its problem was solved by Renormalization.

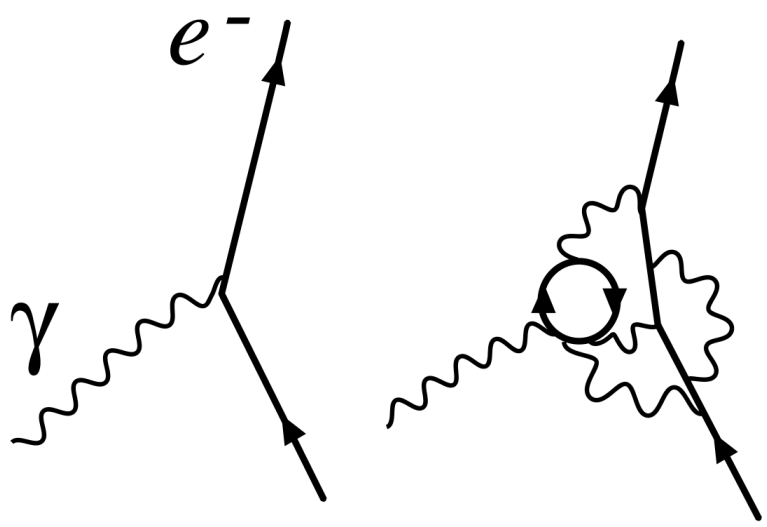

Figure 1.2: The diagram of electron scattering. Left: leading order diagram, Right: next reading order diagram.

In contrast, QCD has color SU(3) gauge symmetry instead of U(1) gauge symmetry in QED. The QCD Lagrangian is quite similar to QED Lagrangian, described as

$$\mathcal{L}_{QCD} = \sum_q \bar{\phi}_q^c (i\gamma^\mu \partial_\mu - m_q)\phi_q^c + \sum_q g_s \bar{\phi}_q^a \gamma^\mu T_{ab}^A \phi_q^b G_\mu^A - \frac{1}{4} G_{\mu\nu}^A G^{A\mu\nu}, \tag{1.5}$$

where g_s is the coupling constant, $\bar{\phi}_q^c$ is a probability of emission or absorption of fermions, and G_μ is a probability of emission or absorption of gluons. A gluon not only carries the color force but also self-interacts in QCD. On the other hand, there is no self-interaction of photons in QED because a photon has no charge. It causes a big difference in a distance dependence of interaction strength between QED and QCD.

1.2.1 Running Coupling and Asymptotic Freedom

The electromagnetic coupling constant α is 1/137.035999139 in case of $Q^2 = 0$ [16]. It depends on Q^2 because of the screening effect of electron-positron pairs in the vacuum. The screening effect denotes that the polarized vacuum from a charged particle screen out a charge for large distance, small Q^2. Therefore, the electromagnetic coupling increases with increasing Q^2, which is called the running coupling. Fig. 1.3 shows the measured electromagnetic coupling and the QED prediction. The QED prediction shows a good agreement with measured data [15].

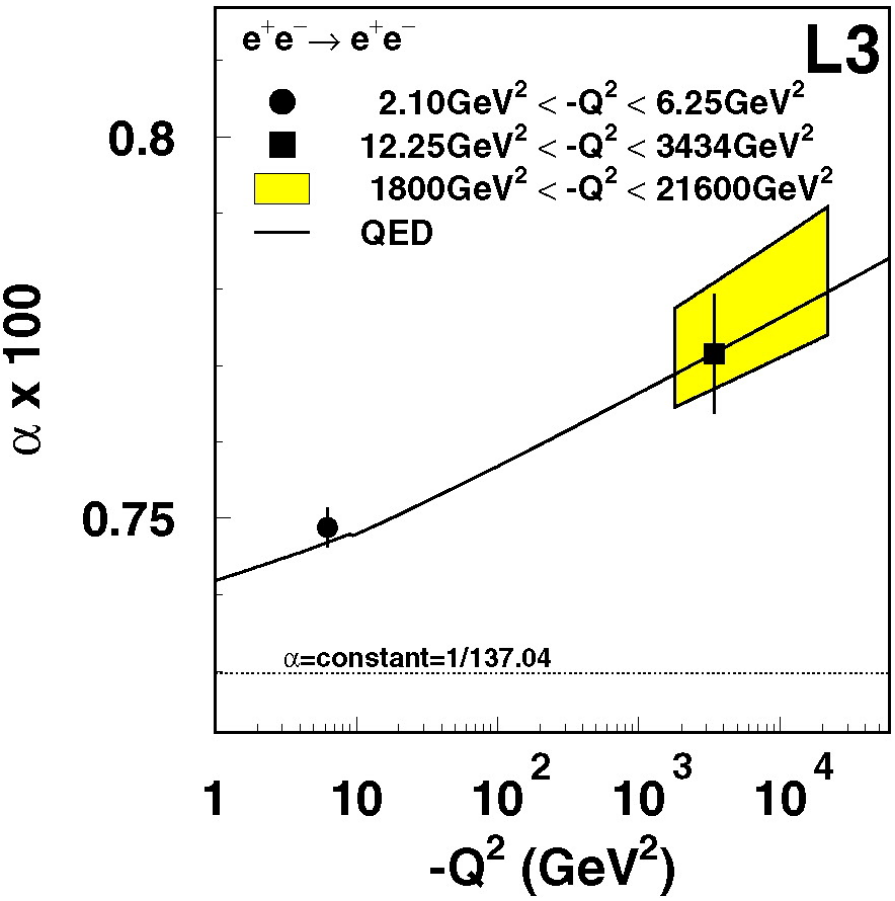

Figure 1.3: The QED running coupling constant increases with increasing Q [15].

In contrast, there are the screening effect from the quark and gluon field and the anti-screening effect from the gluon field in QCD. The anti-screening effect is caused by color dipole moment and the self-interaction of gluons. Since a gluon has larger (8) colors than a quark, the anti-screening effect is stronger than the screening effect. Therefore, the QCD coupling constant becomes smaller with increasing Q^2.

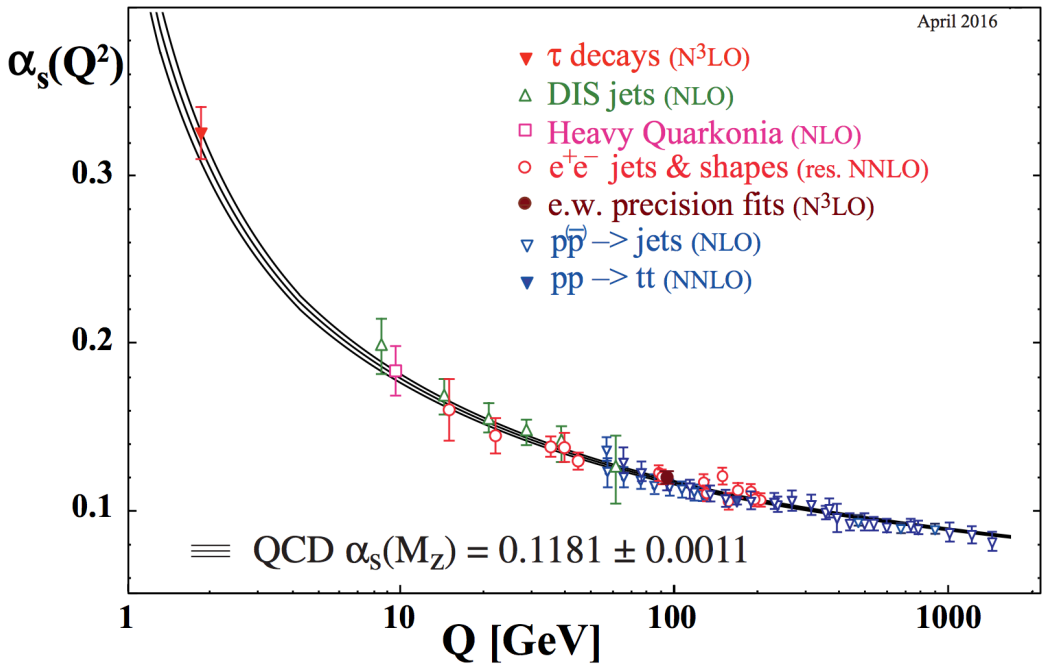

Figure 1.4: The QCD running coupling constant decreases with increasing Q [16].

1.2.2 Quark Confinement

Since QCD coupling increases with increasing distance, a separation of quark and anti-quark pairs needs infinite energy. Before combined quarks become free, quark pairs exited from the vacuum and new pairs are formed. In other words, QCD expects that strong interaction particles, quarks and gluons, are confined ($E_{free} > m_{q\bar{q}}$). However, there is not yet a mathematical proof of color confinement in any non-abelian gauge theory because perturbative QCD calculation breaks down for Q $< \sim$1 GeV. In contrast, lattice QCD provides the first principle calculation for an investigation of quark confinement which is intractable by means of analytic field theories. Fig. 1.5 shows the lattice QCD calculation of potential between quark and anti-quark as a function of distance of a quark pair [17]. Here, r_0 is 0.5 fm and $V(r_0)$ is normalized to 0. Lattice QCD expects the linear rising of the potential till $r/r_0 = 3$. The potential energy is well described as

$$V(r) = V_0 - \frac{\alpha}{r} + \sigma_0 r. \tag{1.6}$$

It indicates that infinite energy is needed to separate quark and anti-quark. In fact, a free quark has never been observed experimentally. On the other hand, the quark pair creation caused by the quark confinement has been observed as the jet, which is indirect evidence of the quark confinement.

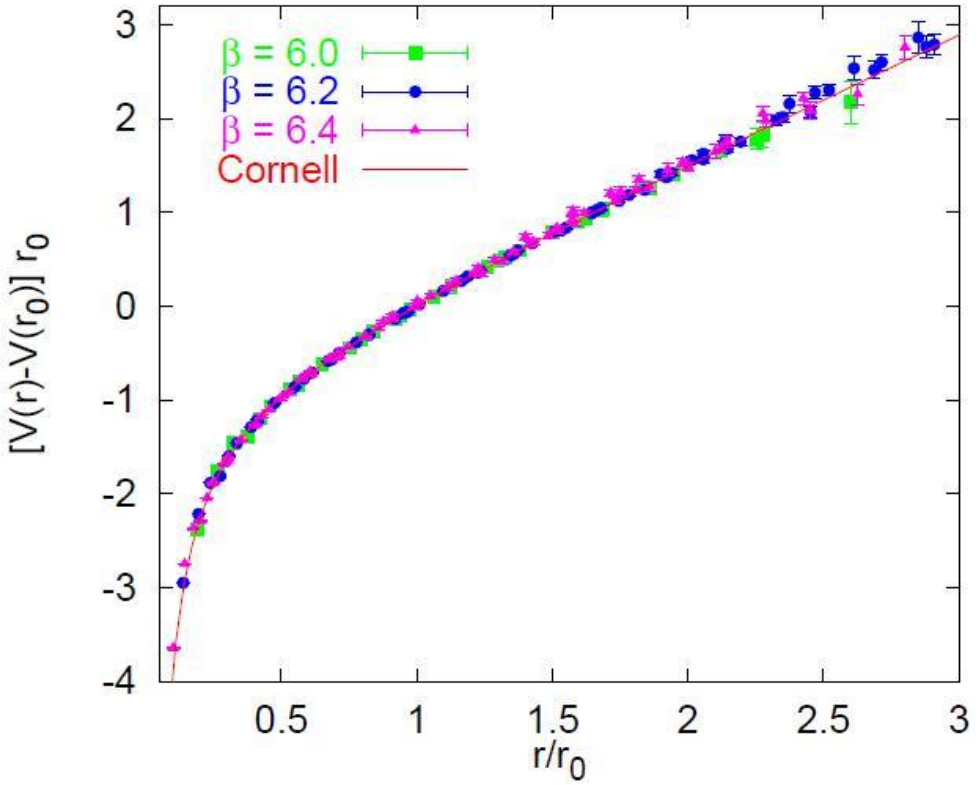

Figure 1.5: The potential between quark and anti-quark as a function of a distance of quark pairs [17].

1.3 History of Universe

The universe or the structure of the vacuum experienced several phase transitions with decreasing temperature as shown in Fig. 1.6 [24]. After the transition of Higgs field, the condensed Higgs field in the vacuum gives the mass of elementary particles [25, 26, 27]. The discovery of Higgs (like) particle by ATLAS and CMS experiments at CERN demonstrated the Higgs mechanism. After the transition of quarks and gluons field, quarks and gluons are confined in hadrons as described in Sec. 1.2.2 and thus acquired the mass as hadrons due to the Yukawa interaction with condensed quarks and antiquarks in the vacuum [30, 31] similar to the Higgs mechanism. However, these mechanisms have not been proved experimentally.

High-energy experiments can track back the history of the universe with increasing temperature and study the phase transition matter existed at the early universe. Heavy-ion colliders at RHIC and LHC can create an extremely high temperature ($> 2\times10^{12}$ °C) matter and track back the universe till $\sim 10^{-5}$ seconds from Big Bang. In this extremely high-temperature state, a matter composed of hadron gas transitions to a matter composed of deconfined quarks and gluons, namely the quark-gluon plasma (QGP). In the QGP, the structure of a matter is completed different from the present and the mass of quarks decreases with de-

creasing the quark condensates in the vacuum [32]. The study of the QGP leads to understanding of the structure of the matter and the mass of hadrons.

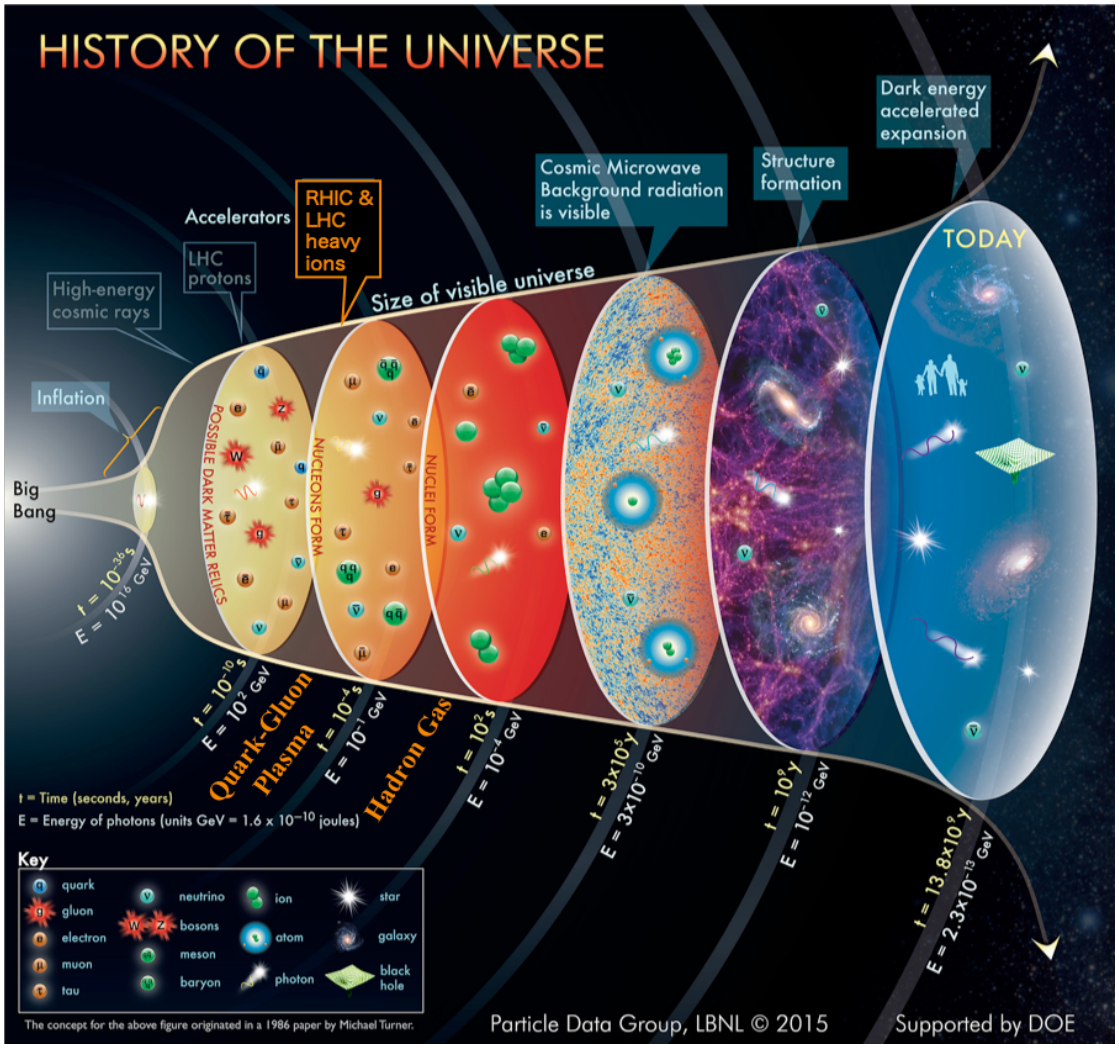

Figure 1.6: The history of the universe [24].

1.4 QCD Phase Transition

The first principle calculation from Lattice QCD provides a theoretical proof of the phase transition from the hadron gas phase to the QGP phase. It calculates the energy density normalized by T^4 with $N_f = 2+1$ flavor dynamical quarks as a function of the temperature as shown in Fig. 1.7 [18]. The energy density (the degree of freedom) is drastically changed around $T = 170$ MeV, which indicates the phase transition from the hadron gas to the QGP. This calculation suggests that the QCD phase transition needs the energy density $\epsilon > 1$ GeV/fm.

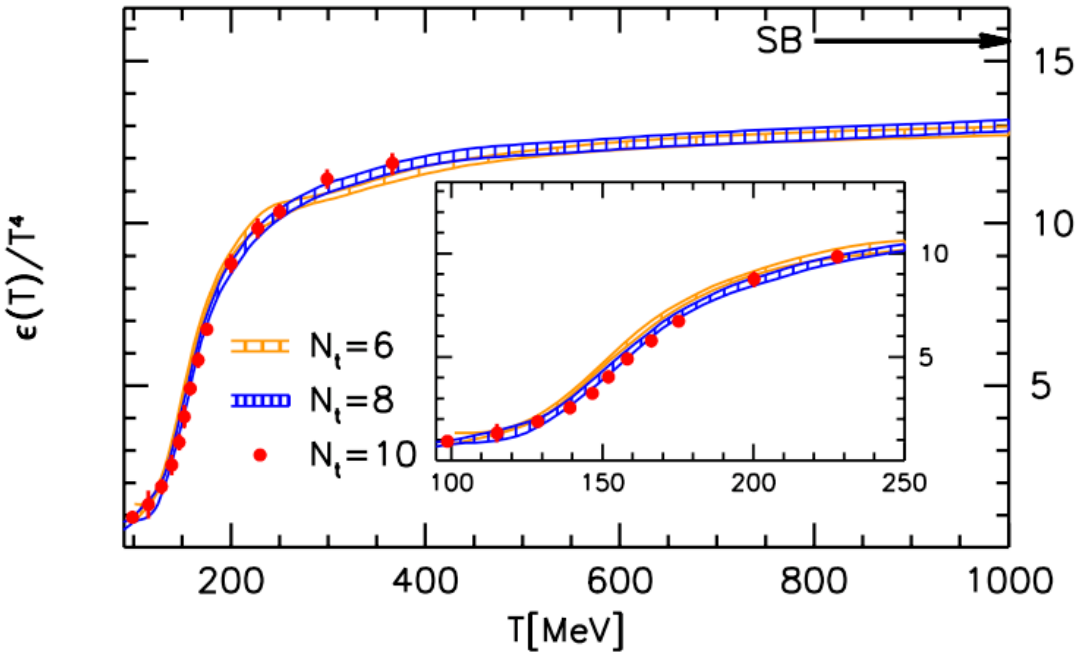

Figure 1.7: The energy density normalized by T^4 as a function of the temperature in case of a number of latices (N_t = 6, 8 and 10). An arrow indicates the Stefan-Boltzmann limit $\epsilon_{SB} = 3p_{SB}$ [18].

In the case of zero net baryon density, the transition from hadron gas phase to QGP phase is a smooth crossover (second-order) phase transition. On the other hand, the first-order phase transition is predicted under a condition of non-zero baryon density [35]. Fig. 1.8 shows the QCD phase as a function of temperature and baryon density. RHIC can address not only the crossover transition but also the critical point and the first-order phase transition. In order to comprehensive understanding of QCD phase, RHIC performs heavy-ion collisions with various collision energies and systems.

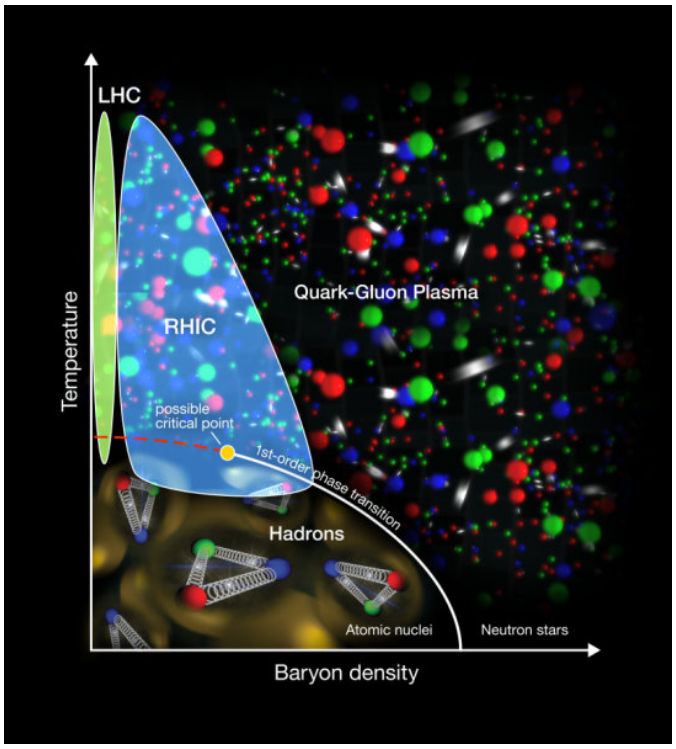

Figure 1.8: The QCD phase diagram as a function of temperature and baryon density [37].

1.5 Quark-Gluon Plasma

The existence of the matter composed of deconfined quarks and gluons, quark-gluon plasma (QGP), was predicted in 1973 [3, 4] immediately after the discovery of the asymptotic freedom of the QCD coupling constant [1, 2]. It was discovered with high-energy heavy-ion collisions at RHIC [5, 6, 7, 8]. Before the discovery, the QGP is expected to be composed of weakly coupled quarks and gluons, namely free gas, because of the asymptotic free theory of QCD. The QCD coupling constant decrease with increasing temperature, which causes the deconfinement of quarks and gluons. However, the discovered QGP shows the strongly coupled matter, namely the nearly perfect fluid property [6]. Its nature is defined by the ratio of shear viscosity to entropy density η/s. The QGP has the lowest η/s compared with all matters as shown in Fig. 1.9 [34]. Extensive measurements suggest that η/s of the QGP is nearly lower bound expected by the anti-de Sitter/conformal field theory correspondence (Ads/CFT), KSS bound [33]. A strongly coupled matter, namely small η/s, has short mean free path. The shortest possible mean free path is decided by order the de Broglie wavelength, which provides a lower limit of η/s.

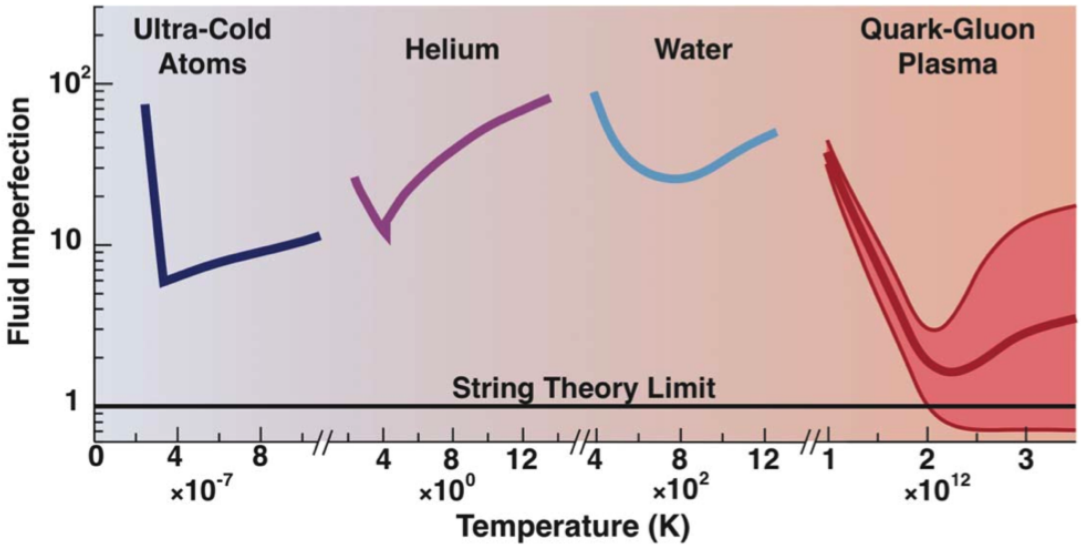

Figure 1.9: The fluid imperfections (the theory limit $(1/4\pi)$ is normalized to unity) for various matters as a function of temperature [34] and the storing theory limit (KSS bound) [33].

The asymptotic free theory of QCD conflicts the nature of strongly coupled QGP. This emergent phenomenon manifested in QCD many-body system has been hidden in the CQD Lagrangian so far. In other words, a developed theory from the asymptotic free theory in QCD two-body system cannot explain the nature of QGP. It is a fundamental question of QCD why the QGP shows strongly coupled fluid with nearly lower bound $\eta/s \sim 1/4\pi$. In addition, it is also a question how does the asymptotically free theory of QCD reconcile with the strongly coupled QGP.

1.6 Relativistic heavy-ion Collisions

Fig. 1.10 shows a space-time evolution of a relativistic heavy-ion collision which is divided into 6 states as the following.

1. **Initial state** Heavy nuclei (e.g.: Au and Pb) are accelerated to near the speed of light and look like a disk due to Lorentz contraction in a laboratory system. Gluons in accelerated nuclei radiate a gluon due to self-interaction and thus saturate due to an equilibrium between radiation and absorption. RHIC and LHC energy cause the gluon saturation in nuclei, which is understood as the Color-Glass Condensate [36].

2. **Collision** A few quarks and gluons are strongly scattered and become a source of a jet via the fragmentation mechanism. On the other hand, the most part (mainly gluons) pass through the nucleus and a lot of color strings appear in overlapped region between nuclei. Since two nuclei stretch color strings by near the speed of light, enormous energy is accumulated in the region of

nucleus size. The Energy density of RHIC heavy-ion collisions is expected to be over 1 GeV/fm^3. It seems to separate the electrode of capacitors in case of the electromagnetic force.

3. **Pre-equilibrium** A lot of partons appear from color strings between nuclei and cause a transition to the thermal equilibrium by multiple scattering. This non-equilibrium matter between the CGC and the QGP is called Glasma.

4. **Quark-Gluon Plasma** When quarks and gluons are sufficiently produced and scattered, a hot and dense matter reaches a local thermal equilibrium, which is the quark-gluon plasma (QGP).

5. **Mixed-phase** The matter causes the crossover phase transition from the QGP to the hadron gas phase with expansion and decreasing temperature. The temperature of the transition is $T \sim 170$ MeV.

6. **Hadron gas** Since collision frequency of hadrons decreases, the chemical potential is fixed firstly, Chemical freeze out, and the kinetic is fixed secondly, Kinetic freeze out. Finally, produced hadrons reach a detector.

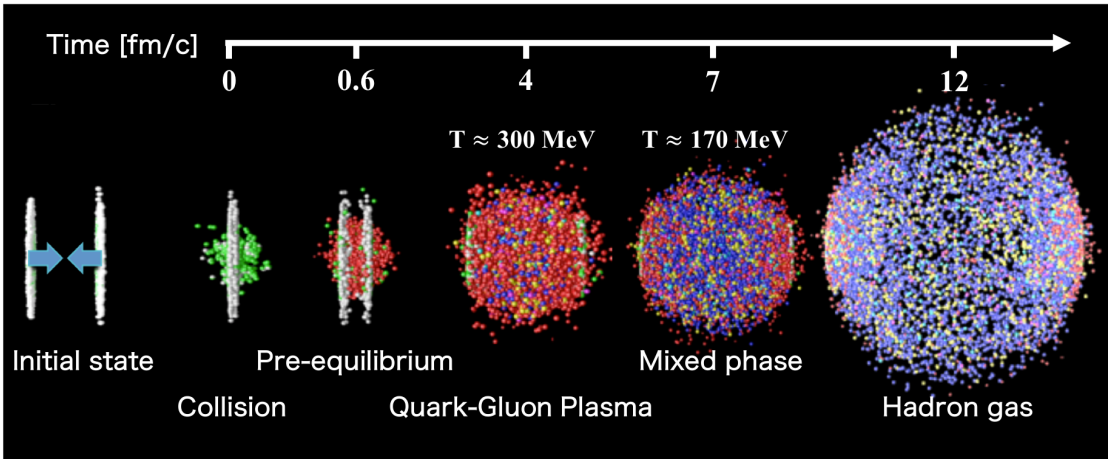

Figure 1.10: The schematic view of a space time evolution of a heavy-ion collision.

1.7 Heavy Quark Probe of QGP

Heavy quarks (charm and bottom) are important proves of the QGP dynamics in high-energy heavy-ion collisions. They are mainly generated by gluon scatterings in the initial stage of high-energy heavy-ion collisions because they have masses ($m_{\rm c} = 1.28$ GeV and $m_{\rm b} = 4.18$ GeV for $\bar{\rm M}$S scheme) much larger than the QGP temperature $T \sim 300$ MeV. After that, they propagate through the QGP while preserving the number of heavy quarks because a heavy-quark pair annihilation hardly occurs as shown in Fig. 1.11. Heavy quarks lose energy via elastic and inelastic scatterings in the QGP as described later in Sec. 1.7.1 and thus their

phase-space distribution such as a momentum distribution is modified. Therefore, the modification of their momentum distribution between initial and final state in heavy-ion collisions strongly reflects the QGP dynamics. The momentum distribution in the initial state can be expected with $p + p$ collisions scaled by the number of nucleon collisions in Au+Au because the production of heavy quarks is limited in the initial gluon scattering, namely no production in the QGP. The modification of momentum distribution of heavy quarks is calculated by comparing Au+Au and $p + p$ collisions. In addition, perturbative QCD (pQCD) precisely calculate the initial momentum distribution of heavy quarks and thus provides knowledge of the QGP physical property such as η/s and gluon density by comparison between measured data and expected modification of momentum distribution with an energy loss model.

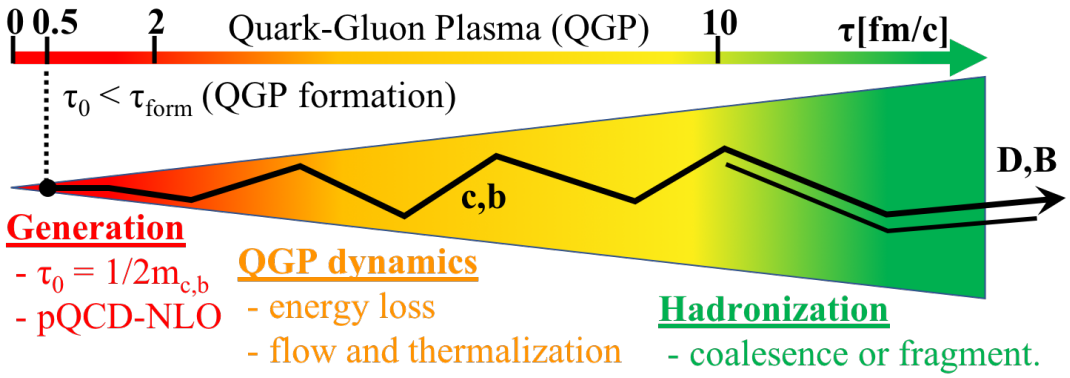

Figure 1.11: A heavy quark production and propagation in heavy-ion collision.

1.7.1 Energy Loss of Heavy Quarks in QGP

Initial scattering partons having high p_{T} propagate through the QGP while losing its energy. Measurement of fraction of parton energy loss is proposed as prove of the QGP dynamics in 1982 [20]. In order to realize this measurement, it is necessary to understand the energy loss mechanism theoretically. However, the energy loss mechanism is still not well understood. According to recent theories, the energy loss mechanism is classified into collisional and radiative energy loss as shown in Fig. 1.12. The collisional energy loss denotes elastic scattering which dominates in low p_{T} region. On the other hand, the radiative energy loss denotes inelastic scattering (i.e. gluon radiation) which dominates in high p_{T} region. These can be expressed in the following equations.

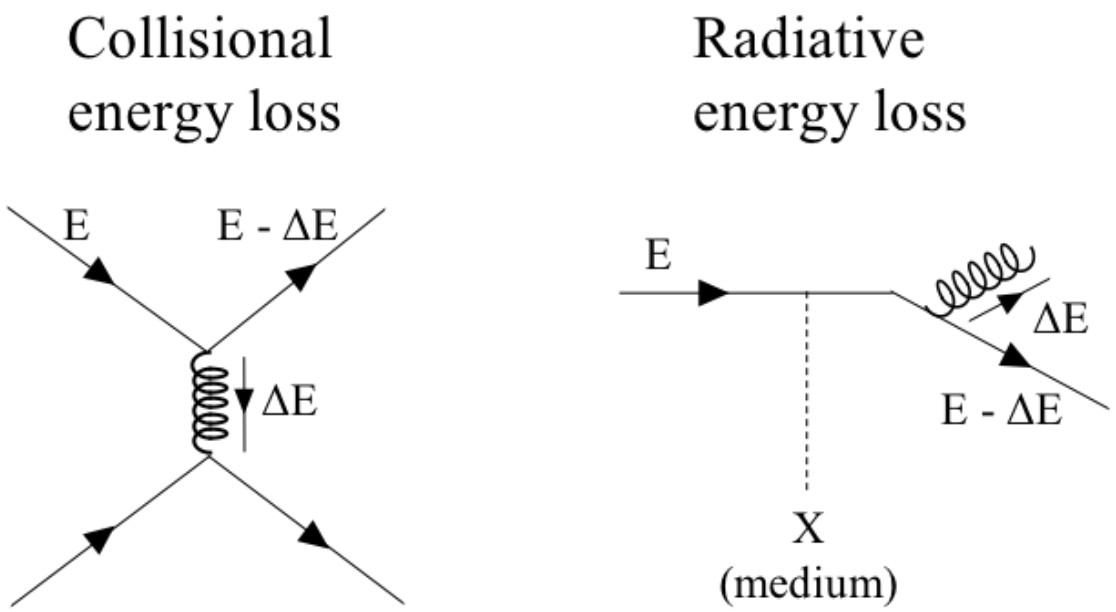

Figure 1.12: A diagram of a collisional energy loss (left) and a radiative energy loss (right).

1. Collisional energy loss [20, 21, 22] described as

$$\frac{dE^{col.}}{dx} = C_R \pi \alpha_s^2 T^2 \left(1 + \frac{n_f}{6}\right) f(v) \log(\mathrm{B_c}), \tag{1.7}$$

where C_R is the color Casimir factor, n_f is active quark flavors, T is temperature. The Coulomb log term is controlled by the ratio B_c which is denoted as

$$B_{TG} = \left(\frac{4pT}{(E_p - p + 4T)}\right)/(\mu), \tag{1.8}$$

$$B_{BT} = \begin{cases} (2^{\frac{n_f}{6+n_f}} 0.85 E_p T)/(\frac{\mu^2}{3}) & (E_p \gg \frac{M^2}{T}), \\ (4^{\frac{n_f}{6+n_f}} 0.36 \frac{(E_p T)^2}{M^2})/(\frac{\mu^2}{3}) & (E_p \ll \frac{M^2}{T}), \end{cases} \tag{1.9}$$

where $E_p = \frac{2M^2}{T}$ is taken for numerical computation around the crossover between $E_P \ll \frac{2M^2}{T}$ and $\frac{2M^2}{T} \ll E_P$. Theories indicate that dE/dx becomes smaller with increasing quark mass (M or $E_p - p$) shown in the Coulomb log term B_c.

2. Radiative energy loss (DGLV model [23]) described as

$$\frac{dE^{rad.}}{E} = \frac{C_F \alpha_s}{\pi} \frac{L}{\lambda_g} \int_{\frac{m_g}{E_p+p}}^{1-\frac{M}{E_P}+p} dx \int_0^\infty \frac{4\mu^2 q^3 dq}{\left(\frac{4E_x}{L}\right)^2 + (q^2+\beta^2)^2} A, \tag{1.10}$$

where C_F is the color Casimir factor, α_s is the coupling constant, L is path length of the medium, and

$$\beta^2 = m_g^2(1-x) + M^2x^2, \quad (1.11)$$

$$\lambda_g^{-1} = \rho_g\sigma_{gg} + \rho_q\sigma_{qg}, \quad (1.12)$$

$$\sigma_{gg} = \frac{9\pi\alpha_s^2}{2\mu^2}, \quad (1.13)$$

$$\sigma_{qg} = \frac{4}{9}\sigma_{gg}. \quad (1.14)$$

A is a correction term. The quark mass M is included in the denominator of DGLV model. It also indicates that dE/E becomes smaller with increasing quark mass.

Theories expect the quark mass dependence of both the collisional and radiative energy loss in the QGP. Fig. 1.13 shows fractions of collisional and radiative energy loss as a function of the energy for each quark flavor [19]. The theory assumes the path length of the Bjorken expanding QGP with L = 5 fm, the initial gluon density $\frac{dN_g}{dy} = 1000$, and the coupling $\alpha_s = 0.3$. These model calculations suggest the mass ordering of energy loss in the QGP, $\Delta E_{u,d} > \Delta E_c > \Delta E_b$.

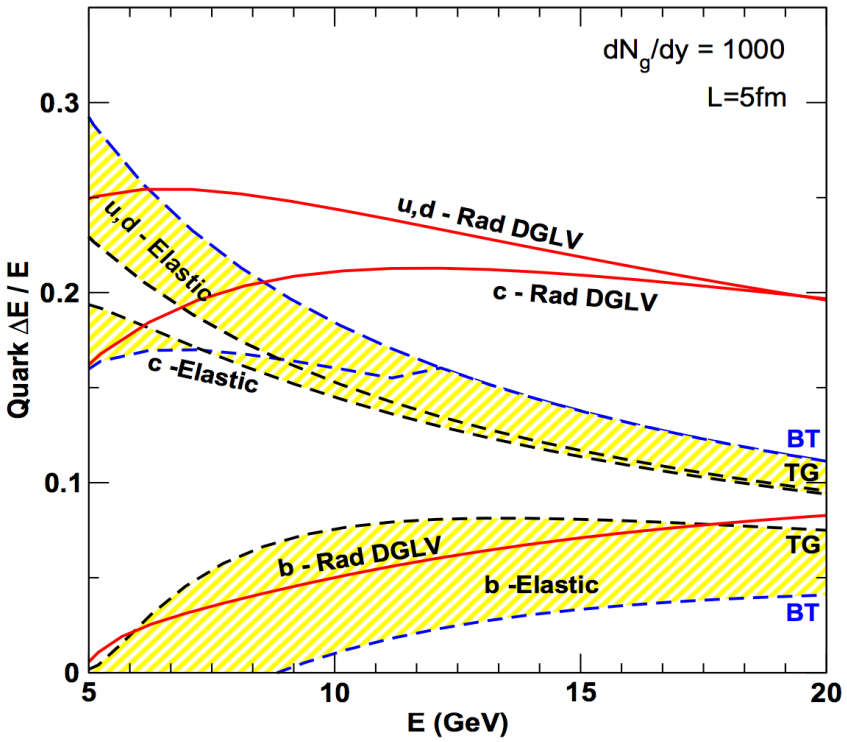

Figure 1.13: The fraction of energy loss as a function of the energy for each quark flavors [19].

Especially, the fractional energy loss of bottom quark is completely different from other quarks. The measurement of bottom quarks is an important subject to

understand the quark mass dependence of energy loss. It has not been sufficiently done so far because of high backgrounds and very low production rate compared with other quarks.

1.7.2 Nuclear Modification Factor of Heavy Quarks

One of the major measurement quantities for the QGP study is the nuclear modification factor $R_{\rm AA}$ which visualizes a degree of modification of the $p_{\rm T}$ distribution due to medium effects. The nuclear modification factor $R_{\rm AA}$ is calculated by the ratio of the invariant yield in Au+Au collisions to the yield in $p+p$ collisions scaled by the number of nuclear collisions $N_{\rm coll}$ as:

$$R_{\rm AA} = \frac{dN_{AA}}{T_{AA} \times \sigma_{pp}} = \frac{dN_{AA}}{< N_{\rm coll} > \times dN_{pp}}. \tag{1.15}$$

$R_{\rm AA} < 1.0$ shows yield suppression. The invariant yield of inclusive heavy flavor decay electrons ($c + b \rightarrow e$) in $p+p$ and Au+Au as shown in Fig. 1.14 [10]. The substantial modification of transverse momentum ($p_{\rm T}$) of heavy quarks has been found.

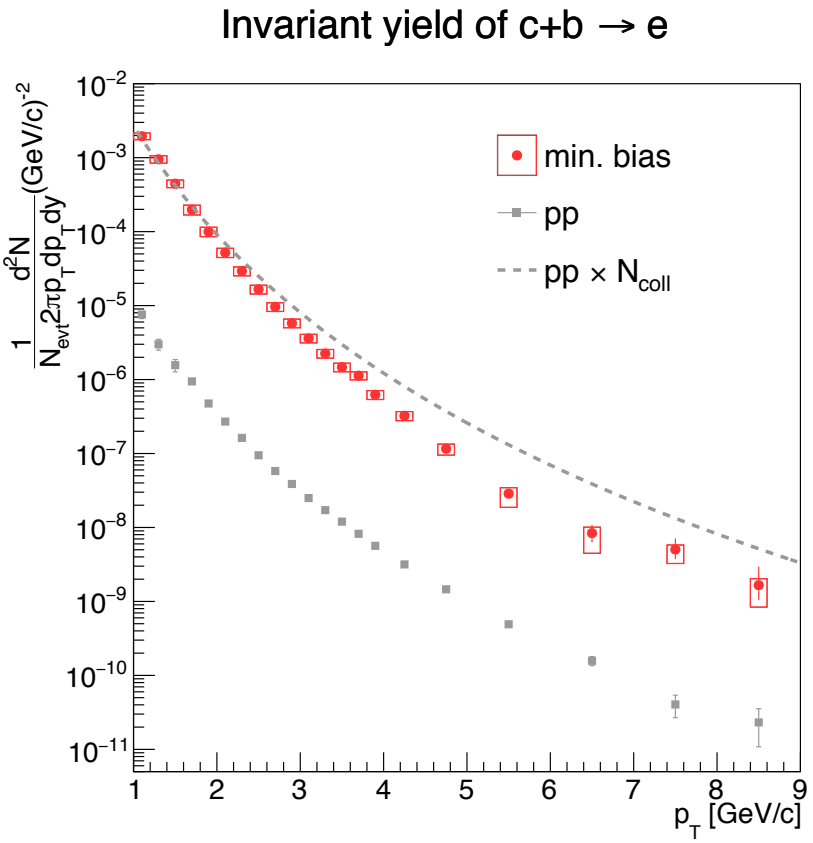

Figure 1.14: The previous measured invariant yield of $c + b \rightarrow e$ in $p+p$ and Au+Au and the $N_{\rm coll}$ scaled yield in $p+p$ [10, 41].

In order to study suppression order, $R_{\rm AA}$ of $c + b \rightarrow e$ has been calculated as shown in Fig. 1.15 [10]. It shows the strong yield suppression in Au+Au collisions and indicates large energy loss of heavy quarks in the QGP. If no modification of $p_{\rm T}$ distribution in Au+Au collisions, $R_{\rm AA}$ should be unity because the initial $p_{\rm T}$ distribution in Au+Au collisions should be described as the $N_{\rm coll}$ scaled that in $p + p$ collisions. The reason of modification of momentum distribution is the energy loss in the medium and the Cold-Nuclear-Matter (CNM) effects [41] such as Cronin enhancement, a shadowing of parton distribution, and energy loss in cold nuclear matter. $R_{\rm AA}$ of heavy quarks in d +Au assuming no QGP has been also measured to study the CNM effects. It shows slightly increase yield due to mainly Cronin enhancement and indicates no significant suppression due to CNM effects [41]. Therefore, the difference of $R_{\rm AA}$ between Au+Au and d +Au collisions shows the yield suppression due to the energy loss in the QGP. The yield suppression depends on $p_{\rm T}$, no suppression at low $p_{\rm T}$ ($\sim$ 1 GeV/c) but the substantial suppression at high $p_{\rm T}$ ($>$ 5 GeV/c).

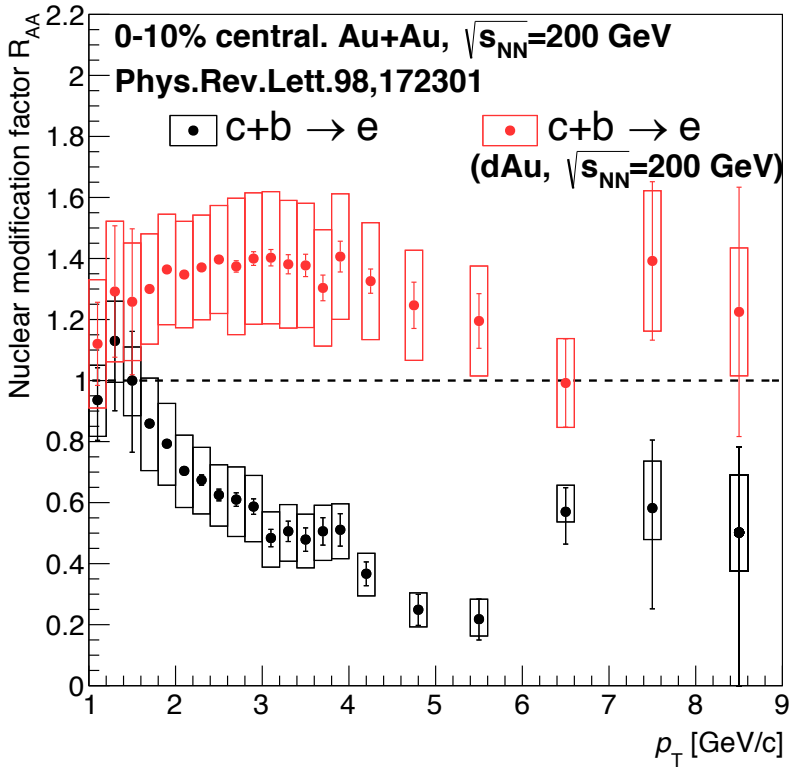

Figure 1.15: The nuclear modification factor $R_{\rm AA}$ of $c + b \rightarrow e$ as a function of $p_{\rm T}$ in Au+Au and d +Au collisions [10].

The substantial yield suppression of inclusive heavy quarks ($c + b \rightarrow e$) at high $p_{\rm T}$ was a big surprise at the time of this discovery. It was expected that heavy quarks hardly lose energy in the QGP because heavy quarks have large

mass compared with QGP temperature. Thus, we need to reconsider the energy loss mechanism and its quark mass ordering with measurement of the separated $R_{\rm AA}$ of $c \rightarrow e$ and $b \rightarrow e$. In the previous measurement, we have measured the separated $R_{\rm AA}$ of $c \rightarrow e$ and $b \rightarrow e$ in minimum bias Au+Au collisions as shown in Fig. 1.16 [11]. It indicates that $R_{\rm AA}$ of $b \rightarrow e$ is higher than $R_{\rm AA}$ of $c \rightarrow e$ for $3.0 < p_{\rm T} < 4.0$ GeV/c. However, there is no significance for 4.0 GeV/c $< p_{\rm T}$ because of large uncertainty. The $p_{\rm T}$ range in this measurement is limited because the baseline measurement in $p+p$ [42] performed for $3.0 < p_{\rm T} < 8.0$ GeV/c. In order to give further understanding of the quark mass dependence of the energy loss, the measurement of centrality dependent $R_{\rm AA}$ of separated $c \rightarrow e$ and $b \rightarrow e$ with high statistics data and precise baseline is measured in this dissertation. Ultimately, we aim to understand the QGP dynamics along with the energy loss mechanism by a comparison between the measured $R_{\rm AA}$ and the theoretical calculation.

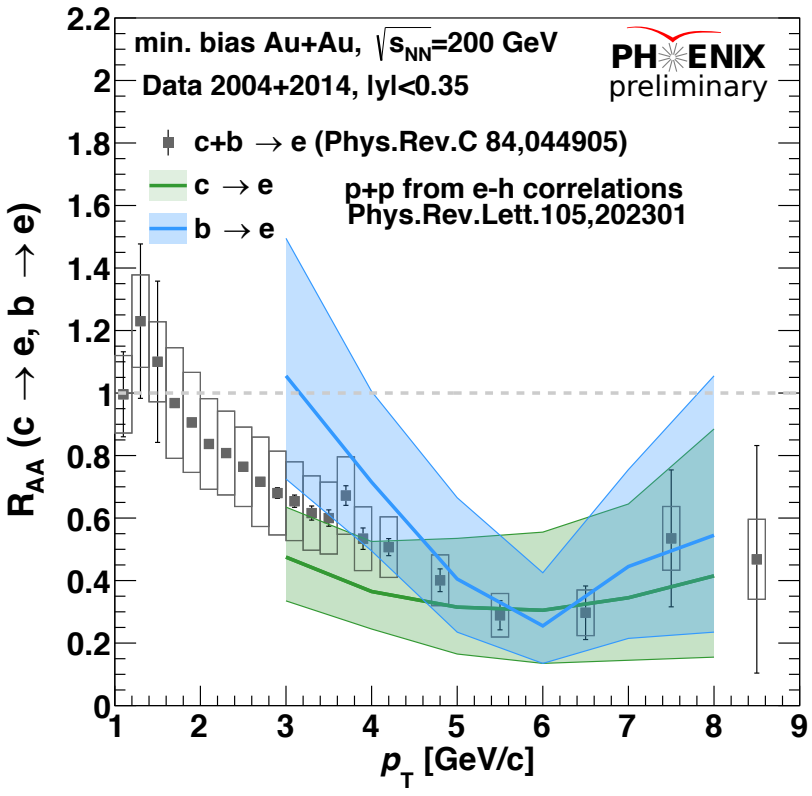

Figure 1.16: The nuclear modification factor $R_{\rm AA}$ of $c \rightarrow e$ (green) and $b \rightarrow e$ (blue) as a function of $p_{\rm T}$ in Au+Au collisions [11].

Chapter 2

Experimental Setup

2.1 Relativistic Heavy Ion Collider (RHIC)

The Relativistic Heavy Ion Collider (RHIC) is one of only two heavy ion colliders and composed of two independent superconducting accelerator rings, located at Brookhaven National Laboratory, Upton, New York. RHIC accelerator complex is composed of a chain of 6 accelerators as shown in Fig. 2.1. Heavy ions (e.g. Au, Cu and U) are generated in the Electron Beam Ion Source (EBIS) accelerator and transported while accelerating by Linear Accelerator and Booster Synchrotron to Alternating Gradient Synchrotron (AGS). AGS is the first accelerator built on the concept of the alternating gradient and strong-focusing principle [54], which is capable to accelerate heavy ions up to 10 GeV/nucleon. Finally, AGS-To-RHIC Transfer Line (ATR) transports heavy ions to RHIC. RHIC is capable to collide variety of ions and nucleons up to $\sqrt{s} = 500$ GeV for $p + p$ and $\sqrt{s_{NN}} = 200$ GeV for Au+Au. There are 6 interaction regions and 4 experimental halls, PHENIX, STAR, PHOBOS, and BRAHMS. RHIC has 3.8 km circumference with 112 bunches and the designed luminosity is 2×10^{26} cm^{-2}sec^{-1} for heavy ions. A luminosity denotes performance of an accelerator defined as

$$\mathcal{L} = \frac{f_{\rm rev} B N_Y N_B}{4\pi \sigma_H^* \sigma_V^*}, \tag{2.1}$$

where $f_{\rm rev}$ is the revolution frequency ($\sim$ 79 kHz at RHIC), B is the number of bunches, σ_H^* (σ_V^*) is the beam size in the horizontal (vertical) axis. RHIC design performance is shown in Table 2.1.

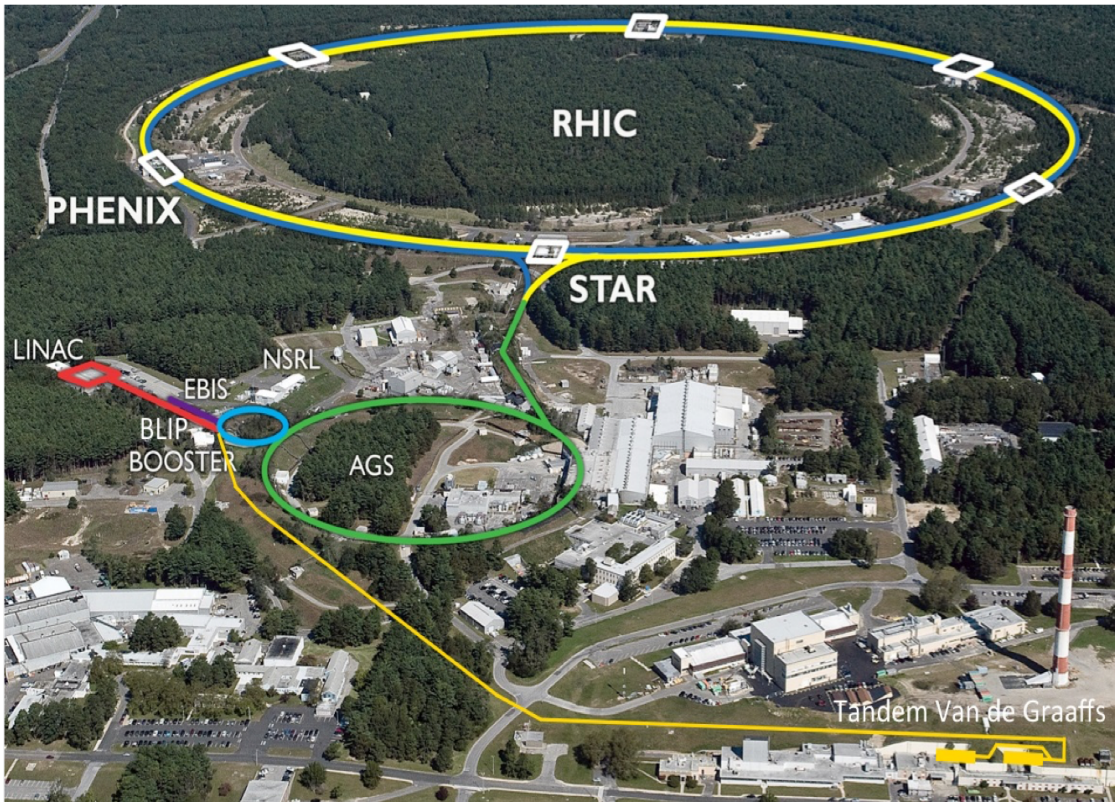

Figure 2.1: RHIC accelerator complex [56].

Table 2.1: RHIC design performance.

	p+p	Au+Au
Beam energy	250 GeV	200 GeV
Number of bunches	112	112
Ions/bunch [10^9]	200.	1.3
β^* [m]	1.0	1.0
Emittance [μm]	20	40
Peak luminosity [$\mathrm{cm}^{-2}/\mathrm{s}^{-1}$]	225×10^{30}	17×10^{28}
Average luminosity [$\mathrm{cm}^{-2}/\mathrm{s}^{-1}$]	150×10^{30}	10×10^{28}

2.2 The PHENIX Detector

Pioneering High Energy Nuclear Interactions eXperiment (PHENIX) is one of the major experiment at RHIC. The PHENIX detector is designed specifically for measurement of electrons and photons at mid-rapidity and muons at forward rapidity. It is composed of 2 central arms with $\pm$ 0.35 pseudo-rapidity and each covering azimuthal 90 degrees, and 2 muon arms with pseudo-rapidity $1.2 < |y| < 2.2$ (or 2.4) as shown in Fig. 2.2 and 2.3.

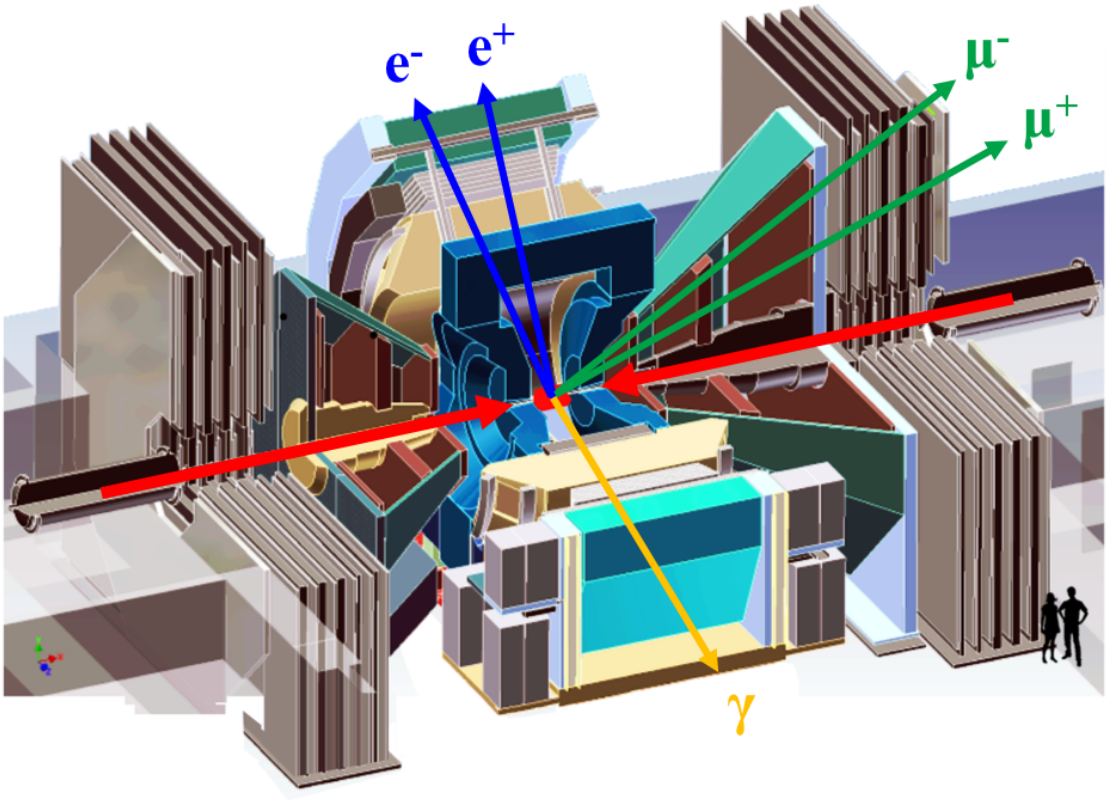

Figure 2.2: Schematic of PHENIX detector complex [43].

2.2.1 Beam-Beam Counter

The Beam-Beam Counter (BBC) [48] is composed of 64 elements, quartz Čerenkov radiators and meshed dynode PMTs as shown in Fig. 2.4 and located at ±144.35 cm from the nominal interaction point along the beam line, and cover the full azimuthal angle in pseudo-rapidity ($3 < |y| < 3.9$). The inner diameter is 10 cm with clearance between the beam pipe and the BBC of 1 cm and the outer diameter of the BBC is 30 cm.

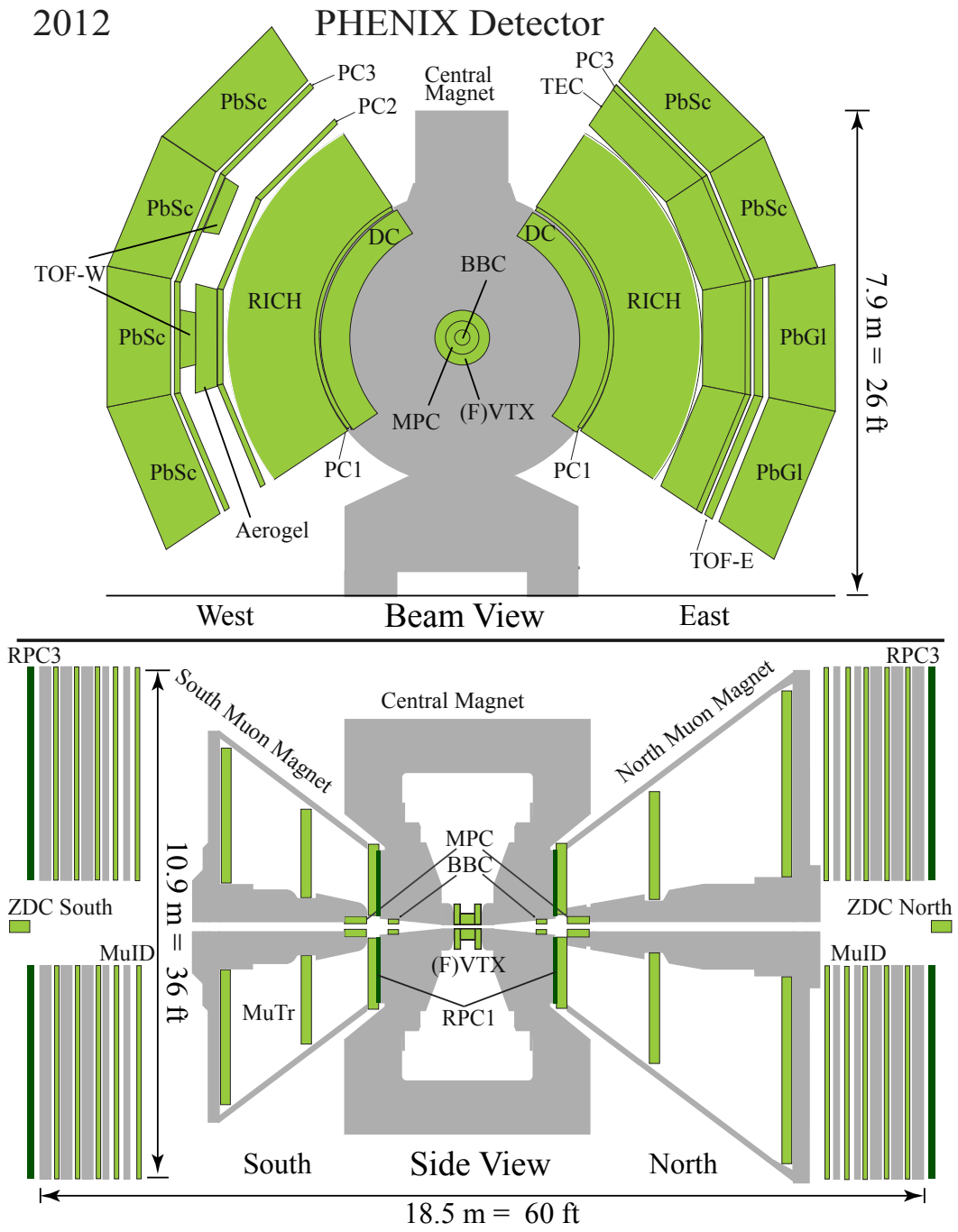

Figure 2.3: Schematic of the PHENIX experimental setup in 2012, which is the same in 2014 and 2015 [43].

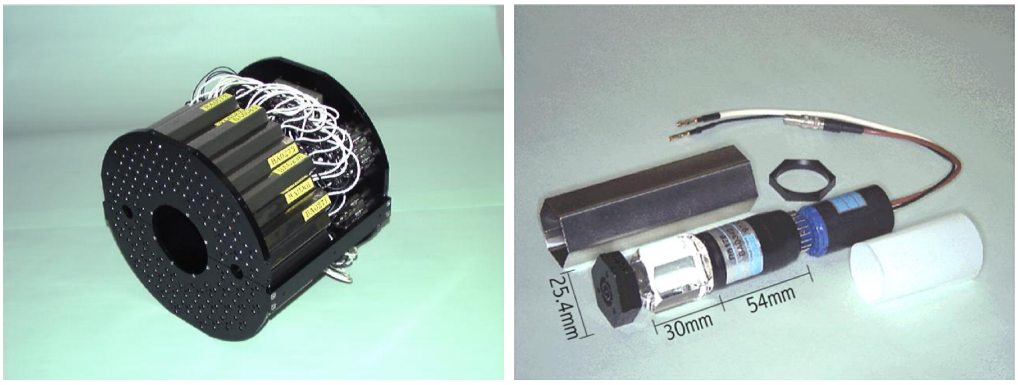

Figure 2.4: The Beam-Beam Counter (left) and One of elements consisting of the quartz Čerenkov radiator and the meshed dynode PMT (right) [48].

The main role of the BBC is to provide the minimum-bias (MB) trigger, to measure the collision vertex in the z-direction via the difference of the average hit time between the North and South side, and to determine the collision centrality via the number of measured charged particles as described later in Sec. 3.4. The MB trigger requires at least one hit for each BBC arrays and the z-vertex is within the North and South BBC arrays, which can detect 93% of a total inelastic cross-section.

2.2.2 Drift Chamber

The Drift Chambers (DC) [45] consists of two cylindrically shaped gas wire chambers and located in the radial region of 2.02-2.46 m from the z-axis as shown in Fig. 2.5. The role of DC is to measure charged particle trajectories in the r-ϕ plane to determine each particle p_{T} and a generation direction. The single wire resolution in the r-ϕ plane is better than 150 mm and the single wire two track separation is better than 1.5 mm.

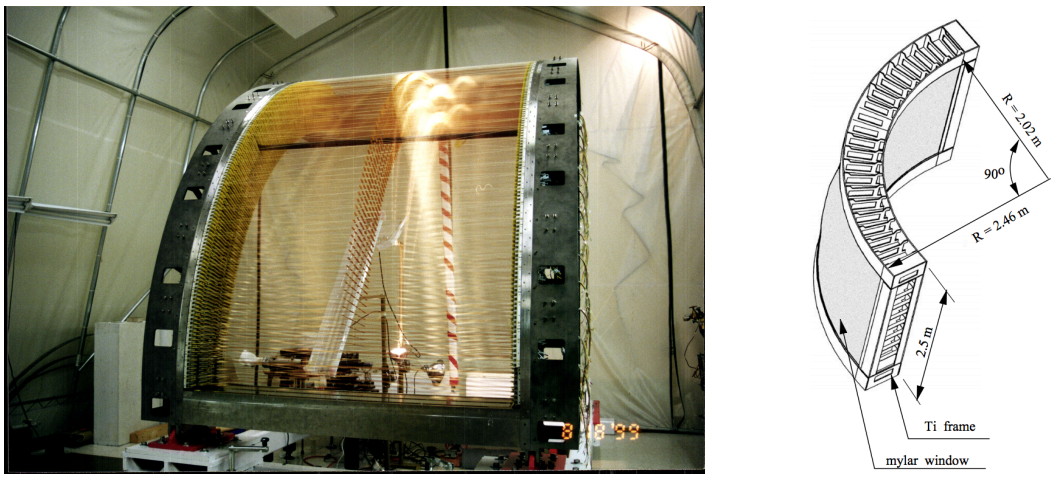

Figure 2.5: The Drift Chamber and the construction [45].

2.2.3 Pad Chamber

The Pad Chambers (PC) [45] are multi-wire proportional chambers consisting of three independent layers as shown in Fig. 2.6. PC1 is located outside DC, in the radial region of 2.47-2.52 m, and PC2 (PC3) is located outside RICH, in the radial region of 4.15-4.21 m (4.91-4.98 m), in the same r-ϕ plane. The PC is composed of two flat panels, the pixel panel and the cathode panel, and an anode wire electrode as shown in Fig. 2.6 (left). It also plays a role in tracking with the DC.

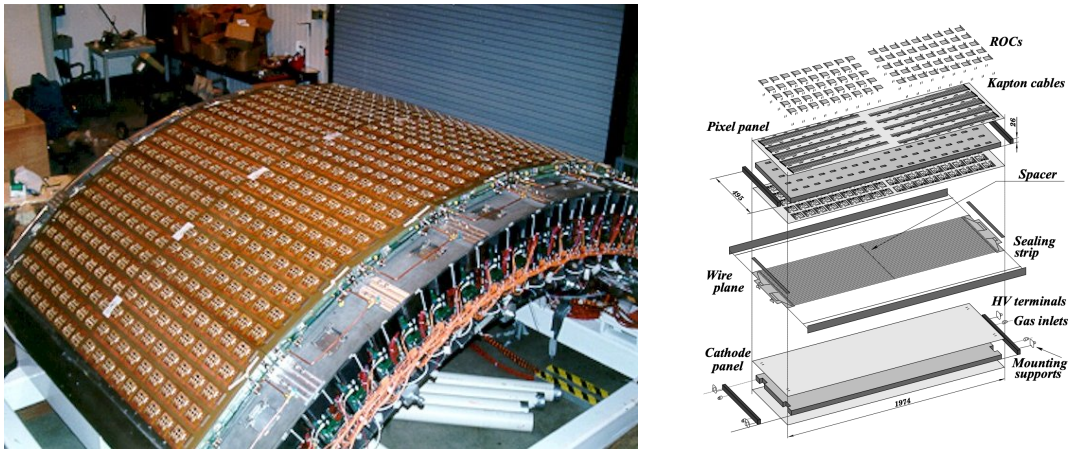

Figure 2.6: The Pad Chamber and the construction [45].

2.2.4 Ring Imaging Cherenkov Counter

The Ring Imaging Cherenkov Detector (RICH) is the primary detector of electron identification in PHENIX [46] and located in the radial region of 2.5-4.1 m. The RICH consists of the CO_2 gas radiator and two arrays of 1280 PMTs. Fig. 2.7 shows the function of the RICH detector which has a Čerenkov threshold of $\gamma = 35.0$ corresponding a momentum threshold of 18 MeV/c for electrons and 4.7 GeV/c for charged pions. Therefore, only electron radiates Čerenkov photons for $p_{\rm T} <$ 4.7 GeV/c. Emitted Čerenkov photons in CO_2 gas are reflected by thin spherical mirrors and are focused to arrays of PMTs to form a ring-shaped emission pattern.

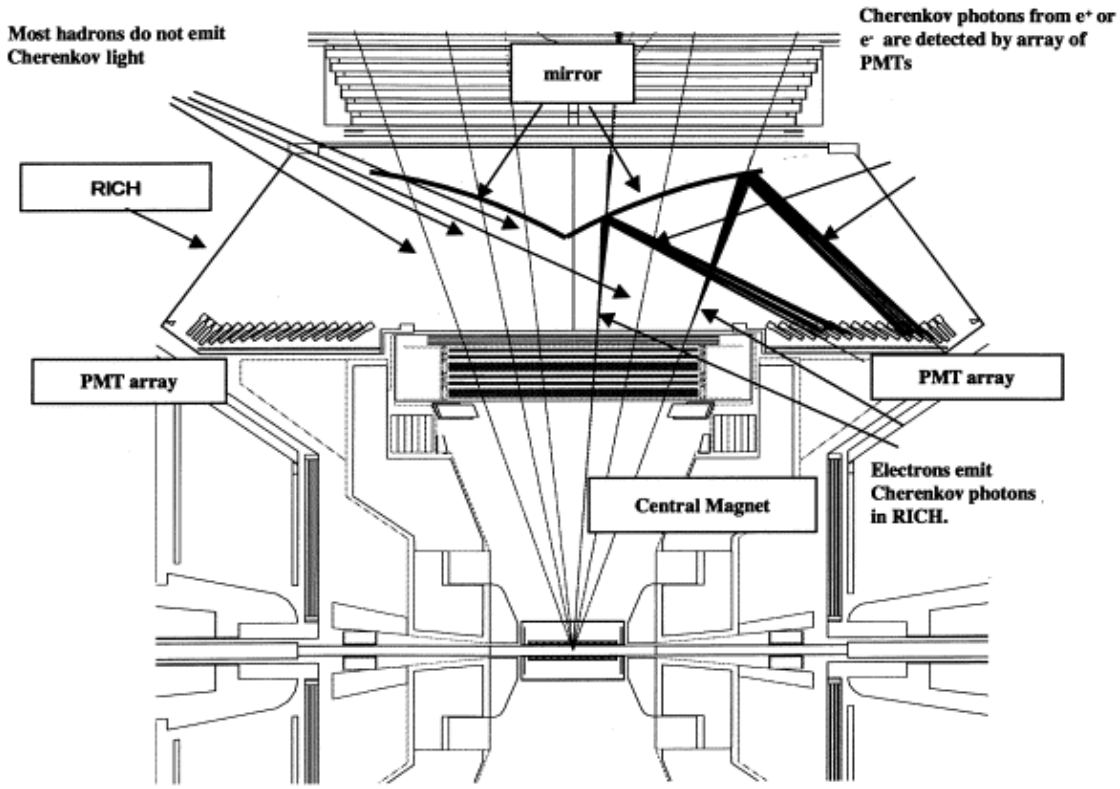

Figure 2.7: The function of the RICH detector [46].

Fig. 2.8 shows the pion rejection as a function of the electron efficiency. RICH has capable to reject charged pions to 1/1000 with electron efficiency = 0.7.

2.2.5 Electromagnetic Calorimeter

The Electromagnetic Calorimeter (EMCal) [47] is to measure the energy and the spatial position of electrons and photons and plays a major role in electron identification. It occupies the full central spectrometer acceptance in pseudorapidity $|\eta| < 0.35$ and azimuthal angle $\pi/2$. EMCal consists of two calorimeter types, lead-glass (PbGl) and lead-scintillator (PbSc). The PbSc calorimeter is a Shashlik-type sampling electromagnetic calorimeters comprising 15,552 towers and has 18.2 X_0 radiation length and ∼6 cm Moliere radius. The energy resolution of PbSc is $8.1\%/\sqrt{E(GeV)} \bigoplus 2.1\%$ and an intrinsic timing resolution better than 200 ps for electromagnetic showers. On the other hand, the PbGl is a Čerenkov type calorimeter, consisting of 9,216 towards having 14.4 X_0 radiation length and ∼4 cm Moliere radius, which was previously used in CERN experiment WA98. The energy resolution of PbGl is $6\%/\sqrt{E(\mathrm{GeV})}$ and an intrinsic timing resolution of better than 300 ps for electromagnetic showers.

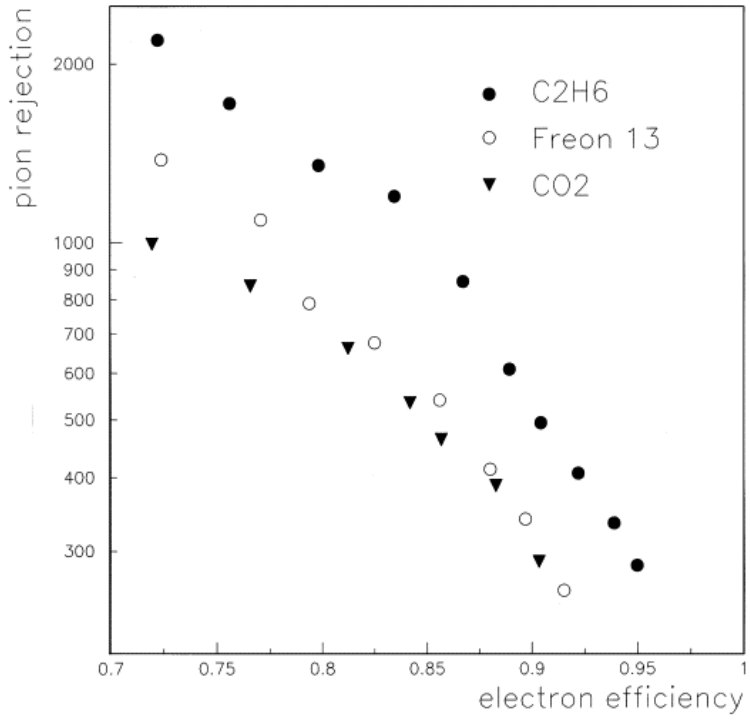

Figure 2.8: The pion rejection as a function of the electron efficiency. PHENIX uses CO_2 gas [45].

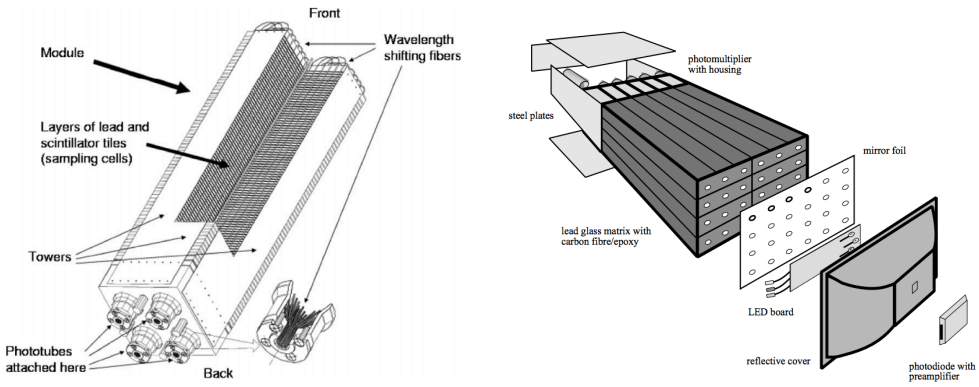

Figure 2.9: The towers of Electromagnetic Calorimeter with PbSc (left) and PbGl (right) [47].

Electrons and photons deposit almost all energy via electromagnetic shower at EMCal. The measured energy at EMCal enables to separate electron tracks from other charged particle tracks because non-electromagnetic particles do not deposit all energy as shown in Fig. 2.10.

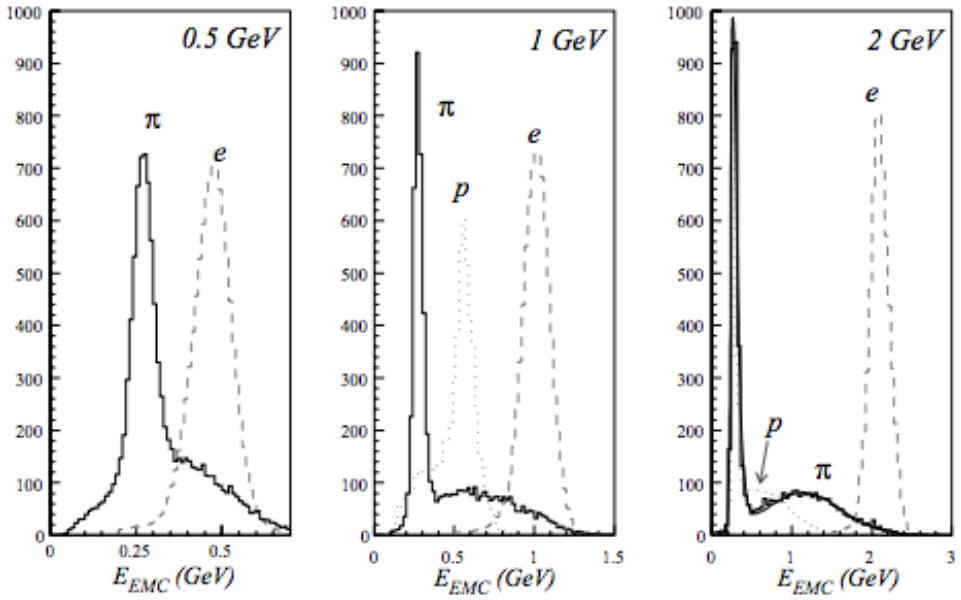

Figure 2.10: The measured energy at EMCal for π, p and e [47].

2.2.6 Silicon Vertex Tracker

The Silicon Vertex Detector (VTX) [50] is composed of 2 silicon pixel layers (B0 and B1) and 2 silicon stripixel layers (B2 and B3) covered pseudo-rapidity $|\eta| < 1.2$ and azimuthal range $\delta\phi \sim 0.8\ \pi$ as shown in Fig. 2.11. It is installed in 2011 to measure the precise collision points and obtain the precise displaced tracking information. The silicon pixel detector has 50 μm(ϕ) $\times$ 425 μm(z) pixel pitch size which provides 14.4 μm position resolution in the azimuthal direction. The B0 (B1) layer is composed of 10 (20) ladders at the radial distance of 2.6 (5.1) cm and the silicon pixel sensor is bounded with the readout chip by a bump, which was developed at CERN [52]. The one-pixel ladder has 4 sensor modules and the one sensor module has 4 readout chips. The number of pixel channels in one readout chip is at B0 (B1) is 256(ϕ)$\times$32(z) and the total number of pixel channels at B0 (B1) is 1.3×10^6 (2.6×10^6). The VTX material is 1.3% radiation length (X_0) for each pixel layer.

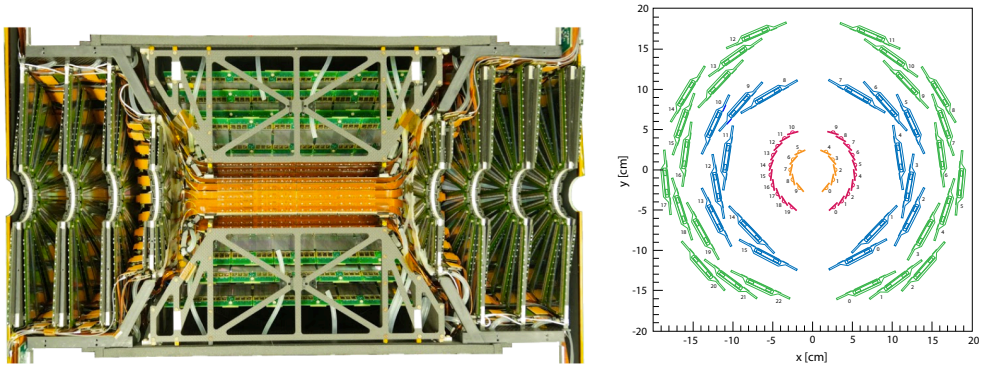

Figure 2.11: The silicon vertex tracker (left) and the beam view of each VTX ladder position, different colored layers (right) [51].

The silicon strip detectors are composed of the silicon stripixel sensors, which was developed at BNL [53]. The B2 (B3) layer is composed of 16 (24) silicon stripixel ladders at the radial distance of 11.8 (16.7) cm and have an effective size of $80\mu\text{m}(\phi) \times 1000\mu\text{m}(z)$ which provides $\sigma_\phi = 23$ μm position resolution. The total number of stripixel channels at B2 (B3) layer is 1.2×10^5 (2.2×10^5) and the material budget is 5.2% X_0 for each stripixel layer. The summary of VTX characteristics is shown in Table 2.2.

Table 2.2: The summary table of VTX parameters

	r (cm)	l (cm)	t (μm)	N_{ladder}	pixel/strip size(μm)	N_{ch}	X_0
B0 pixel layer	2.6	22.8	200	10	50 μm(ϕ), 425 μm(z)	1.3×10^6	1.3
B1 pixel layer	5.1	22.8	200	20	50 μm(ϕ), 425 μm(z)	2.6×10^6	1.3
B2 strip layer	11.8	31.8	625	16	80 μm(ϕ), 3×10^4 μm(z)	1.2×10^6	5.2
B3 strip layer	16.7	38.2	625	24	80 μm(ϕ), 3×10^4 μm(z)	2.2×10^6	5.2

2.3 Data Acquisition

PHENIX Data Acquisition system (DAQ) collects signals from each detector, issues each trigger, digitizes the analog signal, combines each data event by event. PHENIX Local Level-1 (LVL1) trigger is produced by BBC hit information. Therefore, the readout timing of BBC is adjusted with the RHIC beam clock by Master Timing Module (MTM) and other detectors are adjusted with BBC readout timing by Granule Timing Module (GTM). Firstly, signals from each detector are read out with LVL1 trigger and digitized at Front End Module (FEM). Secondly, the Data Collection Module (DCM) executes a data buffering, a zero suppression, and a compression of data. Finally, digital signals from each detector are combined for each collision event at Event Builder (EvB) and transported to the High-Performance Storage System (HPSS).

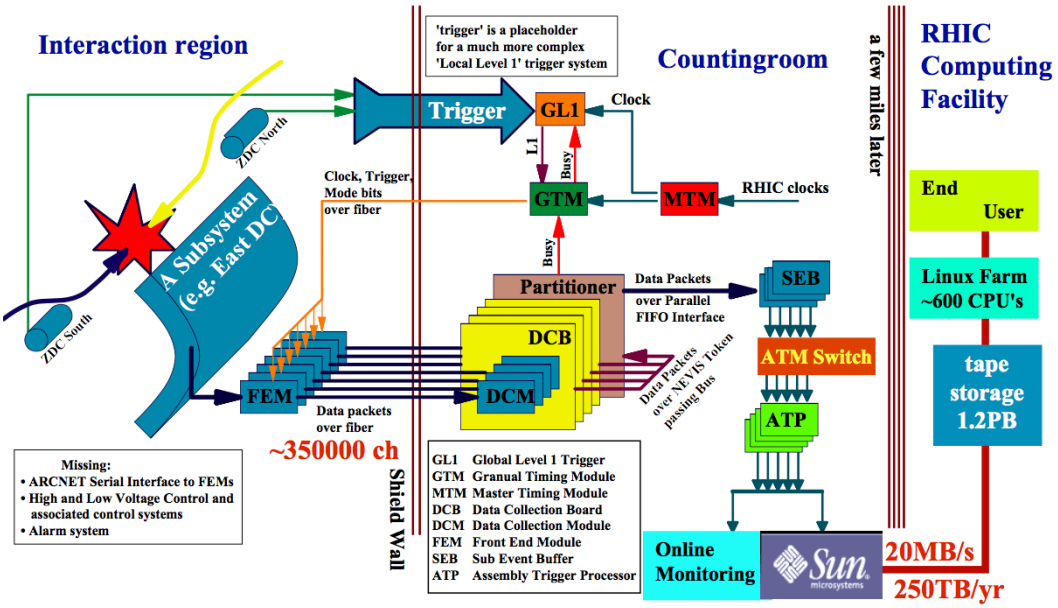

Figure 2.12: PHENIX data acquisition system [55].

Chapter 3

RHIC Year-2014 Au+Au Run at PHENIX

3.1 Summary of RHIC Year-2014 Au+Au Run

The RHIC Year-2014 (Run14) Au+Au collisions at $\sqrt{s_{NN}}$ = 200 GeV runs 13.3 weeks with focus on heavy flavor measurements. Table 3.1 shows summary of the RHIC Run14.

Table 3.1: RHIC Run14 status

Collision spieces	Beam energy [GeV/nucleon]	Number of bunches	Ions/bunch	β^* [m]
$^{197}Au^{79+}$ + $^{197}Au^{79+}$	200	111	1.6	0.7 $\rightarrow$ 0.5

Emittance (RMS) [μm]	Peak luminosity [cm^{-2}/s^{-1}]	Average luminosity [cm^{-2}/s^{-1}]	Run time [weeks]	Total luminosity [nb^{-1}] at PHENIX
2.5 $\rightarrow$ 0.65	84×10^{26}	50×10^{26}	13.3	23.1

In Run14, RHIC performed high-luminosity Au+Au collisions with the 3D beam cooling system and PHENIX collected collision data smoothly. The integrated luminosity reached 23.1 nb^{-1} which is 5 times higher than the previous Au+Au run (year-2011) as shown in Fig. 3.1.

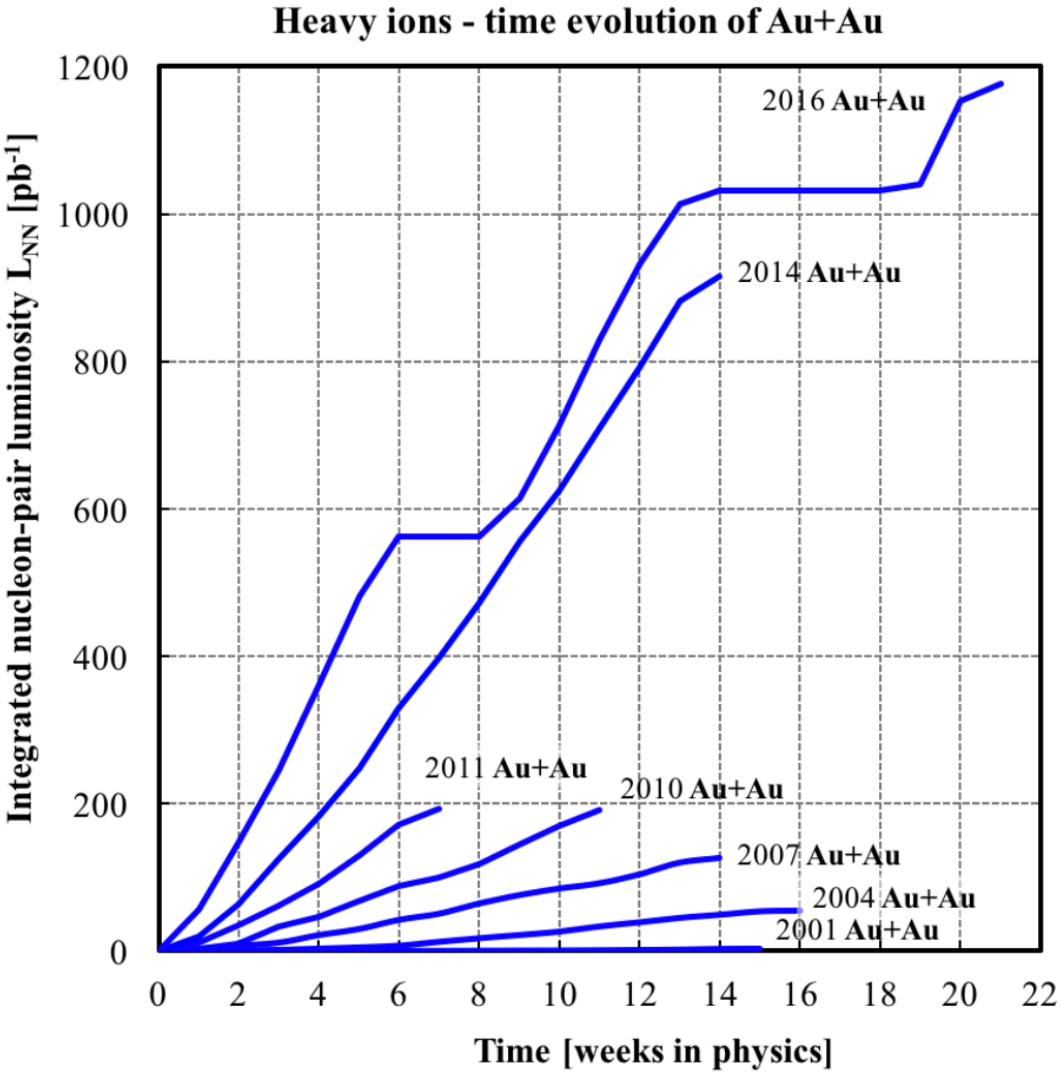

Figure 3.1: The integrated luminosity as a function of time for each year [57].

3.2 Collision Point and Beam Spot-size

PHENIX geometry is defined as shown in Fig. 3.2. PHENIX z-axis denotes the RHIC beam direction. RHIC adjusted collision points to the center of PHENIX geometry (0,0,0). However, the adjustment is not perfect and the Au beam has width with root mean square (RMS) = 0.65 μm and length with 0.3 m. PHENIX measures the collision point event by event with the distance of closest approach of all measured charged tracks.

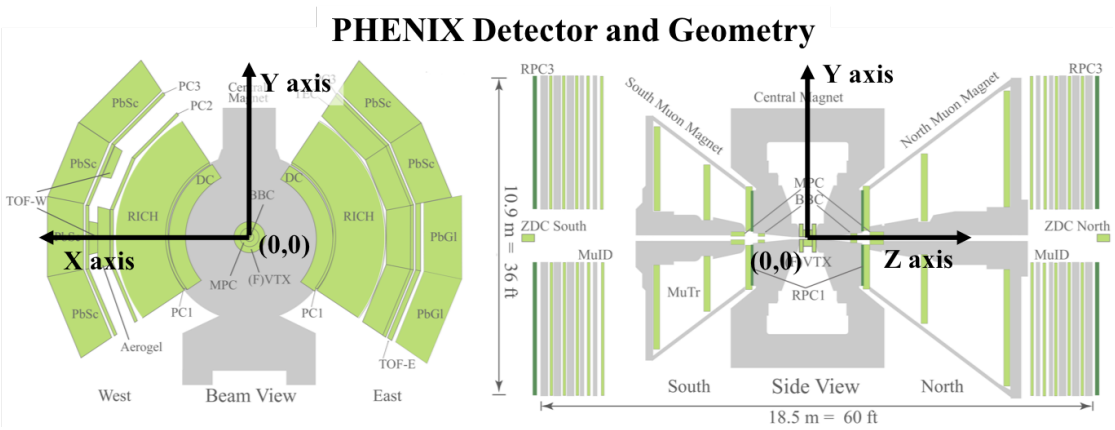

Figure 3.2: The PHENIX detector and geometry definition [43].

Fig. 3.3 shows measured collision points (e.g. primary vertex points). The beam offset from the PHENIX center is 3.43 mm in X-axis and 0.43 mm in Y-axis. On the other hand, collision points in Z-axis flatly distribute in the acceptance of the silicon vertex detector (-10 cm $\sim$ 10 cm) because bunch length is longer. The measured vertex points will be used to calculate momentum of charged particles and the distance of closest approach between the vertex point and each track.

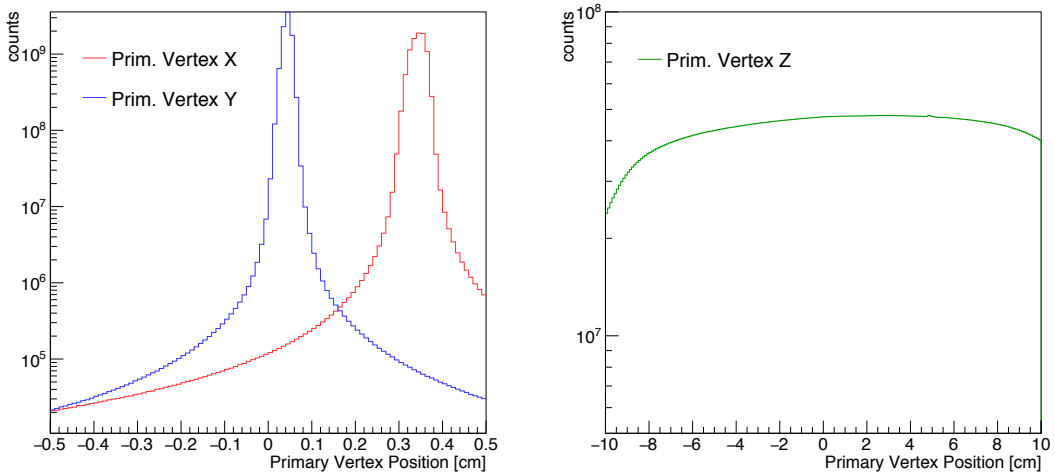

Figure 3.3: The measured primary vertex points in x-y plane (left) and z-direction (right).

3.3 Minimum-bias Trigger Efficiency

3.4 Centrality Determination

In order to systematically study the QGP, we measure the physical quantities as a function of the QGP size. The function of collision centrality is used instead of the QGP size because the size of QGP cannot be measured directly. It is determined by a multiplicity of charged particles because the particle multiplicity strongly depends on a medium volume created by heavy ion collisions. In PHENIX, the collision centrality is determined by the number of charged particles at BBC detector as shown in Fig. 3.4.

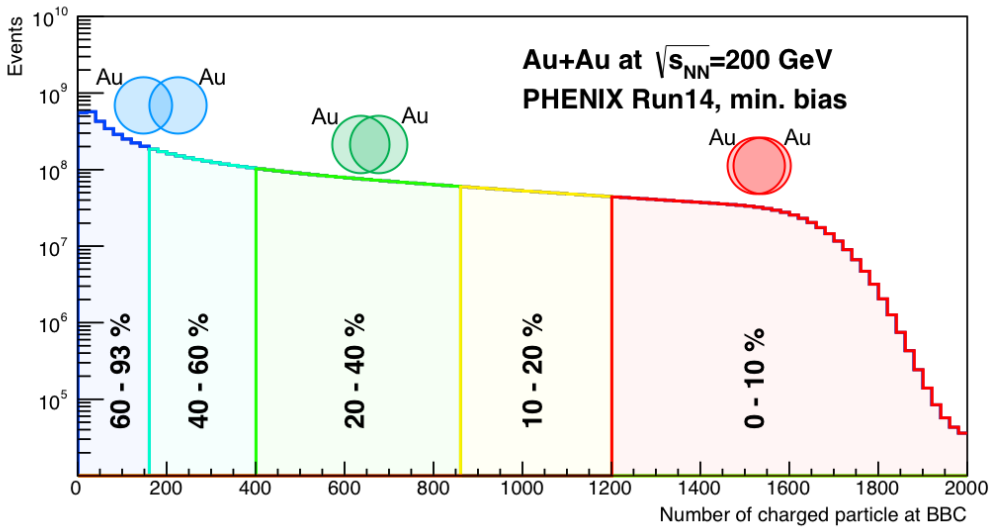

Figure 3.4: Number of charged particles measured at BBC and the centrality determination.

In this analysis, collision events are classified to 5 centrality classes, 0-10%, 10-20%, 20-40%, 40-60%, and 60-93%. 0-10% centrality denotes the most central collisions, namely the highest multiplicity events.

Chapter 4

Data Analysis 1 - Extraction of Heavy Flavor Decay Electrons

This chapter details an analysis method of inclusive electrons from charm and bottom hadron decays in Au+Au collisions at $\sqrt{s_{NN}}$ = 200 GeV. The first section shows the data set for this analysis and describes event and track selection methods.

4.1 Track Reconstruction and Particle Identification

4.1.1 Momentum Reconstruction

A track of charged particles is reconstructed by DC and PC1 using a combinatorial Hough transform (CHT) technique [10]. Fig. 4.1 shows a schematic view of a track, where ϕ is the polar angle at the interaction point for the reference radius at the mid-radius of the drift chamber, α is the inclination angle of the track at the intersection point with reference radius of the DC.

A transverse momentum of charged tracks is defined as:

$$p_{\mathrm{T}} = \frac{K}{\alpha}, \tag{4.1}$$

where K denotes the effective field integral which is expressed as:

$$K = \frac{e}{R}\int Bdl, \tag{4.2}$$

where R is the DC radius (= 220 cm), e is the elementary charge (= 0.2998 GeV/c $\mathrm{T}^{-1}\mathrm{m}^{-1}$), K = 104 mrad GeV/c. Fig. 4.2 shows an example of DC hits in Au+Au central collisions by HIJING simulation. In experimental α and ϕ are only calculated for a track having momentum $p > 150$ MeV/c separated in azimuthal angle to minimize computation time.

The momentum resolution depends on the multiple scattering in DC material and the angle resolution (the interval of wires) of the DC, which is calculated as

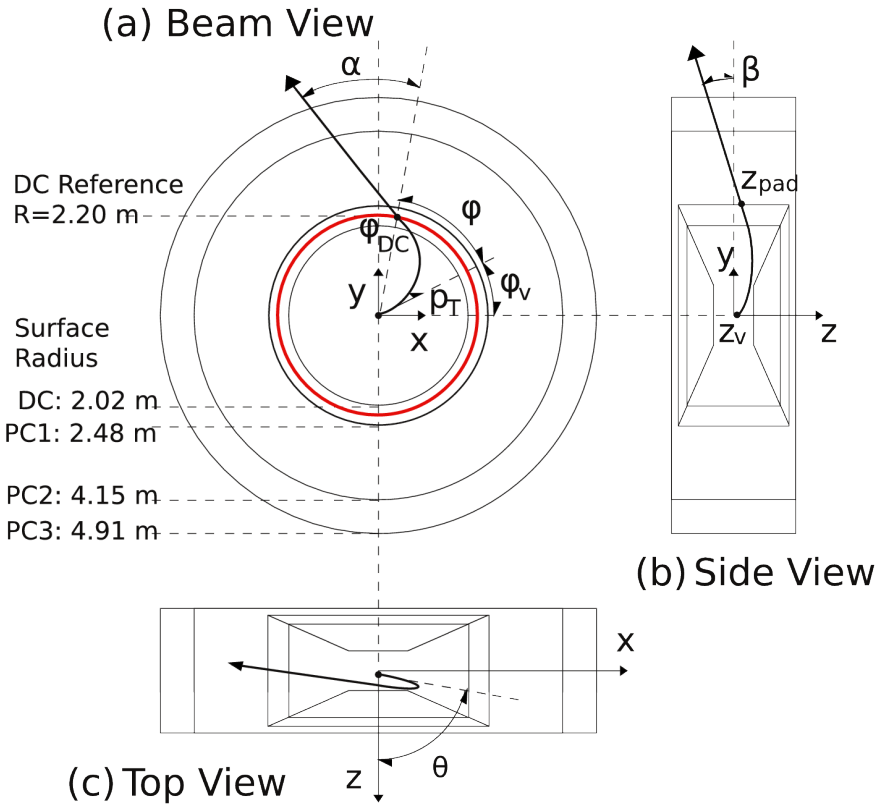

Figure 4.1: The schematic view of the track and momentum reconstruction [10].

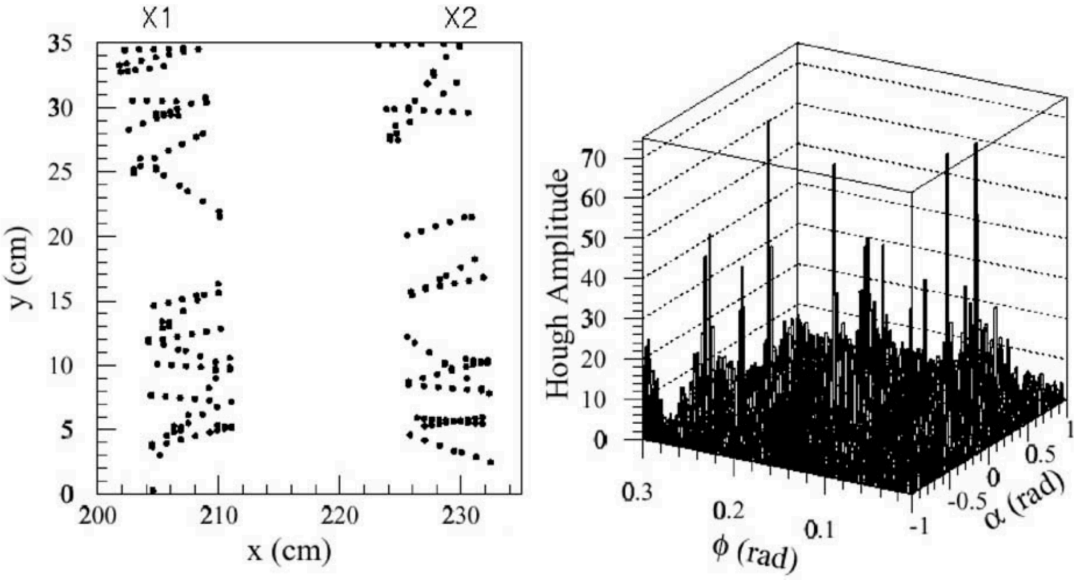

Figure 4.2: The event example of DC by HIJING simulation. Left: DC hit positions in the X1 and X2 wires. Right: A hough amplitude as a function of feature space as a function of ϕ and α [45].

the following equation.

$$\left(\frac{\delta p}{p}\right)^2 = \left(\frac{\delta\alpha}{\alpha}\right)^2 = \left(\frac{c_1}{\beta}\right)^2 + (c_2 p)^2, \tag{4.3}$$

$$c_1 = \frac{\sigma_{ms}}{K} = \frac{1}{K}\sqrt{\sum_i \left(\sigma^i_{ms}\frac{R_i}{R_{DC}}\right)^2}, \tag{4.4}$$

$$c_2 = \frac{\sigma^{int}_{\alpha}}{K}, \tag{4.5}$$

where p is a momentum, βc is a velocity, σ^{int}_{α} is the intrinsic angular resolution of the DC ($\sim$ 1.1 [mrad GeV/c^2]), σ^i_{ms} is a mean spread angle due to a multiple scattering expressed as [16]:

$$\sigma^i_{ms} = \frac{13.6\mathrm{MeV}}{\beta cp} z\sqrt{\frac{x}{X_0}}\left[1 + 0.038 \times \ln(\frac{\mathrm{x}}{\mathrm{X_0}})\right], \tag{4.6}$$

where x/X_0 is the radiation length of a material. Total radiation length is 0.496 x/X_0, which leads the mean spread angle $\sigma^{ms} = 0.76$ [mrad GeV/c^2]. The momentum resolution is $\sim$ 1.3 % at $p_{\mathrm{T}} = 1$ GeV/c.

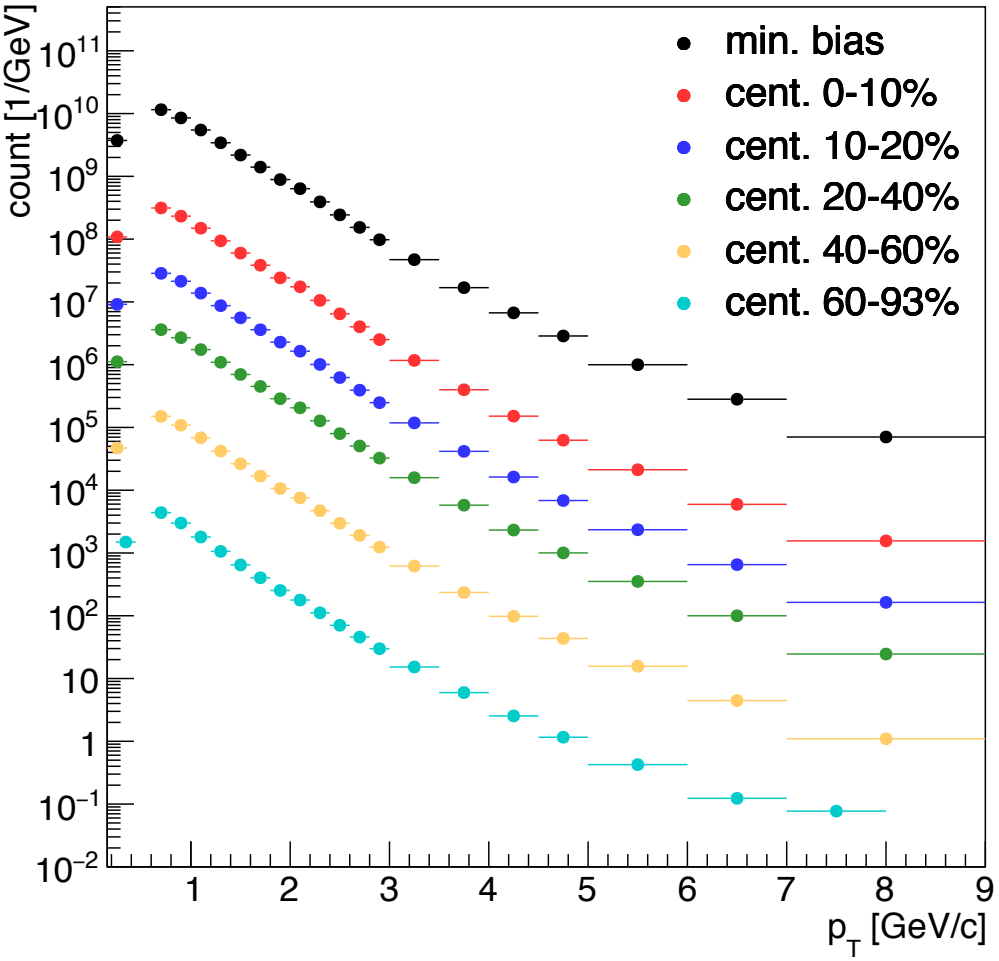

Figure 4.3: The reconstructed p_{T} distributions of charged hadrons for each centrality class.

4.1.2 DC - VTX matching

The track reconstructed at the Central arm (DC + PC1) is associated with the VTX clusters which are composed of 2.6 (6.7) pixels (stripixels) on the average. The central arm track is projected from the DC through the magnetic field to the VTX detector and associated with VTX clusters in the order of B3, B2, B1, and B0 layer by a recursive windowing algorithm. If the VTX cluster is found within a certain $(\delta\phi \times \delta z)$ window around the track projection, the track is associated with the cluster and then projected the next layer with a smaller search window. The search window size depends on p_{T} and is optimized with full GEANT3 simulation [58]. If there is no VTX cluster in the search window, the cluster association is skipped and then the track is projected to the next layer while keeping the window size. The VTX associated track is formed with this chain of the VTX clusters and

fitted as shown in Fig. 4.4 with a track χ^2 model as

$$\chi^2_{VTX} = \sum_{i=0}^{n-1}\left(\frac{\delta\phi_i^2}{\sigma^2_{\phi_i}} + \frac{\delta z_i^2}{\sigma^2_{z_i}}\right) + \sum_{i=0}^{n-2}\left(\frac{\delta\theta^2_{\phi_i}}{\sigma^2_{\phi_i}} + \frac{\delta\theta^2_{z_i}}{\sigma^2_{z_i}}\right) + \frac{\delta\theta^2_{\phi_{n-1}}}{\sigma^2_{\phi_{n-1}} + \sigma^2_{\phi_{DC}}} + \frac{\delta\theta^2_{z_{n-1}}}{\sigma^2_{\theta_{z_{n-1}}} + \sigma^2_{z_{DC}}}, \tag{4.7}$$

where i denotes the number of layers, $\delta\phi$ (δz) is the distance between the cluster position and the track projection in ϕ (z) direction, $\delta\theta_\phi$ is the angle difference between the projected central arm track and the track based on VTX clusters. The mean spread due to a multiple is calculated by radiation length and Eq. 4.6 as the following table. The mean spread angle at the DC $\sigma_{\phi_{DC}}$ ($\sigma_{z_{DC}}$) is 1.1 mrad (7 mrad).

Table 4.1: The mean spread angle due to multiple scattering

$\sigma_{\phi,0 \text{ and } 1} = 14\ \mu$m
$\sigma_{z,0 \text{ and } 1} = 123\ \mu$m
$\sigma_{\phi,2 \text{ and } 3} = 23\ \mu$m
$\sigma_{z,2 \text{ and } 3} = 289\ \mu$m

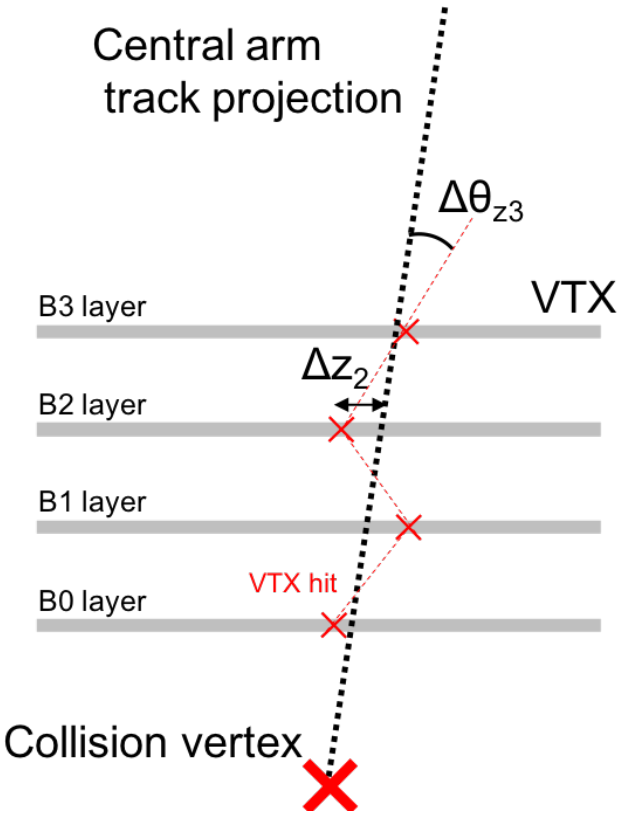

Figure 4.4: The schematic view of a track fit with VTX clusters.

Distance of Closest Approach

The silicon vertex tracker (VTX) allows precise tracking and the Distance of Closest Approach (DCA) between the track and the collision vertex. The DCA is the key information of the measurement for separated charm and bottom quarks. The DCA in the transverse plane, (DCA_T), is used because VTX has better DCA_T resolution than that DCA in the direction of the beam axis, DCA_Z. We calculate DCA_T with the distance between the beam center and the closest point as

$$DCA_T = R - L, \tag{4.8}$$

where R is the radius of the circle, L is the distance from the beam center to the center of the circle of a track as shown in Fig.4.5. In this analysis, the beam center is used instead of the reconstructed vertex because we found the self-bias effect in DCA_T calculated from a reconstructed vertex point. A reconstructed vertex is calculated with the closest approach in all measured tracks, therefore, shifted to tracks have a large DCA. In other words, DCA_T distributions from the reconstructed vertex of long-lived particles such as B and D mesons become narrower. On the other hand, DCA_T from the beam center can ignore the self-bias effect (event by event effect) because the beam center is calculated from the average of collision vertex in one run (∼10 M events).

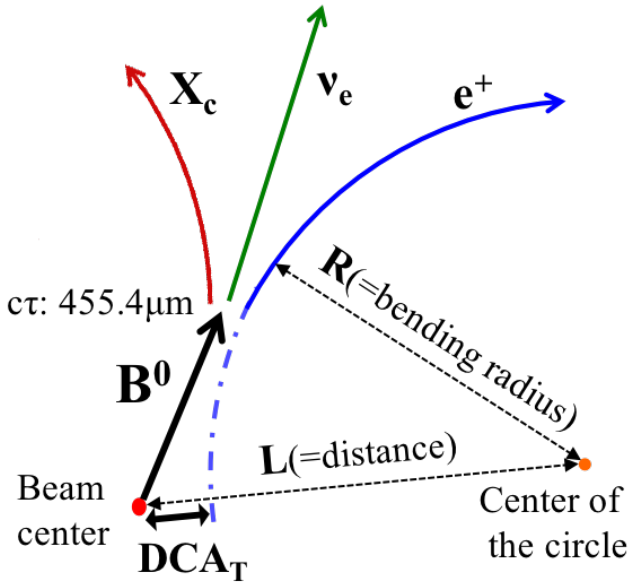

Figure 4.5: Distance to Closest Approach (DCA), the distance between a beam center and a center of the circle.

Fig. 4.6 shows the measured DCA_T distributions from the beam center for each centrality class. DCA_T distribution is composed of a peak structure caused by a primary particle and a tale structure caused by a long-lived particle. The peak structure is Gaussian shape caused by the detector resolution ∼50 μm and

a beam spot size ∼90 μm. The $\mathrm{DCA_T}$ resolution and mean position is extracted by a Gaussian functional fit as shown in Fig. 4.7. The $\mathrm{DCA_T}$ resolution decreases with increasing p_T as the effect of multiple scattering becomes smaller for higher p_T and increases with increasing the centrality as a random hit association caused by high-multiplicity effects. On the other hand, the $\mathrm{DCA_T}$ mean position shows no centrality dependence and increases with increasing p_T as a bias of a tracking algorithm.

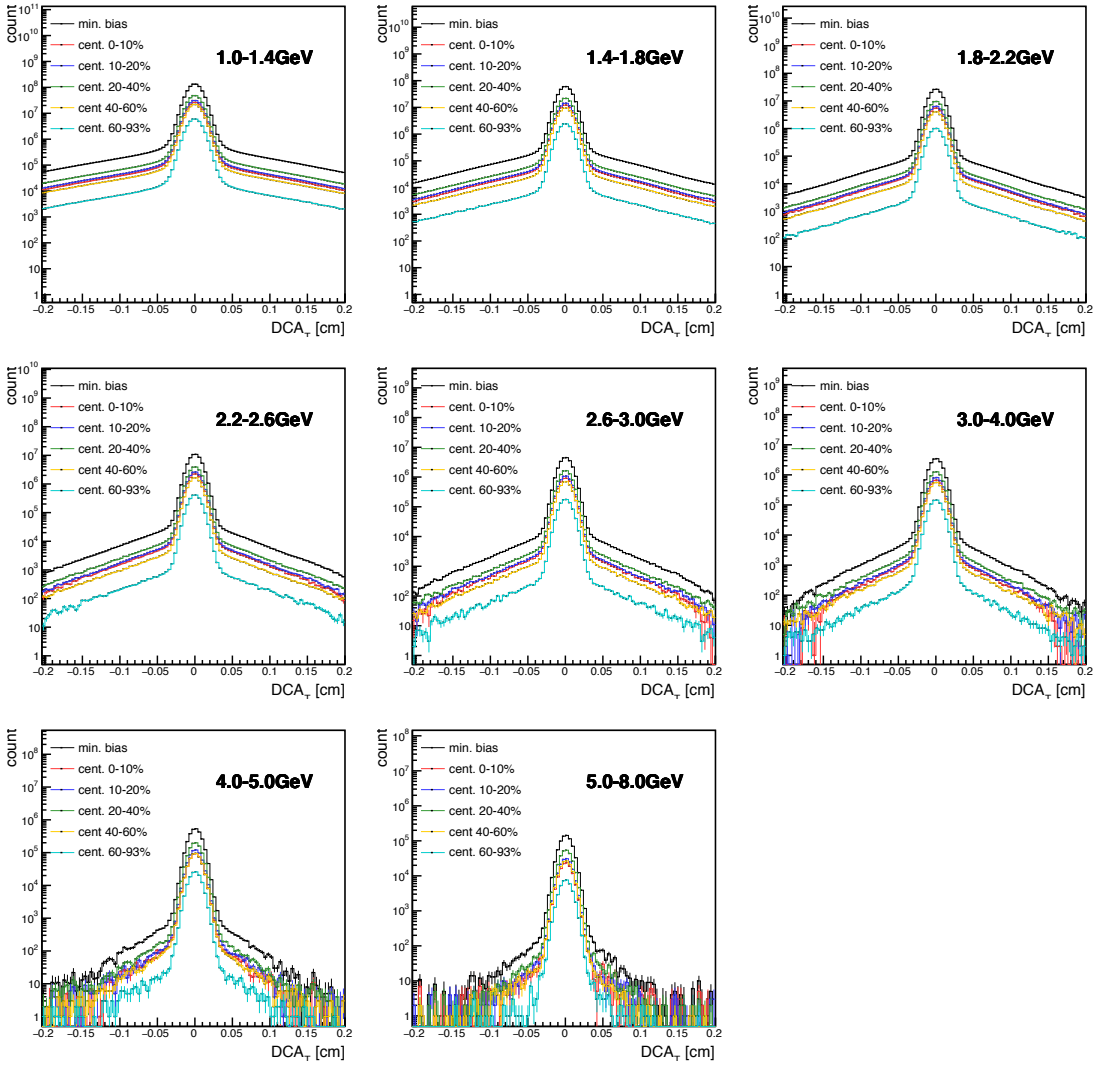

Figure 4.6: $\mathrm{DCA_T}$ distribution of electron candidates for each centrality class

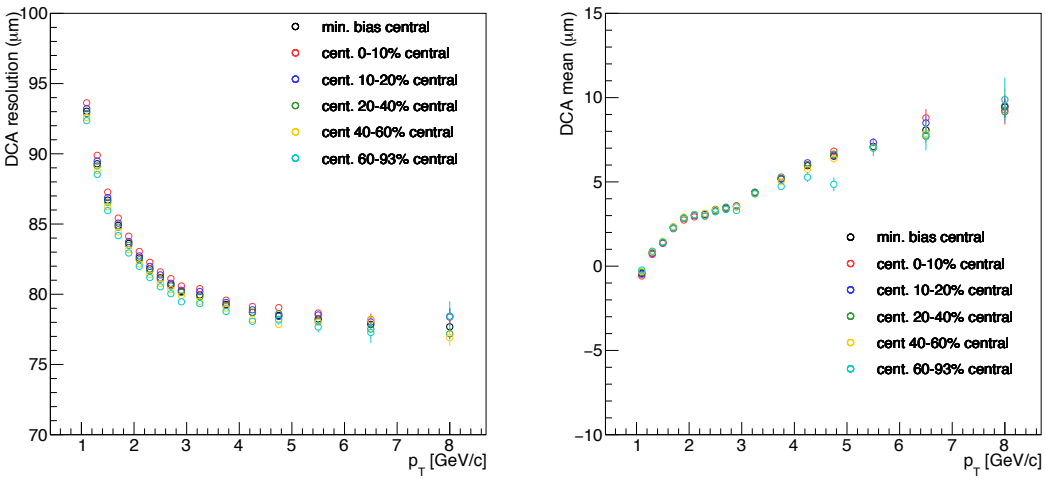

Figure 4.7: The left figure shows $\mathrm{DCA_T}$ resolutions and the right figure shows $\mathrm{DCA_T}$ mean as a function of p_T for all centralities

4.1.3 Nearest VTX Cluster Association

In order to tag heavy flavor decay electrons, the isolation cut is applied to electron candidate tracks. Since heavy flavor hadrons have a large mass, the opening angle of decay particles from heavy flavor hadrons is larger than that from background sources. The main background is a photonic electron produced by internal and external gamma conversions (from π^0, η and direct photon), which produced an electron-positron pair in a very close opening angle. Therefore, the information of the nearest VTX hit from the associated VTX hit with the track can be used for the isolation cut. We determine the window size of the isolation cut by the simulation. Fig. 4.8 shows the residual distribution between the track associated hit and the nearest hit at each VTX layer as a function of track p_T which is simulated by the $\pi^0 \to e$ simulation.

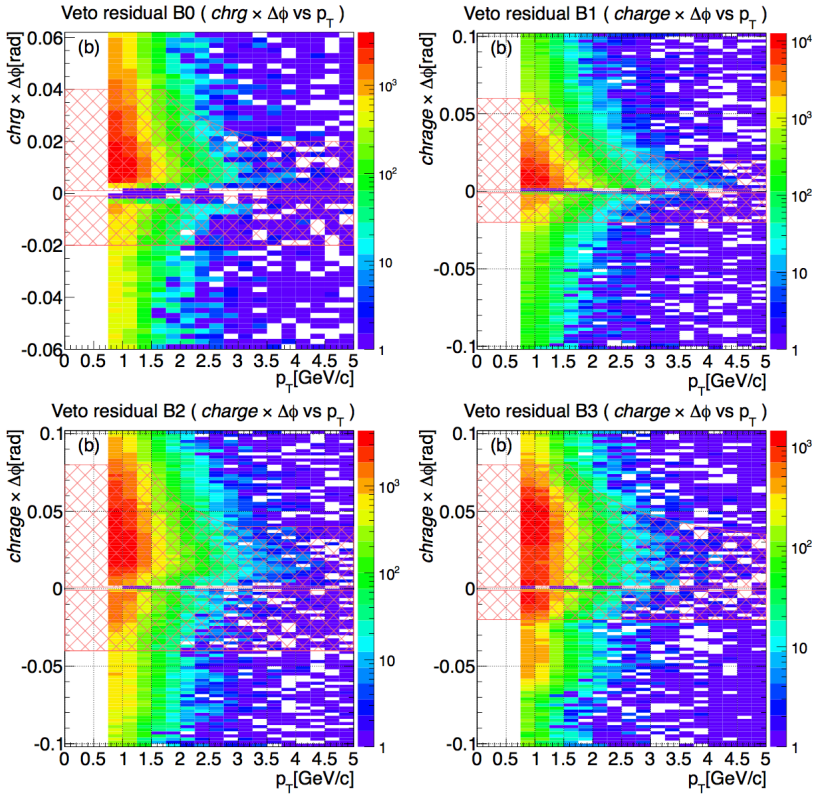

Figure 4.8: The residual distribution between the track associated hit and the nearest hit from the π^0 simulation at each VTX layer as a function of track p_{T}. Electron-positron pairs from internal and external conversion have a close opening angle, which can be killed the isolation cut. Red mesh area means the isolation cut window.

4.1.4 RICH Ring Association

The RICH detector is the most important detector for the electron identification. An electron track is identified with an association of RICH ring which is characterized by the association between a track and hit PMTs in RICH. Fig. 4.9 shows the schematic view of the variable which characterizes the RICH ring. A track projection vector is reflected by the mirror and projected on the PMT array surface (r_0).

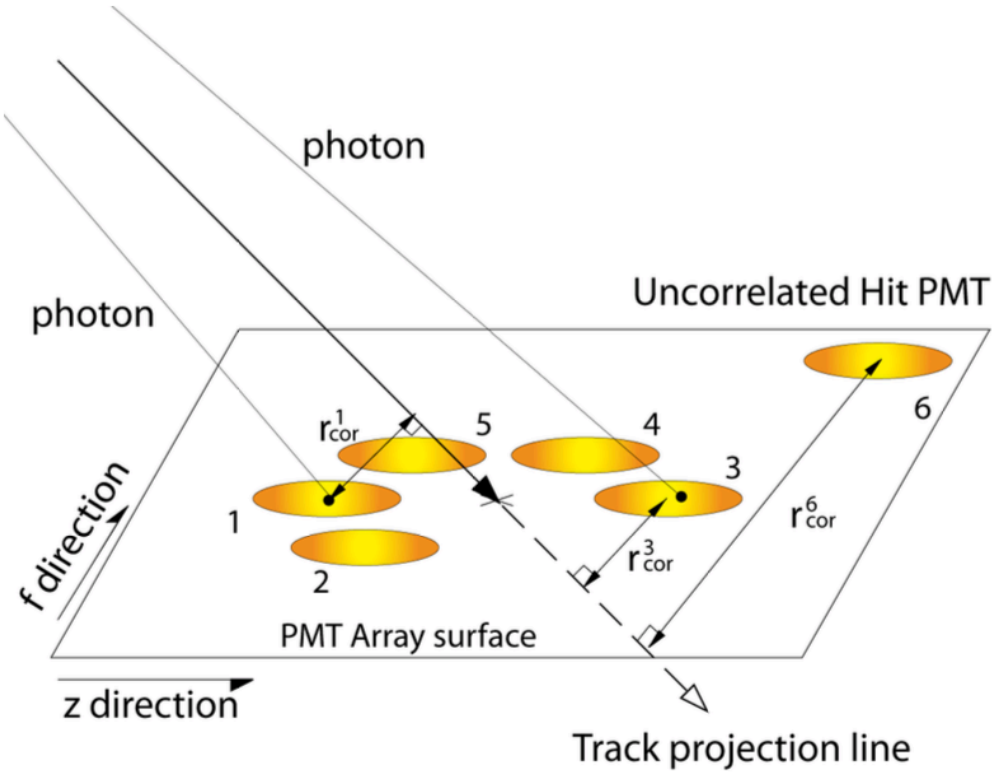

Figure 4.9: The schematic view of the definition of a variable which characterize the RICH ring. There are 5 hit PMTs and one electron track in an example. r^1_{cor}, r^3_{cor}, and r^6_{cor} denote the distance between the center of hit PMT 1, 3, 6 and the track projection vector.

The distance between r_0 and each PMT position vectors (r^i_{corr}) is 5.9 cm ideally, which is confirmed by RICH detector simulation as shown in Fig. 4.10. We define the number of hit PMTs in RICH ring as:

$$n_0 \equiv 3.4\text{cm} < \text{number of PMT hit, } r^i_{corr} < 8.4\text{cm}, \tag{4.9}$$

because the resolution of simulated $< r_{corr} >$ is 2.5 cm.

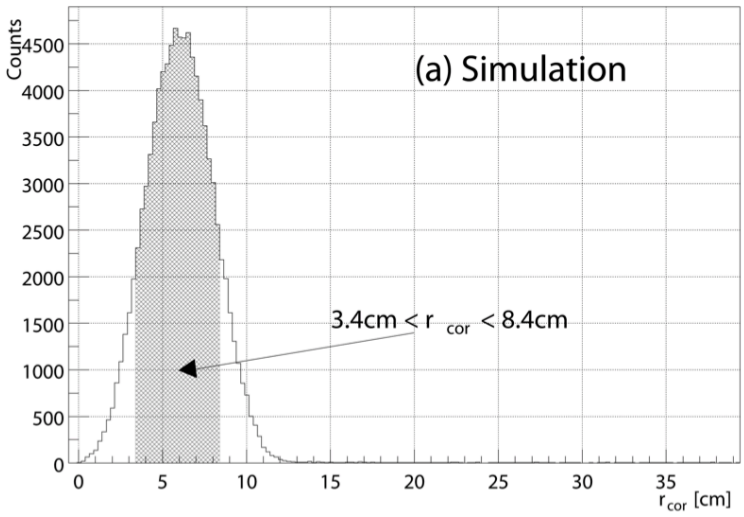

Figure 4.10: The distance between the projected track vector and each PMT position vectors.

Fig. 4.11 shows measured n_0 distributions for different p_T ranges. In high-multiplicity environment, non-electron tracks are associated accidentally with RICH ring, called mis-ID hadrons (read histograms). Mis-ID hadrons are estimated and subtracted by the RICH swap method described in Sec. 4.4.1. We require n0 > 2 to increase the purity of electrons.

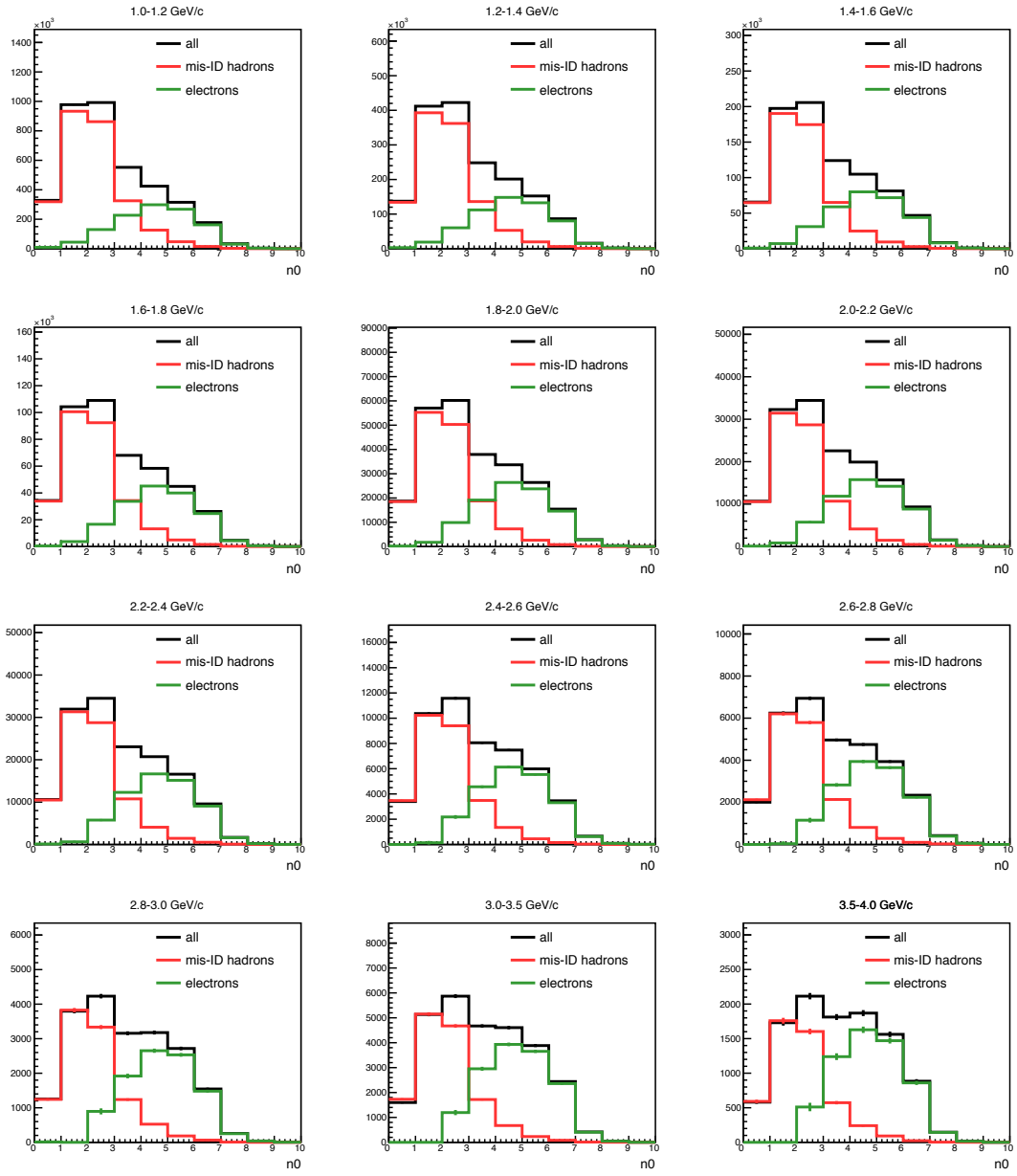

Figure 4.11: n0 distributions each of p_{T} bins. n0 is a number of associated hit PMT in RICH track by track. (black) all electron candidates, (blue) associated electron tracks, (read) mis-associated charged hadron tracks estimated by the RICH swap method.

Another variable is also required the ring shape, **chi2/npe0**, which is the weighted average of the deviation of hit PMT positions from the ideal ring radius, r_0. npe0 denotes the number of photo-electrons which is counted from ADC distribution subtracted the pedestal peak as shown in Fig. 4.12. **chi2/npe0** is defined

as:

$$\text{chi2/npe0} \equiv \frac{\sum_{3.4<r_i<8.4cm}(r_i - r_0)^2 \times \text{npe}_\text{i}}{\text{npe0}}, \tag{4.10}$$

$$\text{npe0} \equiv \sum_{3.4<r_i<8.4cm} \text{npe}_\text{i}, \tag{4.11}$$

In this analysis, we require **chi2/npe0** < 7.0 for the electron identification.

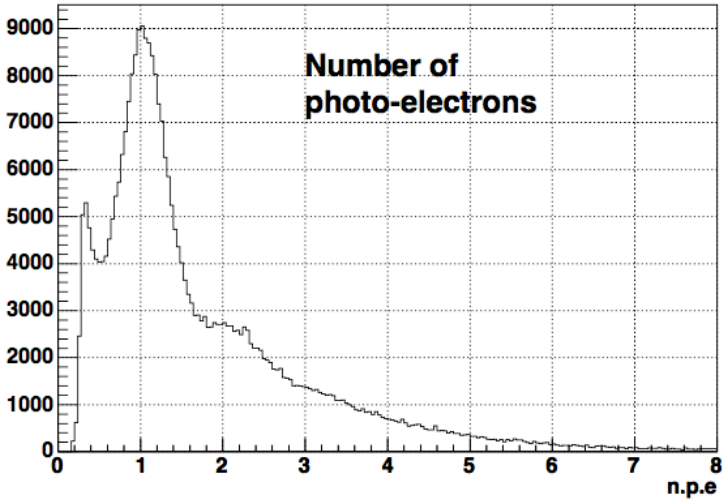

Figure 4.12: The number of photo-electrons in each hit PMTs.

4.1.5 EMCal Cluster Association

The electron purity can be increased by the track - EMCal cluster matching because electrons generate Electromagnetic shower and make a cluster at EMCal. Matching variables of the distance between the projected track position and the hit position at EMCal are defined as:

$$\text{emcsdphi}_\text{e} = \frac{\phi_{track} - \phi_{hit}}{\sigma_\phi(p)}, \tag{4.12}$$

$$\text{emcsdz}_\text{e} = \frac{z_{track} - z_{hit}}{\sigma_z(p)}, \tag{4.13}$$

where ϕ_{track} (z_{track}) is the ϕ (z) position of the projected track at EMCal, ϕ_{hit} (z_{hit}) is the hit position at EMCal, $\sigma_\phi(p)$ ($\sigma_z(p)$) is the p_T dependent width of an electromagnetic shower shape in ϕ (z) direction. For the electron identification, **emcsdphi$_\text{e}$** and **emcsdz$_\text{e}$** are required less than 4.0.

4.1.6 Energy - Momentum Matching

In case of electrons, the measured momentum at the DC and energy at the EMCal are almost the same because electrons deposit full-energy at the EMCal (18 X_0)

and the electron mass is very small compared with a momentum scale (GeV/c). Therefore, electron tracks can be identified by $E/p = 1$. In this analysis, E/p distributions are normalized to use the p_{T} independent cut variable, namely dep defined as:

$$\mathrm{dep} = \frac{\mathrm{E/p} - \mu_{\mathrm{E/p}}}{\sigma_{\mathrm{E/p}}}, \tag{4.14}$$

where $\mu_{E/p}$ and $\sigma_{E/p}$ are the mean and the width of E/p distribution as a function of p_{T}. Fig. 4.13 shows dep distributions in each p_{T} ranges. Mis-ID hadrons in dep distributions are estimated by the track swapping method described in Sec. 4.4.1. dep is required higher than -2.0 for the electron identification.

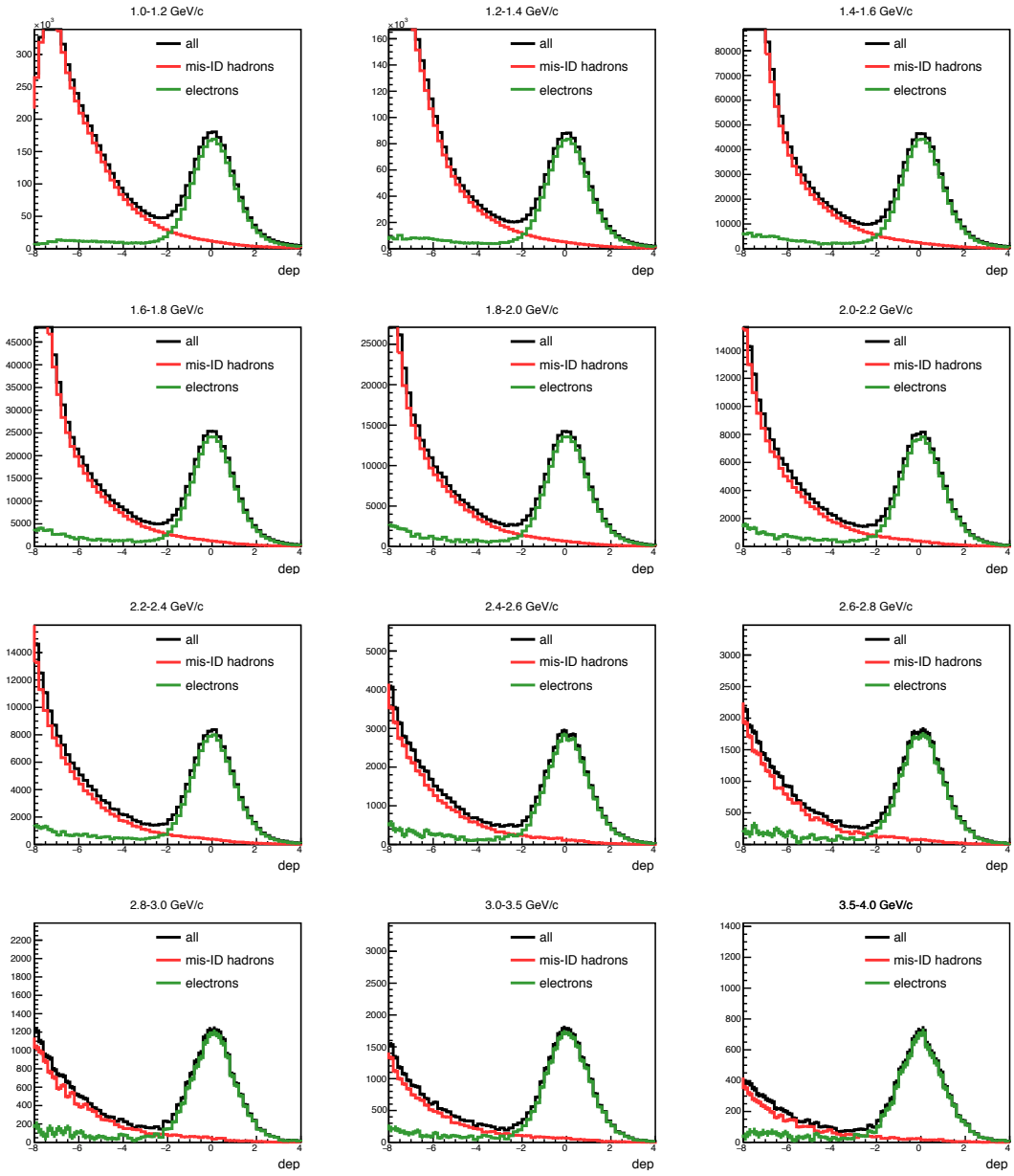

Figure 4.13: dep distributions each of p_{T} bins. dep is a matching variable between the reconstructed track momentum (p) and the energy measured in EMCal (E): $dep = (E/p - \mu_{E/p})/\sigma_{E/p}$. (black) total electron candidates, (blue) assumed pure electron candidates, (read) misidentified charged hadron estimated by the RICH swap method.

4.1.7 Electro-magnetic Shower Shape

The EM shower shape information can be used to reject mis-ID hadron backgrounds because charged hadrons hardly generate EM shower in the EMCal. The

probability of EM shower shape, prob, is defined as:

$$\chi^2 = \sum_i \frac{(E_i - E_i^{pred})^2}{\sigma^2} \tag{4.15}$$

where E_i is the measured energy at each tower, E_i^{pred} is the predicted energy at each tower as an electromagnetic particle, σ_i is the predicted width of E_i^{pred}. prob is required higher than 0.01 for the electron identification.

4.2 Data Quality Assurance

RHIC and PHENIX detector performances are changed run by run (or event by event). Therefore, we have to check the stability of the beam and the detector conditions run by run. In addition, a good quality data sample should be selected track by track. This section summarizes the track and electron selection and details on how to check the stability of the beam and the detector conditions.

4.2.1 Summary of Track Selection

Charged tracks are measured by the Drift Chamber (DC) and VTX. The following variables are calculated and used for the track selection.

DC quality: The DC tracks require hits in both the X1 and the X2 sections of the DC and uniquely associate with hits in the U or V stereo wires. At least one PC1 hit is also required.

DC zed: Z-position of a projected track at the surface of the DC. DC zed is used for the fiducial volume cut to remove the inefficient acceptance region in the DC.

VTX hits: The DC track require VTX (4 layers) hits to calculate the distance of closest approach (DCA) from the collision vertex. At least, we require inner 2 layers hits to gain a good DCA resolution.

χ^2/NDF: χ^2/NDF is calculated by the distance between the track projected positions and the hit positions each detector and the detector position resolutions.

emcsdphi: A variable of the distance in ϕ direction between the associated EMCal cluster position and the projected track position in units of standard deviations. The variable is calibrated for electrons and emcsdphi < 2 means that the position of the associated EMCal cluster in ϕ is within 2σ of the projected track position.

emcsdz: Same as emcsdphi, but for the z-direction.

Table 4.2: Track selection variables

Track selection variables
DC quality = 31 || 63
|DC zed| < 75 cm
VTX hits > 2, require (B0 && B1 && B2 (|| B3))
χ^2/NDF < 1.5 for $p_{\mathrm{T}} > 2$ GeV/c
χ^2/NDF < 2 for $p_{\mathrm{T}} > 2$ GeV/c
emcsdphi < 2, emcsdz < 2

4.2.2 Summary of Electron Selection

Electron candidates are selected from reconstructed charged particle tracks based on information from the RICH and EMCal as the following table. Some non-electron tracks path throw the following electron identification cuts because of mismatching between a non-electron (mis-ID hadron) track and RICH hits or EMCal clusters. These can be estimated by a track swap method as described section 4.4.

n0: Number of hit RICH PMTs in an annular region with an inner radius of 3.4 cm and an outer radius of 8.4 cm around the track projection on the RICH. The expected radius of a Čerenkov ring emitted by an electron is 5.9 cm. Fig. 4.11

χ2/npe0: A χ2-like shape variable of the RICH ring associated with the track.

disp: A variable representing the displacement of the RICH ring center from the projected track position. Units are cm.

dep: A variable of energy-momentum matching. This variable is calculated as dep = (E/p - 1)/σ, where E is the energy measured by EMCal, p is the momentum of the track, and σ E/p is the standard deviation of a Gaussian-like E/p distribution. E/p is less than 1 for hadrons because hadrons do not deposit their full energy in the calorimeter. σE/p depends on the momentum of the electron. Fig. 4.13

emcsdphi_e: Displacement in ϕ of the electron hit position of the associated EMCal cluster from the projected position of the track in units of standard deviations. For example, $\mathbf{emcsdphi_e} < 2$ means that the position of the associated EMCal cluster in ϕ is within 2σ of the projected track position. This variable was calibrated specifically for electrons.

emcsdz_e: Same as $\mathbf{emcsdphi_e}$, but for the z coordinate.

prob: The probability that the associated EMCal cluster is an electromagnetic shower. This variable is calculated from the χ2 value between the actual tower energy distribution of the cluster and the expected distribution for an

electromagnetic shower. For example, a cut, prob > 0.01, has 99% efficiency for a photon or electron shower, while it rejects a large fraction of hadrons.

Table 4.3: Electron selection variables

Electron selection variables
n0 > 2 for $p_{\mathrm{T}} < 5.0$ GeV/c
n0 > 3 for $p_{\mathrm{T}} > 5.0$ GeV/c
disp < 5.0
chi2/npe0 < 7.0
prob > 0.01 for $p_{\mathrm{T}} < 5.0$ GeV/c
prob > 0.2 for $p_{\mathrm{T}} > 5.0$ GeV/c
dep > -2.0
emcsdphi_e < 4.0, emcsdz_e < 4.0

4.2.3 Run/Event Selection

In order to check the stability of detectors, the variables of the electron and HF ID are calculated and compared run by run. We select good runs to minimize the variation of experimental conditions. Good runs are selected with the standard deviation from variations of each variable as the following.

Number of tracks per event: The number of central arm tracks per event, assuring the DC acceptance and condition.

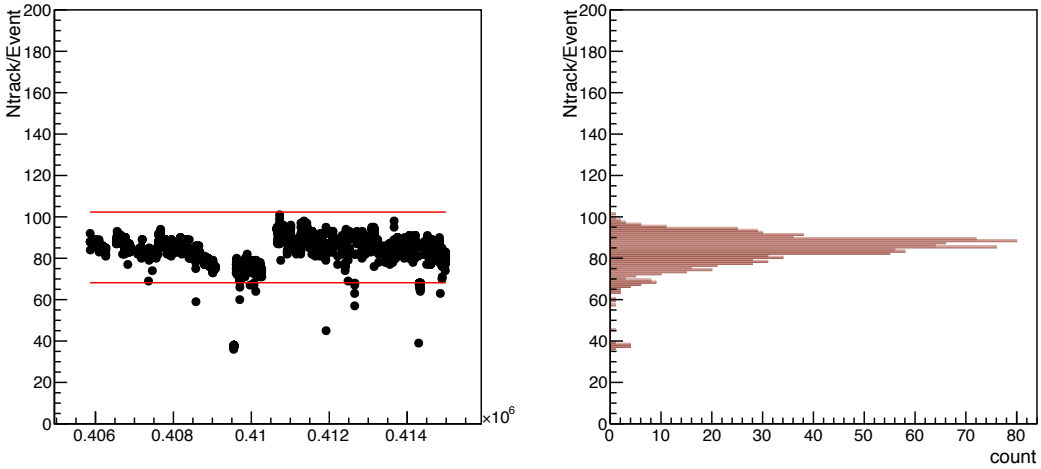

Figure 4.14: The left panel shows the number of tracks per event as a function of a run number and the 3 standard deviation interval (red lines). The right panel shows the dispersion of the number of tracks per event.

Electron to Hadron ratio: The ratio of charged hadron tracks to electron identified tracks, assuring the RICH and EMCal acceptance and condition.

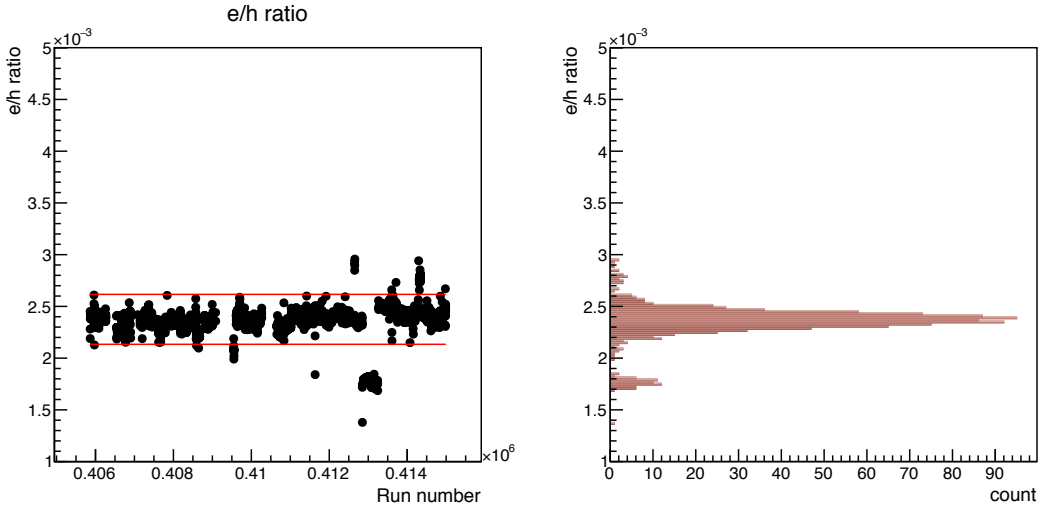

Figure 4.15: The left panel shows the electron/hadron ratio as a function of a run number and the 3 standard deviation interval (red lines). The right panel shows the dispersion of the electron/hadron ratio.

DC - VTX matching efficiency: The ratio of VTX associated tracks to central arm tracks, assuring the VTX acceptance and condition.

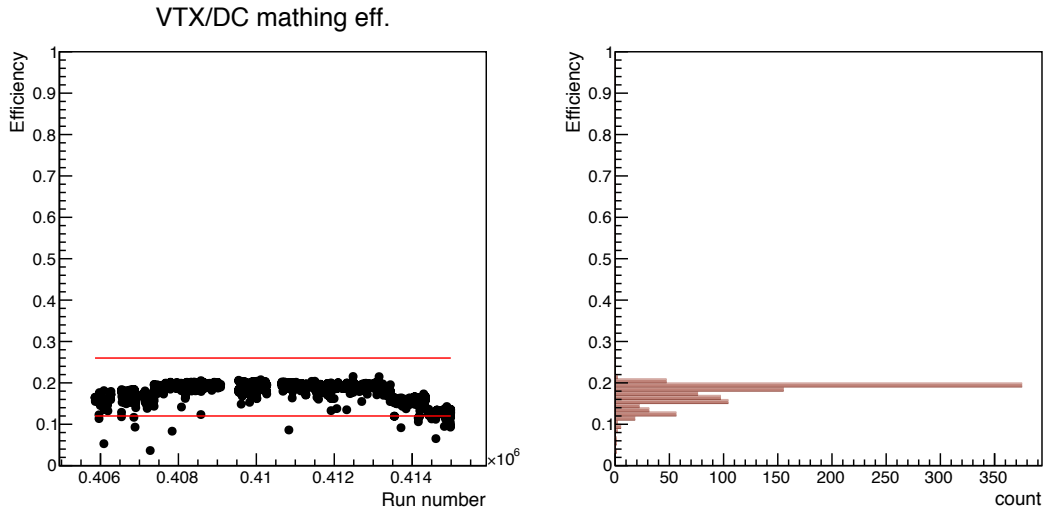

Figure 4.16: The left panel shows VTX/DC matching efficiency as a function of a run number and the 3 standard deviation interval (red lines). The right panel shows the dispersion of VTX/DC matching efficiency.

χ^2/ndf **of** $\mathrm{DCA_T}$ **with respect to the average shape:** The χ^2/ndf of $\mathrm{DCA_T}$ is calculated by the difference between each $\mathrm{DCA_T}$ shape and the average $\mathrm{DCA_T}$ shape. This calculation performs for $600\mu\mathrm{m} < \mathrm{DCA_T} < 3000\mu\mathrm{m}$ because this region does not depend on a beam size fluctuation.

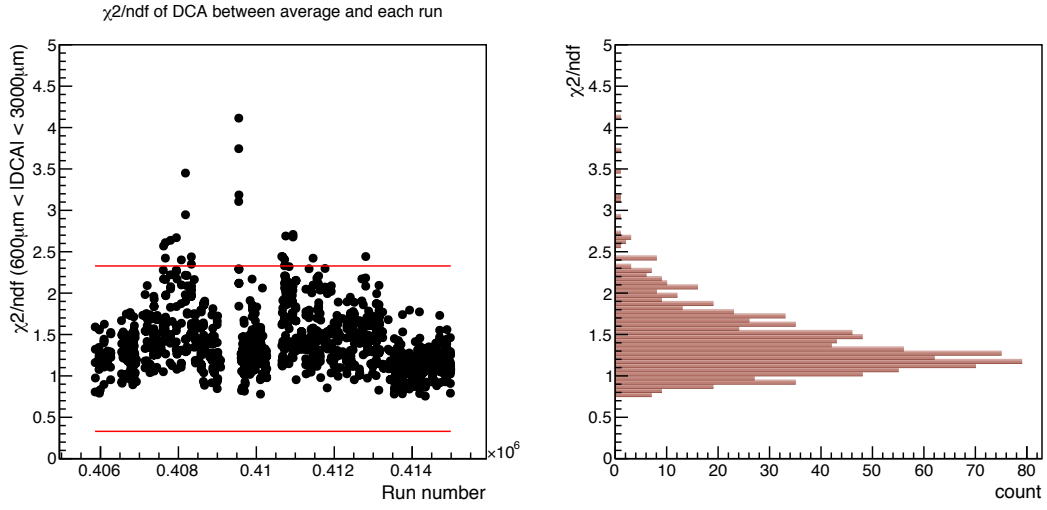

Figure 4.17: The left panel shows χ^2/ndf of $\mathrm{DCA_T}$ with respect to the average shape as a function of a run number and the 3 standard deviation interval (red lines). The right panel shows the dispersion of χ^2/ndf of $\mathrm{DCA_T}$.

DCA_T **resolution:** The DCA_T resolution obtained by Gaussian fit.

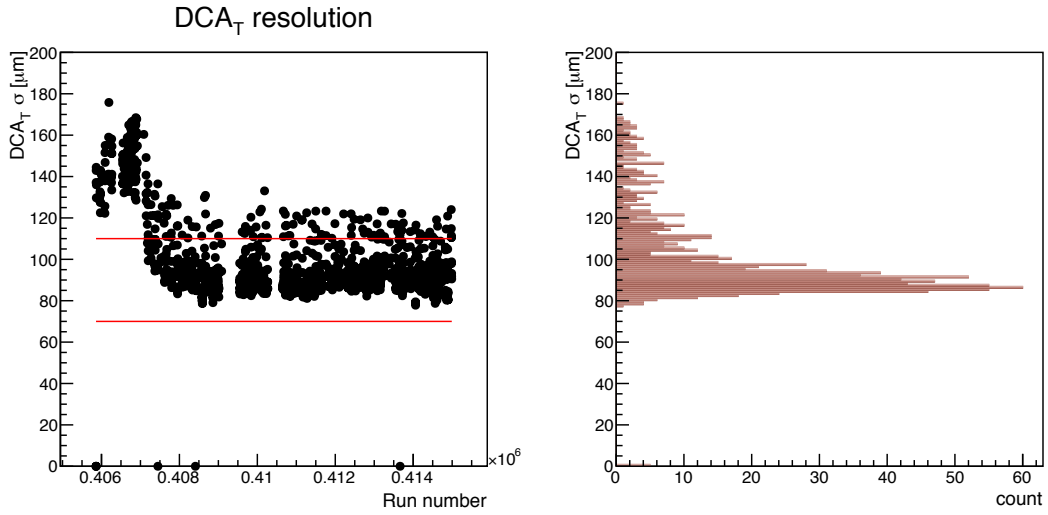

Figure 4.18: The left panel shows DCA_T resolutions as a function of a run number and the 3 standard deviation interval (red lines). The right panel shows the dispersion of DCA_T resolution.

DCA_T **mean:** The DCA_T mean position obtained by Gaussian fit.

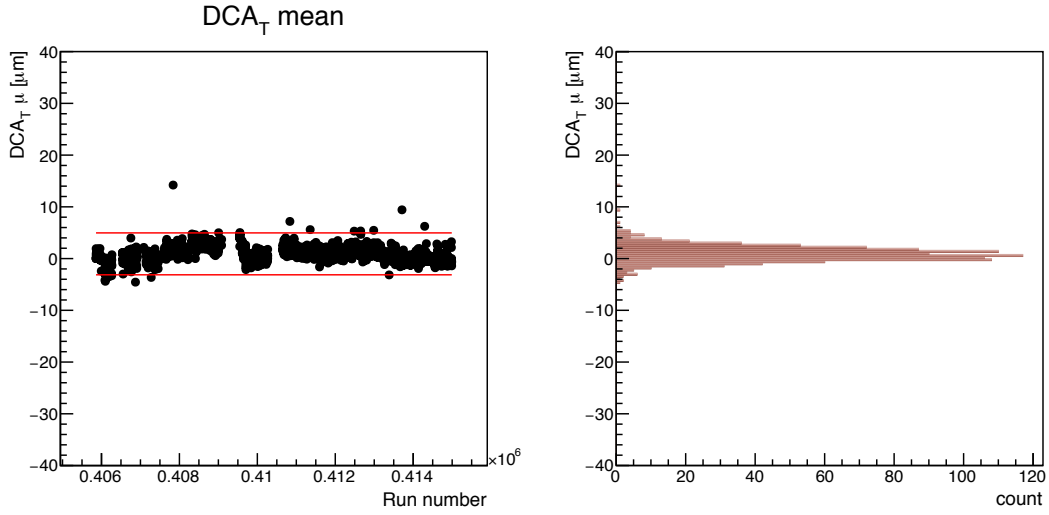

Figure 4.19: The left panel shows DCA_T mean positions as a function of a run number and the 3 standard deviation interval (red lines). The right panel shows the dispersion of the DCA_T mean position.

Survival rate of isolation cut: The survival rate of the isolation cut at VTX calculated by the number of isolated tracks and normal tracks. Stability of the survival rate is the most important variable because the isolation cut is used for tagging heavy flavor electron. Therefore, this selection is applied by titer cut (1 standard deviation).

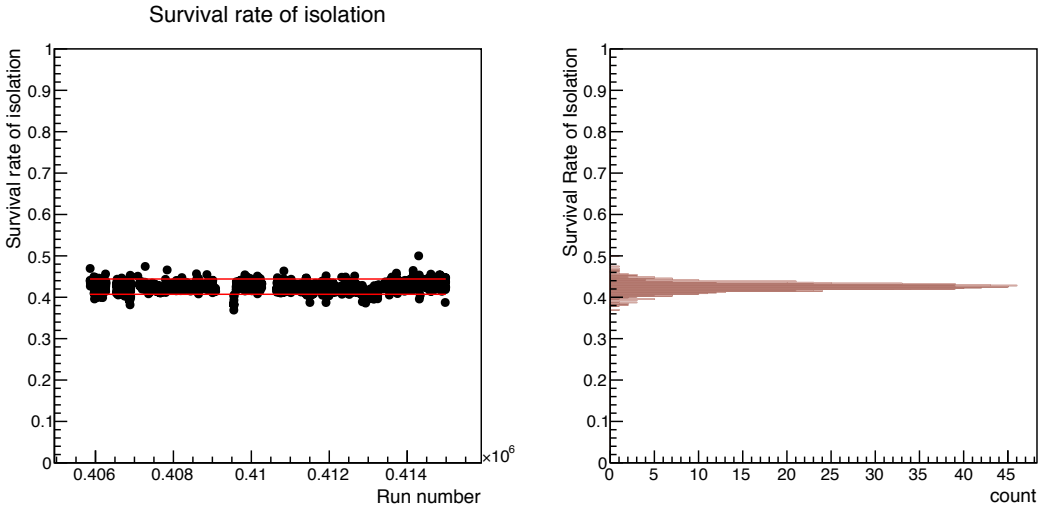

Figure 4.20: The left panel shows the survival rate of the isolation cut as a function of a run number and the 1 standard deviation interval (red lines). The right panel shows the dispersion of the survival rate.

4.2.4 Summary of Quality Assurance

In this analysis, 31% runs are rejected by our run selections. Total event number is 8.51×10^9. Total charged track number ($p_{\mathrm{T}} > 1$ GeV/c) is 9.60×10^9. Total electron count is ($p_{\mathrm{T}} > 1$ GeV/c) 6.58×10^7. Selected run numbers are written in Sec. A.

4.3 Reconstruction in Simulation

Simulation study enables us to understand the detector response to various particles such as charged hadrons, photonic electrons, and heavy flavor electrons. The structure and configuration of PHENIX detectors are reproduced in GEANT3 and the reconstruction procedure as same as the real data performs with GEANT3 hit information. This simulation study is used for verification of the BG estimation method, an estimation of the survival rate for various particles, and a generation of $\mathrm{DCA_T}$ distributions for various particles.

4.3.1 Particle Generation and Reconstruction

This section details how to generate particles and consider p_{T} spectrum. The simulation is divided into the following two sets.

- Photonic Electron Simulation
  A photonic electron means an electron produced by an internal (Dalitz decay) and external conversion form π^0, η, direct photon, and so on. PHENIX has measured the invariant yield of these photonic electron sources. Fig. 4.21 shows the measured p_{T} spectrum of photonic electron sources (π^0, η and direct photon) and the fit result with the Hagedorn function. In the simulation, these photonic electron sources are generated with a flat p_{T} distribution and applied p_{T} weight function in the reconstruction step to secure statistics at high p_{T}. π^0, η and direct photon generate electron-positron pairs by internal and external conversions in GEANT3.

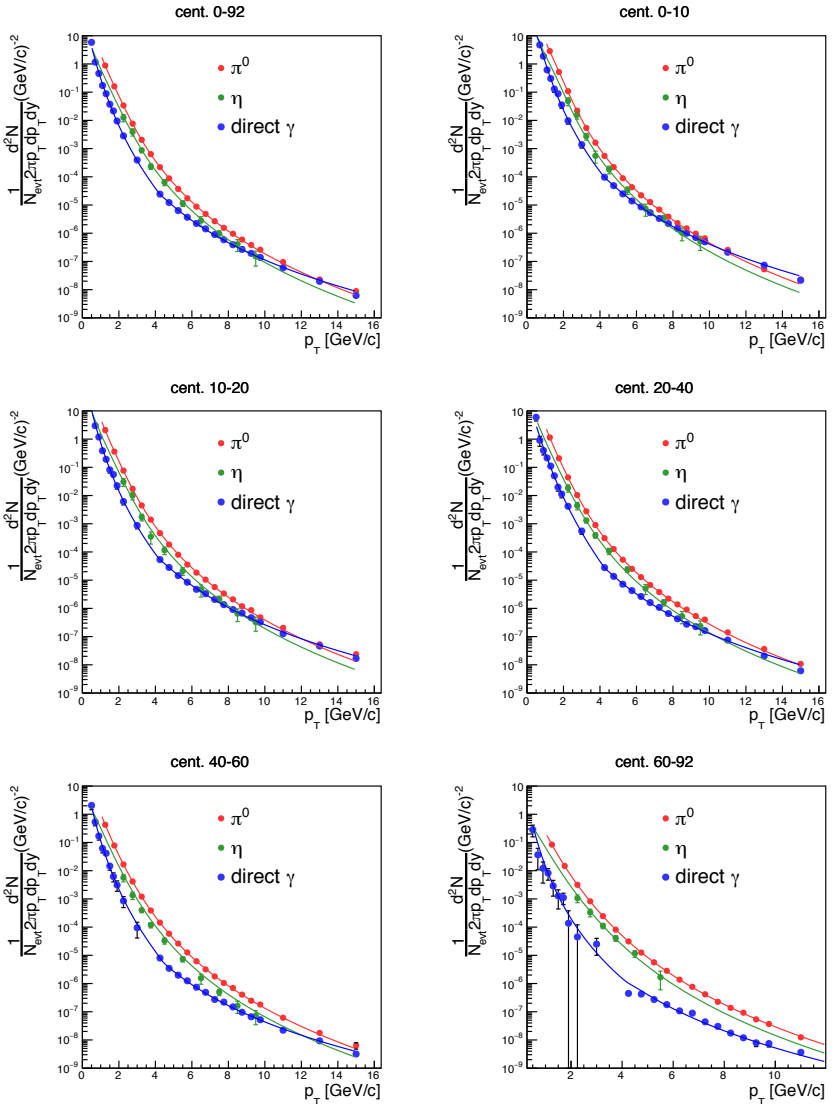

Figure 4.21: The measured invariant yield of π^0, η and γ is fitted by the modified Hagedorn (+ power low) function.

- Multi-hadron Simulation
  This analysis focuses on a single electron analysis, but we have to understand the high-multiplicity effect in the reconstruction, namely mis-ID and mismatch background. We fit with the Hagedorn function to the measured yields of π, K, p and Λ to obtain the realistic p_{T} spectrum and the particle ratio. In the simulation, these particles are generated according to the fit function including the p_{T} spectrum and the relative particle ratio and the number of produced particles follow each multiplicity class such as $\mathrm{d}N/\mathrm{d}\eta = 187$ in minimum bias (0-93%) Au+Au collisions. 1 electron and 2 charged particles are added per event.

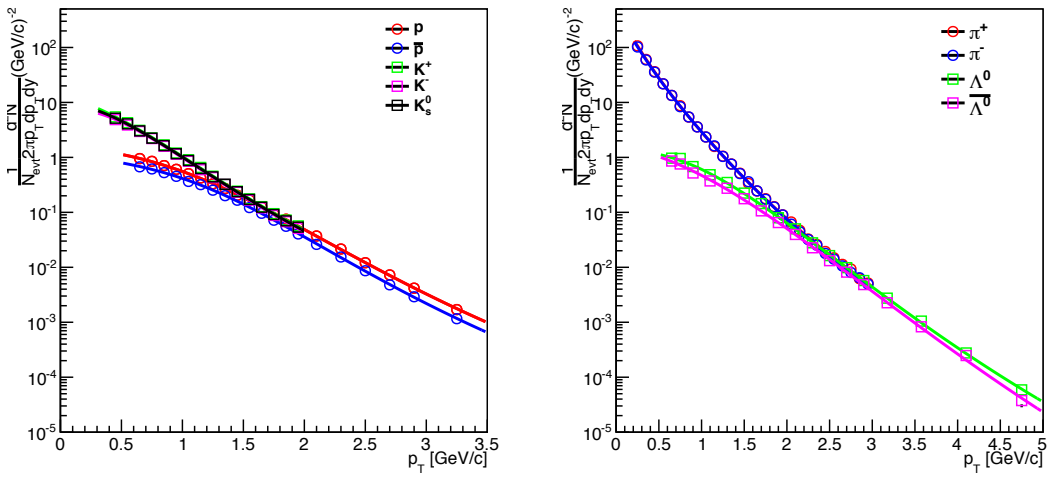

Figure 4.22: The measured charged hadron p_{T} spectrums and Hagedron fit results.

4.3.2 Electron Identification in Simulation

Electron identification in the simulation is studied by single electron simulation. n0 and dep distributions are compared between the data and simulation as shown in Fig. 4.23, 4.24. Simulated n0 distribution well describe the data. Simulated dep distribution is slightly shifted to the positive side because of a slightly miscalibration. However, that effect is very small in this analysis because we do not calculate the detector efficiency. The electron simulation is only used for making DCA distributions and calculating survival rates.

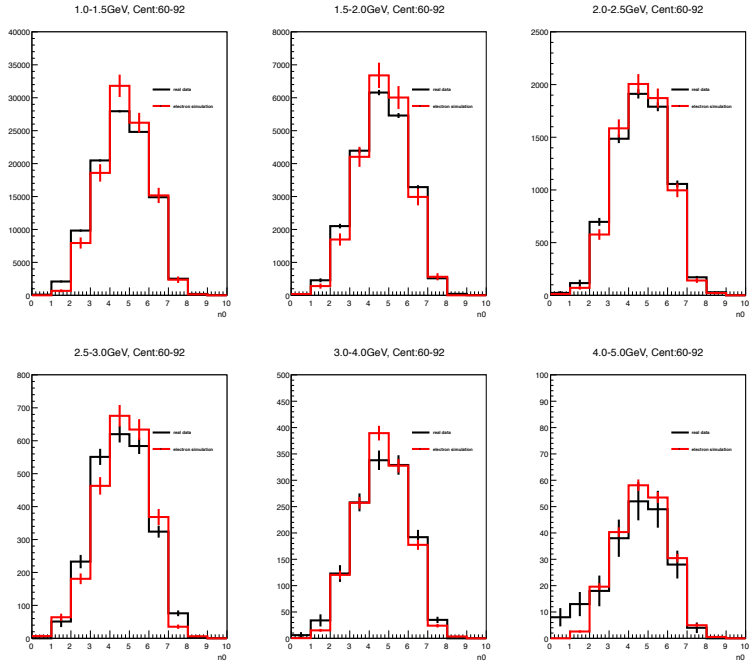

Figure 4.23: n0 distribution in single electron simulation. Simulation: red, Data: black

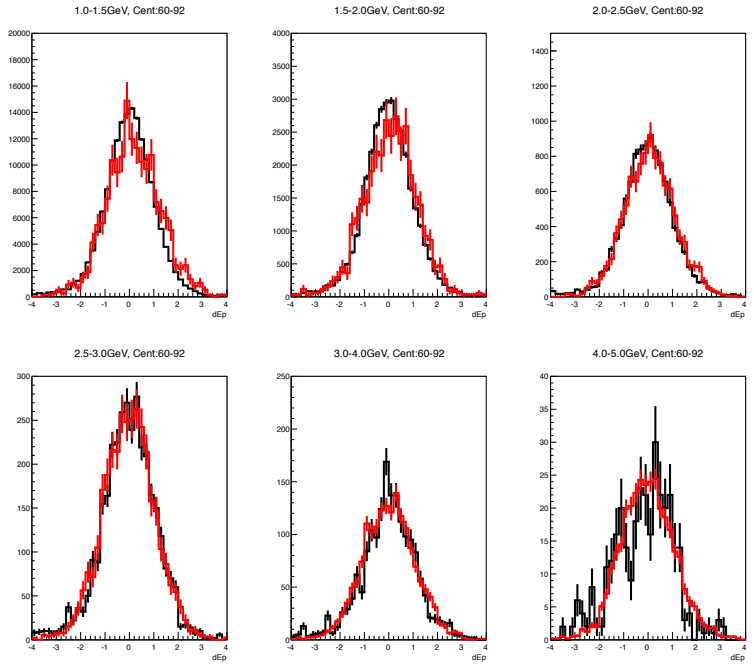

Figure 4.24: dep distribution in single electron simulation. Simulation: red, Data: black

4.3.3 p_{T} and $\mathrm{DCA}_{\mathrm{T}}$ Distribution in Simulation

p_{T} and $\mathrm{DCA}_{\mathrm{T}}$ are reconstructed from GEANT3 hit information with the same reconstruction code as the real data. Photonic electrons are divided into conversion electrons and Dalitz decay electrons because the $\mathrm{DCA}_{\mathrm{T}}$ shape only depends on a generation point. Dalitz decay electrons are generated around collision vertex. On the other hand, conversion electrons are generated at the beam pipe and the VTX B0 layer. Conversion electrons generated at outer B0 layer are rejected by requiring VTX hit at B0 layer. If conversion electron is generated at outer B0 layer, there is no VTX hit at B0 layer. In this analysis, the isolation cut at VTX is applied to reduce photonic electrons. Conversion electrons are more reduced than Dalitz decay electrons by the isolation cut because an electron-positron pair from conversion is generated at outer position (Beam pipe and B0 layer) and pass through the magnetic field for a shorter time than that in case of Dalitz decay electrons. In short, an electron-positron pair from conversion has a narrower pair distance than that from a Dalitz decay electron. Fig. 4.25 shows the simulated p_{T} distribution for conversion and Dalitz decay electrons with and without the isolation cut (left figure) and the $\mathrm{DCA}_{\mathrm{T}}$ distributions for conversion and Dalitz decay electrons with the isolation cut (right figure). Without the isolation cut, the number of conversion electrons and Dalitz decay electrons are almost the same. The isolation cut at VTX rejects conversion electrons by $\sim$80% and Dalitz decay electrons by $\sim$50%. As a result, conversion electrons are reduced by 40% of Dalitz electrons by the isolation cut as shown in Fig. 4.25 (left bottom panel), namely the conversion to Dalitz ratio = $\sim$ 40%. The $\mathrm{DCA}_{\mathrm{T}}$ distribution of conversion electrons shifts to the negative side due to momentum mismatching. Our tracking algorithm uses the primary vertex, but conversion electrons are not produced at the primary vertex. It causes the momentum mismatching (with a higher momentum track) and the shift to the negative side.

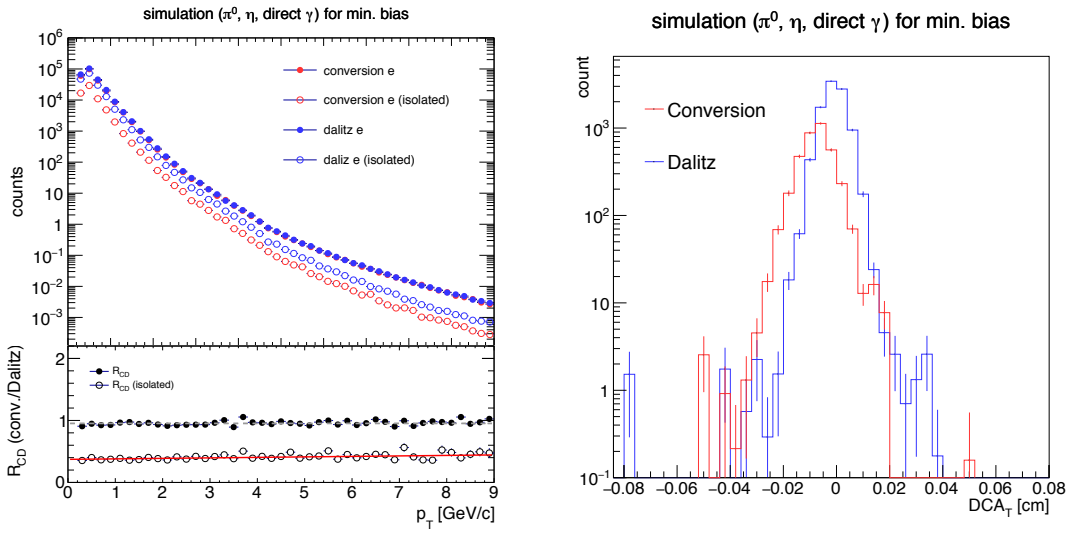

Figure 4.25: (Left) The simulated p_{T} distribution for conversion and Dalitz decay electrons. (Right) The simulated $\mathrm{DCA}_{\mathrm{T}}$ distributions for conversion and Dalitz decay electrons applied by the isolation cut.

Fig. 4.26 shows simulated p_{T} and $\mathrm{DCA}_{\mathrm{T}}$ distributions for multi-hadron simulation. In this analysis, 2 high p_{T} ($>$ GeV/c) particles are added per event. It causes the bump structure around 5 GeV/c in p_{T} distributions. Simulated $\mathrm{DCA}_{\mathrm{T}}$ distribution is scaled to match the data and well reproduce the $\mathrm{DCA}_{\mathrm{T}}$ shape of the data. It indicates that the relative particle ratio is reasonable. The dead map and an edge effect in DCA distribution are ignored in this analysis.

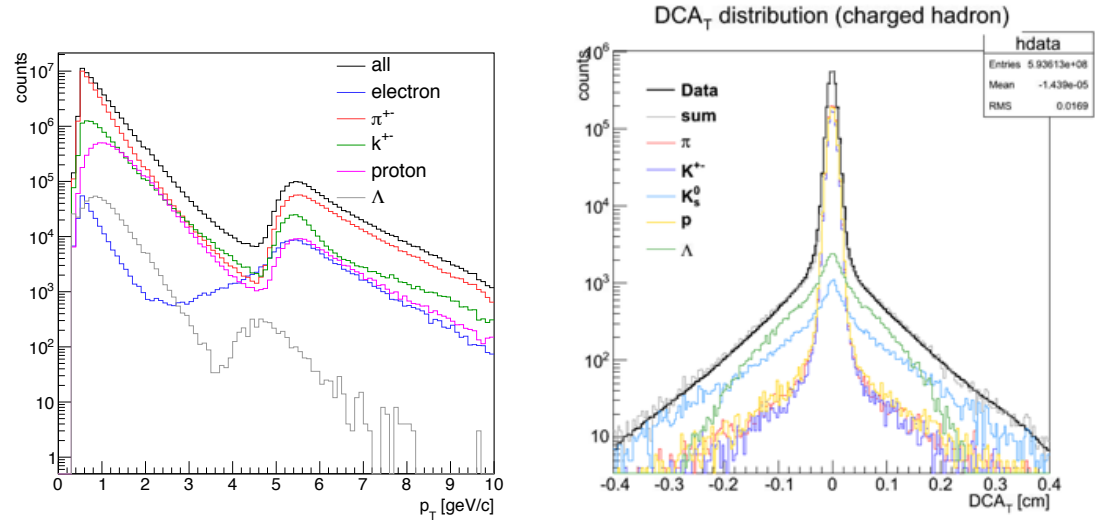

Figure 4.26: (Left) The simulated p_{T} distributions for the multi-hadron simulation. (Right) The DCA distributions for the multi-hadron simulation (gray) compared with the data (black).

We study the dead map effect on $\mathrm{DCA}_{\mathrm{T}}$ shape with the simulation. The $\mathrm{DCA}_{\mathrm{T}}$

distributions of multi-hadrons with and without the dead map which is obtained from the data (Run407143) are compared as shown in Fig. 4.27. There is no different in these distributions, indicating a sufficiently small effect of the dead map.

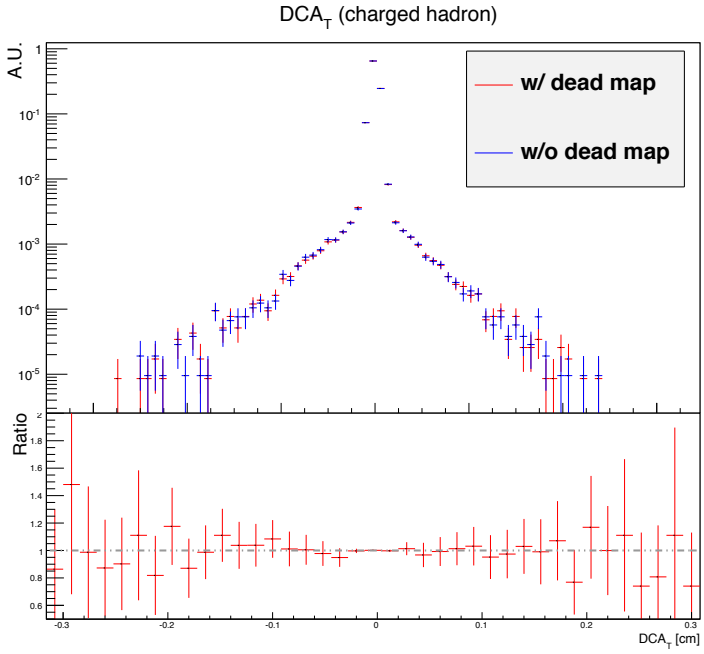

Figure 4.27: The DCA_T distributions with and without the dead map of Run407143 in simulation. Integral is normalized to unity.

4.3.4 PHENIX Electron Cocktail

The invariant yields of electrons from all background sources are extracted by the decay model and the measured invariant yield of background sources, called PHENIX electron cocktail. The input p_T spectrums of background sources are obtained by the fit to the measured invariant yields as shown in Fig. 4.21. Input p_T spectrums for higher mass vector mesons are assumed by the m_T scaling method [10]. Fig. 4.28 shows the simulated invariant yield of electrons from all background sources, PHENIX electron cocktail, which includes the relative ratio of background contributions. Its relative ratio is maintained in reconstructed tracks as shown in Fig. 4.29. These simulated invariant yields and reconstructed tracks are used to estimate backgrounds in Sec. 4.4.

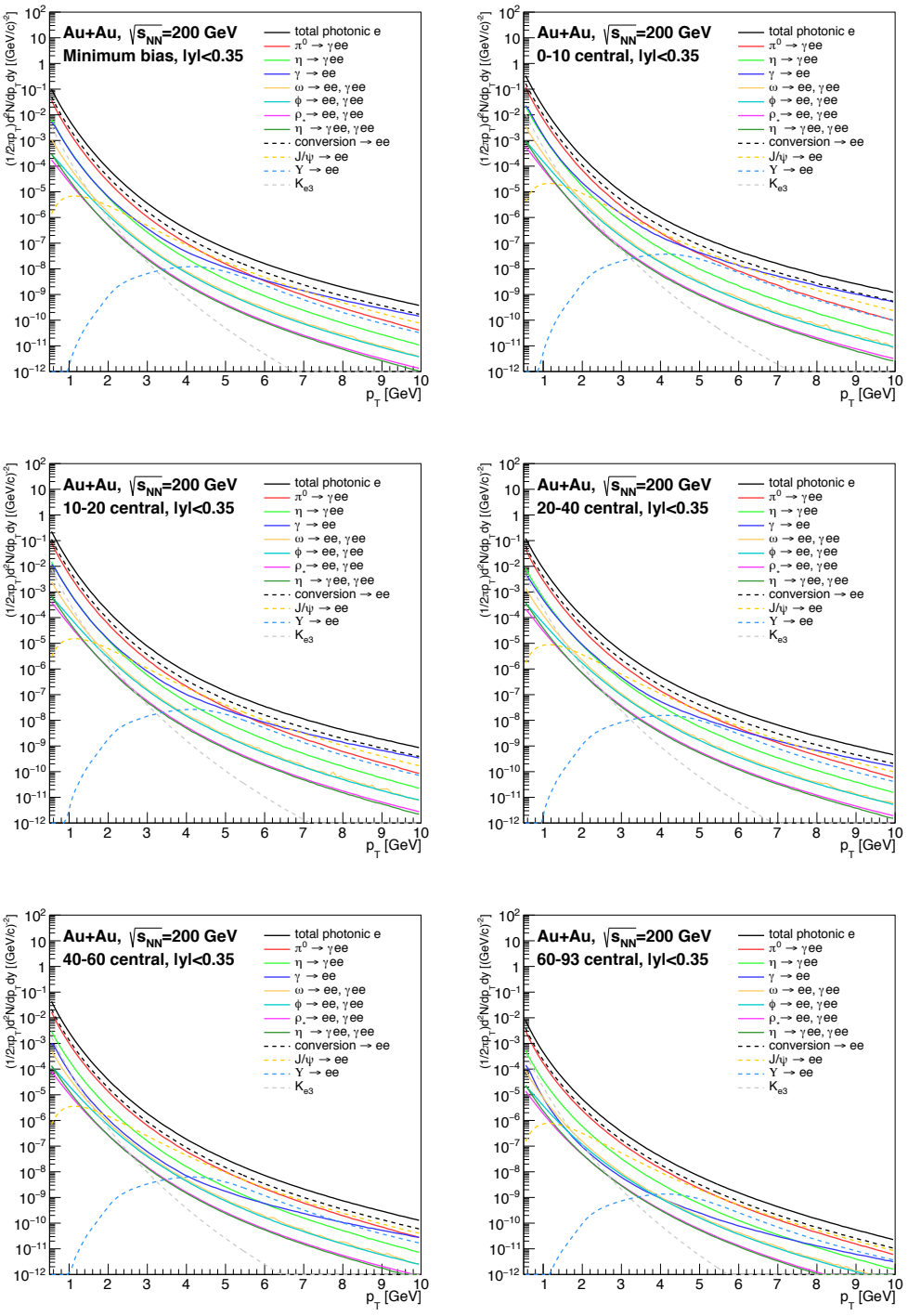

Figure 4.28: The PHENIX electron cocktail generated by EXODUS, updating the photonic electron from an internal and an external conversion.

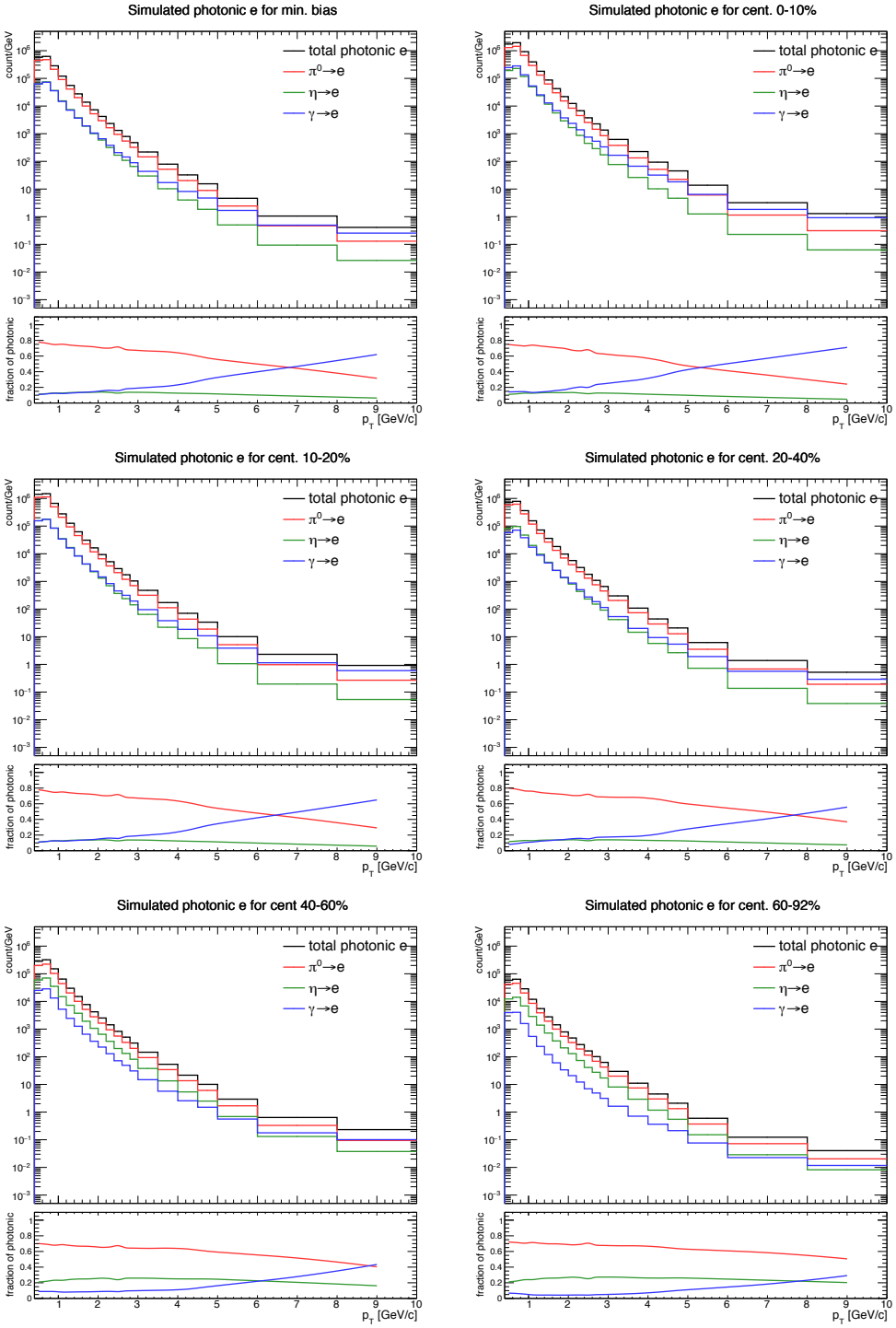

Figure 4.29: Simulated photonic electron spectrum from π^0, η and direct photon. Bottom panel show the fraction of photonic electrons.

4.4 Background Estimation

This section details how to estimate each background component. Expected background components are described in the following.

- Misidentified hadron (Mis-ID hadron)
  The RICH detector can detect Čerenkov lights from a high momentum charged particle. In the case of $p_{\mathrm{T}} < 5.0$ GeV/c, only electrons radiate Čerenkov light in RICH detector, however, high-multiplicity environment causes a mis-matching between a Čerenkov ring and an uncorrelated charged track. On the other hand, charged hadrons radiate Čerenkov light for 5.0 GeV/$c < p_{\mathrm{T}}$ and are often misidentified as an electron track. Both cases are classified to mis-ID hadron.

- Mismatch background (Mis-match BG)
  A Central Arm track accidentally associates uncorrelated VTX hits due to high-multiplicity environment, called Mis-match BG. Mis-match BG is divided into two cases, a random hit association and a random track association. A random hit association denotes a track matching to completely uncorrelated VTX hits at each VTX layer. On the other hand, a random track association denotes a track matching to correlated VTX hits produced by one uncorrelated charged particle.

- Photonic electron
  Photonic electrons mean internal (Dalitz decay) and external conversions from π^0, η and direct photon, which are the main background source in the single electron analysis. Electron-positron pairs produced by the Dalitz decay and the gamma conversion at the beam pipe and VTX B0 layer are considered in this analysis. Conversion electrons produced at materials outside B0 layer are rejected by requiring a VTX B0 hit.

- Kaon decay electron (K_{e3})
  Kaon decay electron denotes an electron from kaon weak decay, K_{e3}. The fraction of K_{e3} is a few percent in all electron tracks. However, it significantly contributes to the large $\mathrm{DCA_T}$ region due to the long lifetime. Kaon decay electrons can be reduced by ∼60% with a track quality cut because Kaon decays at a point away from a collision vertex.

- Heavy-quarkonia decay electron
  J/ψ and Υ, heavy-quarkonia, decay electron pairs significantly contributes to high p_{T} (> 3.0 GeV/c) because of the high mass.

4.4.1 Misidentified Hadron (mis-ID hadron)

In the high-multiplicity environment, a charged hadron track is accidentally identified as an electron track because of accidentally matching between a charged hadron track and RICH or EMCal hits. The mis-ID hadron tracks is estimated by the RICH swap method which performs reconstruction with swapping a sign of

track z-vector in the same event on a software for $p_{\rm T} < 4.5$ GeV/c. This method reproduces accidentally matching between Central Arm tracks and RICH hits and provides a statistical estimate. For 4.8 GeV/$c \leq p_{\rm T}$, Charged hadrons radiate Čerenkov light and make RICH hits, thus, the RICH swap method underestimates the fraction of mis-ID hadron. These contaminations are estimated by the **dep** template-fit method. Measured **dep** distributions of electron candidates are reproduced by two **dep** templates, the **dep** distribution of electrons and the **dep** distribution of charged hadrons as shown in Fig. 4.13. The **dep** template of electrons is obtained from the measured **dep** distribution subtracted mis-ID hadrons by the RICH swap method for $p_{\rm T} \leq 4.5$ GeV/c. Note that the **dep** distribution is sigmalized in each $p_{\rm T}$ bin and does not have $p_{\rm T}$ dependence because of its definition. The **dep** distribution of charged hadrons is obtained with the reverse electron identification cut for each $p_{\rm T}$ bin. These templates are fitted to measured **dep** distributions of electron candidates to extract mis-ID hadron fraction for 4.5 GeV/$c \leq p_{\rm T}$.

Demonstration in simulation

First of all, the extraction method of mis-ID hadrons, the RICH swap and the **dep** template-fit method, is demonstrated in the multi-particle simulation described as Sec. 4.3. The PHENIX GEANT3 simulation reproduces hits at each detector and tracks and **dep** distributions are reconstructed with the same reconstruction code as the real data. Fig. 4.30 shows the demonstration of the **dep** template-fit method for each $p_{\rm T}$ bin. **dep** distributions of all electron candidates (black) are fitted with the true electron **dep** distributions (red) obtained by the RICH swap method and the charged hadron **dep** distributions (green) obtained by charged tracks with reverse electron identification cut. Here, the sum distribution (blue) of independently obtained signal and background shows reasonable agreement with the simulated **dep** distributions of all electron candidates.

The true background distribution is determined by GEANT hit information and compared with both **dep** distributions of mis-ID hadrons determined by the **dep** template-fit and RICH swap method as shown in Fig. 4.31. These are in reasonable agreement, which indicates the **dep** template-fi method works well. Fractions of mis-ID hadron with both methods are calculated for each $p_{\rm T}$ and compared with the true fraction as shown in Fig. 4.32. Here, the mis-ID hadron fraction is calculated for **dep** > -2.0 as same as the electron identification cut. Extracted mis-ID hadron fractions by two methods are in reasonable agreement with true mis-ID hadron fractions, which indicates that two methods work well. Note the RICH swap method underestimates the fraction for $p_{\rm T} < 4.8$ GeV/c. Two methods have the difference by 5$\sim$10%. We assign the conservative 10% systematic uncertainty for both methods. In this analysis, the RICH swap method is applied for $p_{\rm T} \leq 4.5$ GeV/c and the **dep** template-fit method is applied for 4.5 GeV/$c <$ $p_{\rm T}$.

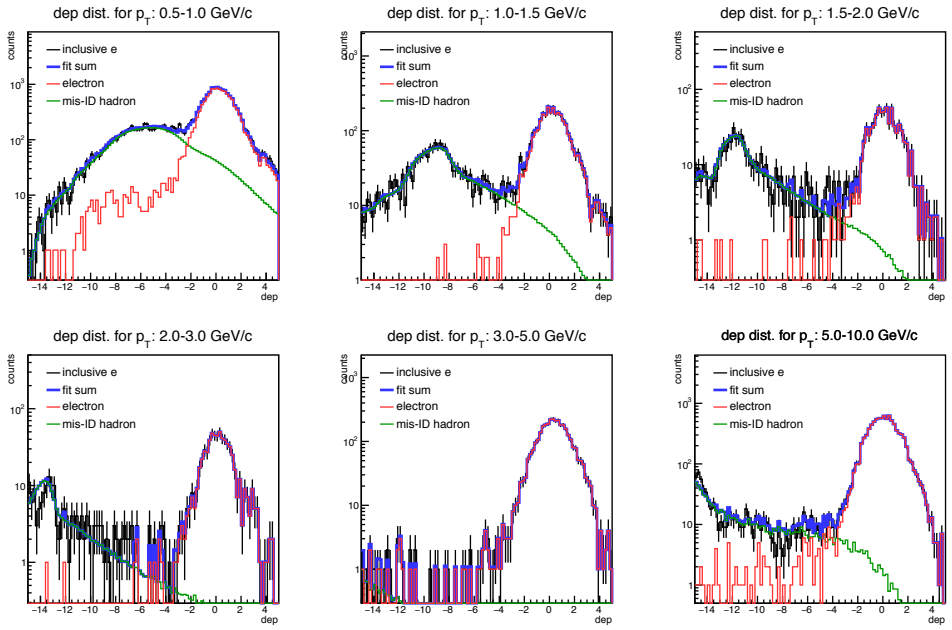

Figure 4.30: The demonstration of the **dep** template-fit method in the multi-particle simulation. (Black) all electron candidates, (Red) electron templates, (Green) BG template, (Blue) total fit.

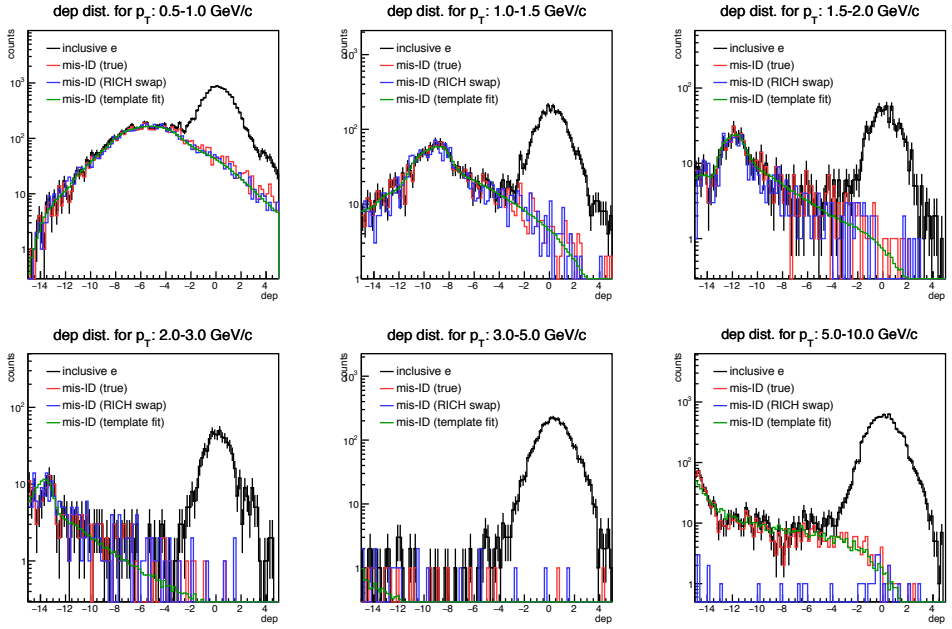

Figure 4.31: The comparison of mis-ID hadron **dep** shapes between the **dep** template-fit method (green), the RICH swap method (blue), and the true BG shape (red).

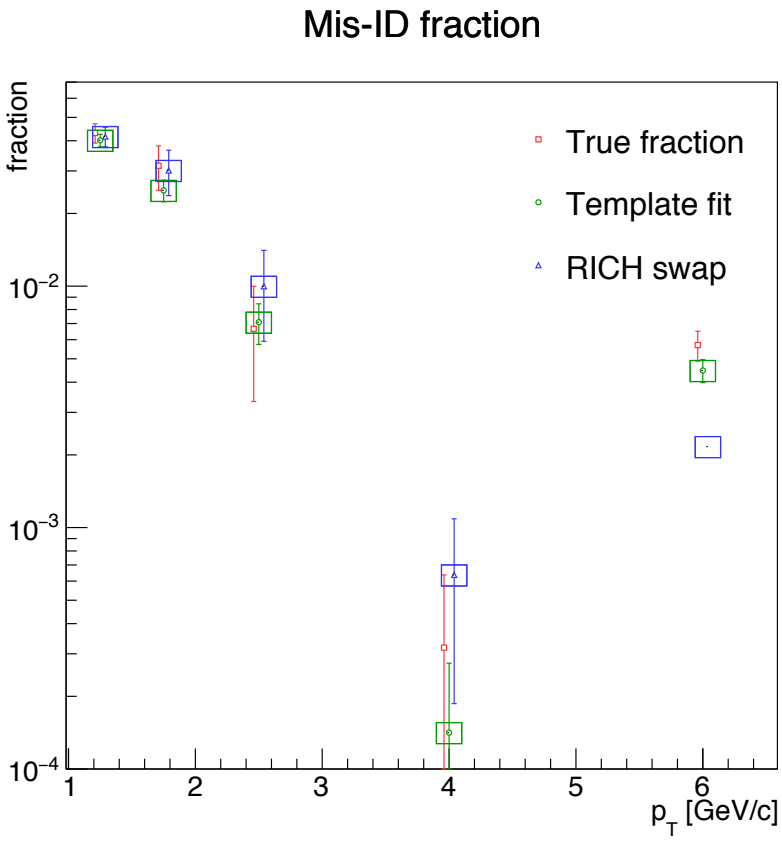

Figure 4.32: The fraction of mis-ID hadrons in the multi-particle simulation estimated by the **dep** template-fit method (green), the RHIC swap method (blue), and GEANT information for the true fraction (red).

Extraction of mis-ID background in real data

In order to calculate fractions of mis-ID hadrons in the real data, the RICH swap method and the **dep** template-fit method are applied to measured data for each p_{T} bin. Fig. 4.33 shows measured **dep** distributions of all electron candidates and fitted template **dep** distributions of electrons and mis-ID hadrons. Fitted templates of mis-ID hadrons are in reasonable agreement with distributions estimated by the RICH swap method. In order to confirm fit status, the ratio of the data to the fit is calculated as shown in Fig. 4.34. The ratios show flat distribution around unity, indicating the success of fits. Fractions of mis-ID hadron are calculated and compared between the RICH swap and the **dep** template-fit method as shown in Fig. 4.45. These fractions are in reasonable agreement within the uncertainty. Fig. 4.46 shows the resulted fraction of mis-ID hadron by the RICH swap method for $p_{\mathrm{T}} \leq 4.5$ GeV/c and the template-fit method for 4.5 GeV/$c \leq p_{\mathrm{T}}$. The mis-ID hadron fraction drastically changes at $p_{\mathrm{T}} = 4.5$ GeV/c because charged hadrons radiate Čerenkov light for 4.8 GeV/$c \leq p_{\mathrm{T}}$ and are mis-identified as an electron. The mis-ID hadron fractions are calculated up to $p_{\mathrm{T}} = 9.0$ GeV/c for each centrality and show strong centrality dependence.

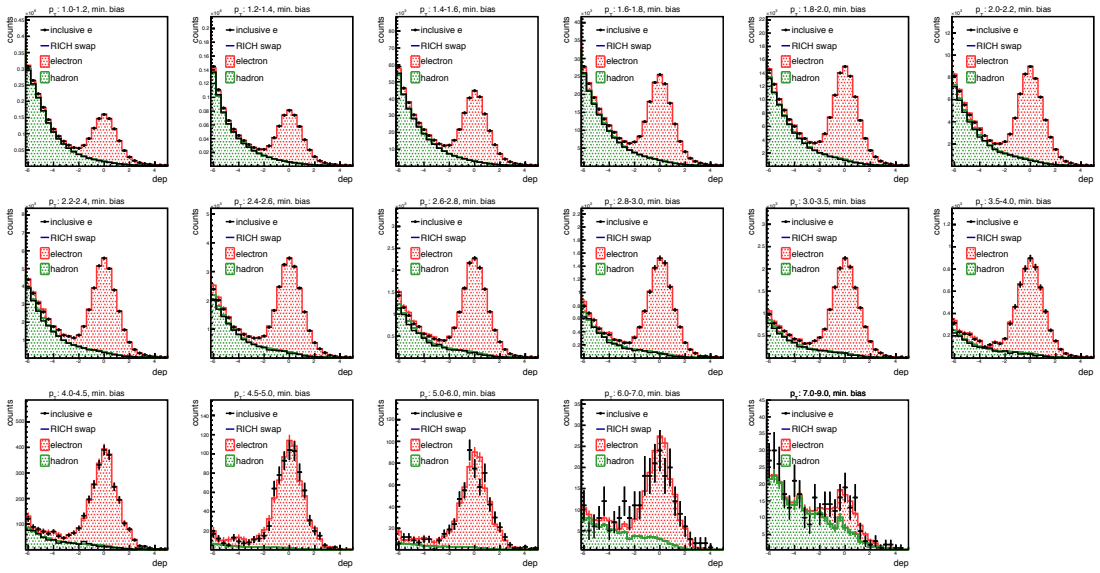

Figure 4.33: (Minimum bias) The measured **dep** distributions and fitted two **dep** templates, the true electron **dep** sample for signal (red) and the charged hadron **dep** sample for background (green).

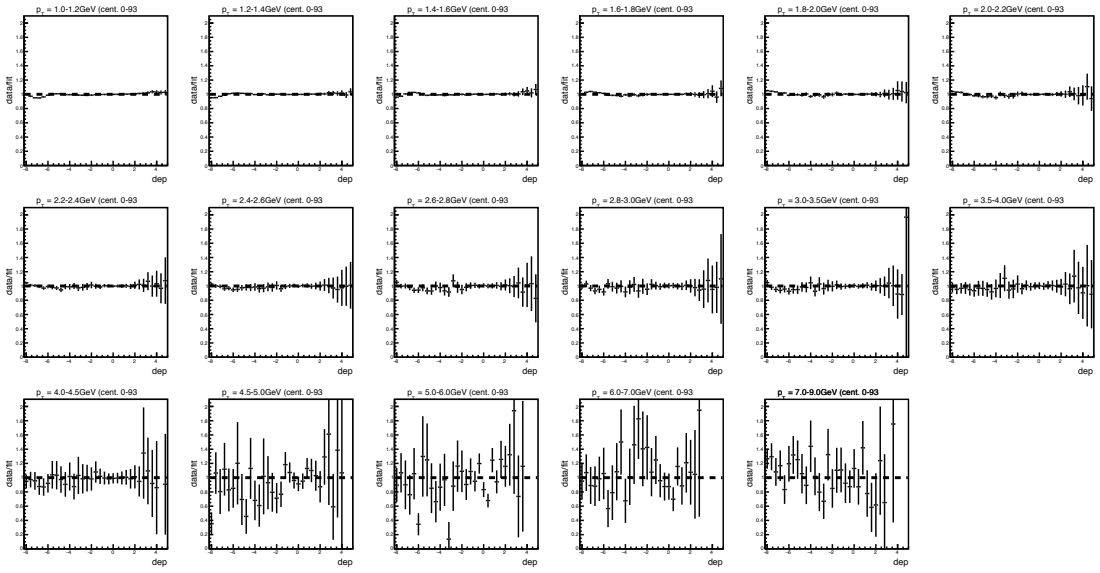

Figure 4.34: (Minimum bias) The ratio of the template-fit to the data.

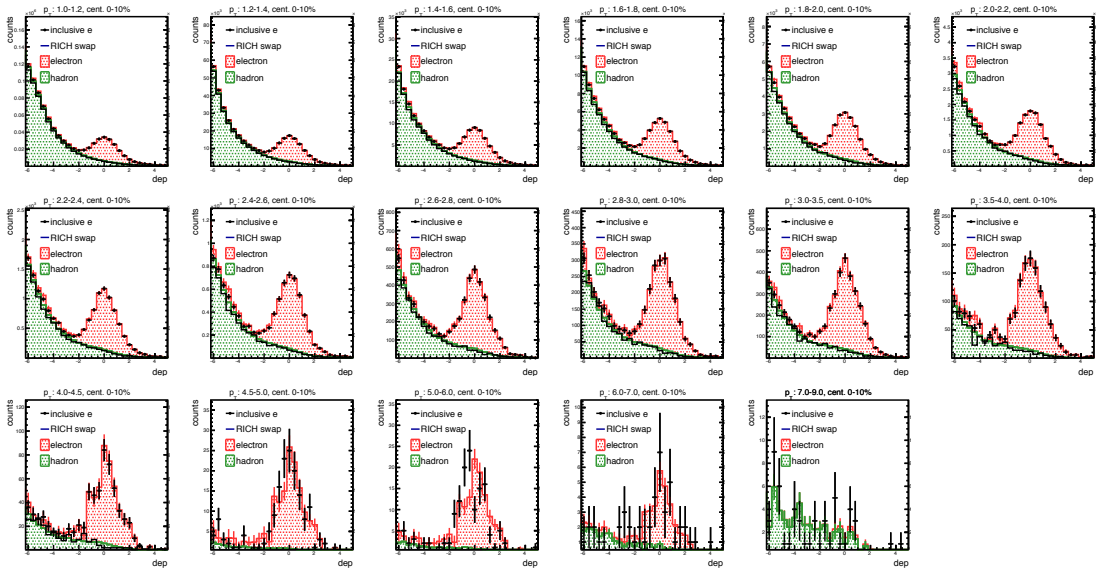

Figure 4.35: (0-10% centrality) The measured **dep** distributions and fitted two **dep** templates, the true electron **dep** sample for signal (red) and the charged hadron **dep** sample for background (green).

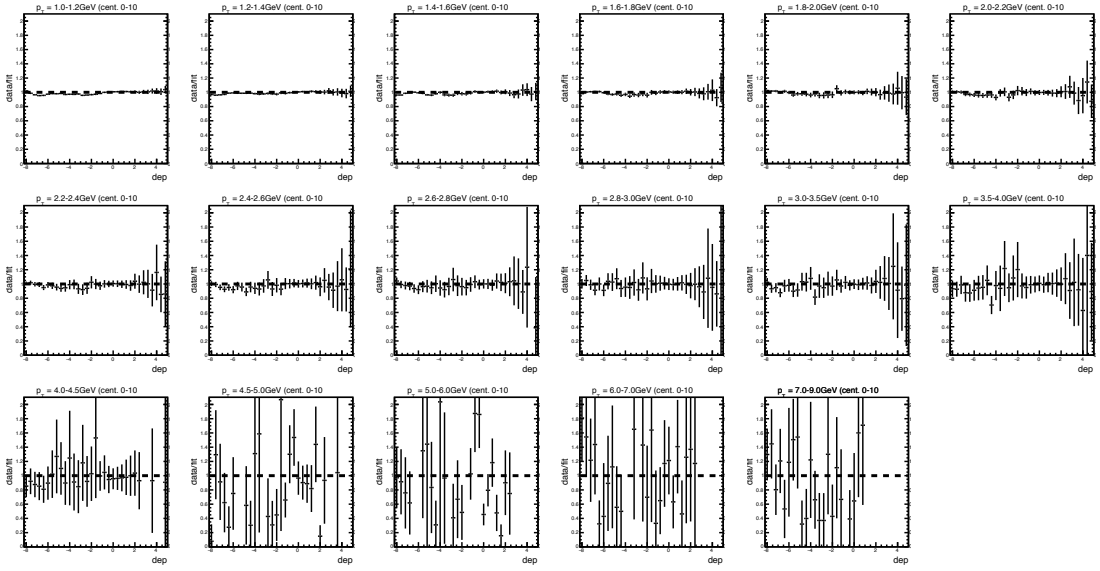

Figure 4.36: (0-10% centrality) The ratio of the template-fit to the data.

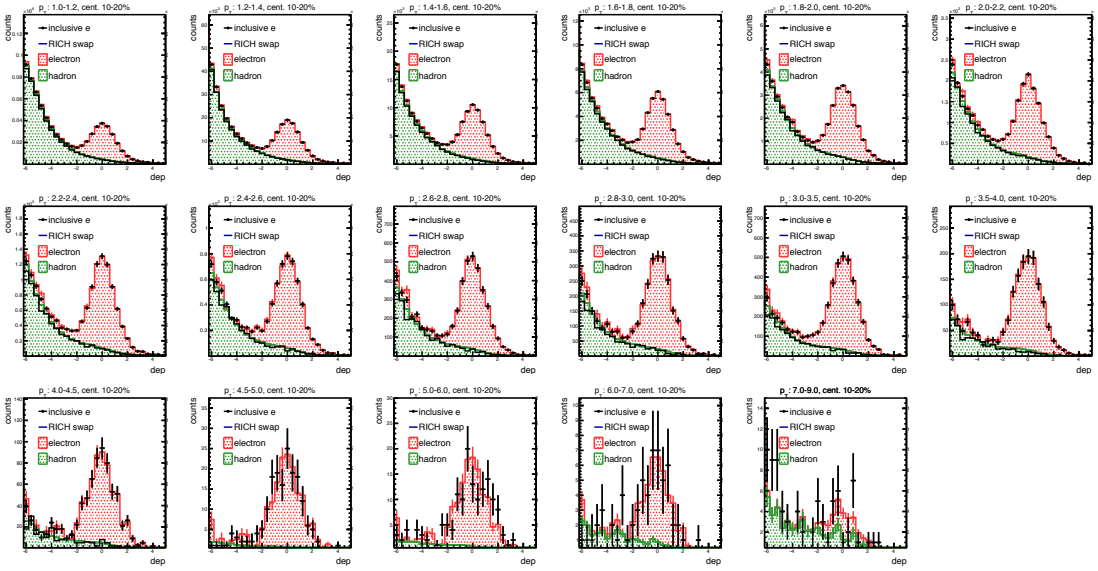

Figure 4.37: (10-20% centrality) The measured **dep** distributions and fitted two **dep** templates, the true electron **dep** sample for signal (red) and the charged hadron **dep** sample for background (green).

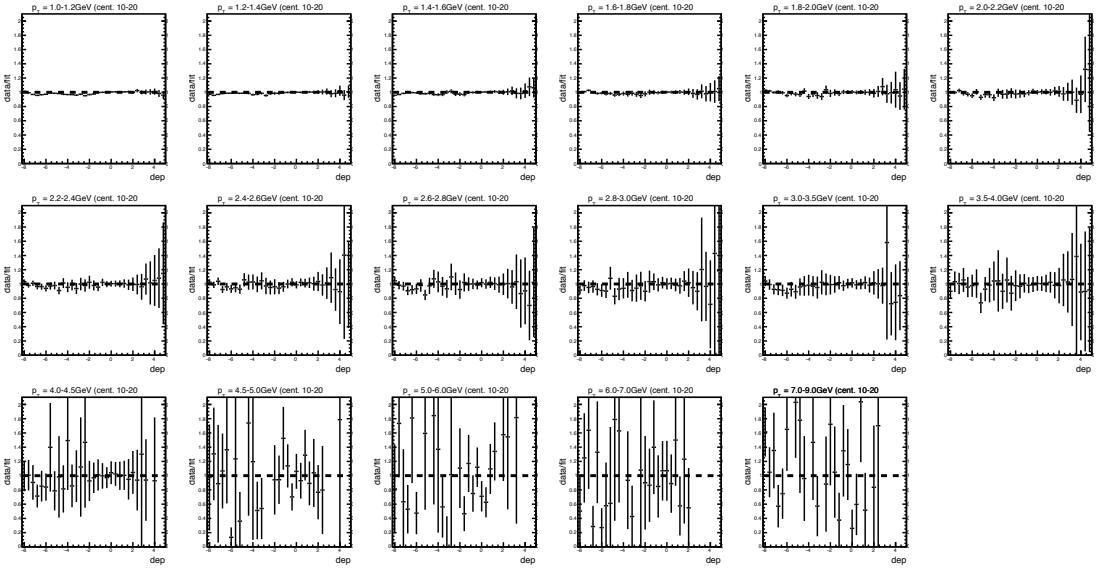

Figure 4.38: (10-20% centrality) The ratio of the template-fit to the data.

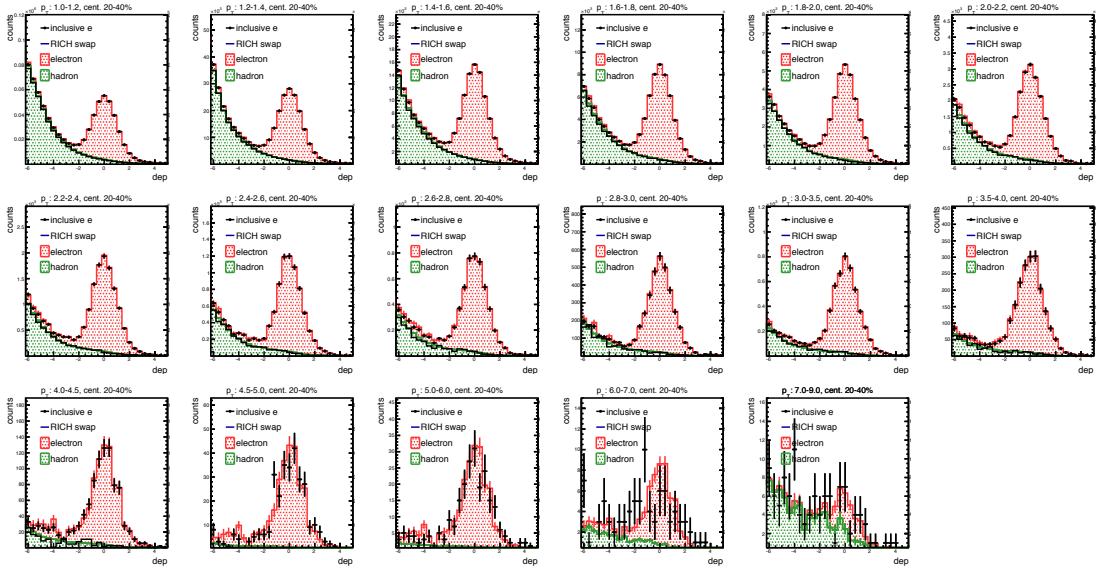

Figure 4.39: (20-40% centrality) The measured **dep** distributions and fitted two **dep** templates, the true electron **dep** sample for signal (red) and the charged hadron **dep** sample for background (green).

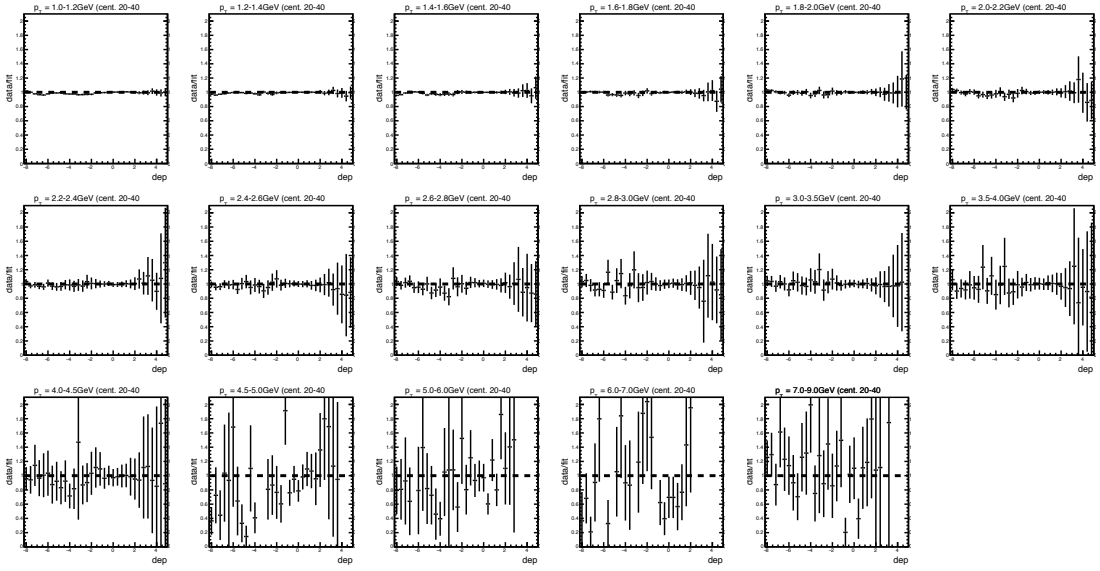

Figure 4.40: (20-40% centrality) The ratio of the template-fit to the data.

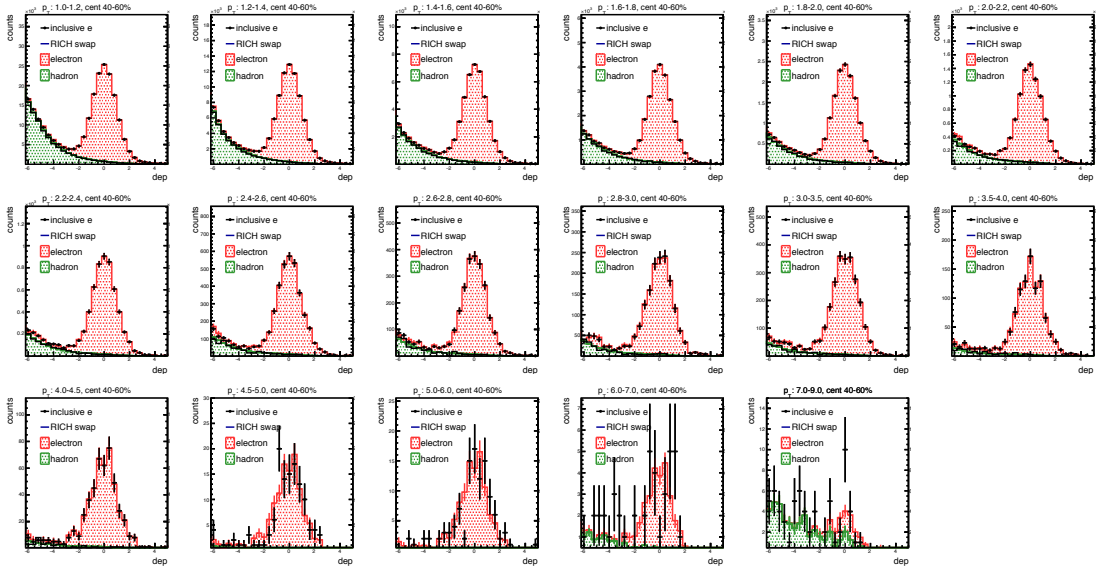

Figure 4.41: (40-60% centrality) The measured **dep** distributions and fitted two **dep** templates, the true electron **dep** sample for signal (red) and the charged hadron **dep** sample for background (green).

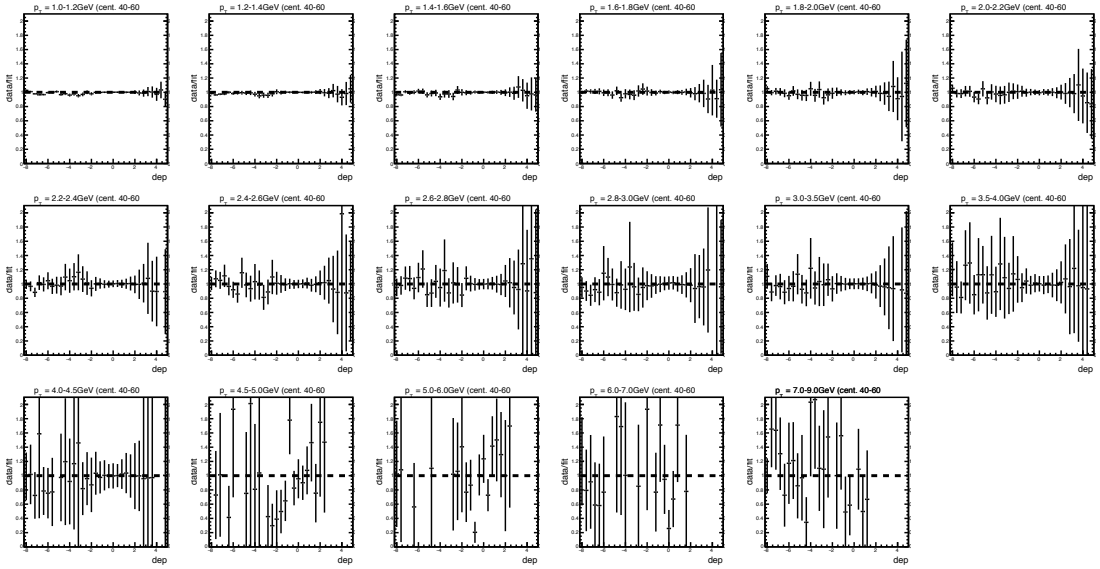

Figure 4.42: (40-60% centrality) The ratio of the template-fit to the data.

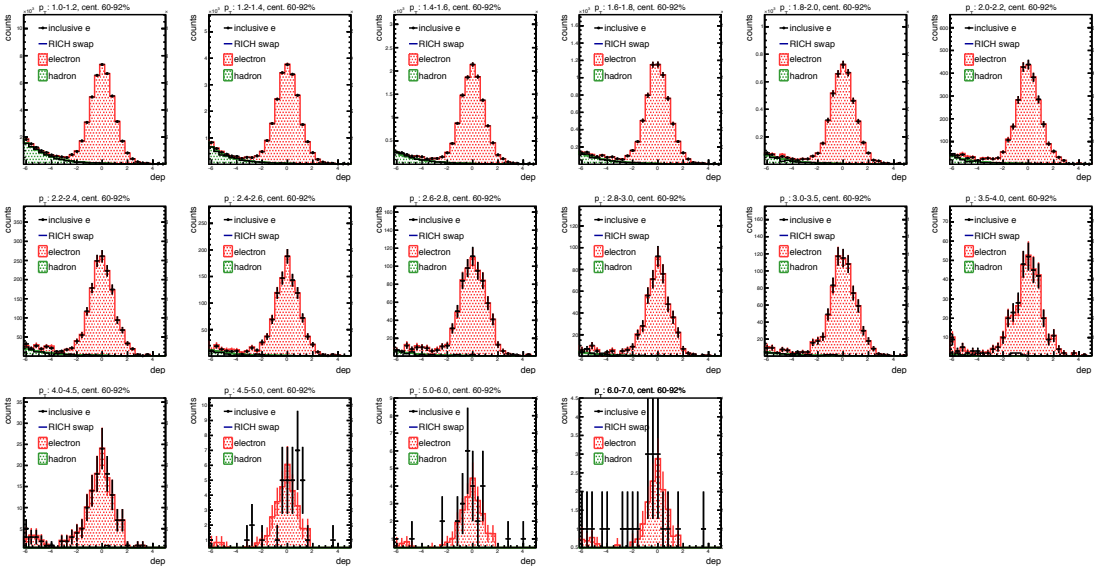

Figure 4.43: (60-92% centrality) The measured **dep** distributions and fitted two **dep** templates, the true electron **dep** sample for signal (red) and the charged hadron **dep** sample for background (green).

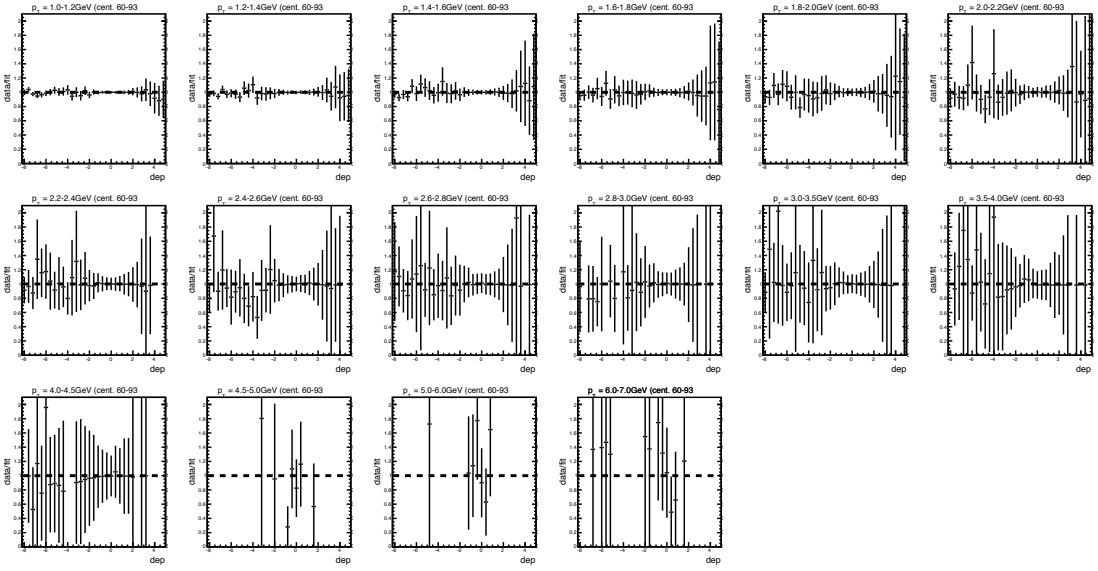

Figure 4.44: (60-92% centrality) The ratio of the template-fit to the data.

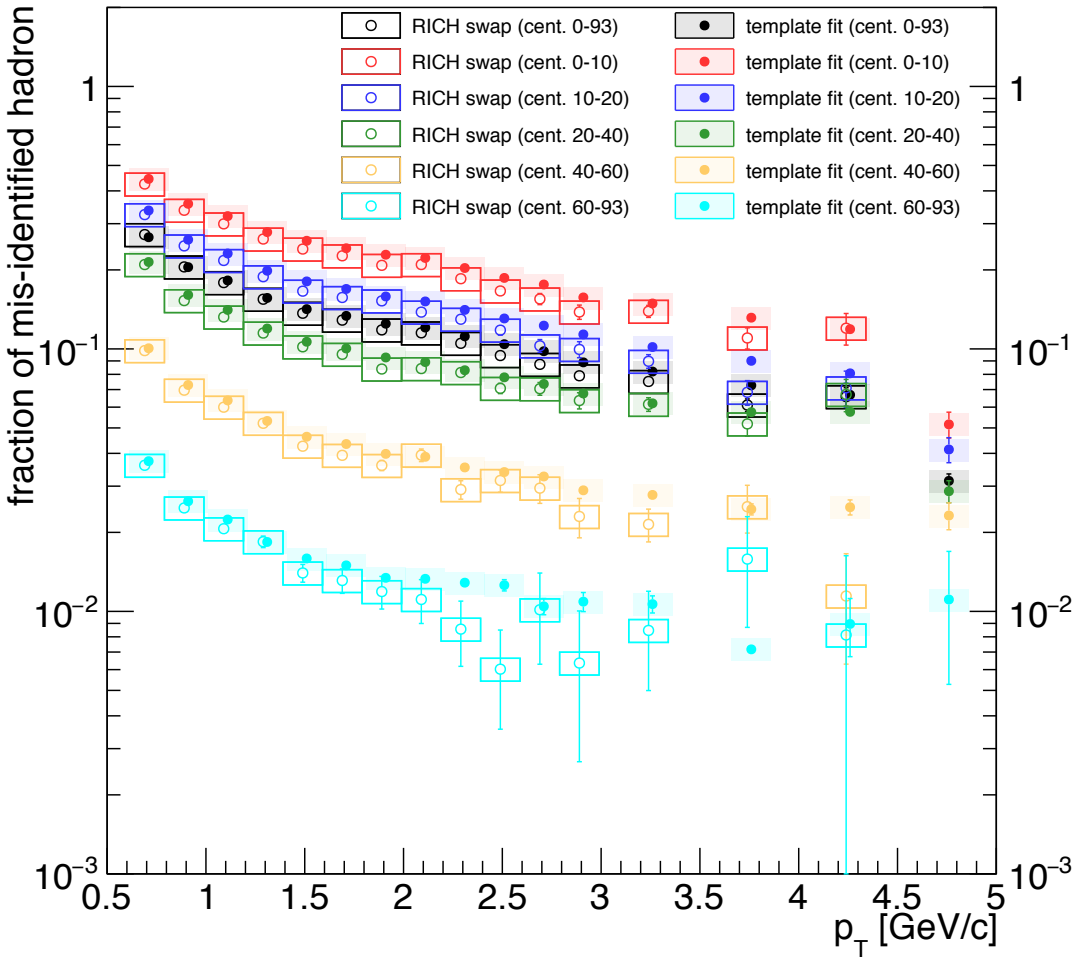

Figure 4.45: The comparison of mis-ID hadron fraction between the RICH swap method and **dep** template-fit method at 5 GeV/$c \leq p_{\mathrm{T}}$. It show reasonable agreement.

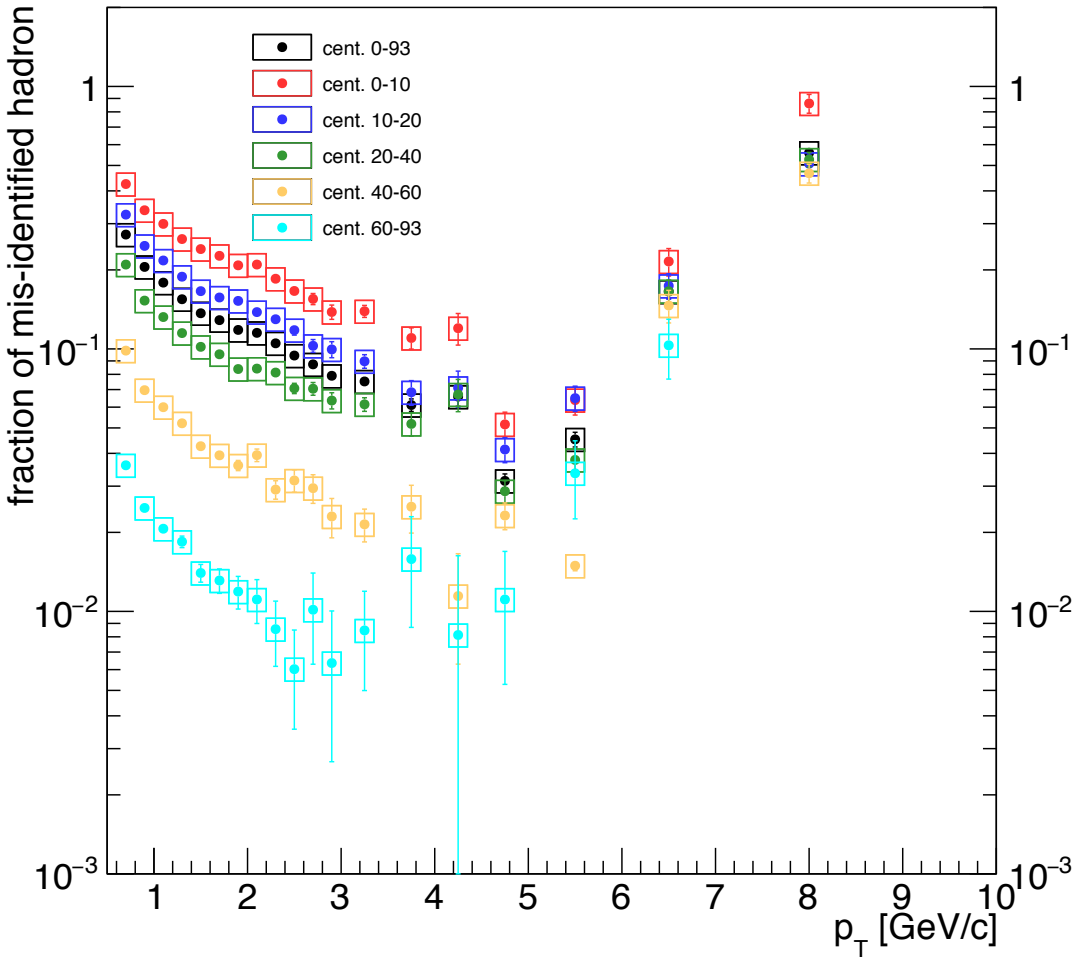

Figure 4.46: The fraction of mis-ID hadrons in all electron candidates. The RICH swap method is applied at 5 GeV/$c \leq p_{\mathrm{T}}$, and the **dep** template-fit method is applied at 5 GeV/$c \leq p_{\mathrm{T}}$

4.4.2 Mis-mathced Background (mis-match BG)

A Central Arm track accidentally associates uncorrelated VTX tracks or hits due to high-multiplicity environment. The probability of mismatching is a few percent, however, such accidental association significantly contributes to large $\mathrm{DCA}_{\mathrm{T}}$ region. This background can be estimated by the VTX swap method which reproduces a mis-matching intentionally with changing the angle of a DC track by 10 degrees in ϕ or η plane. 10 degrees rotation is sufficiently larger than the DC angle resolution, therefore, angle rotated tracks are never connected with their origin tracks. This method provides statistical estimate and does not need normalization, which is an important advantage compared with an event mixing method.

Demonstration in simulation

The VTX swap method is demonstrated with the multi-particle simulation. In the simulation, the track reconstruction performs with GEANT hit information and calculates DCA_T for each track. DCA_T distributions are divided into two cases, correct-matching and mis-matching, as shown in Fig. 4.47. The DCA_T distribution of mis-match backgrounds (blue) is broad with the peak around $DCA_T = 0$ because it is composed of random track-match or random hit-match. DCA_T distribution of mis-math is divided by GEANT hit information into the random track-match and random hit-match as shown in Fig. 4.48. Random track-match makes peak structure and causes shift to the positive side due to momentum mismatching between a DC track and a VTX track. The shift to positive side results from mis-matching of a high-momentum DC track and a low-momentum uncorrelated VTX track. Random hit-match makes broad distribution because a random hit is uncorrelated to a collision vertex.

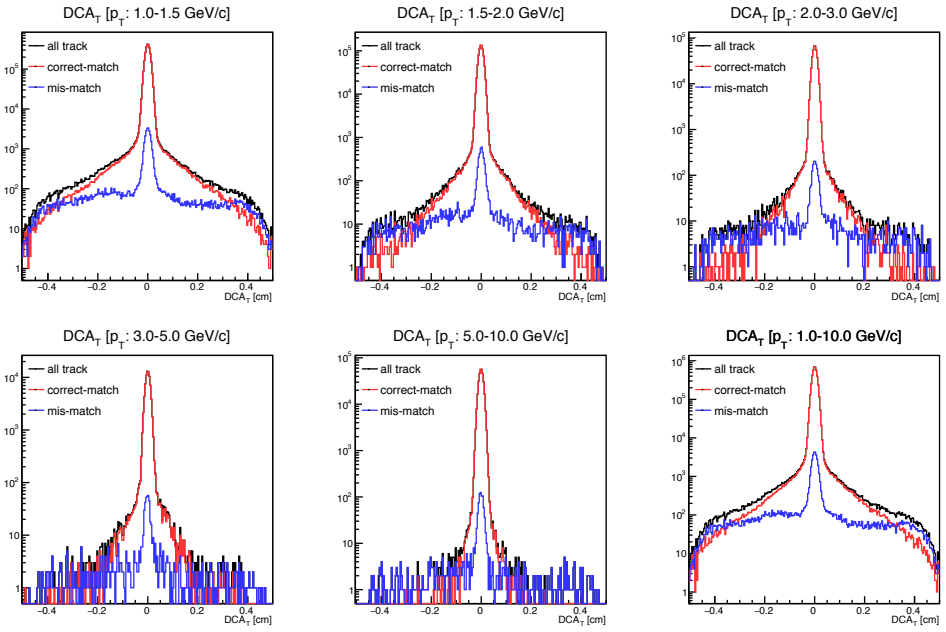

Figure 4.47: The DCA distributions of all charged hadrons in simulation, all tracks (black), correct-match tracks (red), and mis-match tracks (blue).

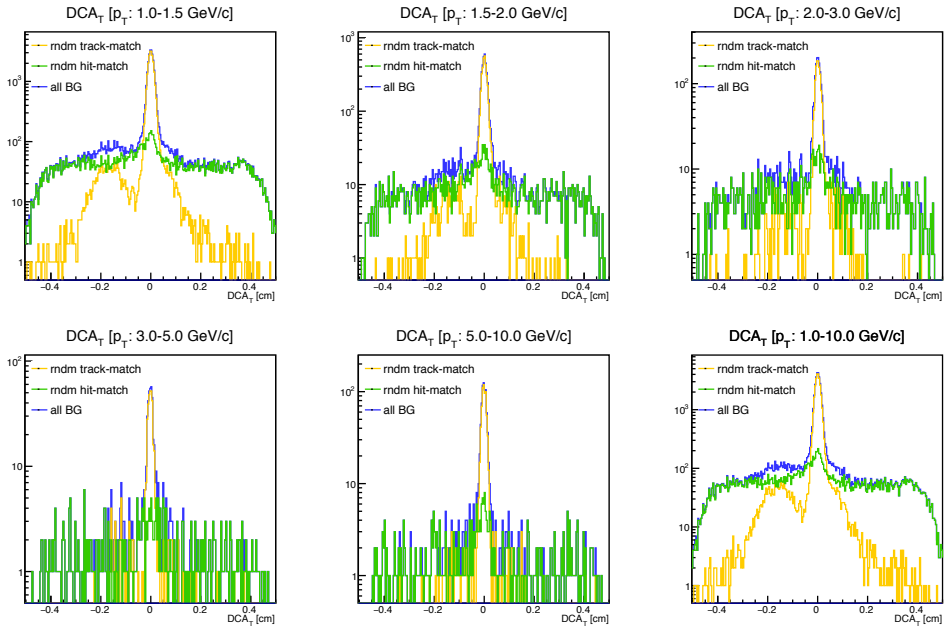

Figure 4.48: The DCA distributions of the mis-match background estimated in simulation, all mismatch background (blue), random track-match requiring VTX hits from same particle origin (yellow), random hit-match requiring VTX hits from different particle origins (green).

The results of the VTX swap method is consistent with the true background distributions, but the central peaks are underestimated as shown in Fig. 4.49. A correlated track-matching such as matching with decay partners makes the difference because only uncorrelated matching is reproduced by the VTX swap method. It is confirmed with the simulation without decay particles as shown in Fig. 4.50. The DCA_T distributions of the correlated and uncorrelated track-match background are determined by GEANT information. Specifically, we confirm whether the parents of particle associated a DC track and VTX hits are the same.

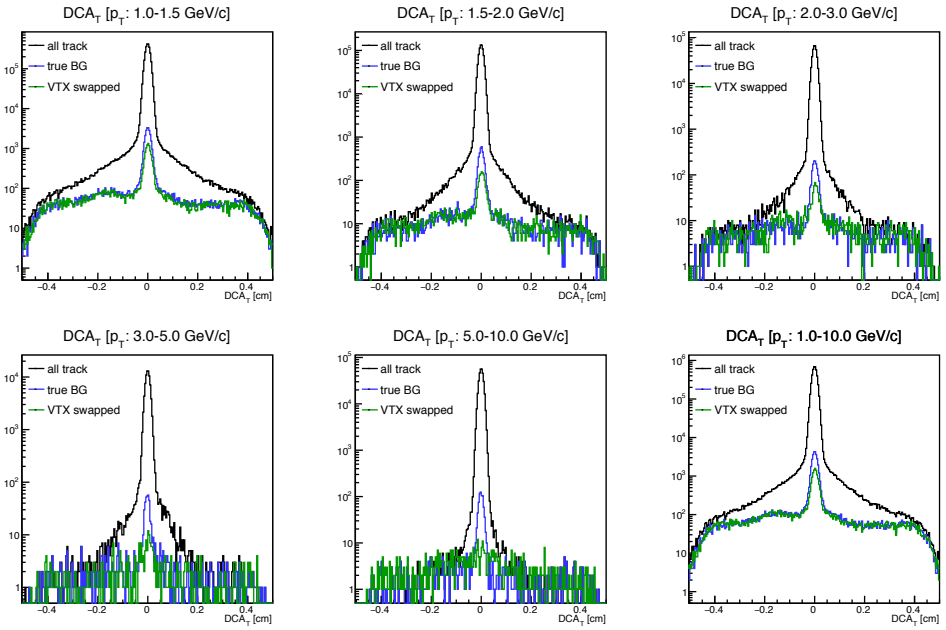

Figure 4.49: The comparison of DCA distributions between mis-match tracks and VTX swapped tracks in simulation. (black) all charged hadron tracks, (blue) mis-match tracks, (green) VTX swapped tracks.

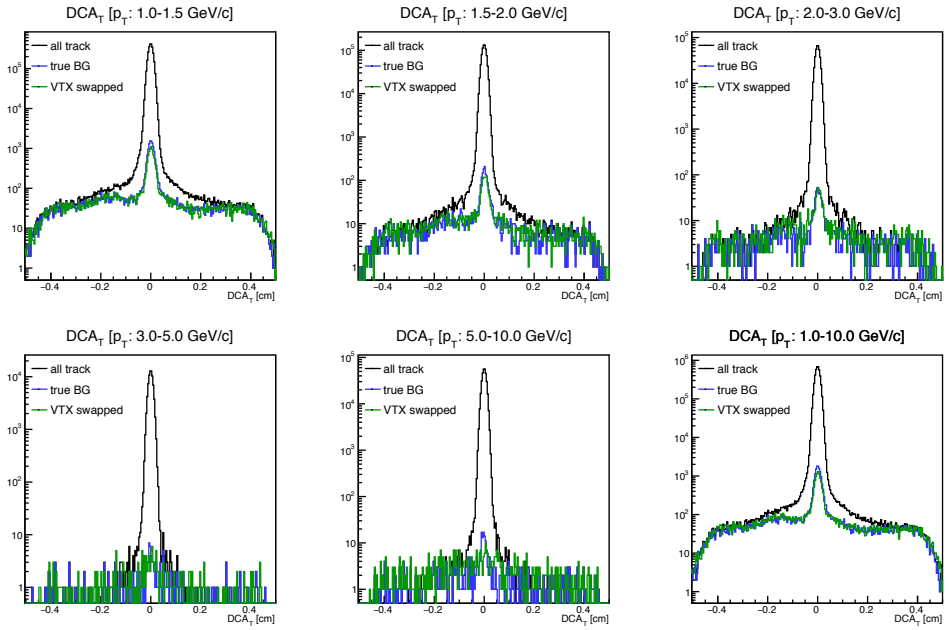

Figure 4.50: The comparison of DCA distributions between mis-match tracks and VTX swapped tracks under condition of no decay particle. (black) all charged hadron tracks, (blue) mis-match tracks, (green) VTX swapped tracks. In case of no decay particle, the VTX swap method can reproduce well mis-match DCA_T distributions.

In order to investigate the influence of the underestimation of the VTX swap method, the DCA_T shape of correlated track-match background is compared with that of correct-match and uncorrelated track-match background as shown in Fig. 4.51. It is found that the DCA_T shape of correlated track-match background is almost consistent with the DCA_T shape of correct-match since a mis-matched decay partner has similar momentum and trajectory with origin particle. The fraction of correlated track-match background is less than 0.5 % compared with the correct-match, the signal distribution. Therefore, correlated track-match background is ignored in this analysis. In summary, it is demonstrated that the VTX swap method reproduce random hit-match and random track-match background without correlated-match background caused by decay partners.

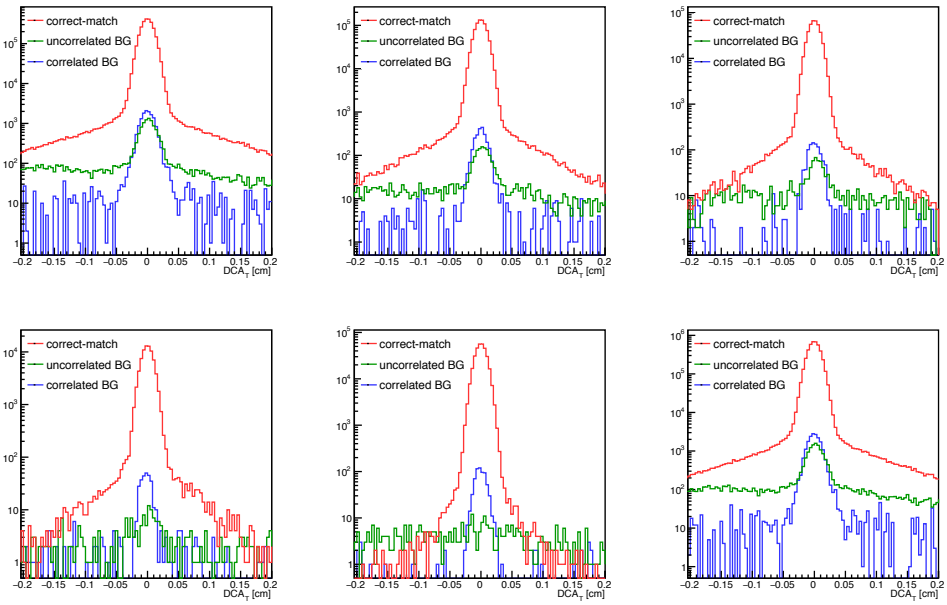

Figure 4.51: The DCA distribution of correct- and mis-match tracks estimated in simulation. (red) correct-match tracks, (green) mis-match with uncorrelated tracks, (blue) mis-match with correlated tracks, decay partners.

Extraction of mis-match background in real data

The VTX swap method performs to estimate mis-match background in DCA_T distributions for the real data analysis. The rotation angle dependence of the VTX swap method is investigated with two different rotation angles, 10 and 15 degrees, to evaluate an effect of local particle density (i.e. jet effects). Fig. 4.52 shows DCA distributions of mis-match backgrounds with two different rotation angles. The DCA distributions with 10 and 15 degrees rotations show consistent, indicating very small effect of local particle density. In this analysis, we ignore the effect and employ 10 degrees rotation for the VTX swap method.

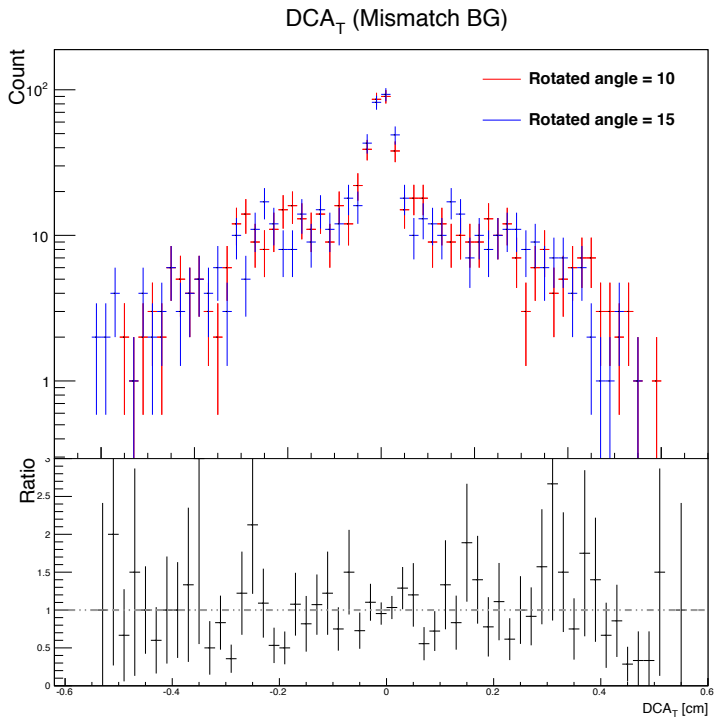

Figure 4.52: The DCA distribution of mismatch background estimated by the VTX swap method with 10 and 15 degrees in the real data.

The DCA_T distributions of mis-match background estimated by the VTX swap method in the real data for each centrality as shown in Fig. 4.53. The strong centrality dependence of the mis-match background fraction can be seen because the mis-match background is caused by the high-multiplicity effect.

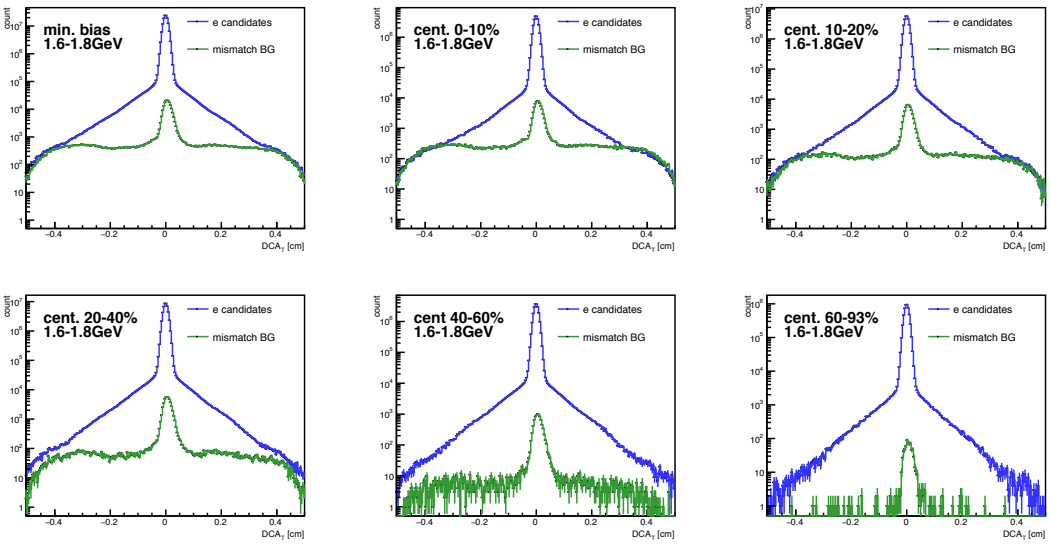

Figure 4.53: The DCA_T distributions of all electron candidates and mismatch background estimated by the VTX swap method in the real data.

4.4.3 Photonic Electron Background

Photonic electrons denote electrons produced by internal conversions (Dalitz decay) and external conversions (gamma conversion) of π^0, η and direct photon. It is are the main background source of this analysis. As for external conversions, we concern only external conversion pairs at the beam pipe and VTX B0 layer since external conversion pairs from outer layers can be rejected by requiring a B0 hit. Almost the same number of internal and external conversion electrons are produced in case of PHENIX material budget. The isolation cut at VTX greatly reduces photonic electrons because photonic electrons have narrow pair angle as described in Sec. 4.1.3. It rejects conversion electrons by $\sim$80% and Dalitz decay electrons by $\sim$50% as shown in Fig. 4.54. The survival rate of external conversions is smaller than that of internal conversions since electron-positron pairs from external conversions are produced at beam pipe and B0 VTX layer and have smaller opening angle due to shorter transit time in the magnetic field.

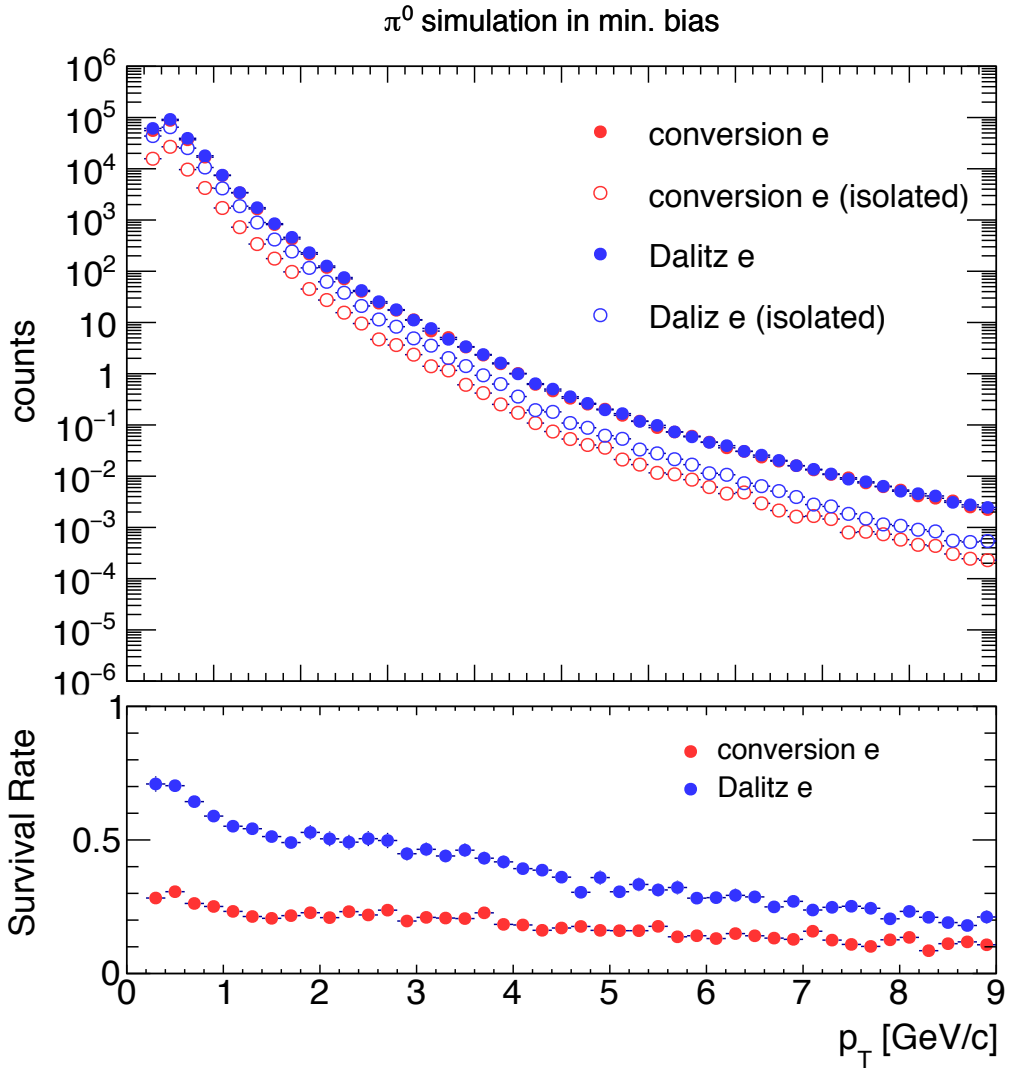

Figure 4.54: The simulated p_{T} distribution of electrons from external (conversion) and internal (Dalitz) conversions and the survival rate of the isolation cut at VTX.

After applying the isolation cut, the ratio of external to internal conversion is ∼40% as shown in Fig. 4.25. The isolation method provides statistical estimate of photonic and non-photonic electron fractions with the following formulas including 4 variables, the number of electron tracks (N_e), isolated electron tracks (N_e^*), and the survival rate of the isolation cut for conversion electrons (ϵ_C) and random associations (ϵ_R).

$$F_{NP} = \frac{N_e^* - \epsilon_R * \epsilon_C * N_e}{(1 - \epsilon_C) * \epsilon_R * N_e}. \tag{4.16}$$

- N_e: The number of total electron tracks.
  The number of total electron tracks including photonic and non-photonic electrons after subtracting mis-ID hadrons and mis-match backgrounds.

- N_e^*: The number of isolated electron tracks.
  The number of isolated electron tracks with by the isolation cut at VTX, enriched non-photonic electron tracks.

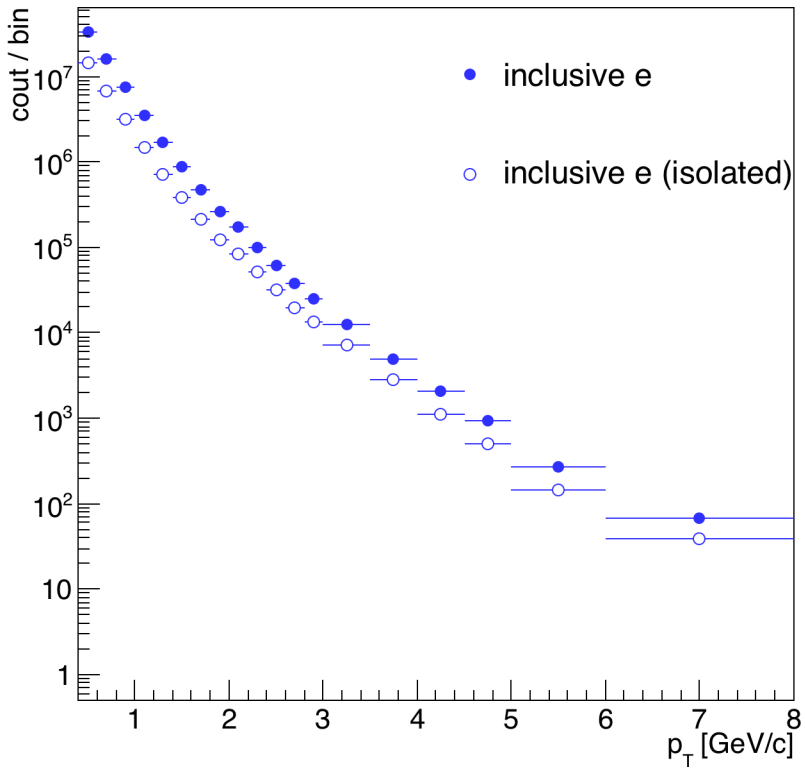

Figure 4.55: The raw yield of electron candidates in the real data without and with the isolation cut at VTX.

- ϵ_C: The survival rate of conversion electrons.
  The survival rate of conversion electrons is calculated by the ratio of the number of simulated photonic electron tracks (from π^0, η, and direct photons) with and without the isolation cut shown in Fig. 4.56. Note that the isolation cut window is very narrow for non-photonic electrons, therefore, ϵ_C of non-photonic electrons is about 0.98 as shown in Fig. 4.58. In this analysis, ϵ_C of non-photonic electrons is assumed to 1.0.

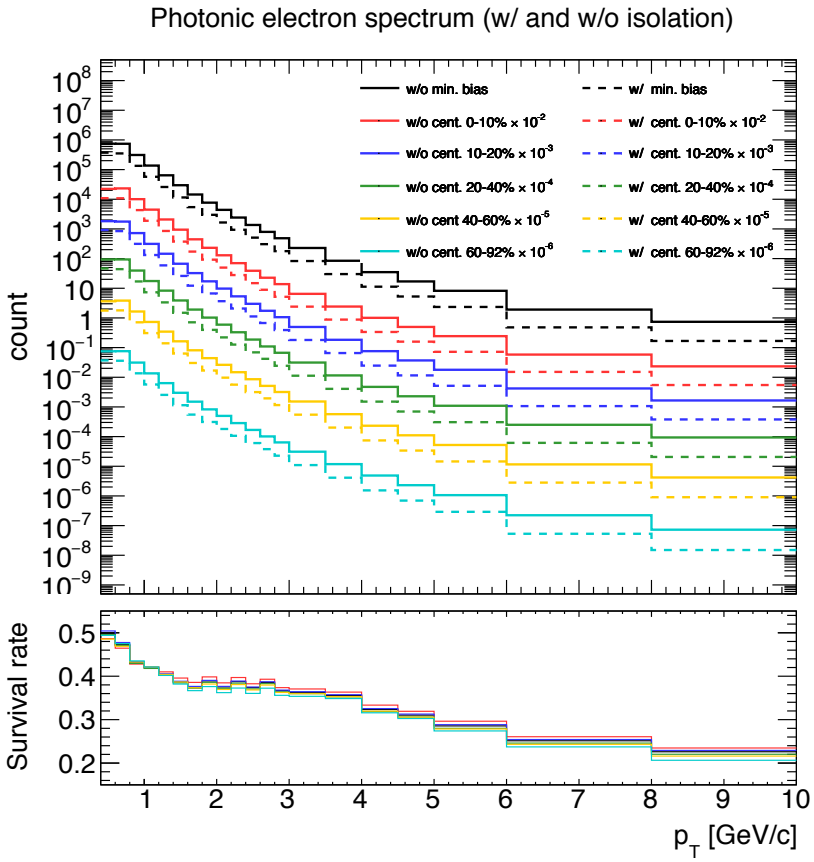

Figure 4.56: (top) Simulated p_{T} distribution of photonic electrons from π^0, η decay and direct photons without (solid line) and with (dashed line) the isolation cut for each centrality. (bottom) The survival rate of conversion electrons calculated from ratio of total photonic electron (solid line) to isolated photonic electron (dashed line).

- ϵ_R: The survival rate of a random associations.
  Non-photonic electrons are accidentally rejected by random associations with uncorrelated VTX hits under the high-multiplicity environment. The survival rate of random associations, (ϵ_R), is calculated by the ratio of the number of charged hadrons with and without the isolation cut in the data. Almost all tracks of charged hadrons are long-lived particles and rejected by the isolation cut due to random associations. It has the centrality dependence as shown in Fig. 4.57.

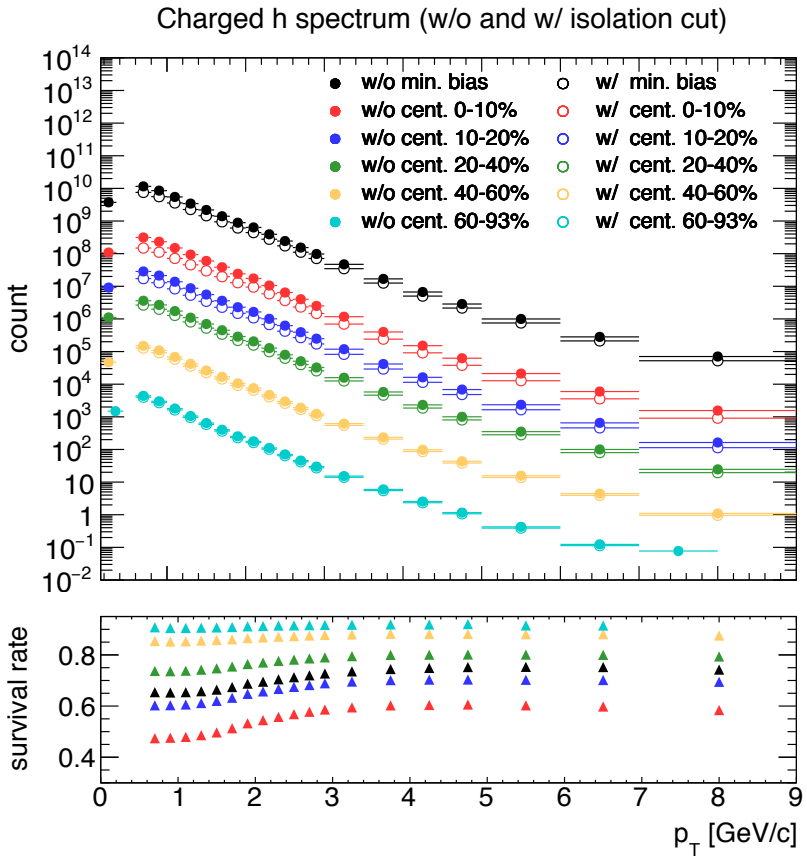

Figure 4.57: (top) Charged hadron spectrum in data without and with the isolation cut, (bottom) The survival rate of random associations, calculated from ratio of charged hadron to isolated charged hadron.

The numbers of electron tracks (N_e) and isolated electron tracks (N_e^*) are described by the numbers of photonic electrons (N_e^P) and non-photonic electrons (N_e^{NP}) in the following:

$$N_e = N_e^{NP} + N_e^P, \tag{4.17}$$

$$N_e^* = \epsilon_R * N_e^{NP} + \epsilon_R * \epsilon_C * N_e^P. \tag{4.18}$$

Finally, the simultaneous equations are solved to obtain the fraction of non-photonic electrons, F_{NP} (and photonic electron, F_P) as

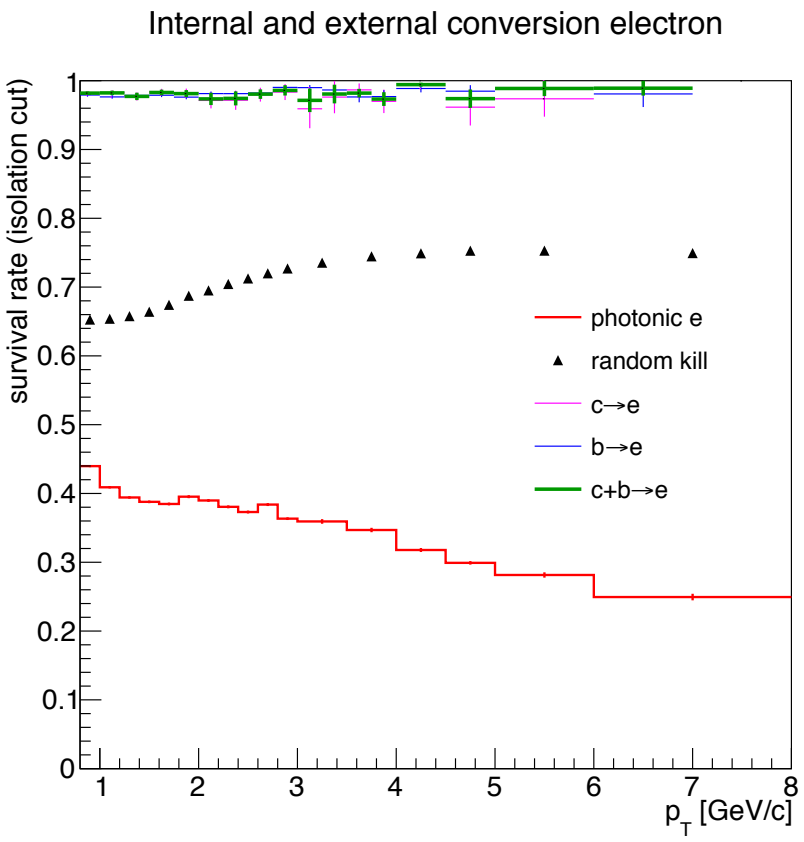

Figure 4.58: The summary of survival rates.

$$N_e^{NP} = \frac{N_e^* - \epsilon_R * \epsilon_C * N_e}{\epsilon_R * (1 - \epsilon_C)}, \tag{4.19}$$

$$N_e^{P} = \frac{\epsilon_R * N_e - N_e^*}{\epsilon_R * (1 - \epsilon_C)}, \tag{4.20}$$

$$F_{NP} = \frac{N_e^{NP}}{N_e^{NP} + N_e^{P}}, \tag{4.21}$$

$$= \frac{N_e^* - \epsilon_R * \epsilon_C * N_e}{(1 - \epsilon_C) * \epsilon_R * N_e}. \tag{4.22}$$

Fig. 4.59 shows the fraction of non-photonic electrons as a function of p_{T} for each centrality. The $\mathrm{F_{NP}}$ increases with increasing p_{T} because heavy flavor hadrons have higher mass than that light flavor hadrons. On the other hand, the $\mathrm{F_{NP}}$ increases in low p_{T} region with increasing the centrality because low mass hadrons are strongly suppressed than heavy flavors.

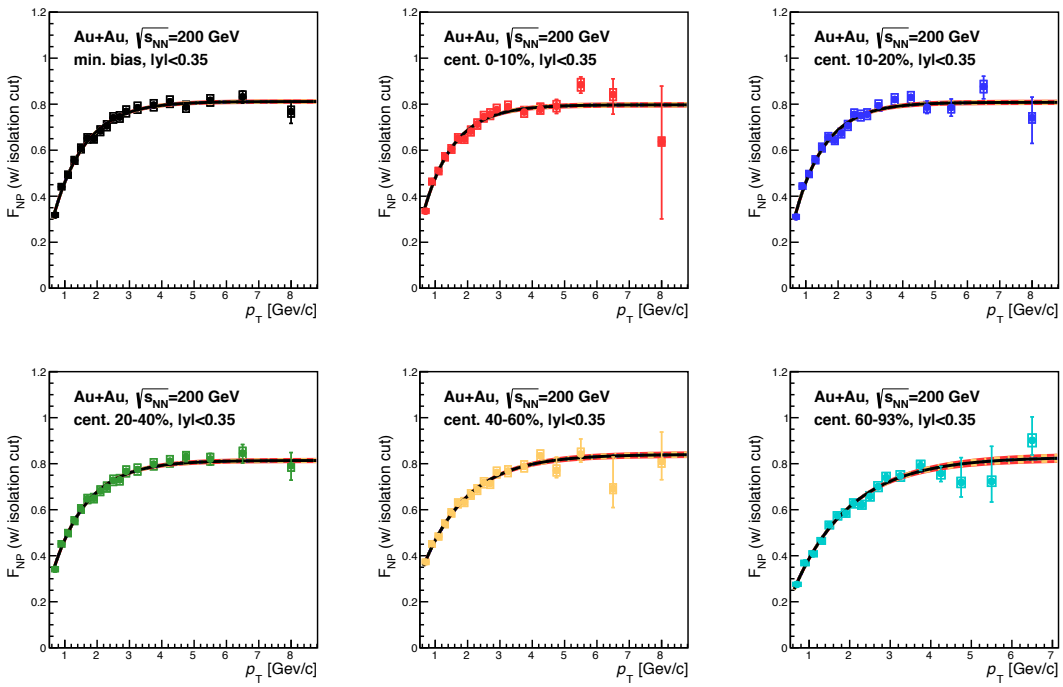

Figure 4.59: The fraction of non-photonic electrons (F_{NP}) estimated by the isolation method.

4.4.4 Non-photonic Electron Background (K_{e3}, J/ψ, Υ)

The PHENIX electron cocktail which is described in Sec. 4.3.4 provides the relative ratio of electrons for each non-photonic electron background. Fig. 4.60 shows the invariant yields of electrons from photonic sources, kaon decays, J/ψ decays, and Υ decays. The electron fractions each background are shown in Fig. 4.61. Note

that Fig. 4.61 shows the fractions in reconstructed tracks. The relative ratio of photonic electrons is reduced by the isolation cut and the non-photonic electrons is enriched for the heavy flavor analysis.

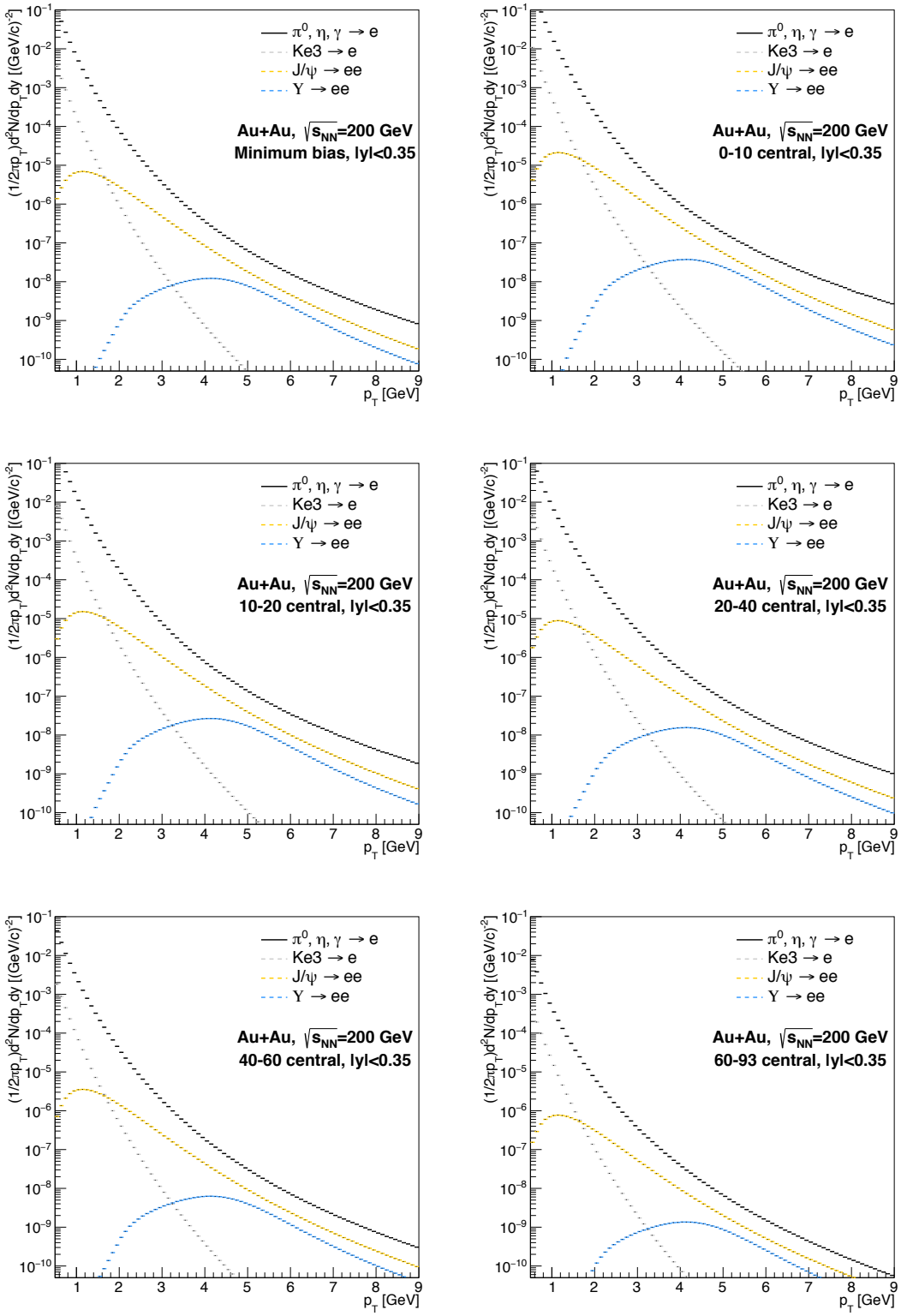

Figure 4.60: The invariant yield of electrons from photonic sources, kaon decays, J/ψ decays, and Υ decays assumed by the measured yield of parent particles.

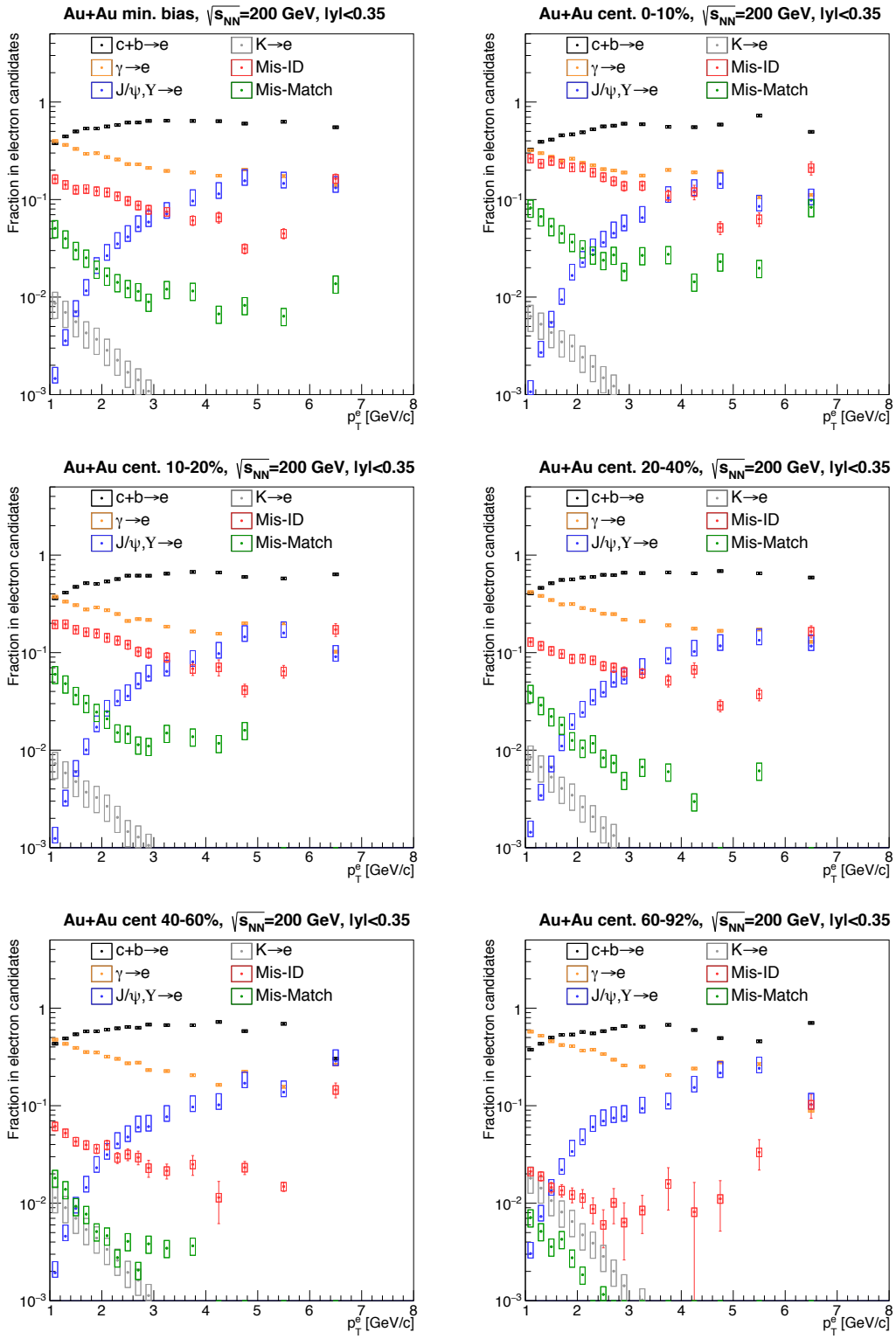

Figure 4.61: The fractions of electron tracks with the isolation cut as a function of p_{T} for each centrality.

4.5 Yield Extraction of Heavy Flavor Electrons

This section details how to extract the invariant yield of inclusive charm and bottom hadron decay electrons. It is extracted by the invariant yield of photonic electrons and the relative ratio of non-photonic electrons. Since the invariant yield of photonic electrons, PHENIX electron cocktail, provides the absolute normalization for the heavy flavor yield, this method provides smaller systematic uncertainty because of the precise yield measurement of π^0 and does not need an efficiency collection.

4.5.1 Invariant Yield of Heavy Flavor Electrons

The invariant yield of inclusive charm and bottom hadron decay electron is calculated by the invariant yield of photonic electrons from PHENIX electron cocktail as shown in Fig. 4.62 and the fraction of non-photonic electrons, k_{e3}, J/ψ, and Υ as

$$\frac{d^2N_e^{c,b}}{dp_T dy} = \frac{d^2N_e^p}{dp_T dy} \times \frac{F_{NP}}{1-F_{NP}} \times (1 - F_{J/\psi}(p_T) - F_{k_{e3}}(p_T)), \tag{4.23}$$

where N_e^p is the yield of photonic electrons and F is the fraction of electrons. Fig.4.63 shows the invariant yield of inclusive charm and bottom hadron decay electrons for all centralities.

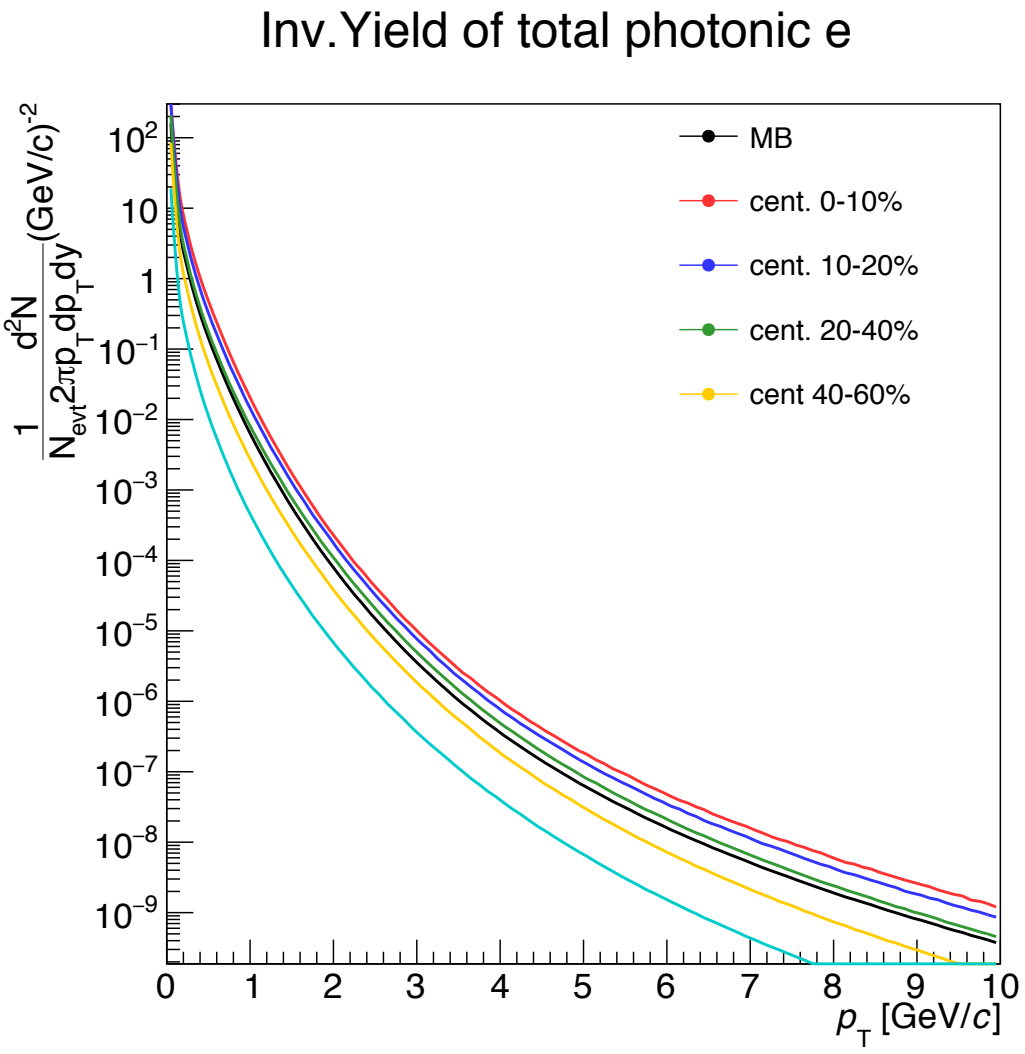

Figure 4.62: The invariant yield of total photonic electrons by PHENIX electron cocktail for each centrality.

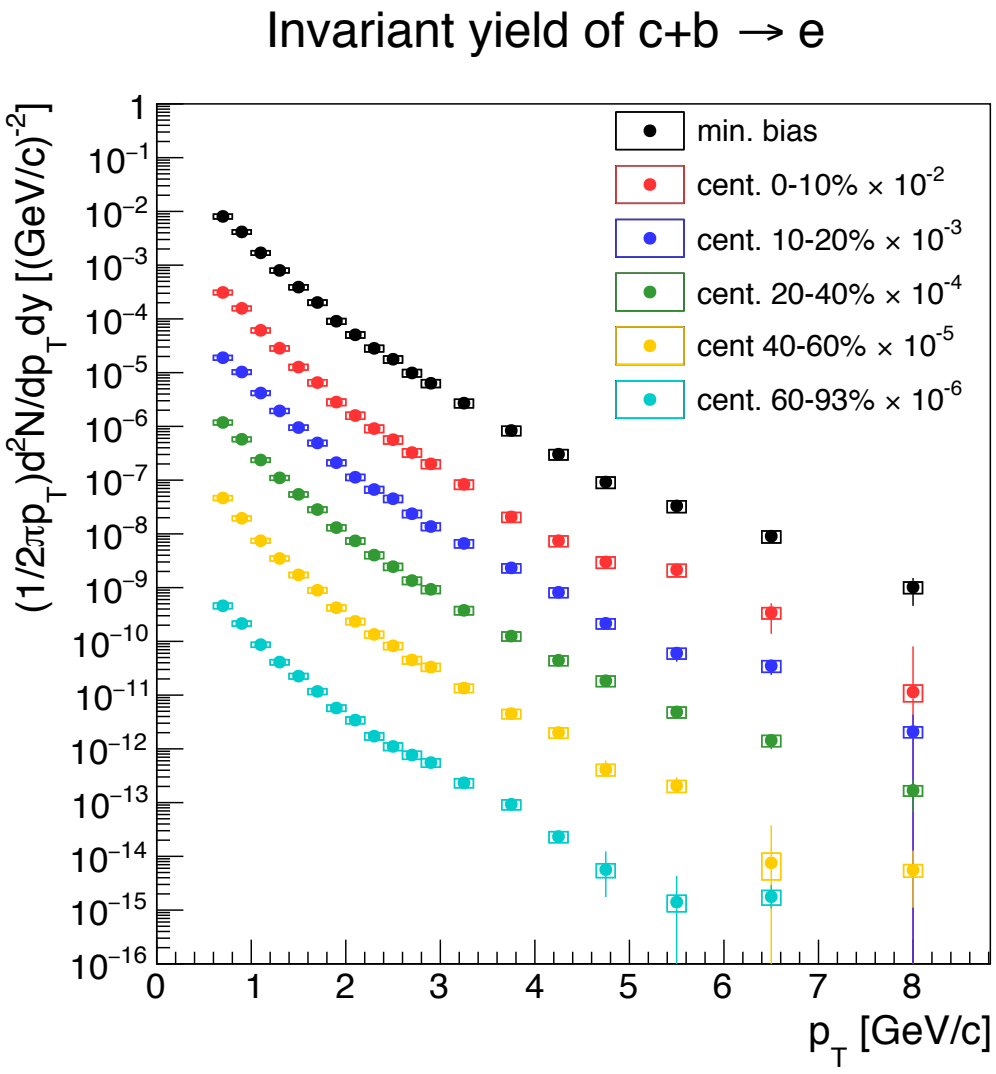

Figure 4.63: The invariant yield of electrons from charm and bottom hadron decays for each centrality.

4.5.2 Systematic Uncertainty of Cocktail

Systematic uncertainties from PHENIX electron cocktail, F_{NP} calculations, and non-electron background subtractions are considered in the systematic uncertainty of the invariant yield of electrons from charm and bottom hadrons. The systematic uncertainty of PHENIX electron cocktail is estimated by variations of fit to measured parent yields. Each fit variation is propagated to a decay electron space by the decay model and added in quadrature to calculate the total systematic uncertainty as shown in Fig. 4.64. Other systematic uncertainties are described in Sec. 4.4. These systematic uncertainties are propagated in the yield calculation Eq. 4.23

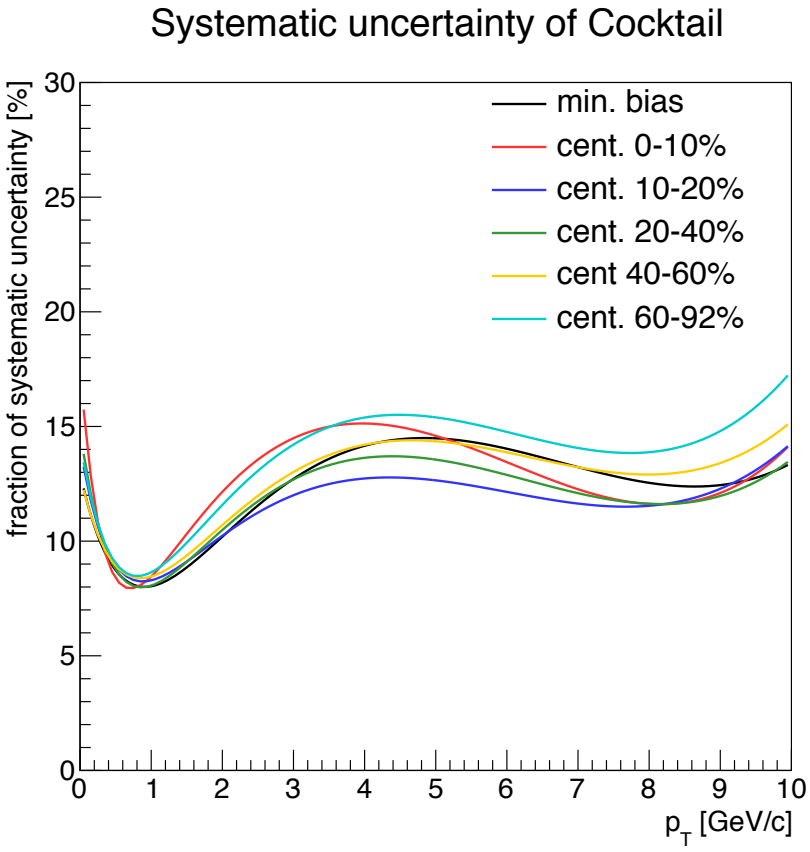

Figure 4.64: The fraction of systematic uncertainty on photonic e cocktails

4.5.3 Comparison to Previous Measurements

The extracted invariant yields of inclusive electrons from charm and bottom hadron decays are compared with the published invariant yields [10] for each centrality. New results represent well the published results using the PHENIX Run4 data as shown in Fig. 4.65, indicating new method works well.

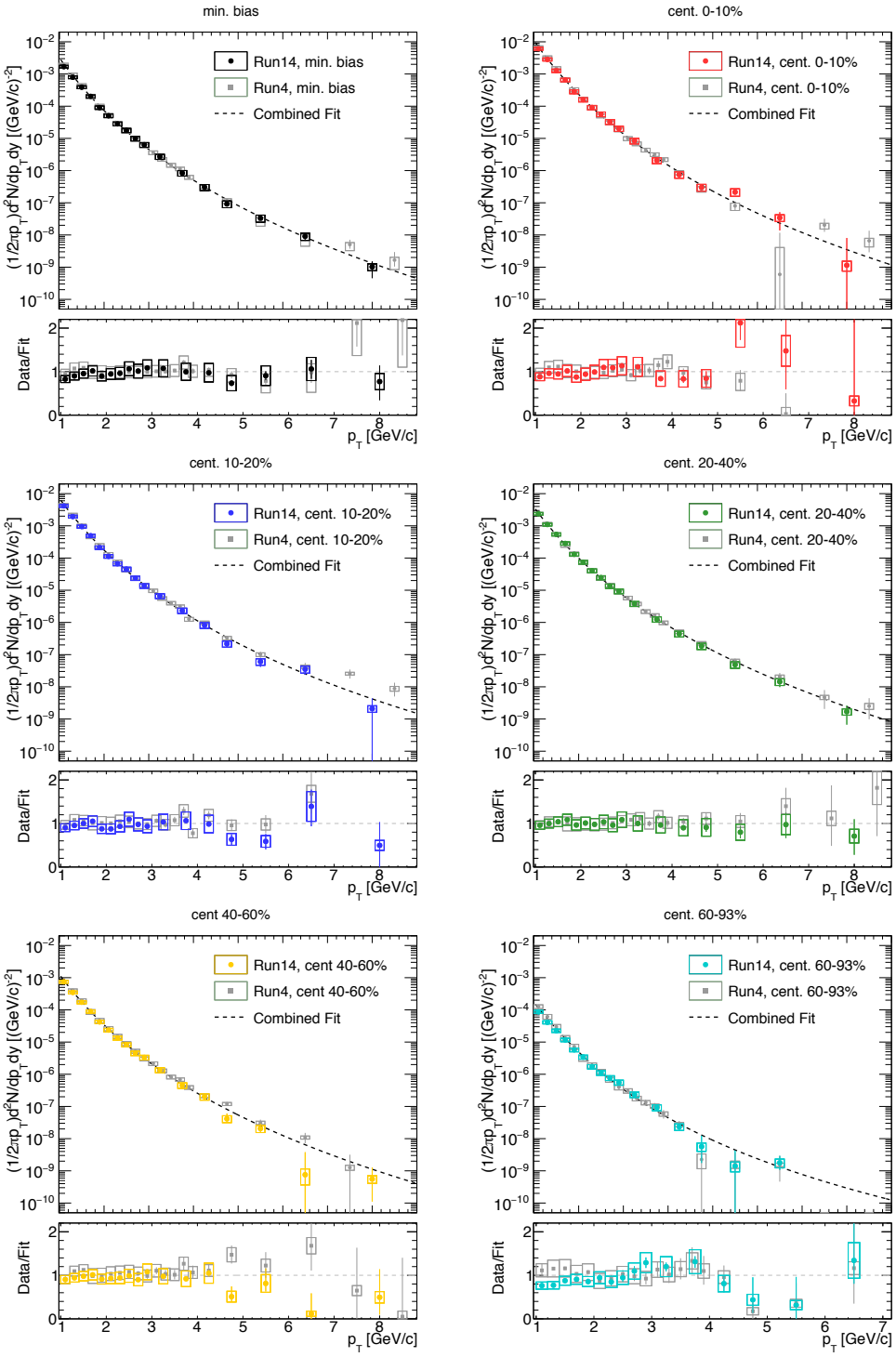

Figure 4.65: The invariant yield of inclusive charm and bottom hadron decay electrons (black) compared with the published invariant yield [10] (gray), shown in upper panel. The ratio of this result and the published result to fit, shown in bottom panel.

4.6 DCA_T Distribution of Backgrounds

DCA_T distributions of background components are determined by the full simulation and normalized by F_{NP} and PHENIX electron cocktail.

4.6.1 Photonic Electron

DCA_T shapes of photonic electrons from Dalitz decays and conversions are determined with the full simulation. π^0, η, and direct γ are generated with the realistic p_T distributions and decay to electrons in the simulation described in Sec. 4.3. The relative ratio of photonic electrons, π^0, η, and direct γ, are assumed by the measured yield of parent particles. Simulated DCA_T distributions of conversion and Dalitz decay electrons are fitted by Gaussian function to obtain smooth template shapes as shown in Fig. 4.66. DCA_T distributions of photonic electrons shift to the negative side due to a radiative energy loss which is well reproduced in GEANT3 simulation. Its effect decreases with increasing p_T. In addition, DCA_T distributions of conversion electrons shift to the negative side more due to the momentum mis-matching as discussed in Sec. 4.3. Its effect decreases with increasing p_T because a track becomes liner for high p_T.

4.6.2 Mis-ID hadrons and Mis-macth BG

Mis-ID hadron and mis-match BG denote an accidentally track-association with a random RICH ring or a random VTX hits due to high-multiplicity environment. It is estimated by the data driven method, the RICH swap and VTX swap method as described in Sec. 4.4.1 and 4.4.2. Estimated BG DCA_T distributions are fitted by Gaussian function and 2 Laplace functions (or pol0) to obtain smooth template shapes as shown in Fig. 4.72. In the case of mis-ID hadrons, the DCA_T shape is consistent with a charged hadron DCA_T shape. Therefore, if the number of mis-ID hadrons is less than 4000, a template shape of DCA_T is obtained by fit to a charged hadron DCA_T distribution in the high p_T for a small uncertainty of DCA_T shape and scaled to match the integration of mis-ID hadrons.

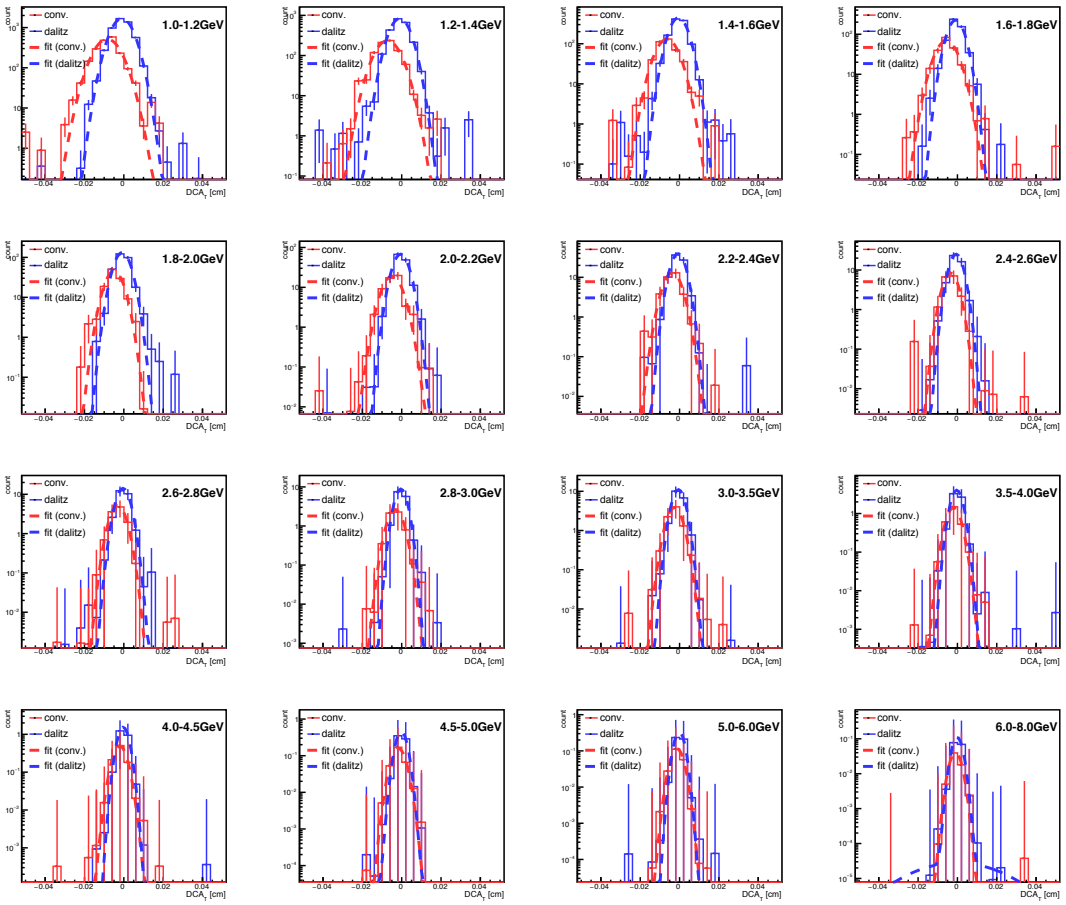

Figure 4.66: The simulated $\mathrm{DCA_T}$ distributions of conversion and Dalitz decay electrons for each p_T bin.

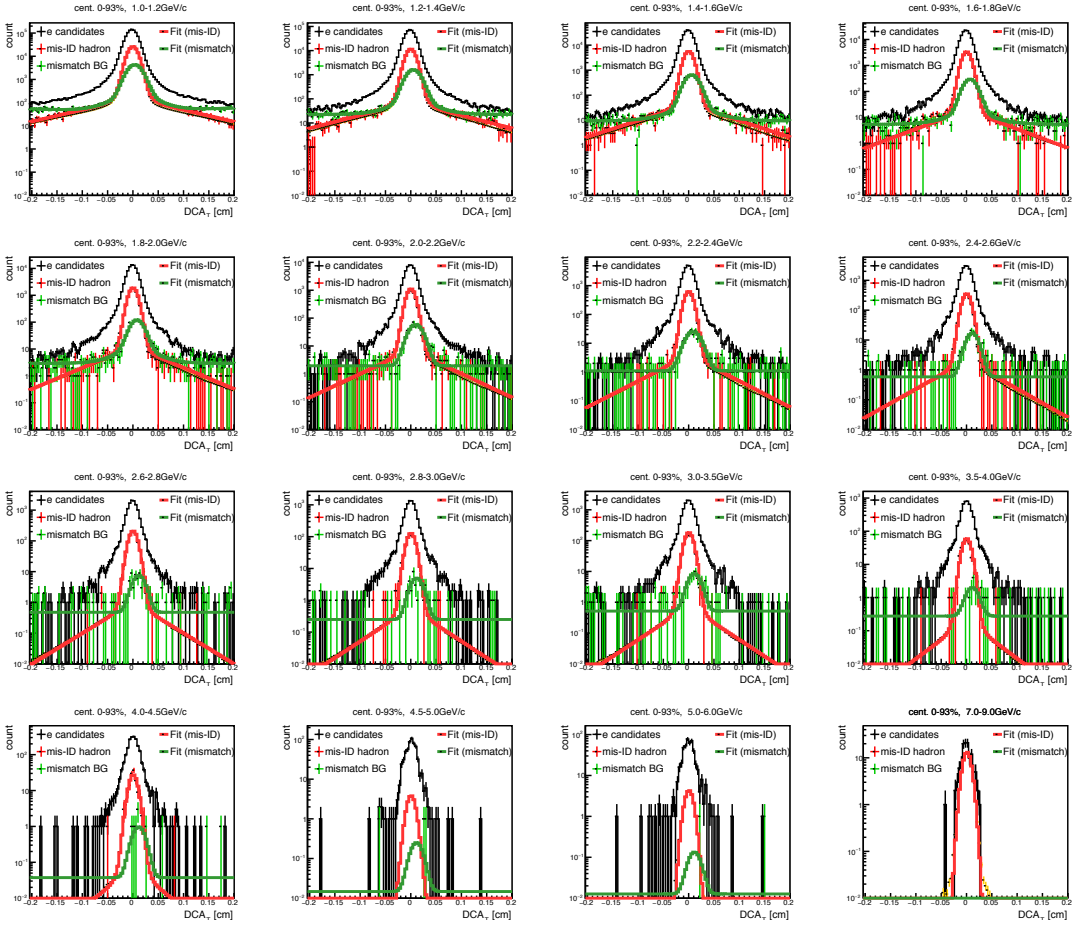

Figure 4.67: [Minimum bias] The $\mathrm{DCA_T}$ distribution of electron candidates (black), mis-ID hadrons (red), and mis-match BG (green) estimated by the track swap method for each p_T bin.

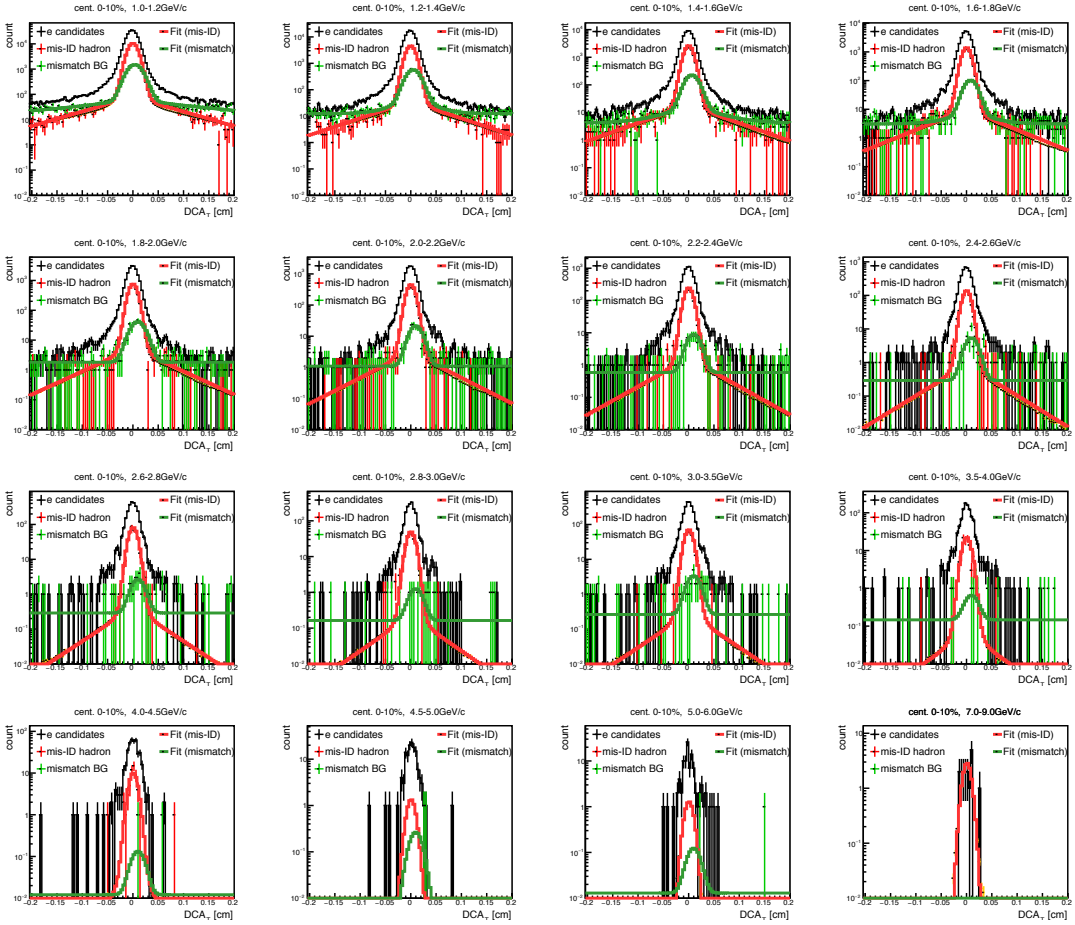

Figure 4.68: [0-10% centrality] The $\mathrm{DCA_T}$ distribution of electron candidates (black), mis-ID hadrons (red), and mis-match BG (green) estimated by the track swap method for each p_T bin.

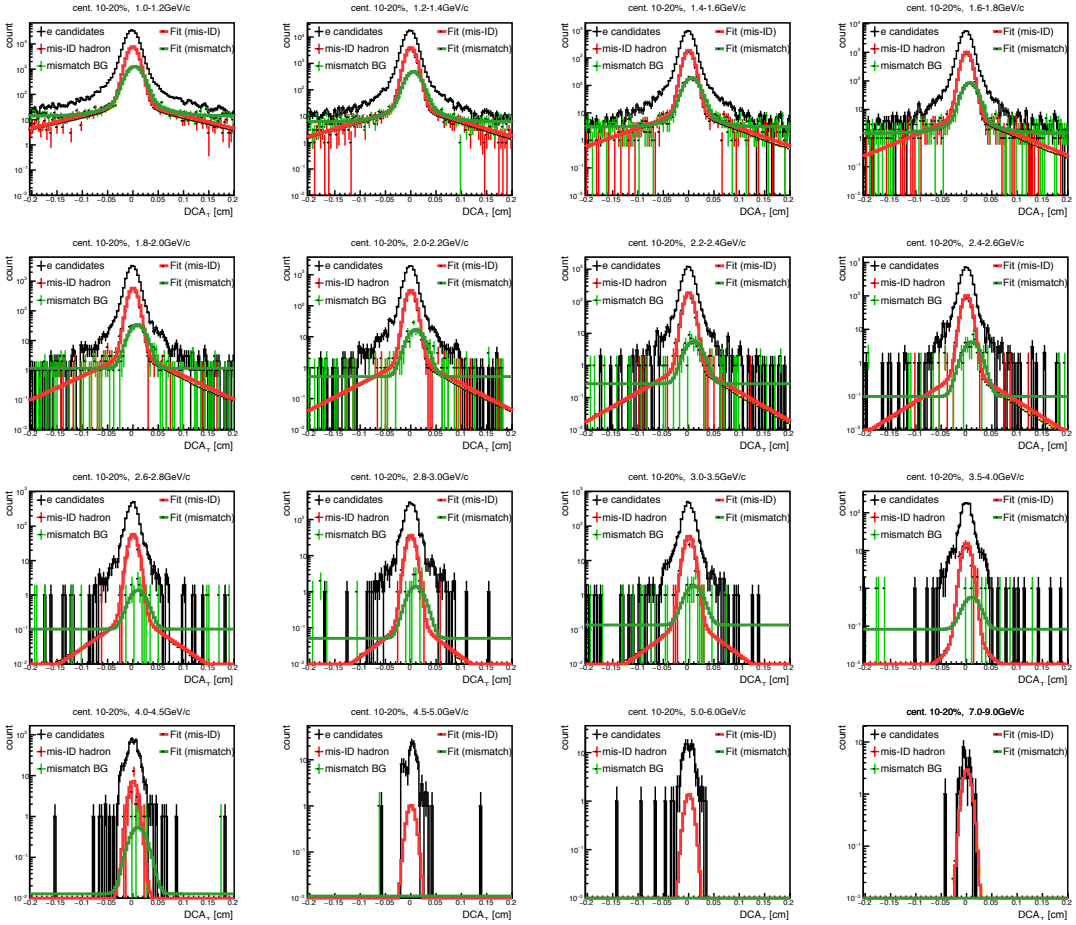

Figure 4.69: [10-20% centrality] The $\mathrm{DCA_T}$ distribution of electron candidates (black), mis-ID hadrons (red), and mis-match BG (green) estimated by the track swap method for each p_T bin.

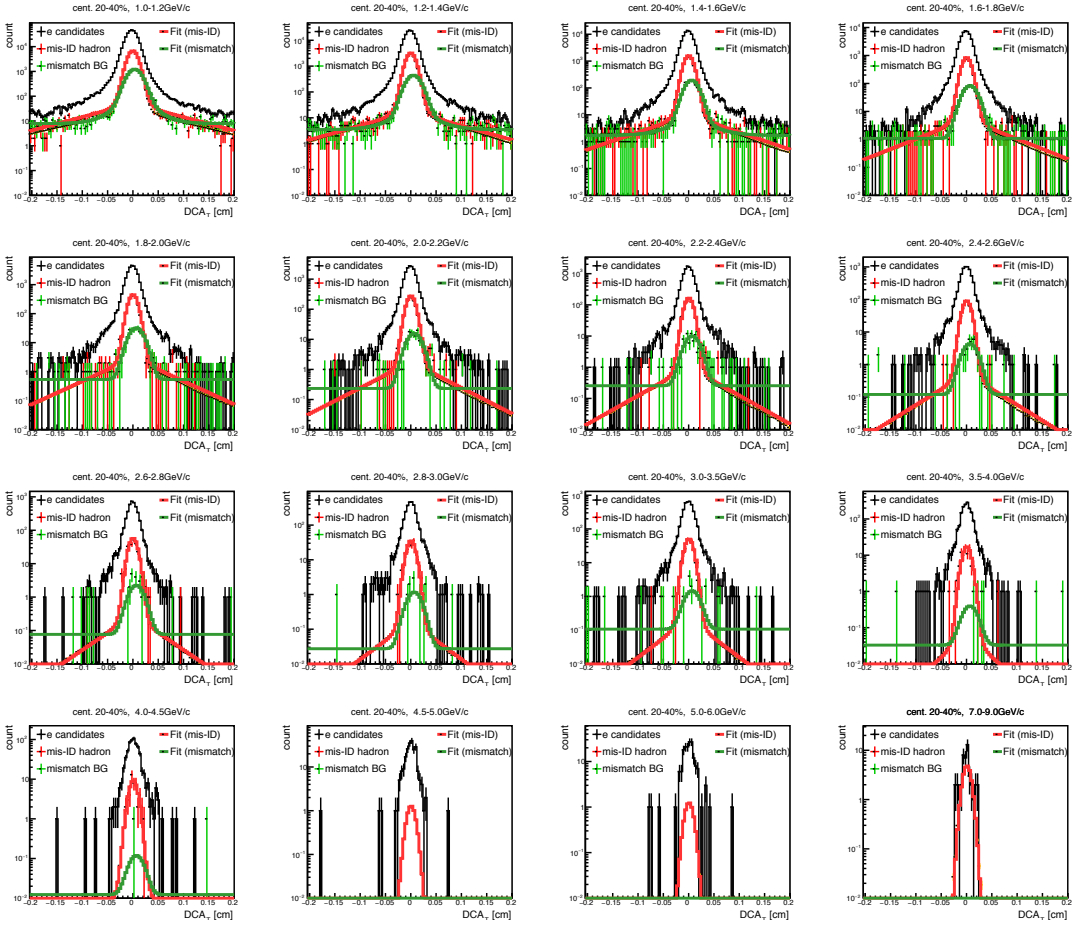

Figure 4.70: [20-40% centrality] The $\mathrm{DCA_T}$ distribution of electron candidates (black), mis-ID hadrons (red), and mis-match BG (green) estimated by the track swap method for each p_T bin.

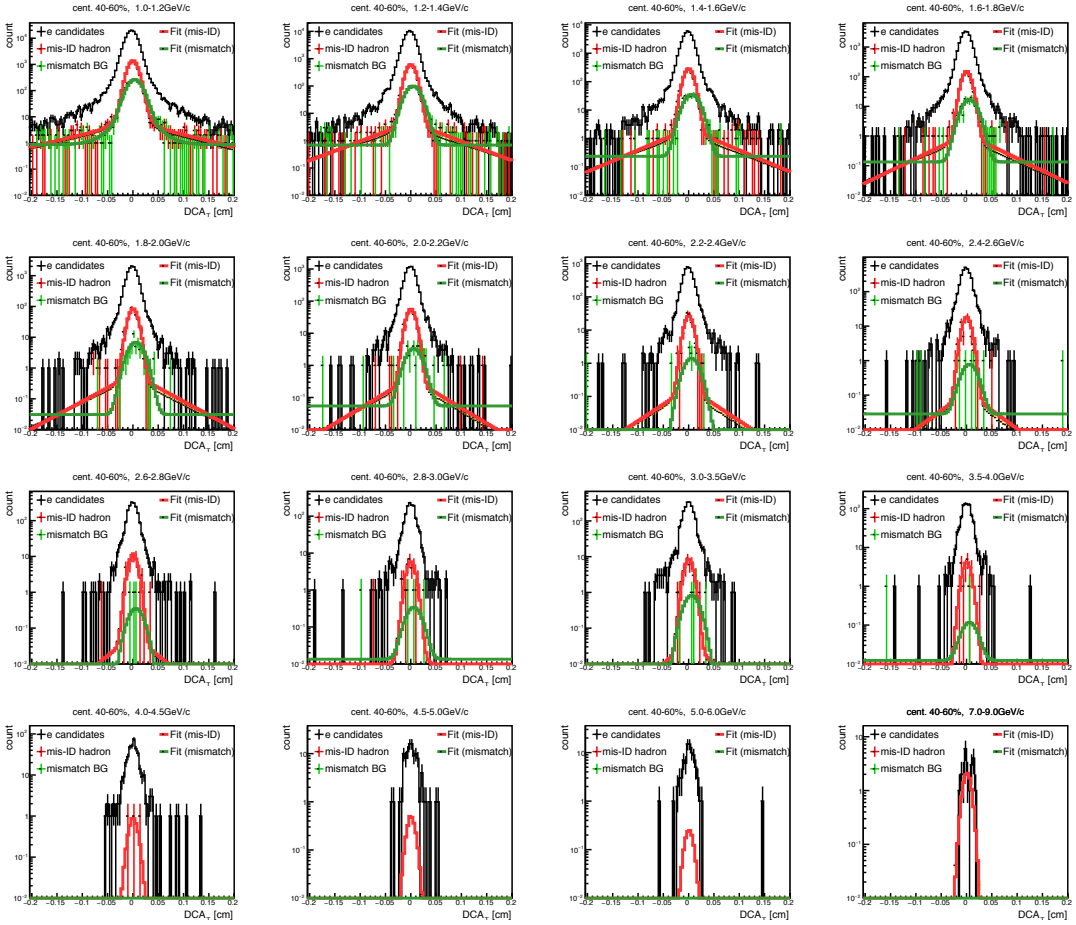

Figure 4.71: [40-60% centrality] The DCA_T distribution of electron candidates (black), mis-ID hadrons (red), and mis-match BG (green) estimated by the track swap method for each p_T bin.

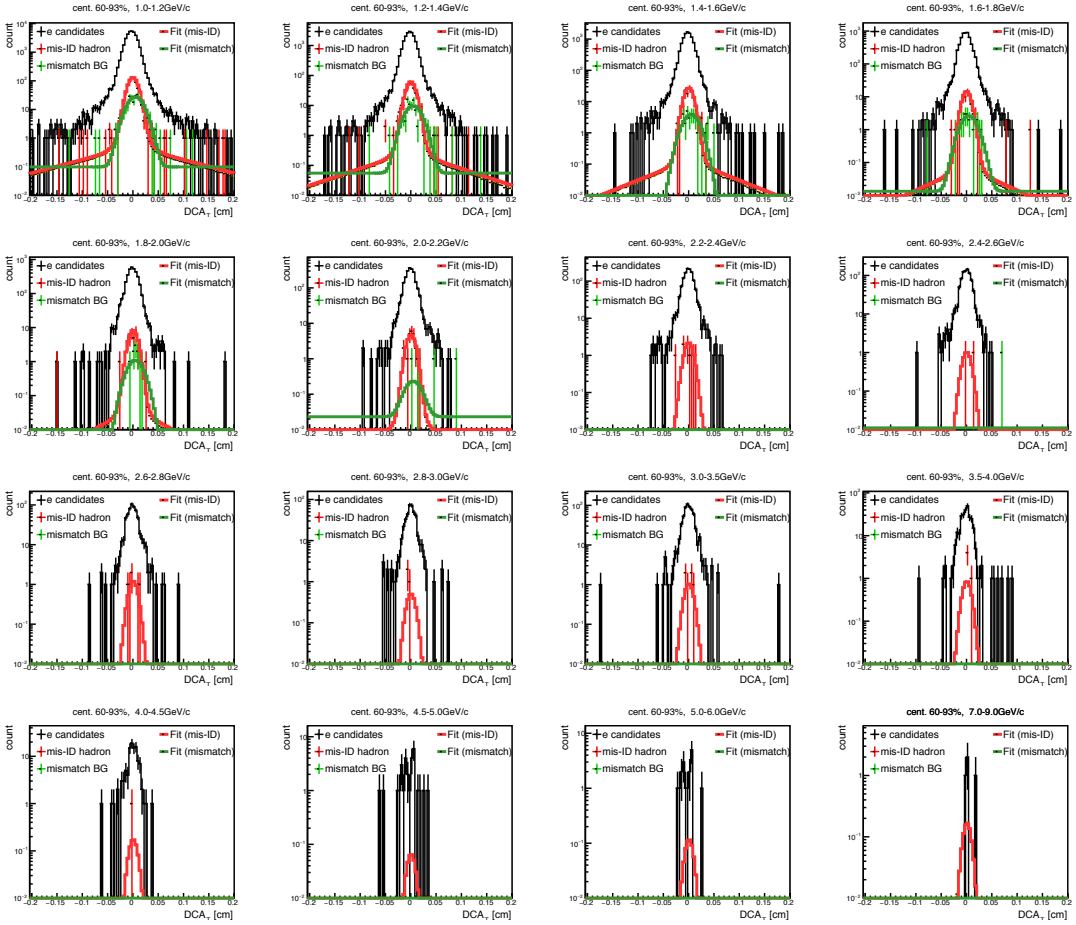

Figure 4.72: [60-92% centrality] The DCA_T distribution of electron candidates (black), mis-ID hadrons (red), and mis-match BG (green) estimated by the track swap method for each p_T bin.

4.6.3 Non-photonic Electron BG

$\mathrm{DCA_T}$ distributions of J/Ψ and K_{e3} are also estimated by the simulation. J/Ψ in the simulation is generated by a flat p_T distribution and scaled by the weight function calculated from the PHENIX cocktail shown in Fig. 4.73. On the other hand, K_{e3} in the simulation is generated by PYTHIA generator which includes the realistic p_T distribution as shown in Fig. 4.73. $\mathrm{DCA_T}$ distributions of J/Ψ are fitted by Gaussian function for smoothness. $\mathrm{DCA_T}$ distributions of K_{e3} at the lowest p_T bin are fitted by two Laplace functions and the fitted shape is used for high p_T bin because of low statistics. The effect from this assumption is small because the fraction of K_{e3} is very small at high p_T.

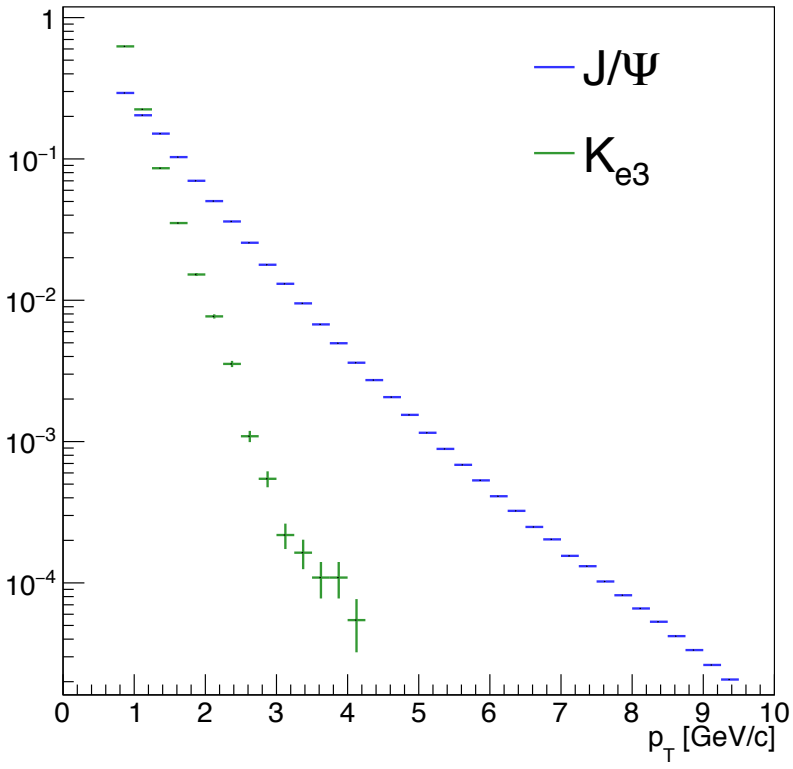

Figure 4.73: Simulated p_T distributions of decay electrons from J/Ψ and kaon. The integration is normalized to 1.

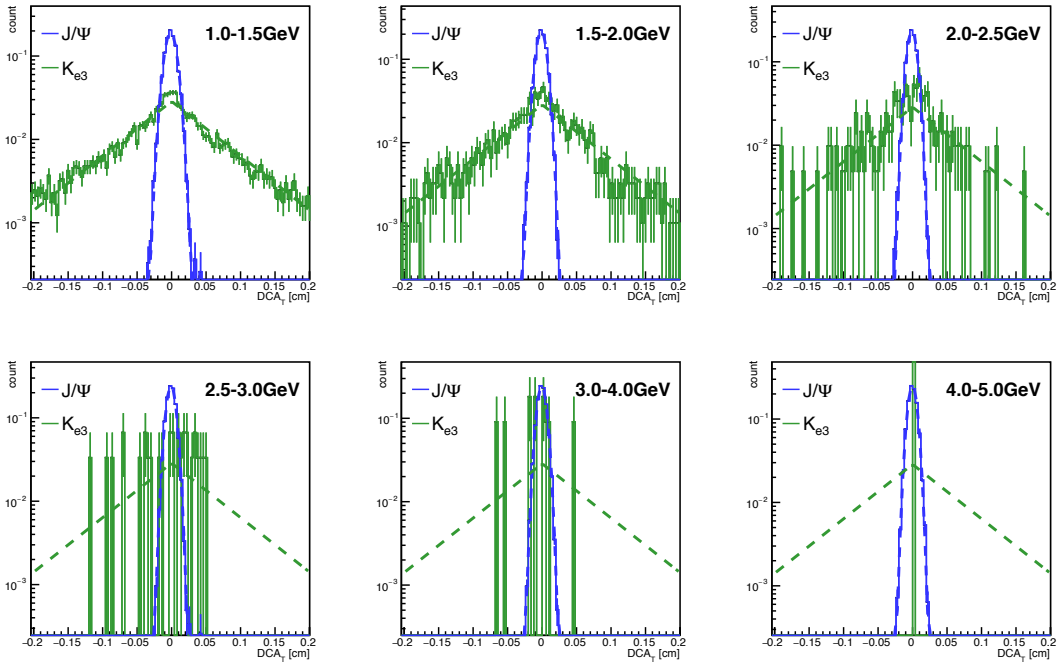

Figure 4.74: Simulated $\mathrm{DCA_T}$ distributions of decay electrons from J/Ψ and kaon. Dashed lines show fit results.

4.6.4 $\mathrm{DCA_T}$ Smearing to Match Data

Simulated $\mathrm{DCA_T}$ width for background templates is adjusted to the width in the data. $\mathrm{DCA_T}$ resolution includes the detector (VTX) angle resolution, a misalignment effect, and the beam spot size. These resolutions are convoluted in quadrature as

$$\sigma_{\mathrm{DCA}} = \sqrt{(\sigma^{\mathrm{angle}})^2 + (\sigma^{\mathrm{align.}})^2 + (\sigma^{\mathrm{beam}})^2}. \tag{4.24}$$

The simulated $\mathrm{DCA_T}$ distribution only includes the detector angle resolution. Therefore, the simulated $\mathrm{DCA_T}$ distribution should be smeared for the misalignment effect and the beam spot size. In addition, a $\mathrm{DCA_T}$ mean position in the data is different from that in the simulation due to the misalignment effect. In this analysis, the $\mathrm{DCA_T}$ smearing factor and magnitude of mean shift are determined by the difference of $\mathrm{DCA_T}$ distribution between the simulation and the data. Simulated charged pions are generated at PHENIX(0,0,0) and reconstructed to obtain $\mathrm{DCA_T}$ distributions which include only the VTX angle resolution under a perfect alignment environment. Both $\mathrm{DCA_T}$ distributions in the simulation and the data are fitted by Gaussian function to extract the $\mathrm{DCA_T}$ width and mean position as shown in Fig. 4.75. $\mathrm{DCA_T}$ distribution of charged hadrons in the data includes long lived particles, Kaon and Λ, which make large $\mathrm{DCA_T}$ tail. To estimate the smearing factors, the central peak is only fitted. Fig. 4.76 shows the $\mathrm{DCA_T}$ smearing factors calculated with the difference of width between the data and the simulation. The $\mathrm{DCA_T}$ mean position in the simulation is also adjusted

to the data as shown in Fig. 4.77. We assume that these smearing factor can be used for electron tracks because the difference between charged pion tracks and electron tracks is only the radiative energy loss effect which is well reproduced in GEANT simulation.

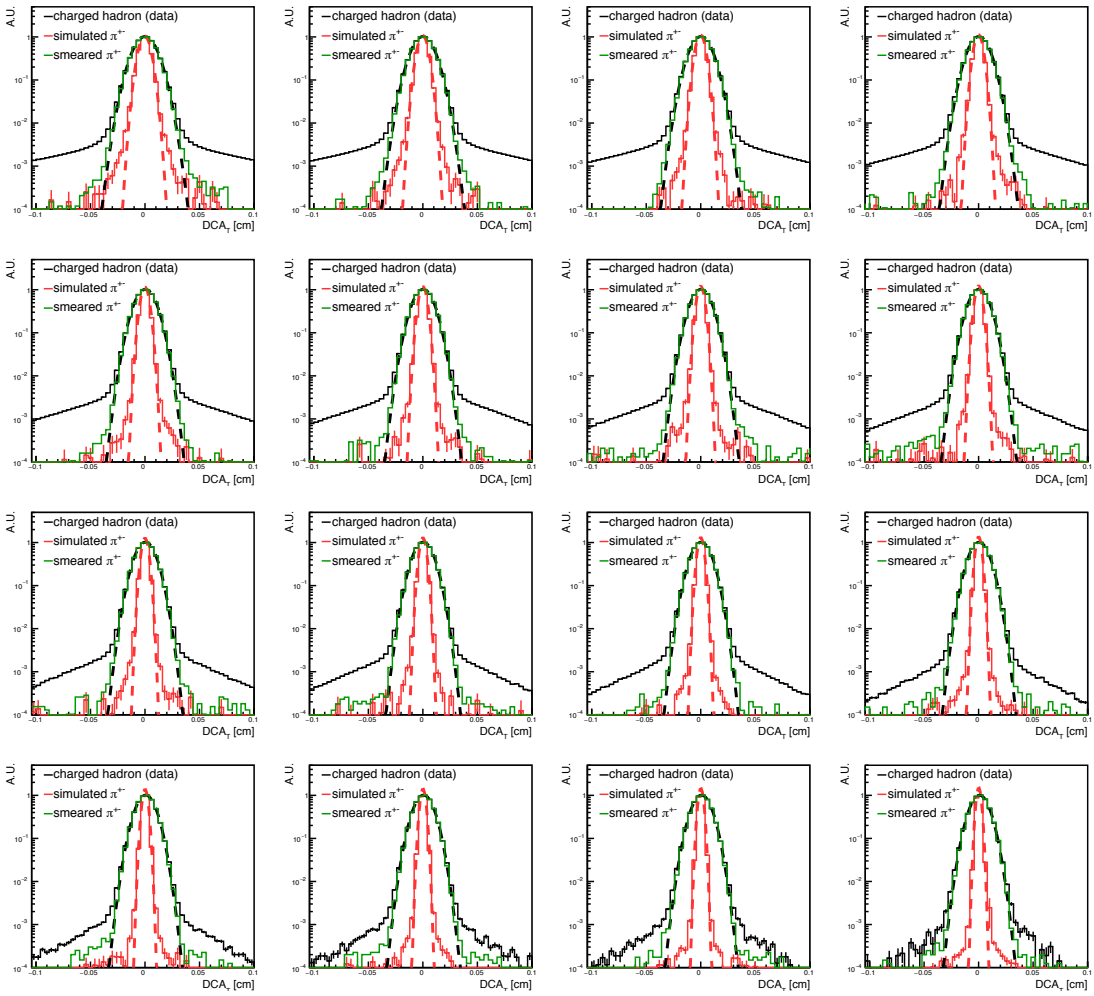

Figure 4.75: The comparison of DCA distributions between the data (black), the simulation (red), and the smeared distribution (green).

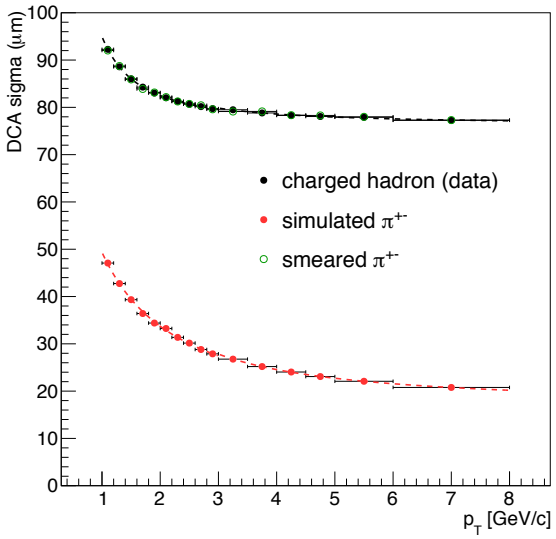

Figure 4.76: The DCA_T resolution for the data (black), the simulation (red) and the smeared distribution (green).

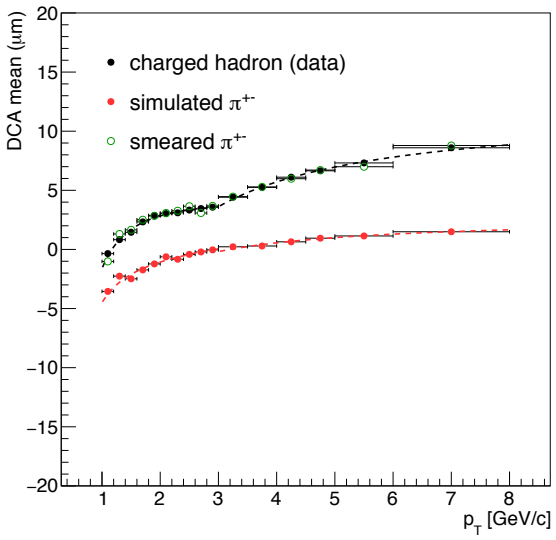

Figure 4.77: The DCA_T mean for the data (black), the simulation (red) and the smeared distribution (green).

The smeared DCA_T distributions in the simulation well describe the DCA_T resolution and mean position in the data. These smearing factors are applied to all background templates of DCA_T distribution.

4.6.5 Summary of $\mathrm{DCA_T}$ Backgrounds

The $\mathrm{DCA_T}$ smearing factors and the normalization factors are applied to all background templates of $\mathrm{DCA_T}$ distributions for each p_T bin and centrality class as shown in Fig. 4.78.

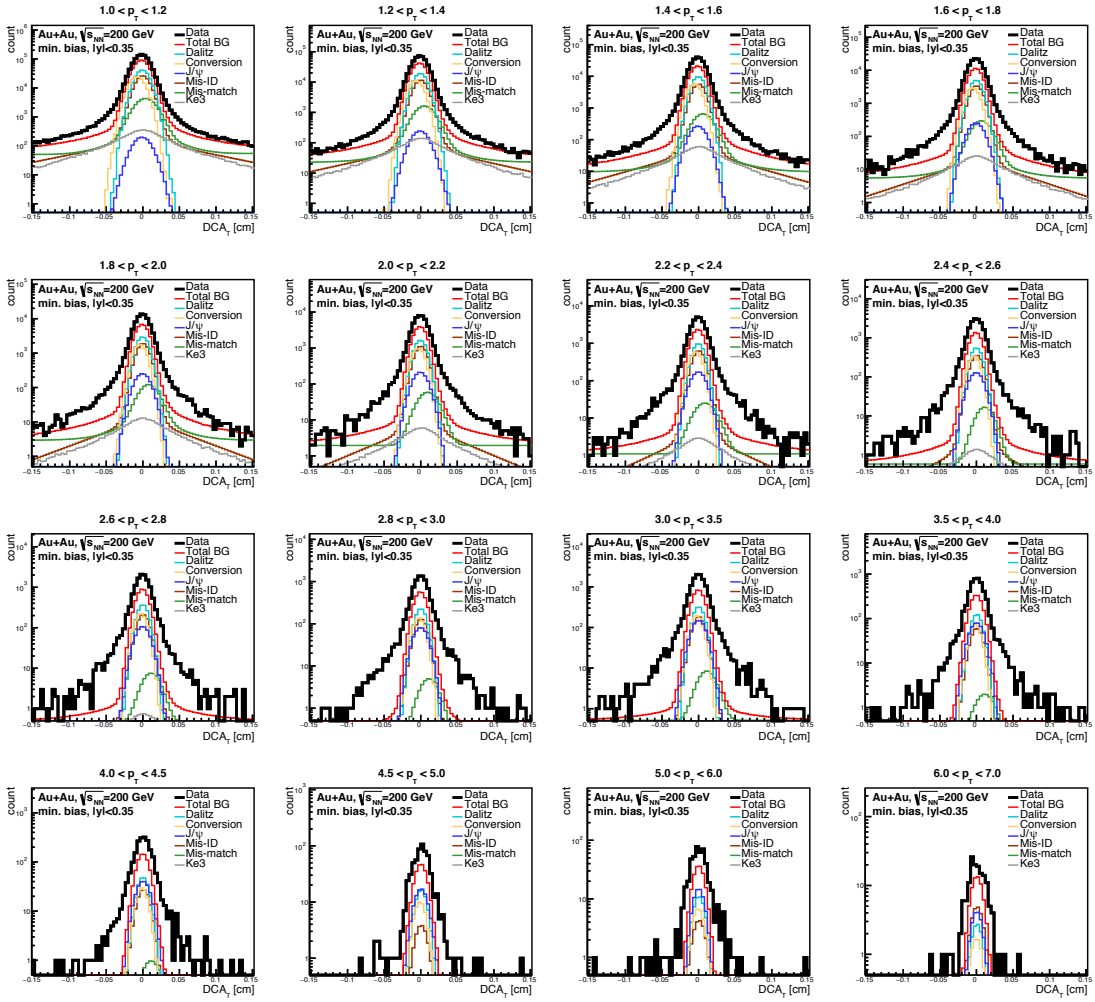

Figure 4.78: The $\mathrm{DCA_T}$ distribution of electrons and each background component in minimum bias.

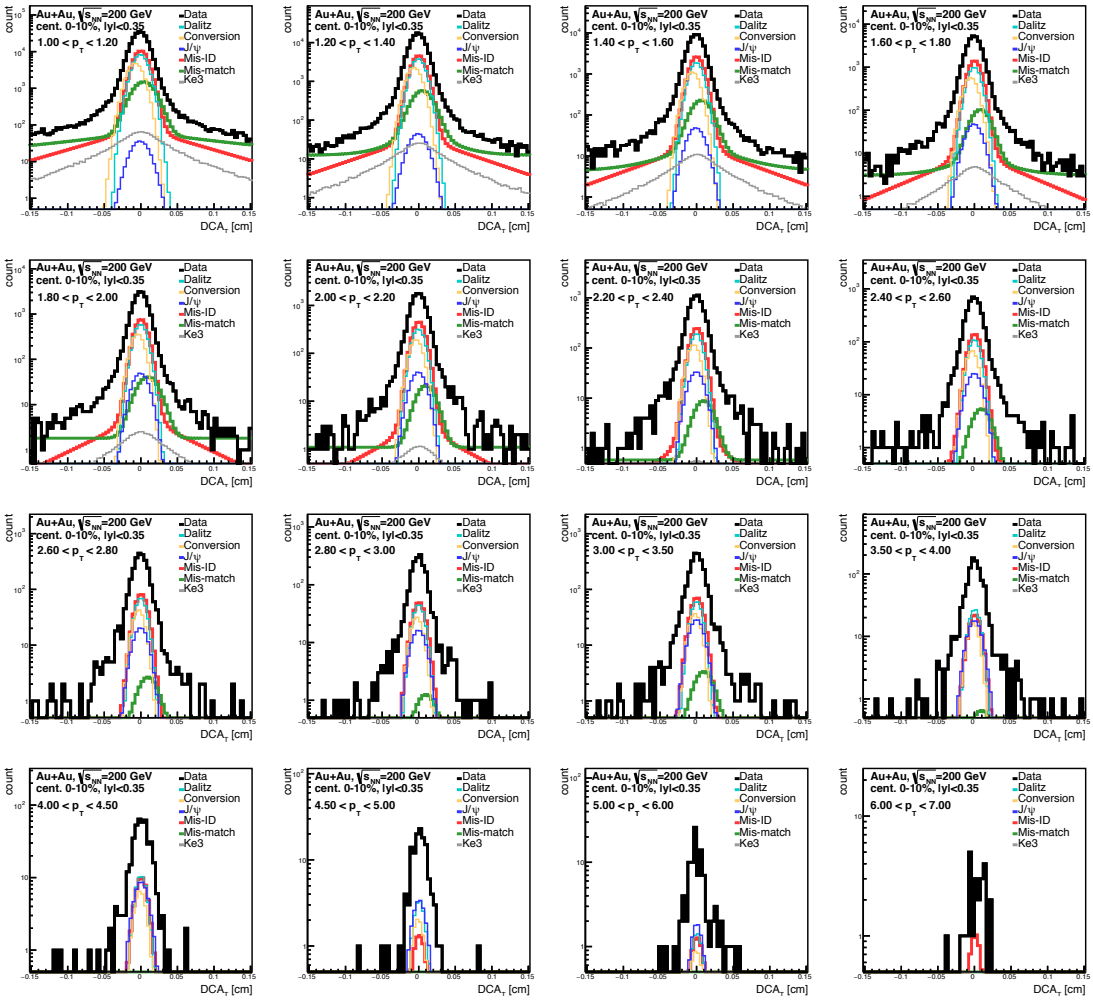

Figure 4.79: The DCA_T distribution of electrons and each background component in 0-10% centrality.

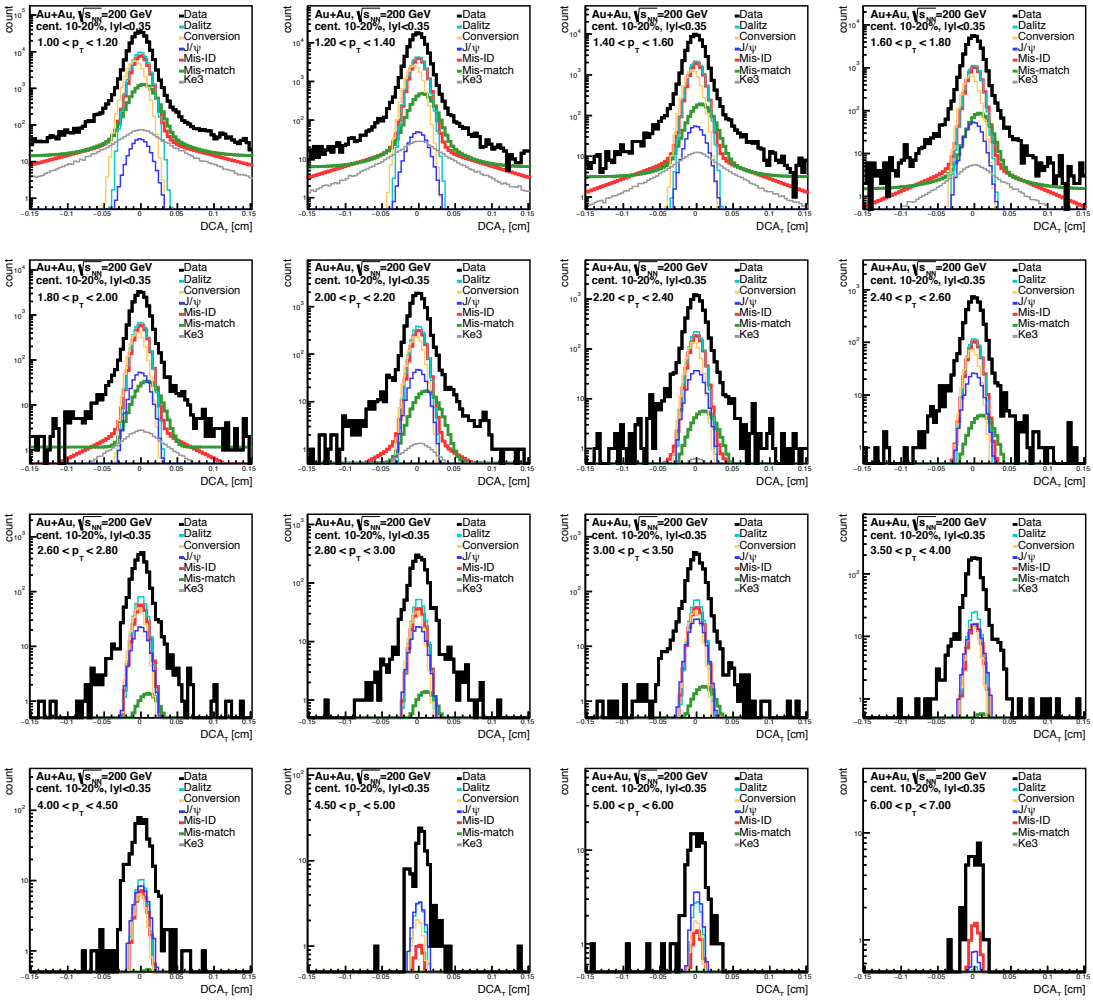

Figure 4.80: The DCA_T distribution of electrons and each background component in 10-20% centrality

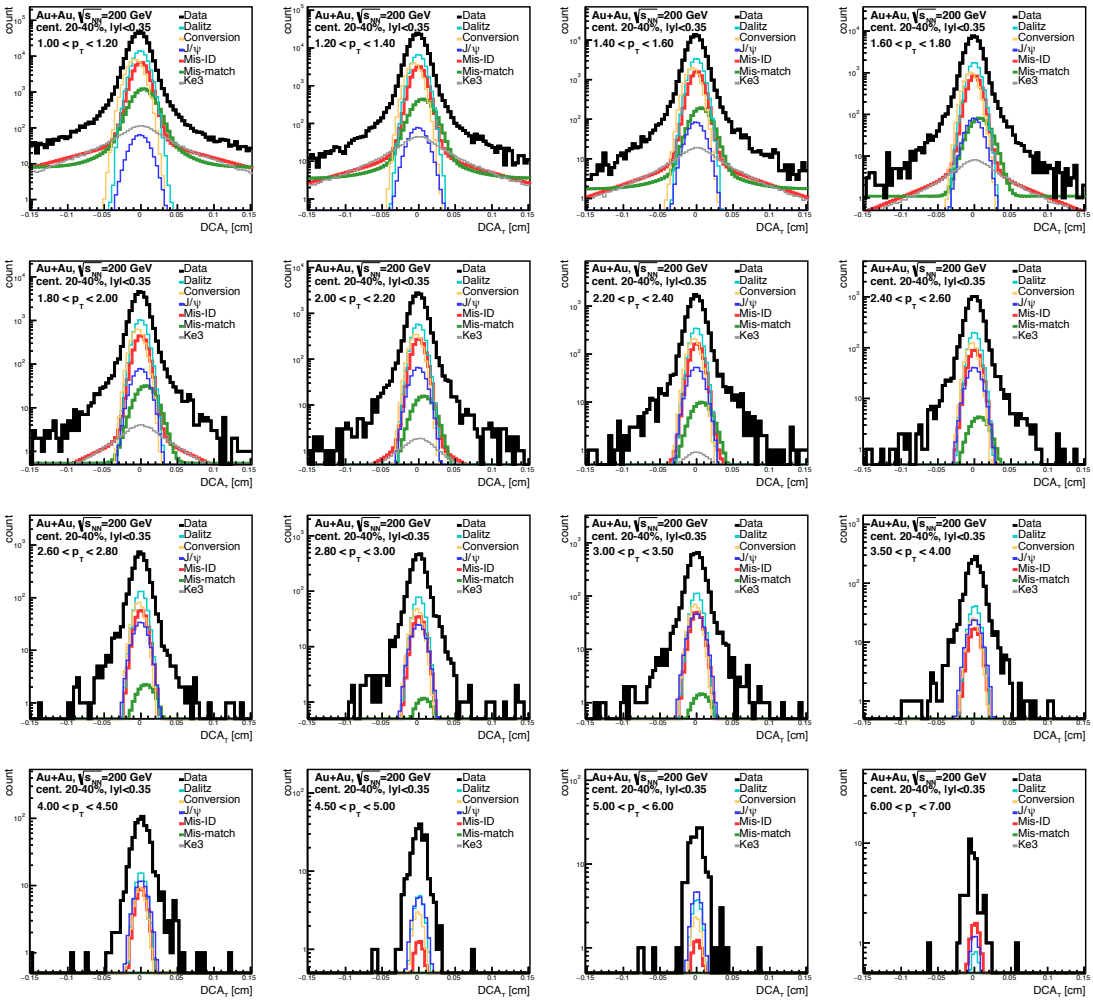

Figure 4.81: The DCA_T distribution of electrons and each background component in 20-40% centrality

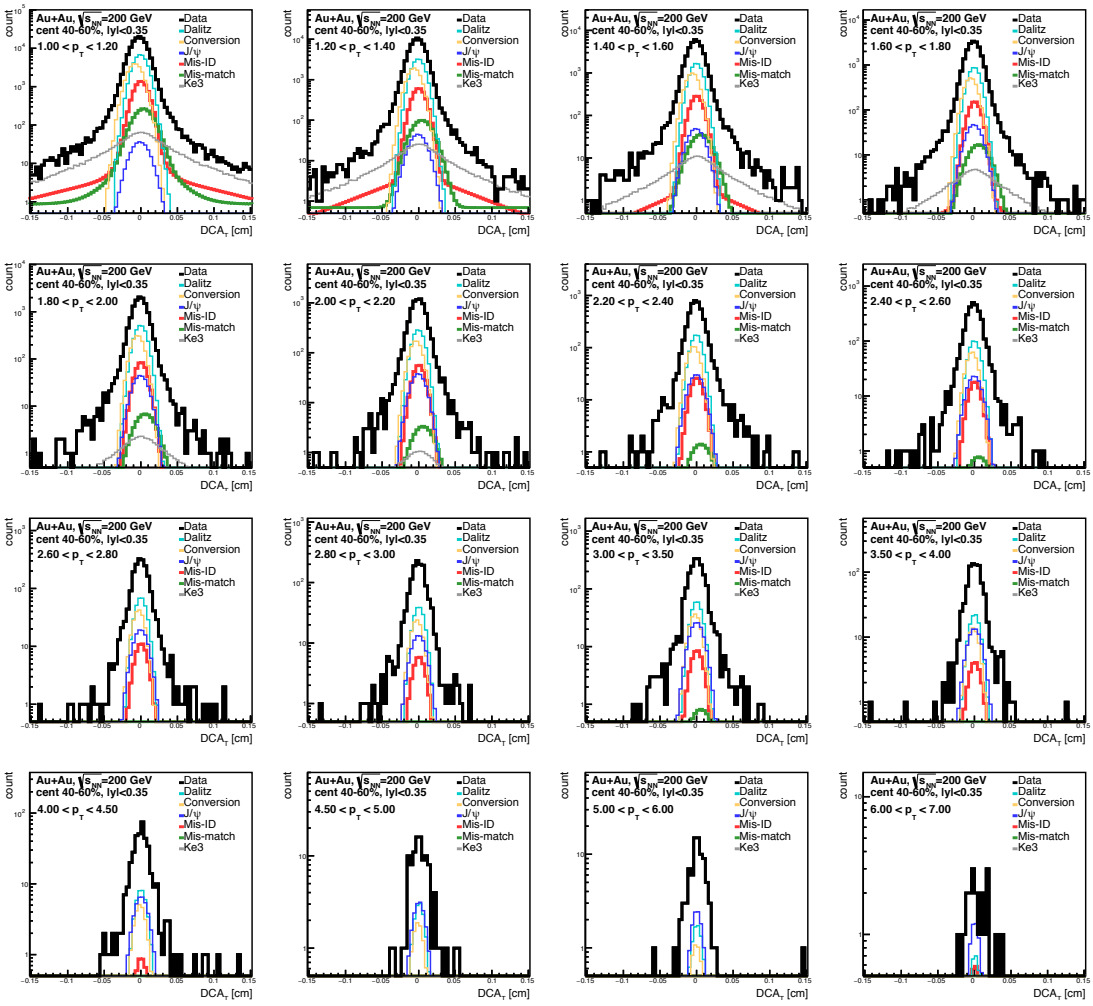

Figure 4.82: The DCA_T distribution of electrons and each background component in 40-60% centrality

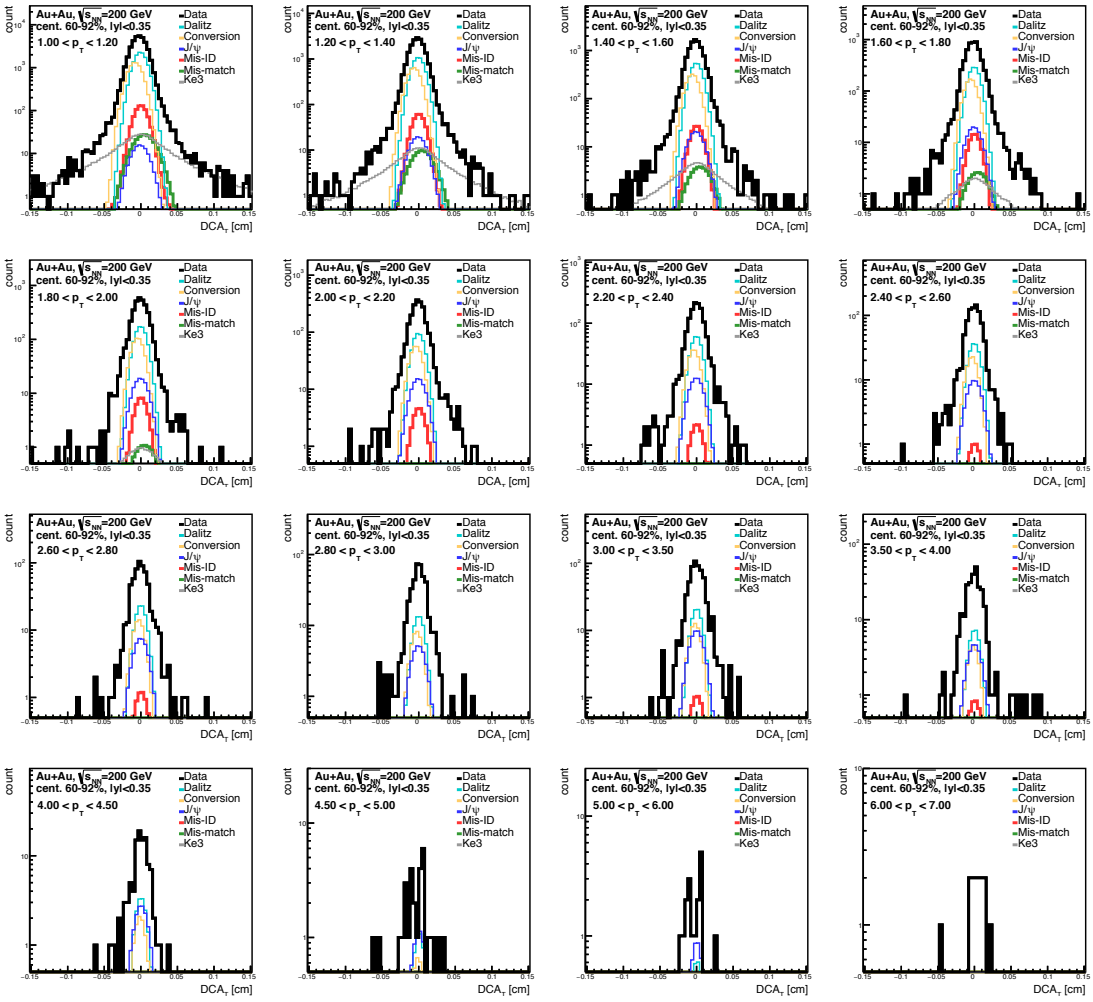

Figure 4.83: The DCA_T distribution of electrons and each background component in 60-92% centrality

Chapter 5

Data Analysis 2 - Unfolding of Charm and Bottom Hadrons

5.1 Unfolding method

The invariant yield of $c \rightarrow e$ and $b \rightarrow e$ is extracted with the invariant yield of $c + b \rightarrow e$ and the $\mathrm{DCA_T}$ distributions of electrons. A simultaneous fit to the p_T and the $\mathrm{DCA_T}$ distributions enable decomposing $c \rightarrow e$ and $b \rightarrow e$ components because the p_T distributions and the decay lengths of charm and bottom hadrons are significantly different. This procedure needs templates of p_T and $\mathrm{DCA_T}$ distributions for both $c \rightarrow e$ and $b \rightarrow e$. However, these template shapes are dependent on an unmeasured parent charm and bottom hadron p_T distributions. Therefore, there is an unfolding problem that the amount of charm and bottom hadron yields must be estimated to extract the components of $c \rightarrow e$ and $b \rightarrow e$.

To solve this unfolding problem, we employ the Bayesian inference technique involuting a sampling method with a Markov chain Monte Carlo (MCMC) algorithm. MCMC construct a Markov chain having the desired distribution as its equilibrium distribution and provides the sample distribution closely matching the actual desired distribution after a sufficient sampling [62, 63]. Therefore, this unfolding technique provides a joint probability density over the full sets of model parameters. In this analysis, p_T binned parent charm and bottom hadron yields are set as the vector of model parameters, $\boldsymbol{\theta}$, and a measured data is set as a vector $\mathbf{x}$ in Bayes' theorem.

$$p(\boldsymbol{\theta}|\mathbf{x}) = \frac{P(\mathbf{x}|\boldsymbol{\theta})\pi(\boldsymbol{\theta})}{P(\mathbf{x})}, \tag{5.1}$$

where $p(\boldsymbol{\theta}|\mathbf{x})$ is the posterior probability density calculated by the likelihood $P(\mathbf{x}|\boldsymbol{\theta})$ and prior information $\pi(\boldsymbol{\theta})$. The likelihood $P(\mathbf{x}|\boldsymbol{\theta})$ is given from comparison between a vector of measured data and model parameters. In case of Bayesian inference, the analyzer's a priori knowledge about model parameters can be included as opposed to frequentist statistics. The denominator $P(\mathbf{x})$ is to normalize the combined likelihood $P(\mathbf{x}|\boldsymbol{\theta})\ \pi(\boldsymbol{\theta})$ for an interpretation of a probability den-

sity $p(\boldsymbol{\theta}|\mathbf{x})$. However, this term is exempted because we want to know only the parameters which maximize a likelihood to a fit.

5.1.1 Model of Likelihood Function

A vector of measured data is composed of 16 (or 15) data points of the inclusive invariant yield, $\mathbf{Y}^{\rm data}$, in $p_{\rm T}$ range 1.0-8.0 GeV/c and 15 (or 14) DCA$_{\rm T}$ distributions, $\mathbf{D}_j^{\rm data}$, in $p_{\rm T}$ range 1.6-6.0 GeV/c as the following equation.

$$\mathbf{x} = (\mathbf{Y}^{\rm data}, \mathbf{D}_0^{\rm data}, ..., \mathbf{D}_{15}^{\rm data}), \tag{5.2}$$

To approximate the posterior distribution of parent charm and bottom hadron yields, a prediction should be compared with the measured data in a decay electron space. Therefore, predicted charm and bottom hadron yields are converted to decay electron yields and DCA distributions with a decay model as

$$\mathbf{Y}(\boldsymbol{\theta}) = \mathbf{M}^{(\mathbf{Y})}\theta_c + \mathbf{M}^{(\mathbf{Y})}\theta_b, \tag{5.3}$$

$$\mathbf{D}_j(\boldsymbol{\theta}) = \mathbf{M}_j^{(\mathbf{D})}\theta_c + \mathbf{M}_j^{(\mathbf{D})}\theta_b, \tag{5.4}$$

where $\mathbf{M}^{(\mathbf{Y})}$ and $\mathbf{M}_j^{(\mathbf{D})}$ are decay matrices discussed in Sec. 5.1.2. Finally, the total log likelihood is obtained from a difference between each measurement and the prediction of decay electron yields and DCA distributions by

$$\ln P(\mathbf{x} \mid \boldsymbol{\theta}) = \ln P(\mathbf{Y}^{\rm data} \mid \mathbf{Y}(\boldsymbol{\theta})) + \sum_{j=0}^{15} \ln P(\mathbf{D}_j^{\rm data} \mid \mathbf{D}_j(\boldsymbol{\theta})), \tag{5.5}$$

Here, the calculation of total log likelihood only considers statistical uncertainties in $\mathbf{Y}^{\rm data}$. Thus, $P(\mathbf{Y}^{\rm data} \mid \mathbf{Y}(\boldsymbol{\theta}))$ can be modeled as a $p_{\rm T}$ uncorrelated multivariate Gaussian. The handling of systematic uncertainties is described in Sec. 5.3. On the other hand, $P(\mathbf{D}_j^{\rm data} \mid \mathbf{D}_j(\boldsymbol{\theta}))$ is described by a multivariate Poisson distribution because each $\mathbf{D}_j^{\rm data}$ is composed of integer-valued entries. The region around a peak (DCA$_{\rm T}$ = 0) dominates the likelihood because of high-statistics and thus is very sensitive of an imperfect DCA$_{\rm T}$ template shape. In contrast, $c \rightarrow e$ and $b \rightarrow e$ dominant region at large DCA$_{\rm T}$ are not sensitive of a detector performance because the region is sufficiently larger than the DCA$_{\rm T}$ resolution. In this analysis, 10% uncertainty is added in quadrature to the statistical uncertainty for each DCA bin if DCA counts are higher than 100 counts. This framework considers a systematic uncertainty of DCA$_{\rm T}$ template shape and focuses on the separation of $c \rightarrow e$ and $b \rightarrow e$ in the large DCA$_{\rm T}$ region. When this uncertainty is applied, the modeling of $P(\mathbf{D}_j^{\rm data} \mid \mathbf{D}_j(\boldsymbol{\theta}))$ is changed from a Poisson to a Gaussian distribution because of the calculation of a squared-summed uncertainty. Detector acceptance and efficiency effects are not accounted in $\mathbf{D}_j^{\rm data}$. Therefore, each prediction including the background is normalized to match the number of counts in the measured data.

5.1.2 Decay Model and Matrix

The decay matrix from charm and bottom hadrons to electrons is generated with PYTHIA-6 generator [65]. Charm and bottom hadron decay electrons are counted within $|\eta| < 0.35$ corresponding to the PHENIX acceptance. Here the feed-down decay B→D→e is included in a bottom hadron decay and excluded from charm hadron decays. Fig. 5.1 shows an example of the decay matrix for charm hadrons.

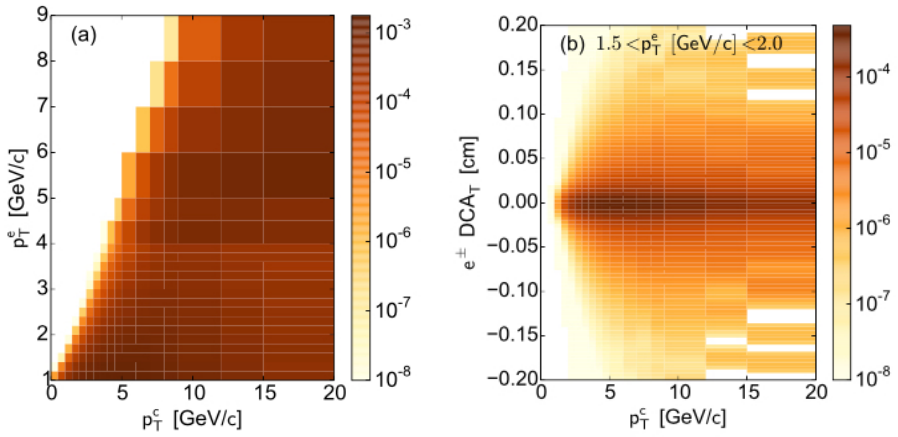

Figure 5.1: The decay matrix for charm hadrons decaying to electrons within $|\eta| < 0.35$ as a function of both electron p_T (or electron DCA$_T$) and charm hadron p_T. The shade represents the probability.

Parent charm and bottom hadrons are generated in all rapidity ranges. Therefore, this decay model assumes that the rapidity distributions of hadrons are the same between $p + p$ and Au+Au. BRAHMS measurement which found the R_{AA} for π and proton did not depend strongly on rapidity $|y| < 3$ justifies our assumption [20]. PYTHIA-6 generator performs for $p + p$ collisions and does not consider the baryon enhancement in Au+Au collisions. However, STAR experiment found the charm baryon enhancement in Au+Au collisions [21]. Thus, we have tested a possible baryon enhancement for charm and bottom hadrons. Here, we assumed the order of magnitude of a baryon enhancement for charm and bottom is similar to the baryon enhancement of strangeness as the following [22]. The decay matrix is modified to include an enhanced baryon branching ratio. The unfolding with modified decay matrix shows a lower charm hadron yield and a higher bottom hadron yield at high p_T, but the difference is within the systematic uncertainties. The model dependence of decay matrix has not been included in the final result.

5.1.3 Regularization as Prior

The discontinuity of unfolded charm and bottom hadron yields increases unfolding uncertainty in the decay electron space because the integrated yield of decay electrons from each hadron yield point is fitted to the measured yield. In order to suppress the unfolding uncertainty, we penalize discontinuities in the unfolded

distributions of charm and bottom hadrons as the analyzer's a priori knowledge which is a smoothness of a p_{T} spectrum. This regularization term is accounted in the likelihood function as

$$\ln \pi(\boldsymbol{\theta}) = -\alpha^2(|\mathbf{L}\mathbf{R}_c|^2 + |\mathbf{L}\mathbf{R}_b|^2), \tag{5.6}$$

where L is a 17×17 second-order finite-difference matrix, $\mathbf{R_c}$ ($\mathbf{R_b}$) is a ratio of the parent charm (bottom) hadron yields for 17 bins to the reference spectrum as the prior (θ), α is a regularization parameter. In this analysis, a modified PYTHIA spectrum by the blast-wave R_{AA} model [64] is used as the reference spectrum as shown in Fig. 5.2. A difference of unfolding results between using the modified PYTHIA spectrum and using the PYTHIA spectrum is defined as systematic uncertainty of prior described in Sec. 5.3.

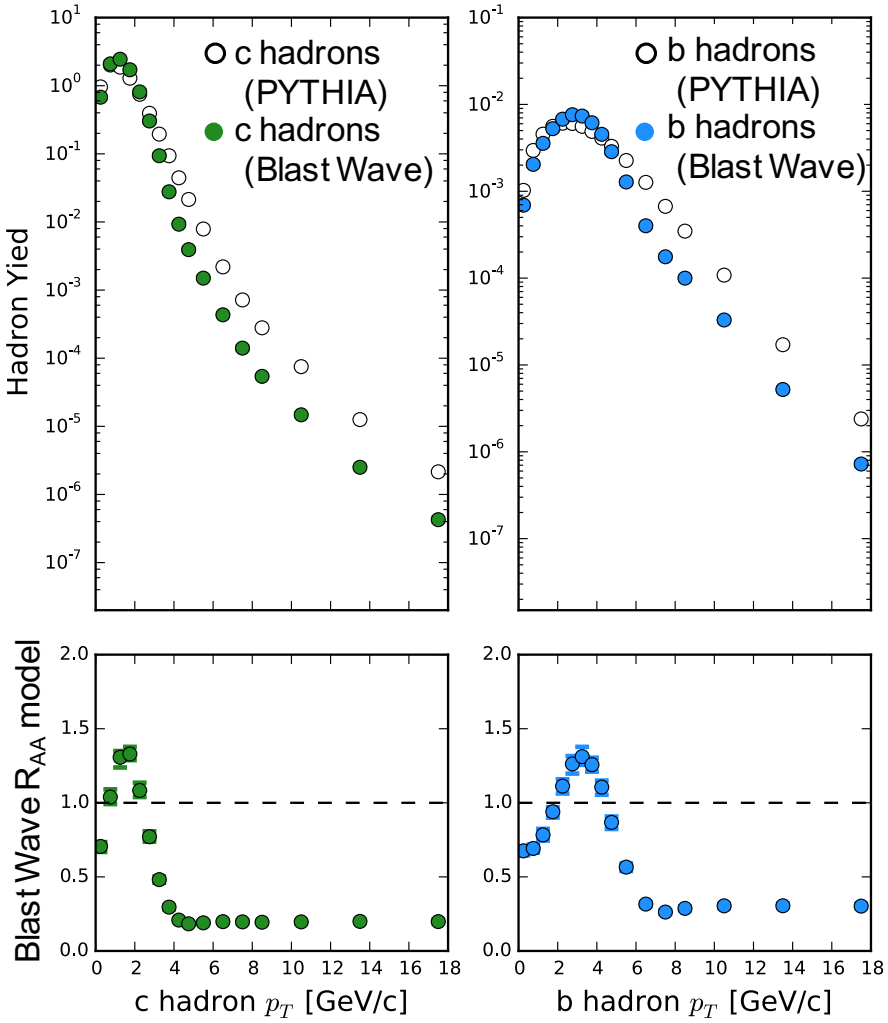

Figure 5.2: The reference spectrum of charm and bottom hadrons from PYTHIA and the modified blast-wave model. Bottom panels show blast-wave $R_{\rm AA}$ models.

We have determined the regularization parameter α with scanning over α and choosing the value of α which maximizes the resulting sum of the log likelihood as shown in Fig. 5.5. We choose systematic limits on α by finding where the maximum likelihood drops by one. The regularization parameter α is determined for each centrality.

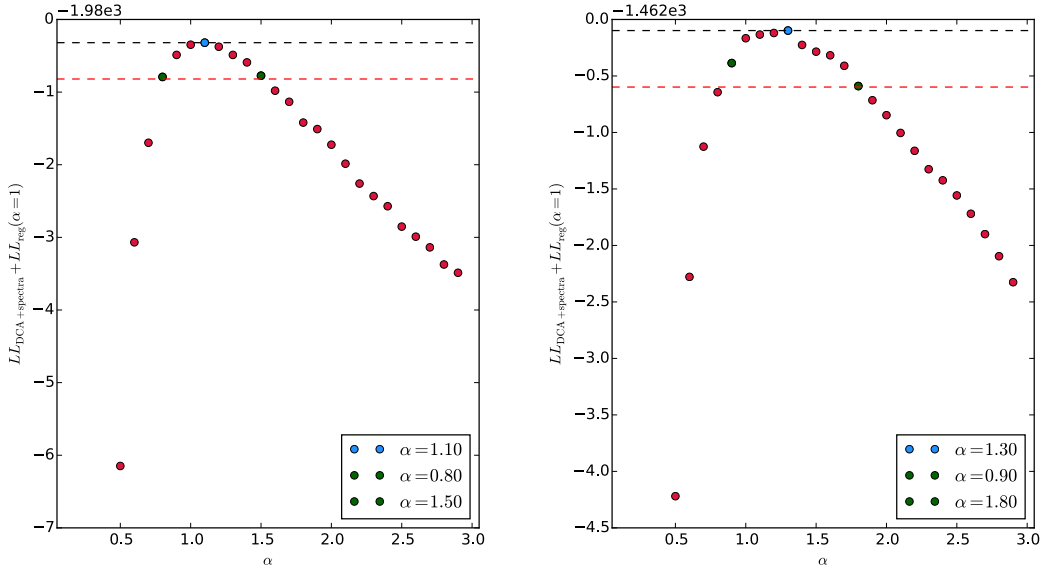

Figure 5.3: Total Log-Likelihood as a function of the regularization parameter α in minimum bias (left) and 0-10% centrality (right)

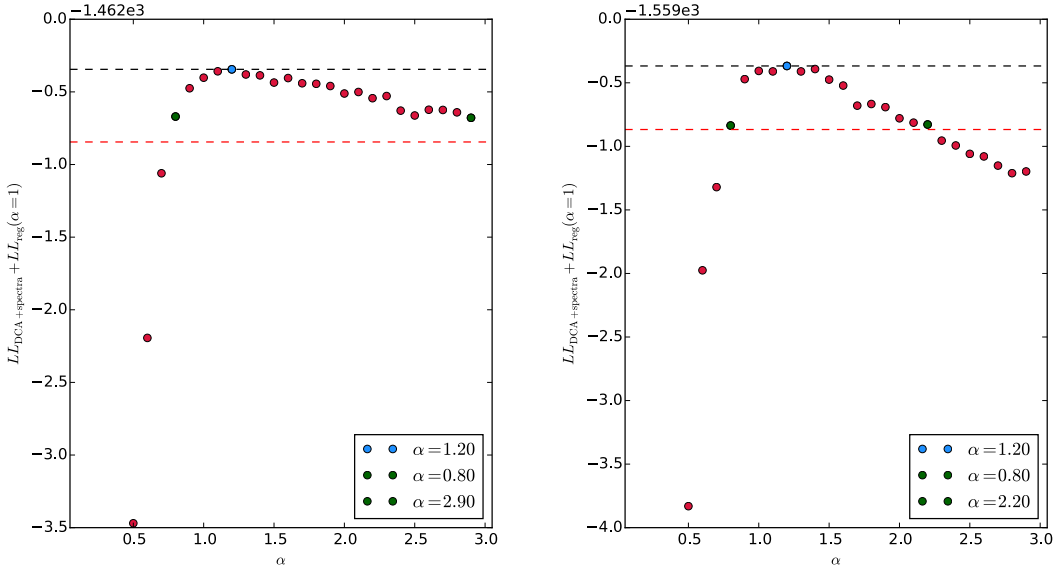

Figure 5.4: Total Log-Likelihood as a function of the regularization parameter α in 10-20% centrality (left) and 20-40% centrality (right)

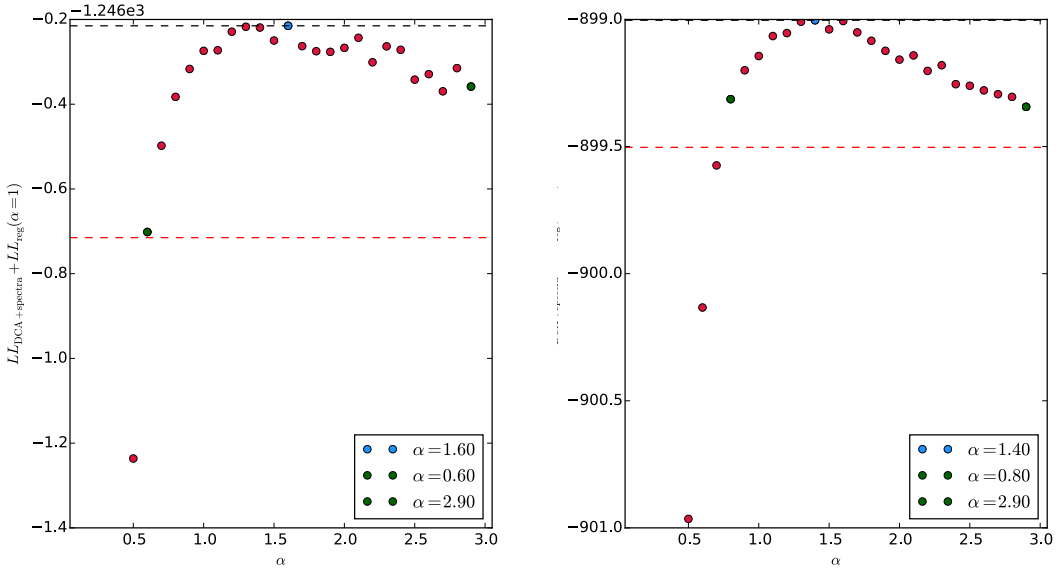

Figure 5.5: Total Log-Likelihood as a function of the regularization parameter α in 40-60% centrality (left) and 60-93% centrality (right)

The variation of total log-likelihood is very small for $\alpha > 3.0$ in 10-20%, 40-60%, and 60-93% centrality and unfolding results with higher α (> 3.0) are almost same. Therefore, we stop α scan up to 3.0 and it is defined as upper limit of α. Selected regularization parameters α are shown in Table 5.1.

Table 5.1: Summary of regularization parameter α.

centrality	α for mean	α for lower limit	α upper limit
0-93%	1.2	0.9	1.4
0-10%	1.3	1.1	1.6
10-20%	1.2	0.9	3.0
20-40%	1.2	0.8	2.0
40-60%	1.4	1.0	3.0
60-93%	1.6	1.2	3.0

5.1.4 Convergence of Unfolding

In our unfolding procedure, Markov chains composed of 500 chains is produced and an average log-likelihood is obtained in each step. The sampling algorithm starts from a burn-in period of 1000 steps to eliminate the influence of initial values and then stores 500 steps. The sampling procedure runs 3 times and monitors log-likelihood values in each step as shown in Fig. 5.11. We confirm that there is no further increase in the log-likelihood in the final sampling procedure, which denotes sufficient convergence of the unfolding.

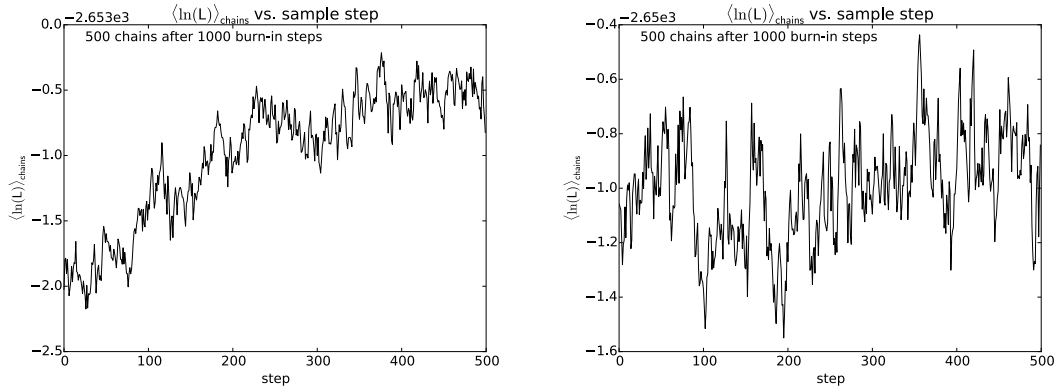

Figure 5.6: Total log-likelihood as a function of sampling step in minimum bias. Left: 1st sampling procedure, Right: final sampling procedure.

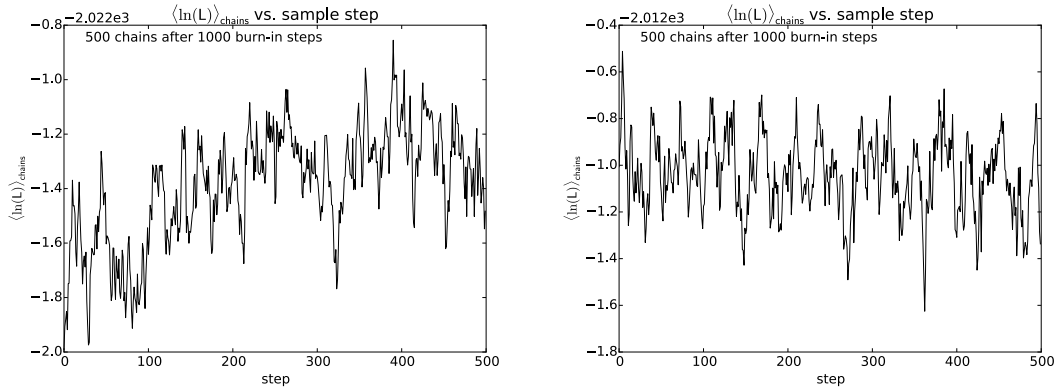

Figure 5.7: Total log-likelihood as a function of sampling step in 0-10% centrality. Left: 1st sampling procedure, Right: final sampling procedure.

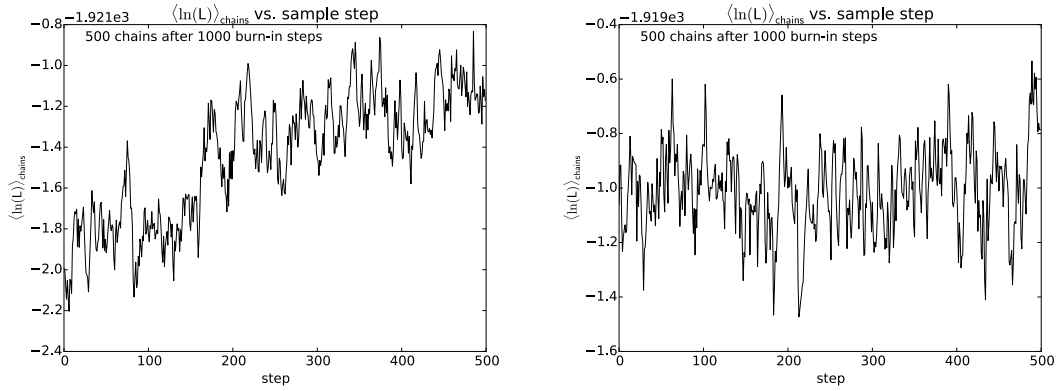

Figure 5.8: Total log-likelihood as a function of sampling step in 10-20% centrality. Left: 1st sampling procedure, Right: final sampling procedure.

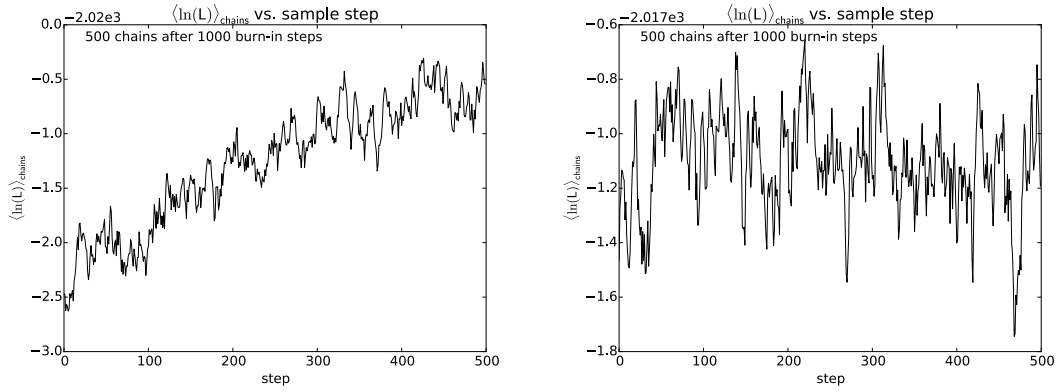

Figure 5.9: Total log-likelihood as a function of sampling step in 20-40% centrality. Left: 1st sampling, Right: final sampling.

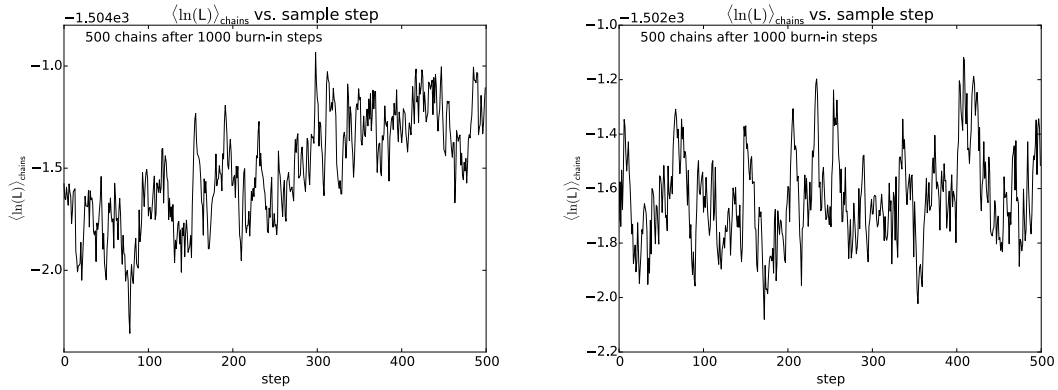

Figure 5.10: Total log-likelihood as a function of sampling step in 40-60% centrality. Left: 1st sampling procedure, Right: final sampling procedure.

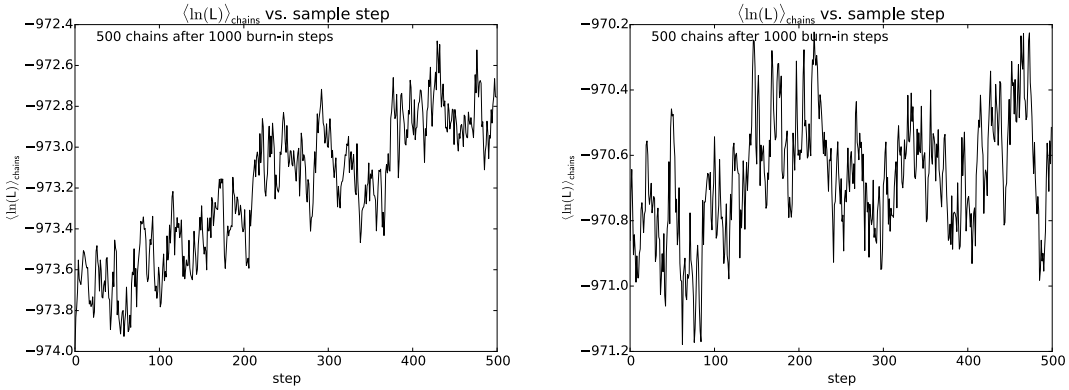

Figure 5.11: Total log-likelihood as a function of sampling step in 60-93% centrality. Left: 1st sampling procedure, Right: final sampling procedure.

5.1.5 Probability Distributions

After sufficient sampling, MCMC provides the sample distribution closely matching the actual desired distribution. Therefore, sampled charm and bottom yields can be regarded as probability distributions. Fig. 5.12 shows the joint probability distributions of charm and bottom hadron yields. Diagonal plots show probability distributions and others show correlations. We confirm a positive correlation in charm hadron yields (green) and bottom hadron yields (blue), on the other hand, a negative correlation can be shown in the correlation between charm and bottom hadron yields (orange). It indicates that our unfolding correctly samples probability distributions and sufficiently converges.

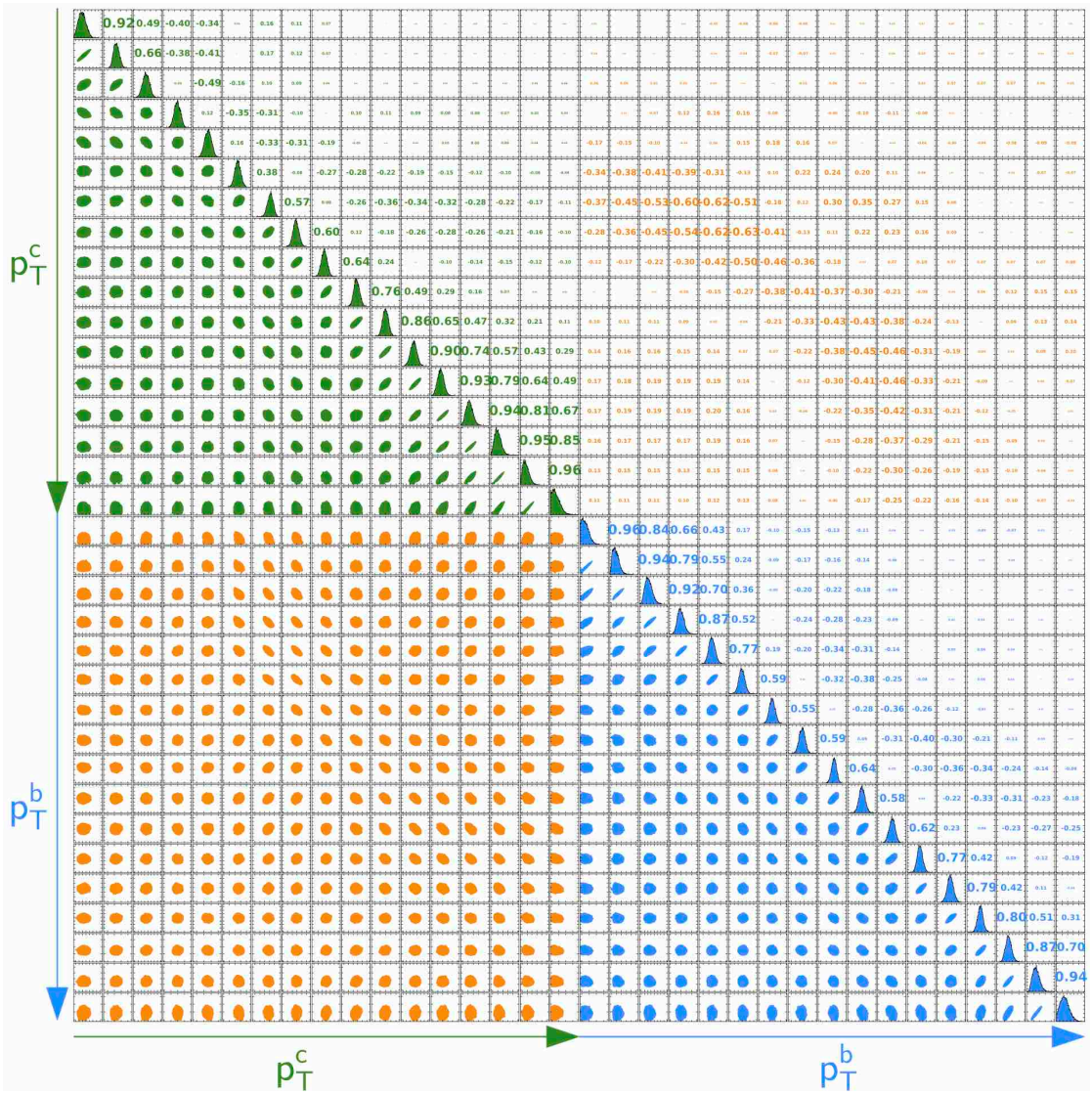

Figure 5.12: (minimum bias) The joint probability distributions of charm and bottom hadron yields. The diagonal plots show the probability distributions of charm (green) and bottom (blue) hadron yields for each p_T bin. The green colored plots show the correlations between charm hadron yields. The blue colored plots show the correlations between bottom hadron yields. The orange colored plots show the correlations between charm and bottom hadron yields. The top-right region shows the strength of the correlation.

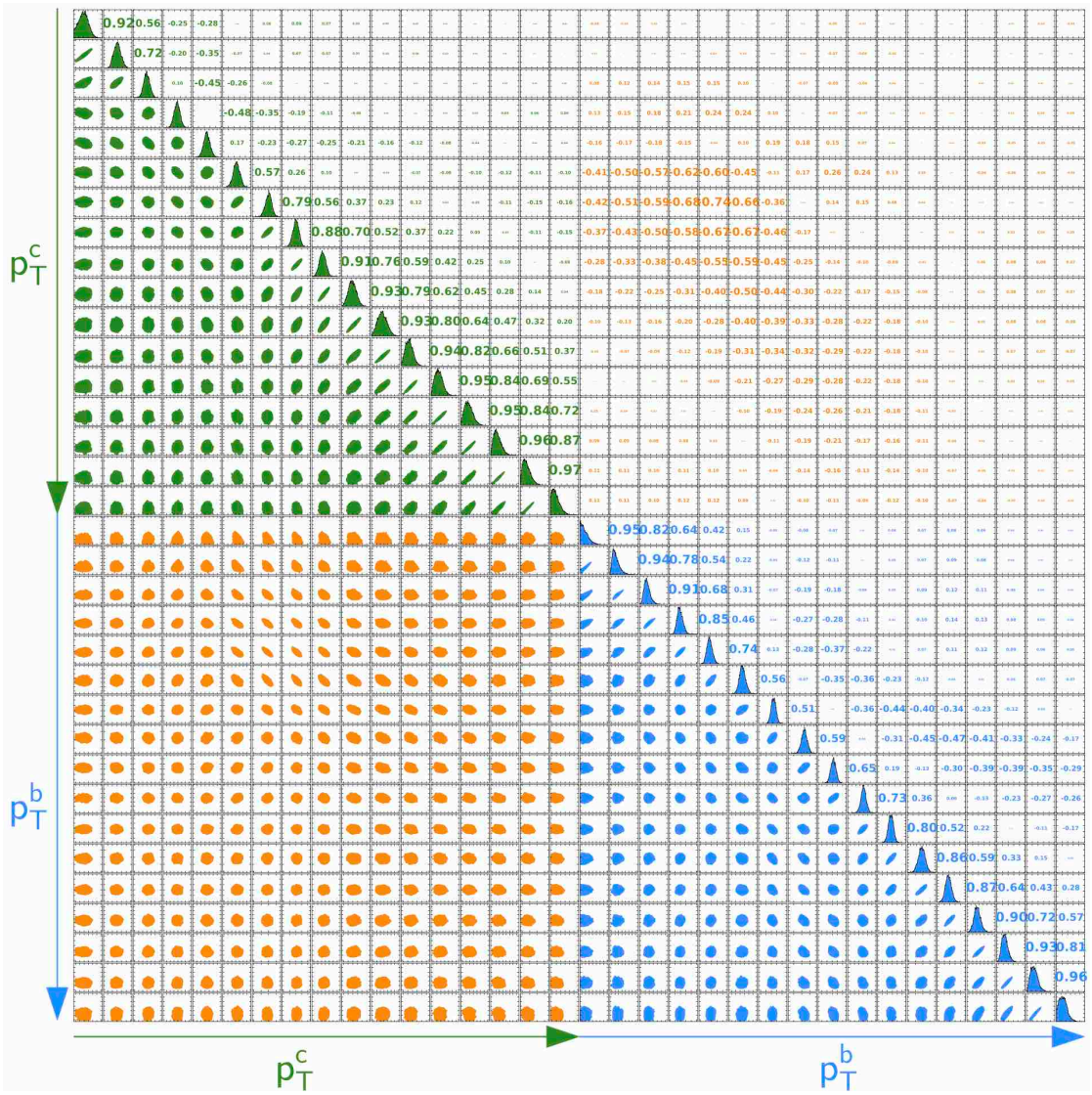

Figure 5.13: (0-10% centrality) The joint probability distributions of charm and bottom hadron yields. The diagonal plots show the probability distributions of charm (green) and bottom (blue) hadron yields for each p_T bin. The green colored plots show the correlations between charm hadron yields. The blue colored plots show the correlations between bottom hadron yields. The orange colored plots show the correlations between charm and bottom hadron yields. The top-right region shows the strength of the correlation.

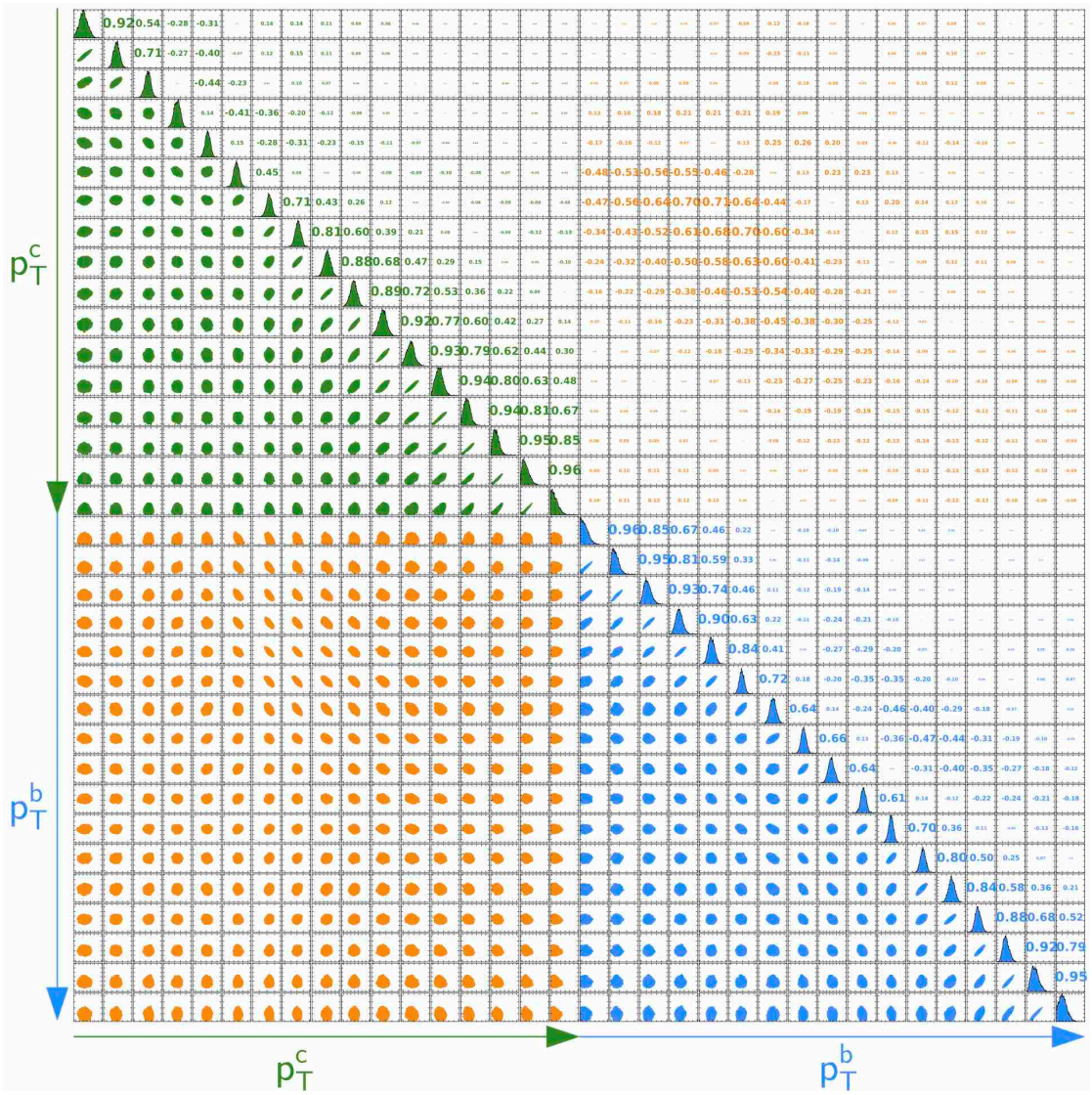

Figure 5.14: (10-20% centrality) The joint probability distributions of charm and bottom hadron yields. The diagonal plots show the probability distributions of charm (green) and bottom (blue) hadron yields for each p_T bin. The green colored plots show the correlations between charm hadron yields. The blue colored plots show the correlations between bottom hadron yields. The orange colored plots show the correlations between charm and bottom hadron yields. The top-right region shows the strength of the correlation.

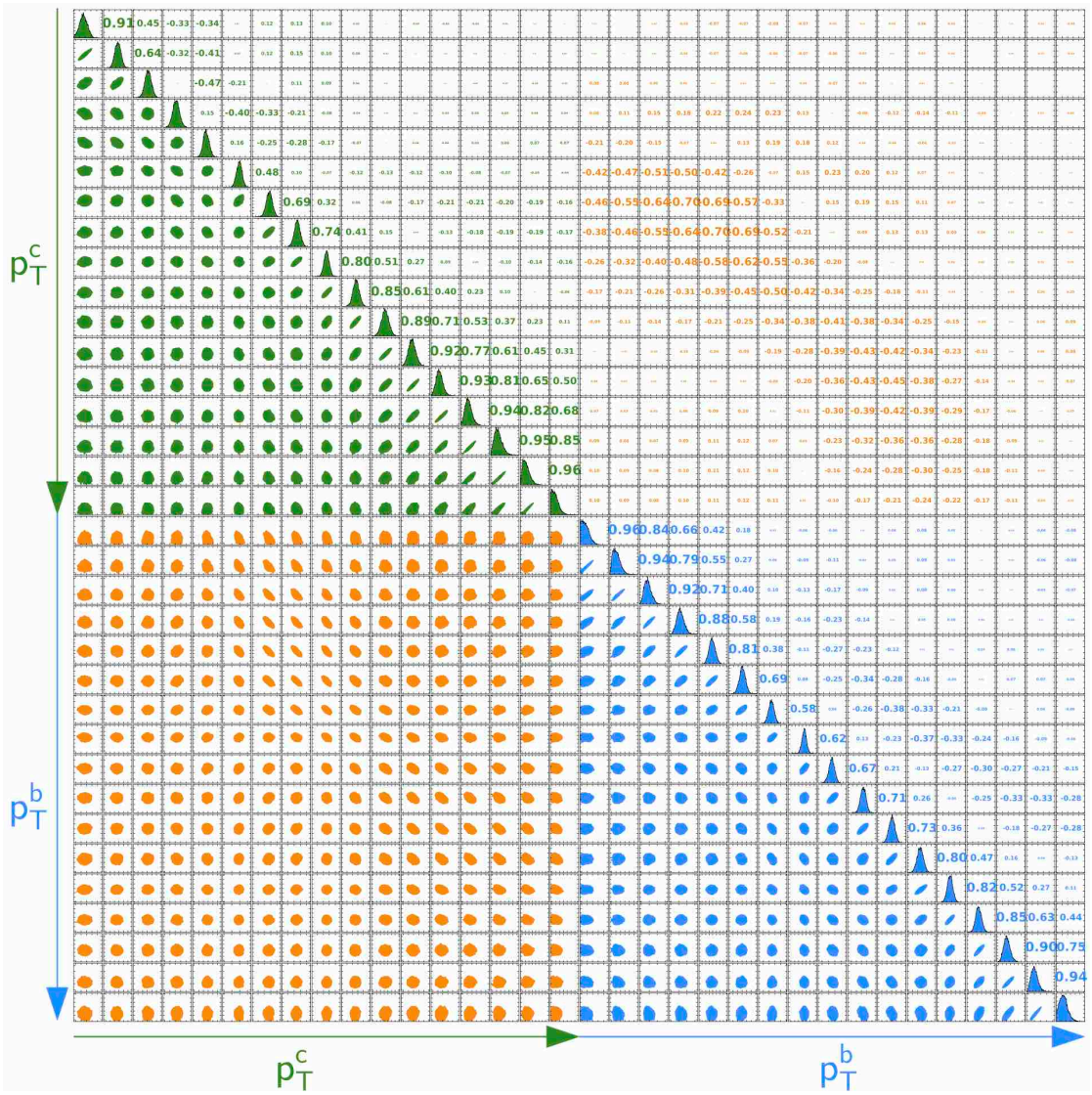

Figure 5.15: (20-40% centrality) The joint probability distributions of charm and bottom hadron yields. The diagonal plots show the probability distributions of charm (green) and bottom (blue) hadron yields for each p_T bin. The green colored plots show the correlations between charm hadron yields. The blue colored plots show the correlations between bottom hadron yields. The orange colored plots show the correlations between charm and bottom hadron yields. The top-right region shows the strength of the correlation.

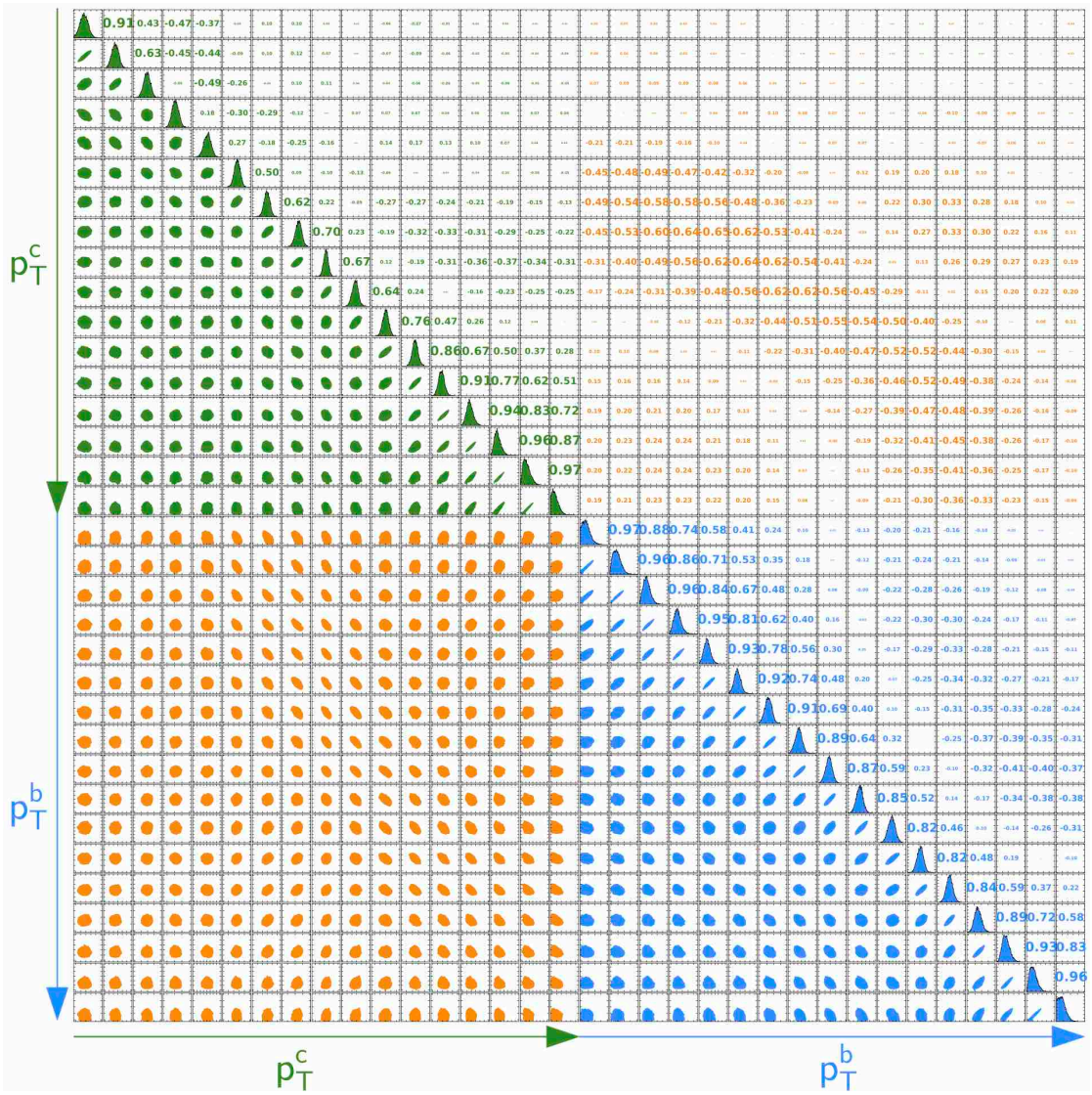

Figure 5.16: (40-60% centrality) The joint probability distributions of charm and bottom hadron yields. The diagonal plots show the probability distributions of charm (green) and bottom (blue) hadron yields for each p_T bin. The green colored plots show the correlations between charm hadron yields. The blue colored plots show the correlations between bottom hadron yields. The orange colored plots show the correlations between charm and bottom hadron yields. The top-right region shows the strength of the correlation.

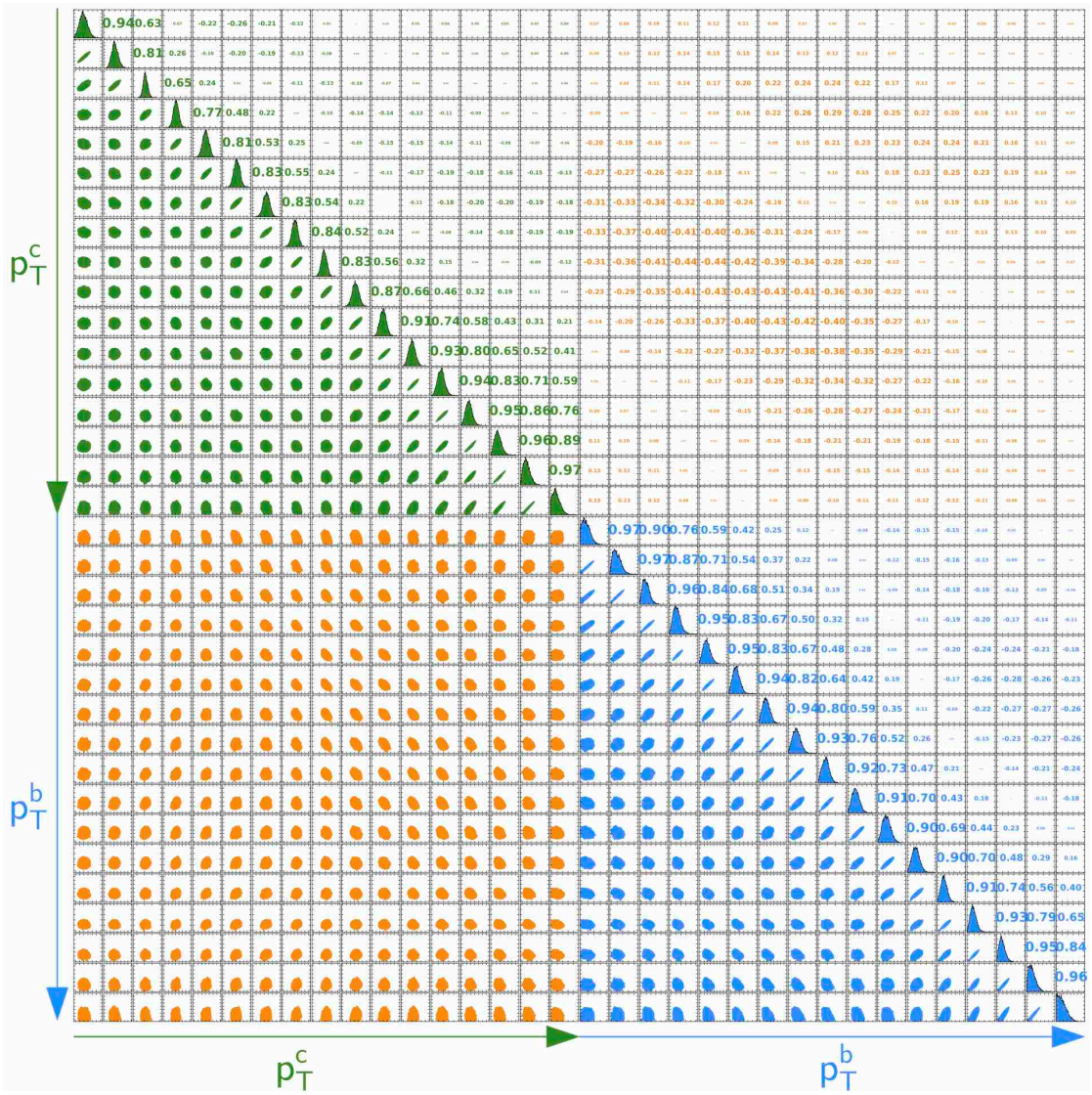

Figure 5.17: (60-93%) The joint probability distributions of charm and bottom hadron yields. The diagonal plots show the probability distributions of charm (green) and bottom (blue) hadron yields for each p_T bin. The green colored plots show the correlations between charm hadron yields. The blue colored plots show the correlations between bottom hadron yields. The orange colored plots show the correlations between charm and bottom hadron yields. The top-right region shows the strength of the correlation.

5.2 Comparisons of Refold to Data

The unfolded charm and bottom hadron yields are refolded to the decay electron yields and DCA_T distributions. The refolded yields and the DCA_T distributions of charm and bottom hadron decay electrons are compared to the measured data.

5.2.1 Invariant Yield of Charm and Bottom Hadron Decay Electrons

In our unfolding method, the likelihood value is calculated with the difference between the refold and the data and the statistical uncertainty. Therefore, the unfolding uncertainty only includes a contribution from the statistical uncertainty in the measured yield and DCA_T distributions. The systematic uncertainty is described in Sec. 5.3.

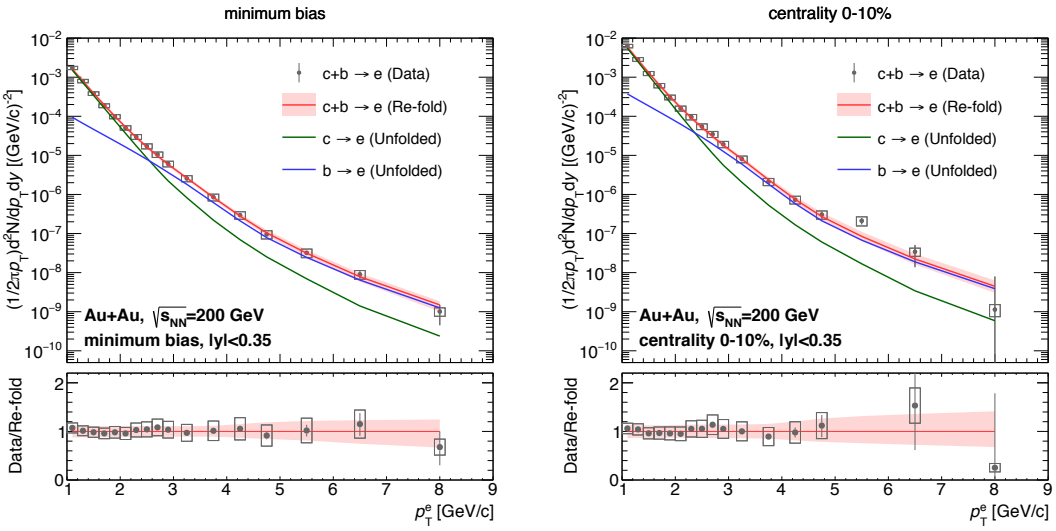

Figure 5.18: (Left: min. bias, Right: 0-10%) The invariant yield of charm and bottom hadron decay electrons as a function of p_T from the measured data compared to the re-folded yields. The red band represents the unfolding uncertainty. The bottom panel shows the ratio of the data to the re-fold.

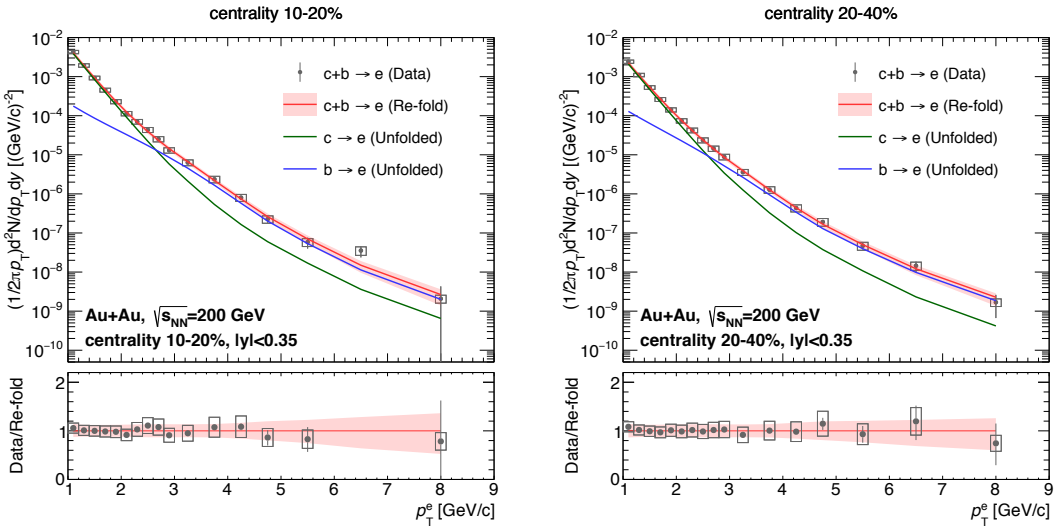

Figure 5.19: (Left: 10-20%, Right: 20-40%) The invariant yield of charm and bottom hadron decay electrons as a function of p_{T} from the measured data compared to the re-folded yields. The red band represents the unfolding uncertainty. The bottom panel shows the ratio of the data to the re-fold.

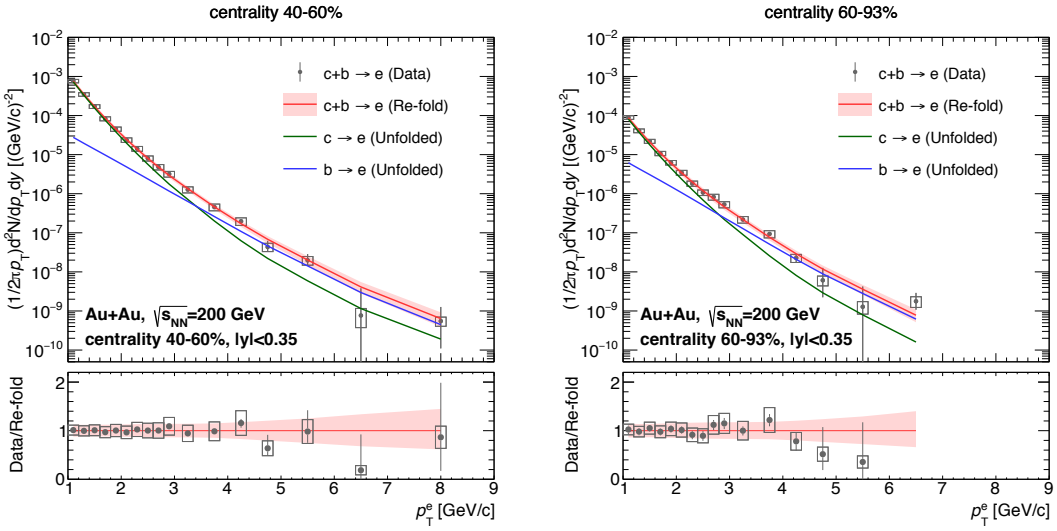

Figure 5.20: (Left: 40-60%, Right: 60-93%) The invariant yield of charm and bottom hadron decay electrons as a function of p_{T} from the measured data compared to the re-folded yields. The red band represents the unfolding uncertainty. The bottom panel shows the ratio of the data to the re-fold.

5.2.2 Refolded $\mathrm{DCA_T}$ Distributions

In order to account the systematic uncertainty of $\mathrm{DCA_T}$ template shapes, we add 10% uncertainty in quadrature to the statistical uncertainty for each DCA bin

if DCA counts are higher than 100 counts. In addition, this account improves the sensitivity of separation of charm and bottom contributions because these contributions dominate in large DCA_T region.

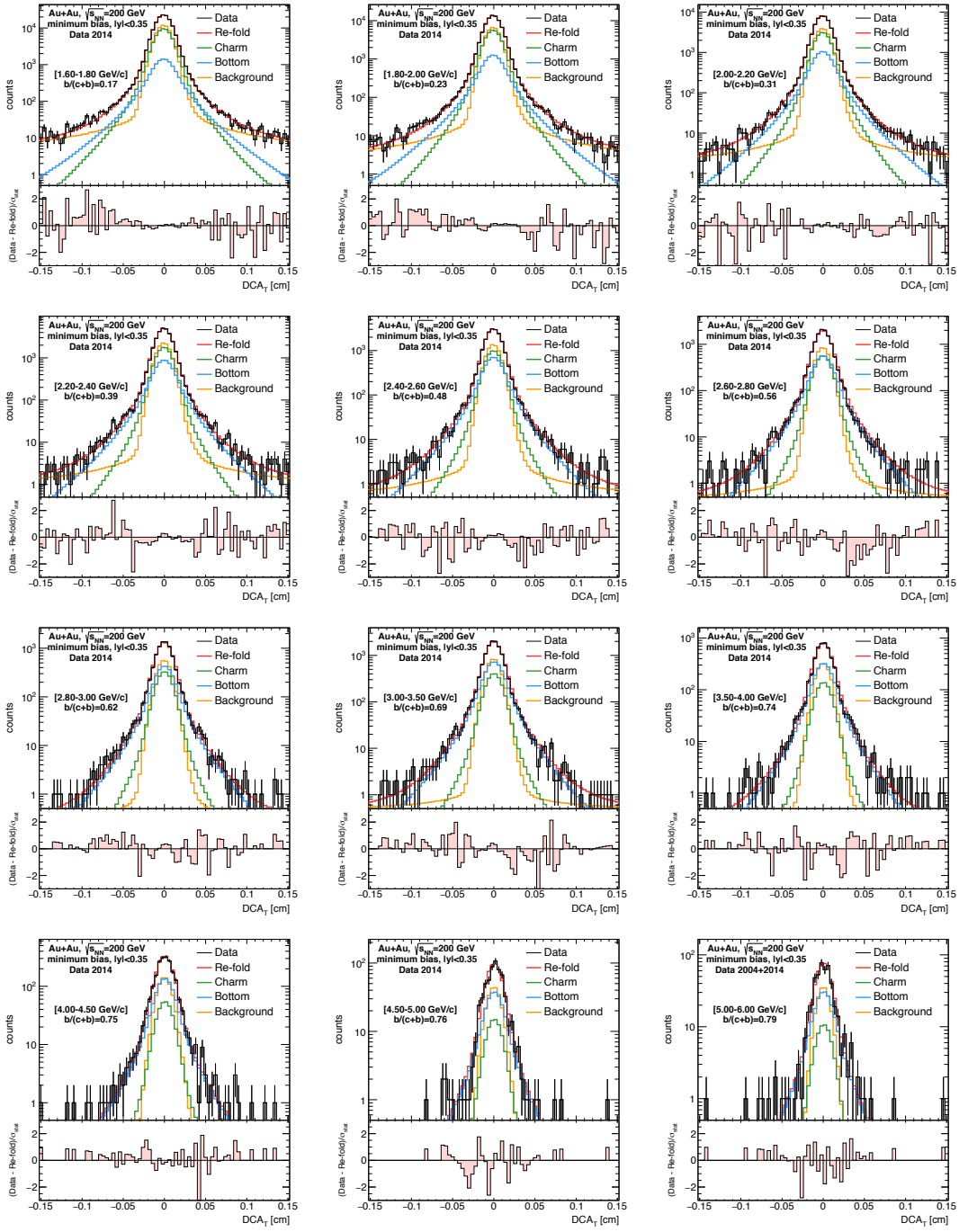

Figure 5.21: [Minimum-bias, p_T range: 1.6-6.0 GeV/c] The DCA_T distribution for measured electrons compared to the decomposed DCA_T distributions for background components (orange line), electrons from charm decays (green line), and electrons from bottom decays (blue line).

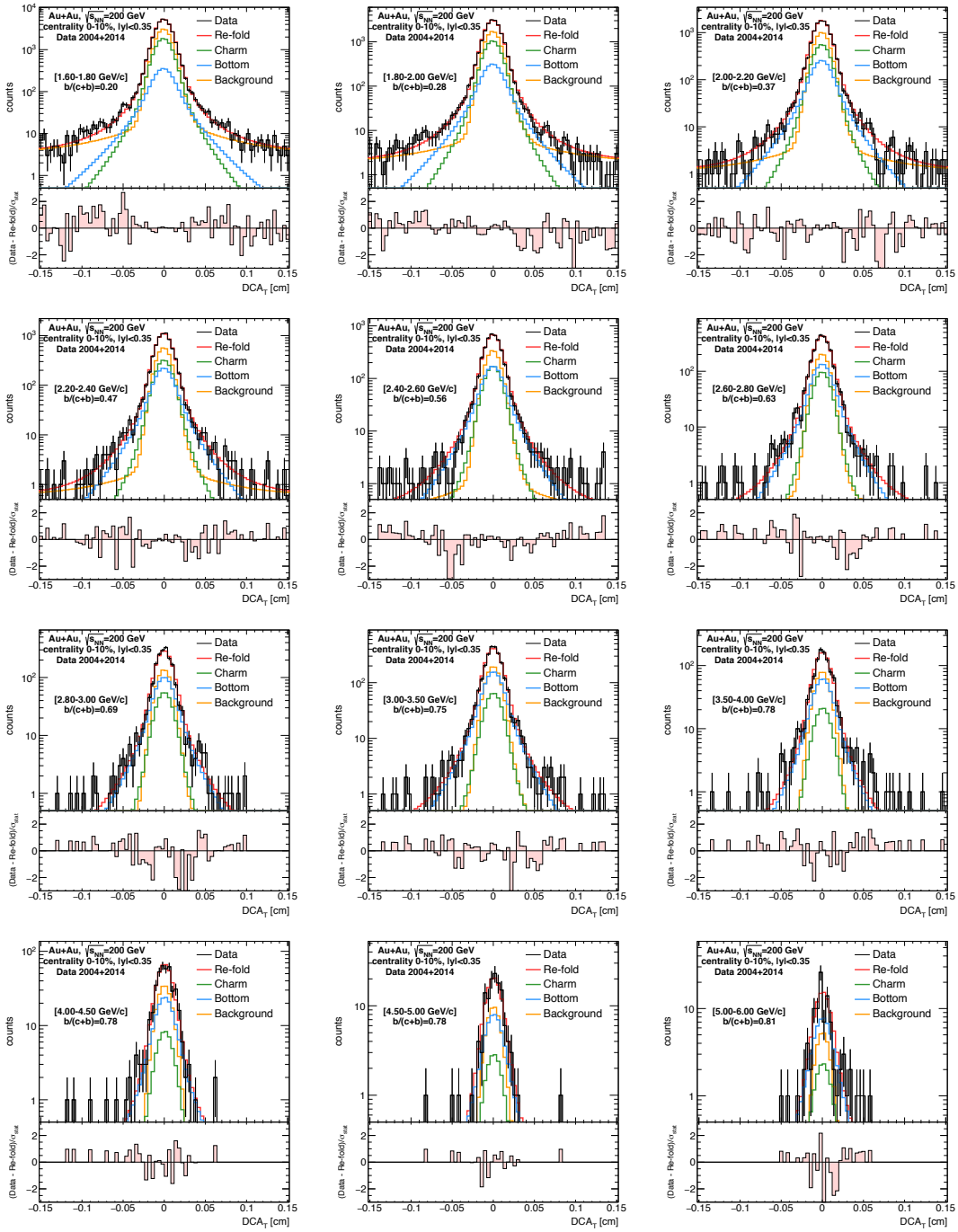

Figure 5.22: [Centrality 0-10%, p_T range: 0-6.0 GeV/c] The DCA$_T$ distribution for measured electrons compared to the decomposed DCA$_T$ distributions for background components (orange line), electrons from charm decays (green line), and electrons from bottom decays (blue line).

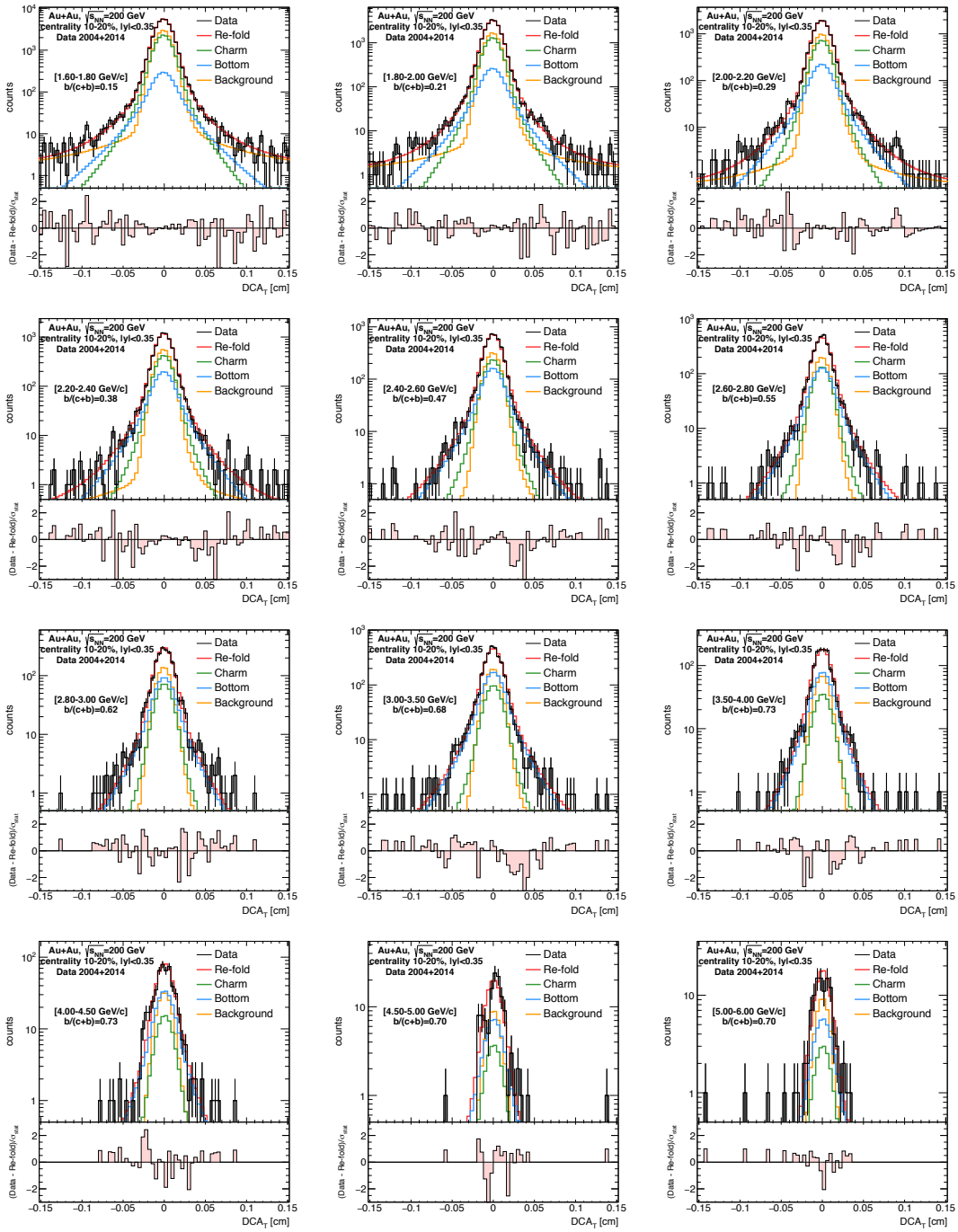

Figure 5.23: [Centrality 10-20%, p_{T} range: 0-6.0 GeV/c] The $\mathrm{DCA_T}$ distribution for measured electrons compared to the decomposed $\mathrm{DCA_T}$ distributions for background components (orange line), electrons from charm decays (green line), and electrons from bottom decays (blue line).

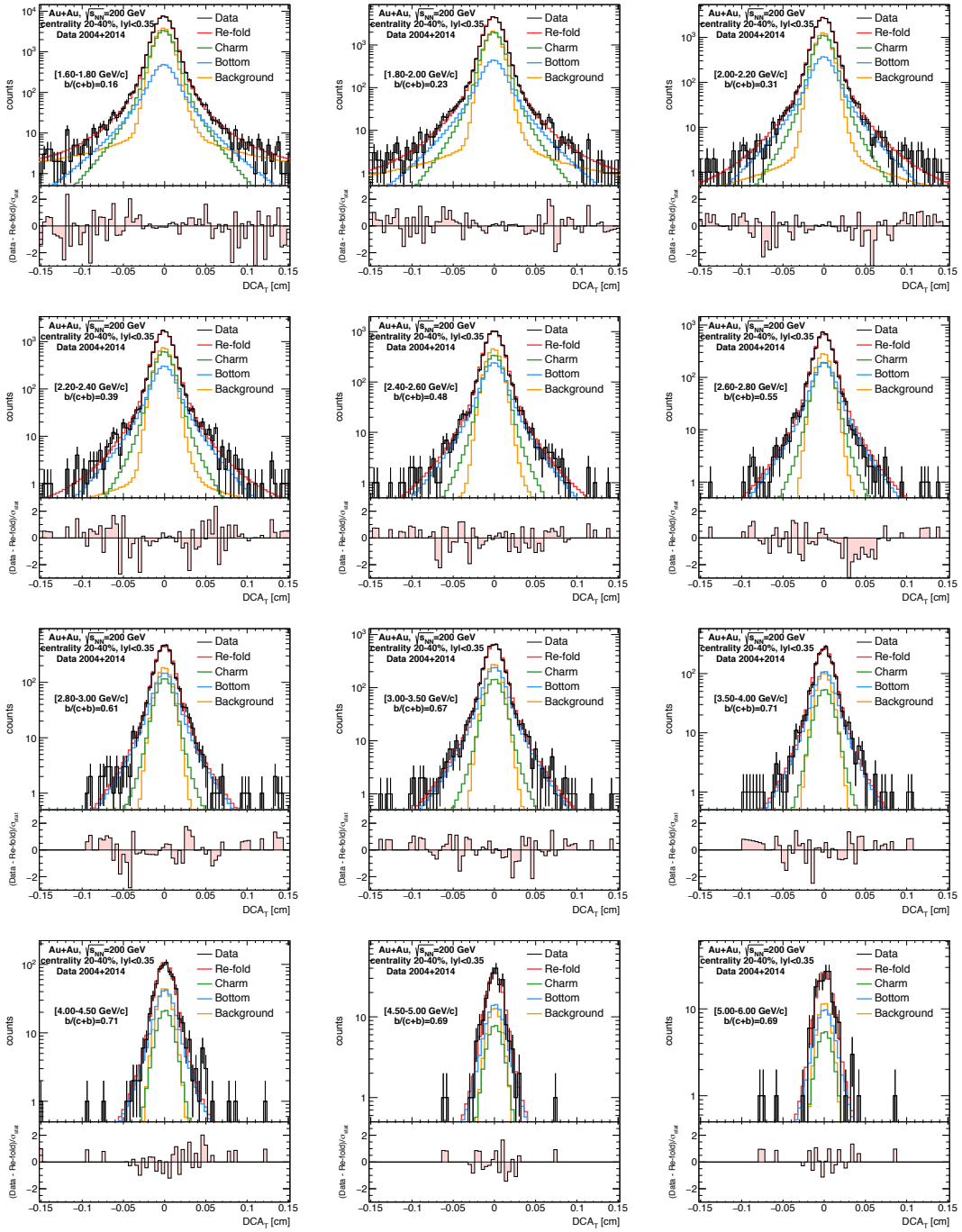

Figure 5.24: [Centrality 20-40%, p_T range: 0-6.0 GeV/c] The DCA_T distribution for measured electrons compared to the decomposed DCA_T distributions for background components (orange line), electrons from charm decays (green line), and electrons from bottom decays (blue line).

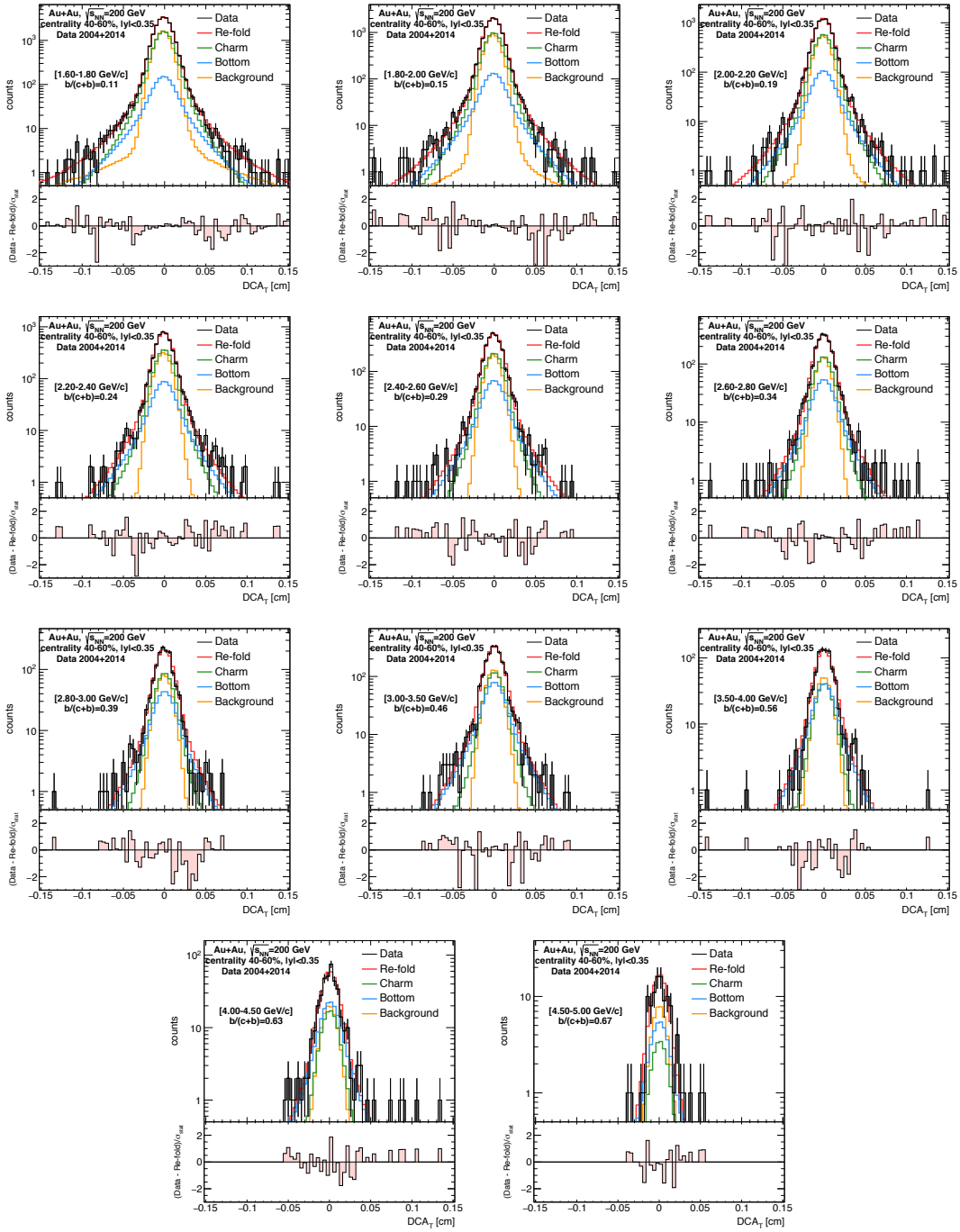

Figure 5.25: [Centrality 40-60%, p_T range: 0-5.0 GeV/c] The DCA$_T$ distribution for measured electrons compared to the decomposed DCA$_T$ distributions for background components (orange line), electrons from charm decays (green line), and electrons from bottom decays (blue line).

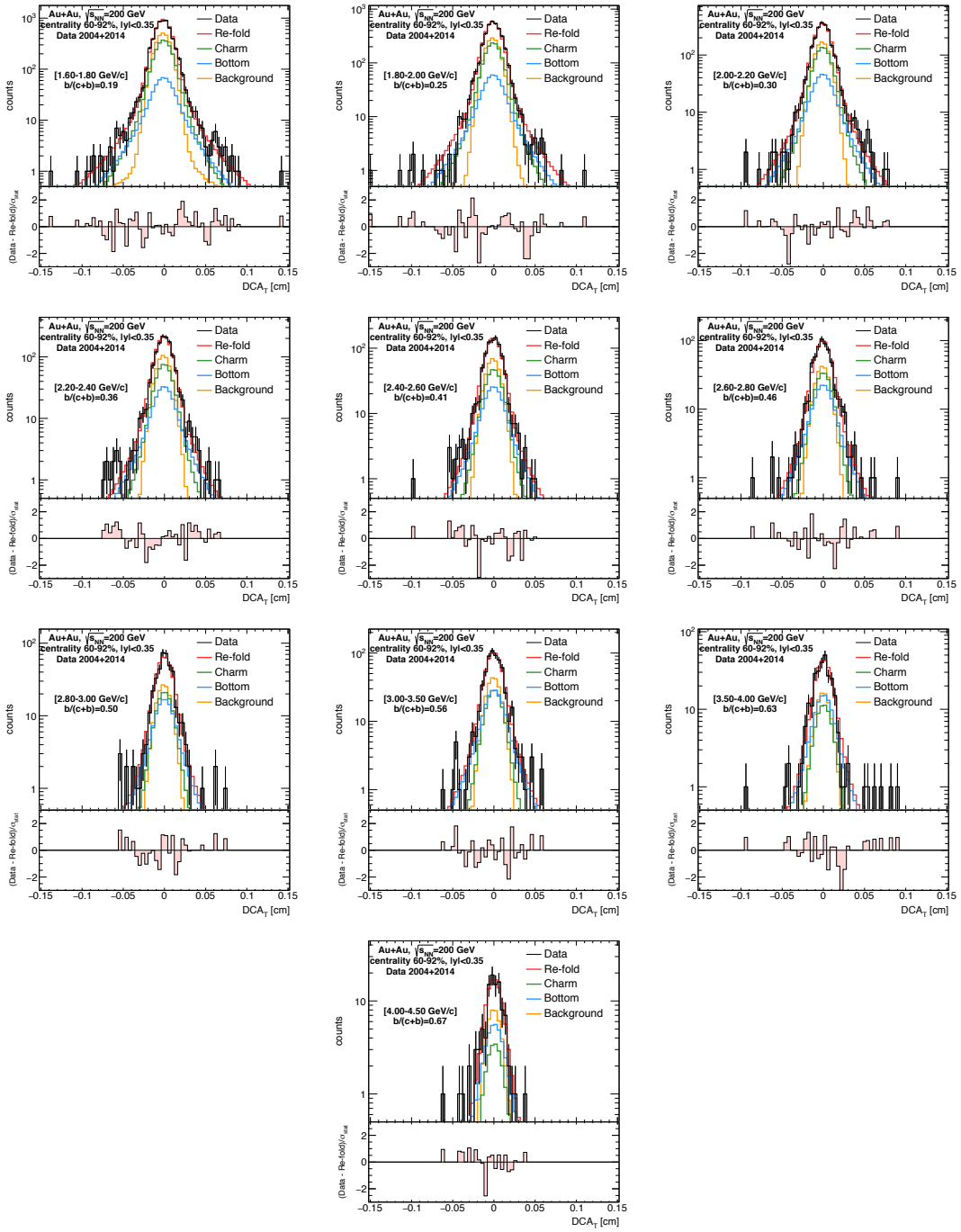

Figure 5.26: [Centrality 60-92%, p_{T} range: 0-4.0 GeV/c] The $\mathrm{DCA_T}$ distribution for measured electrons compared to the decomposed $\mathrm{DCA_T}$ distributions for background components (orange line), electrons from charm decays (green line), and electrons from bottom decays (blue line).

5.3 Systematic Uncertainties

The unfolding procedure considers only statistical uncertainties on the electron p_{T} spectra and $\mathrm{DCA}_{\mathrm{T}}$ distributions. Therefore, we estimate the systematic uncertainties on the measured data and the unfolding procedure which are considered as uncorrelated uncertainties described in the following. Each uncorrelated systematic uncertainty is added in quadrature in Fig. 5.28, 5.29 and 5.30.

- **Background normalization in $\mathrm{DCA}_{\mathrm{T}}$ distributions**
  The background fractions have the uncertainties and thus the background $\mathrm{DCA}_{\mathrm{T}}$ normalizations should be modified with varying each independently by $\pm 1\sigma$. The unfolding procedure runs independently for each modified background DCA template. Each difference of the unfolding result between using normal templates and using modified templates is added in quadrature to the systematic uncertainty. The uncertainty of background fraction is shown in Fig. 4.61.

- **Systematic uncertainty in the measured yield**
  Our unfolding procedure considers only a statistical uncertainty on the measured yield of $c + b \rightarrow e$ in likelihood calculation. Therefore, systematic uncertainty on the measured yield of $c + b \rightarrow e$ should be accounted in additionally. In order to calculate the systematic uncertainty, an input p_{T} spectrum is modified by either kicking or tilting the spectrum shown in Fig. 5.27. Tilting means that a modified spectrum pivots based on the nominal spectra about the given point. The lowest p_{T} point goes up by the systematic uncertainty and the highest p_{T} point goes down by the systematic uncertainty and the intermediate points are modified with linear interpolation. On the other hands, kinking means that a modified spectrum is folded based on the nominal spectrum. A control point for both tilting and kinking is at $p_{\mathrm{T}} = 1.8$ GeV/c or 5.0 GeV/c because analysis cuts are changed at these points. The unfolding procedure run with 8 modified spectrums, and then a root mean square of difference from the nominal result is assigned as systematic uncertainty.

- **Choice of prior**
  We use two reference spectrums, PYTHIA and modified PYTHIA by the blast-wave model, to smooth an unfolded spectrum as a prior. Therefore, a difference of result when using different reference spectrum is assigned to systematic uncertainty of prior.

- **Regularization hyper-parameter**
  We control the strength of the regularization (spectrum smoothness) with a hyper-parameter α. A hyper-parameter and systematic limits are chosen by maximum likelihood method described in section. 5.1.3. We run unfolding with 3 different hyper-parameters and add a difference to a systematic uncertainty in quadrature.

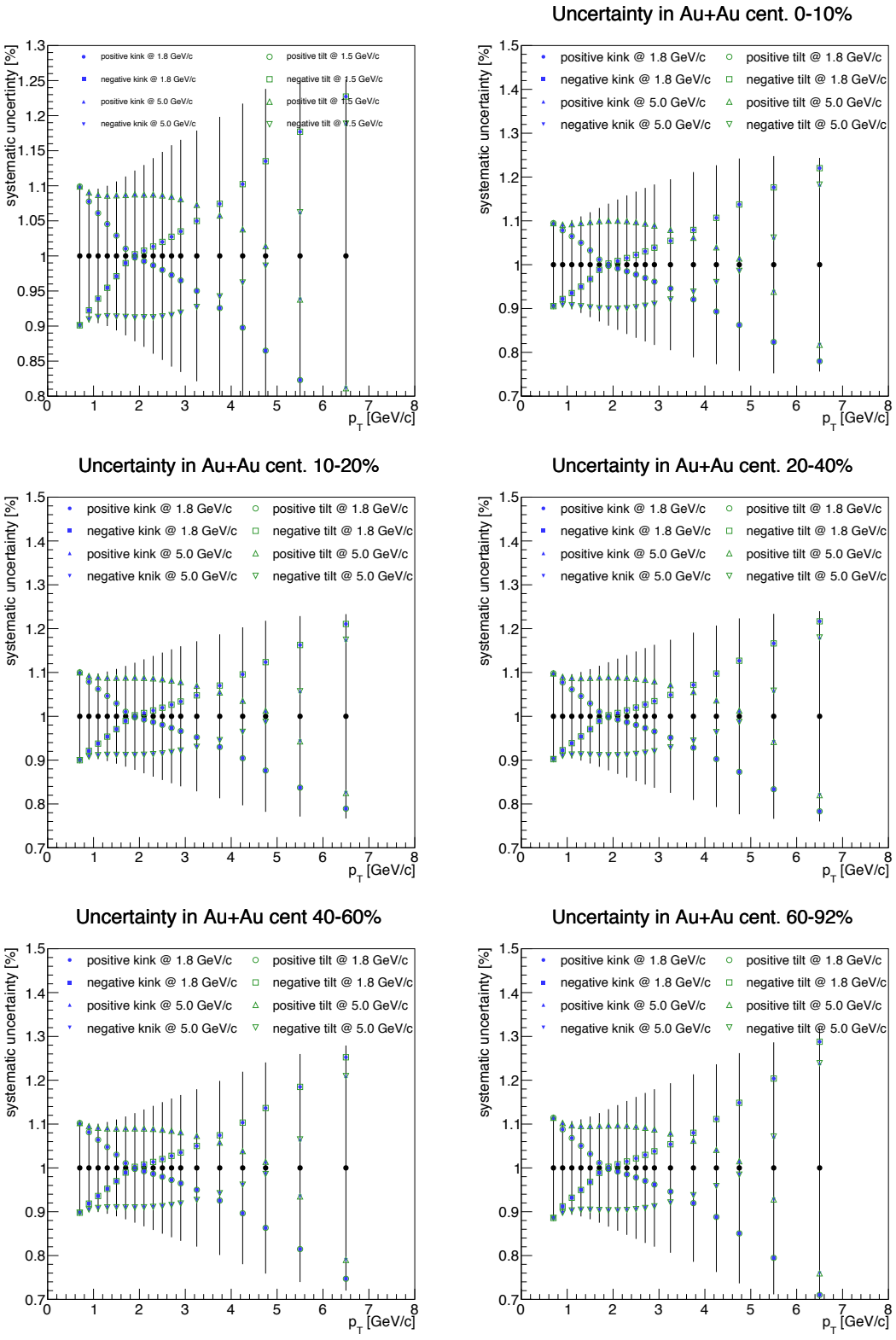

Figure 5.27: The fraction of systematic uncertainty on the invariant yield of $c + b \rightarrow e$ and the relative ratio of 8 pattern modified spectrums based on the nominal spectrum.

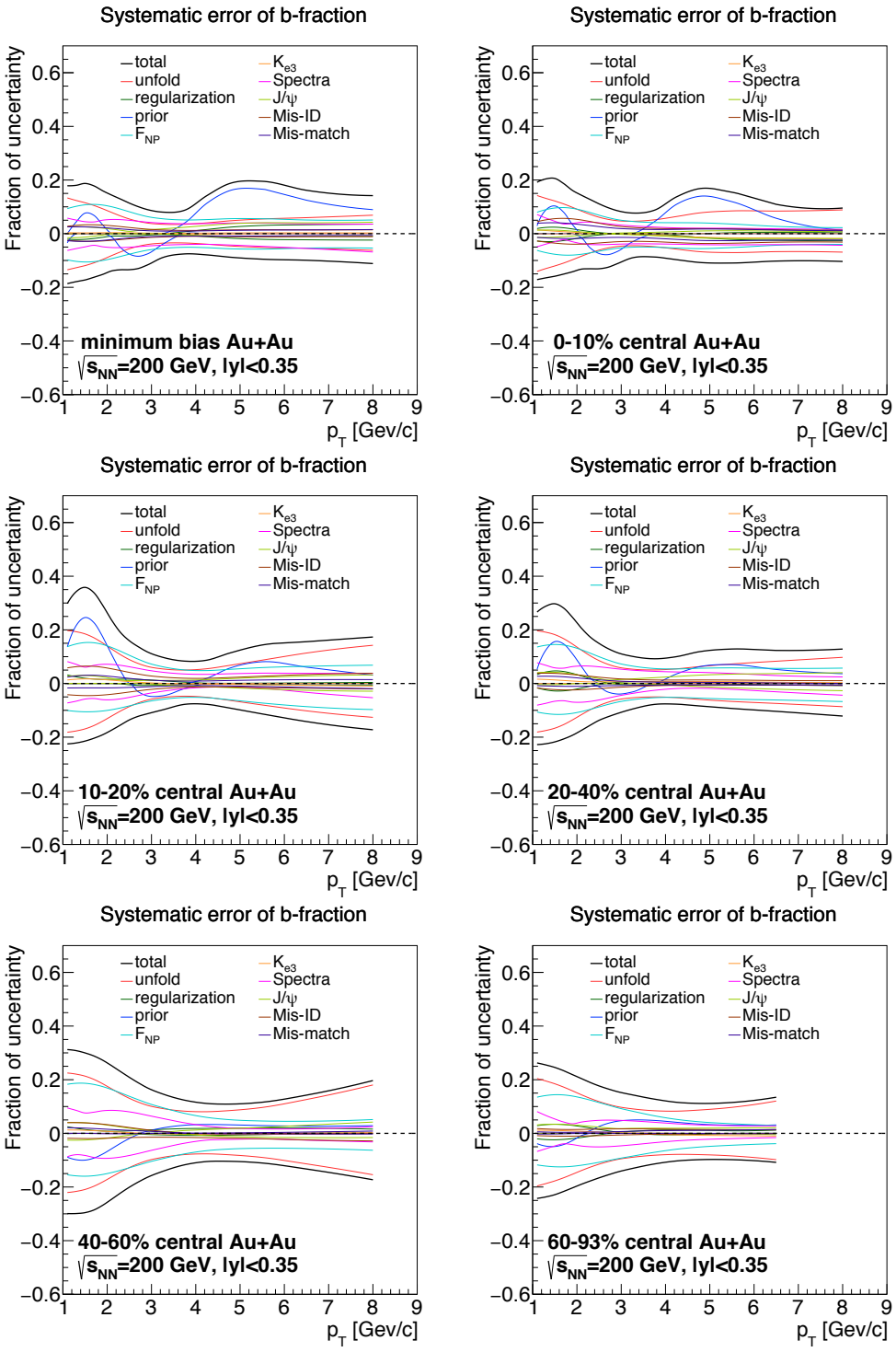

Figure 5.28: The fraction of each uncertainty on the bottom electron fraction, $b \rightarrow e/(c \rightarrow e + b \rightarrow e)$, as a function of p_{T}.

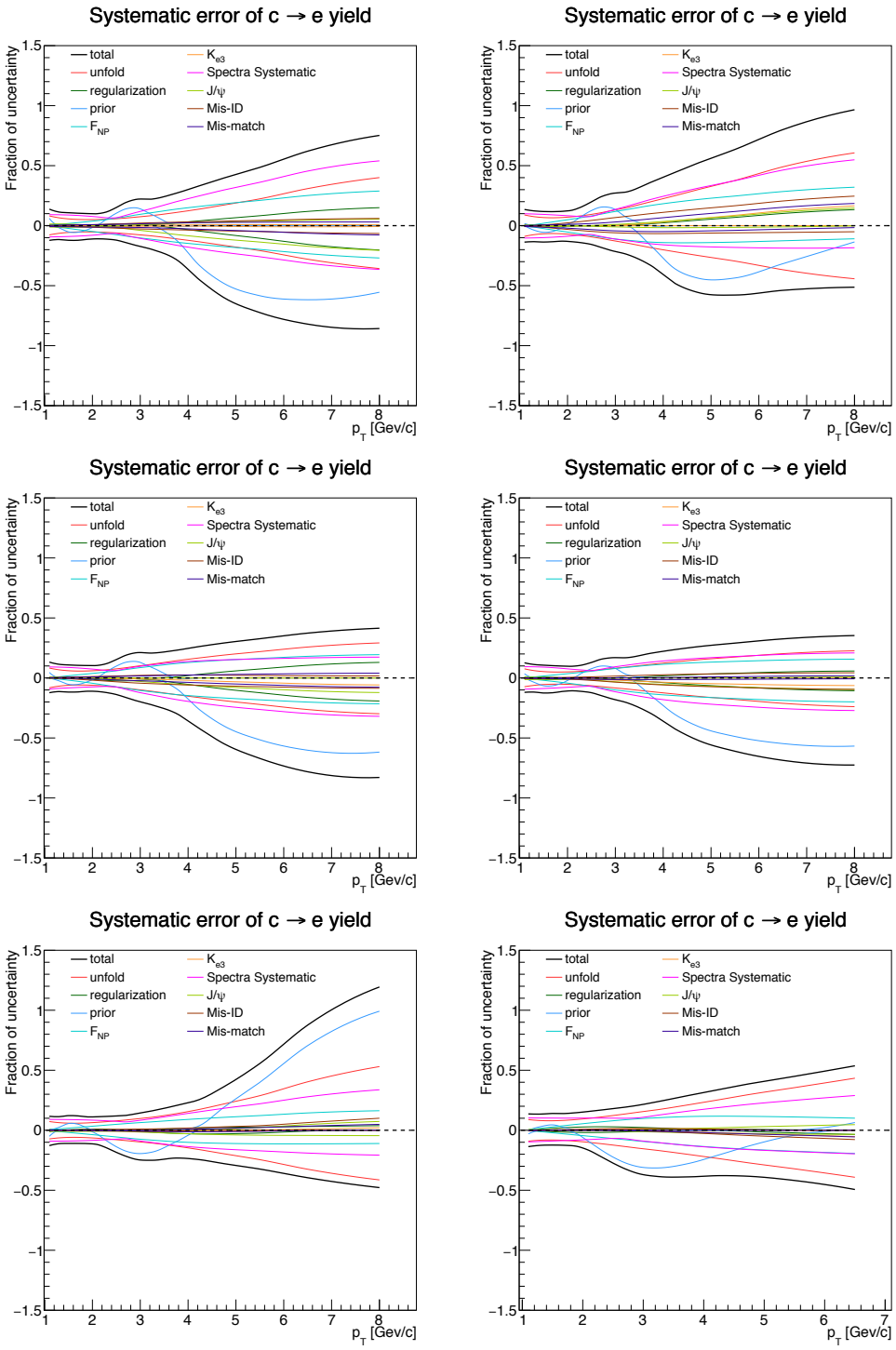

Figure 5.29: The fraction of each uncertainty on the invariant yield of $c \rightarrow e$ as a function of p_{T}.

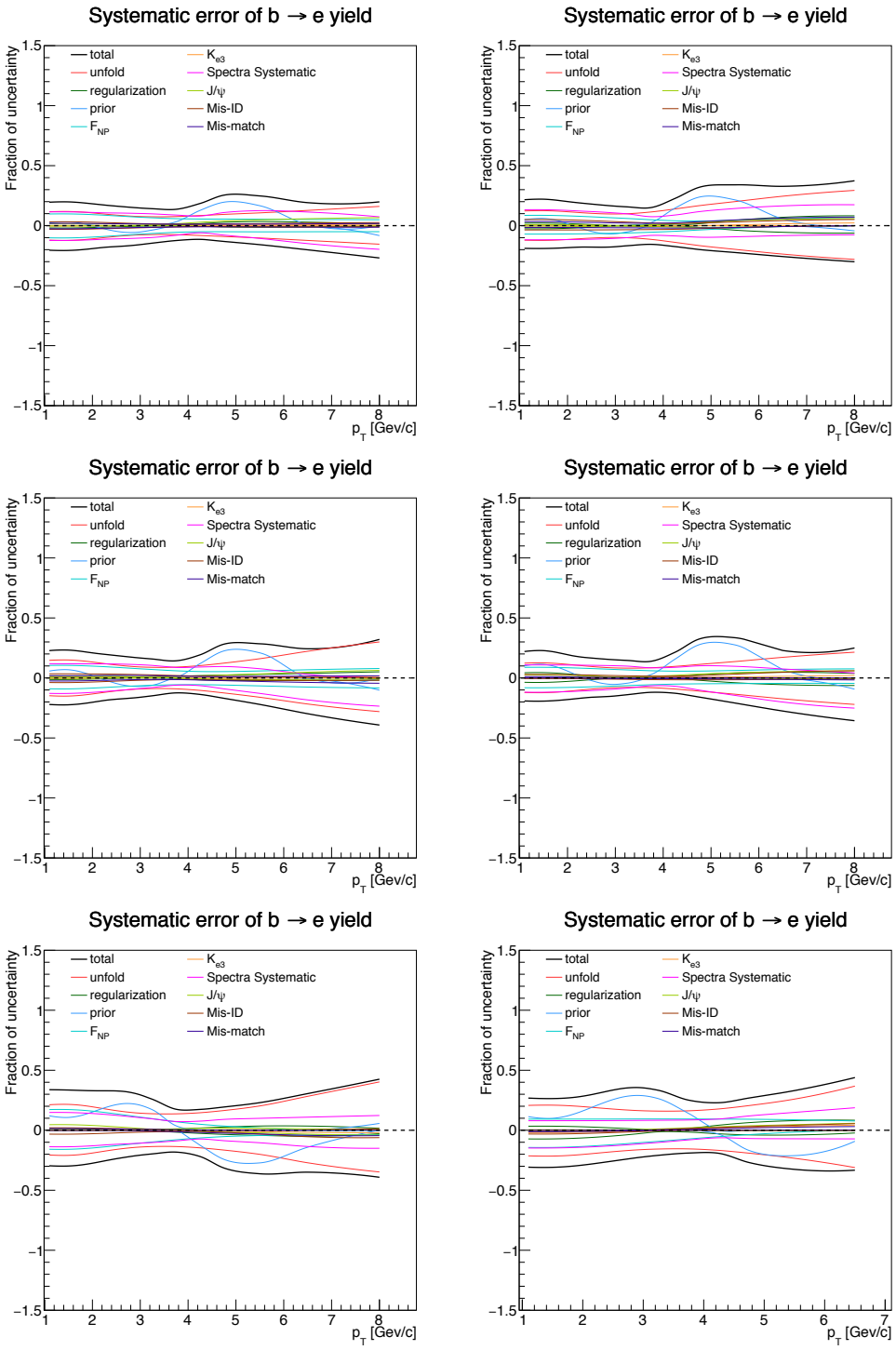

Figure 5.30: The fraction of each uncertainty on the invariant yield of $b \rightarrow e$ as a function of p_{T}.

Chapter 6

Results

6.1 Bottom Electron Fraction

The fraction of electrons from bottom hadron decays, $b \rightarrow e/\,(c \rightarrow e + b \rightarrow e)$, is estimated by both refolded yields of electrons from charm and bottom hadron decays. Here, the electrons from bottom hadron decays, $b \rightarrow e$, includes the cascade decay $b \rightarrow c \rightarrow e$. The bottom electron fractions in Au+Au collisions are compared with that in $p + p$ collisions [72] as shown in Fig. 6.3. The solid-lines denotes central values for each p_{T} range and the band denotes the 1σ limits of p_{T} correlated uncertainties. The bottom electron fraction seems to be increasing in central Au+Au collisions compared to that in $p + p$ collisions, which indicates charm quark is suppressed stronger than bottom quark in Au+Au collisions. On the other hand, bottom electron fractions in peripheral Au+Au collisions are similar to that in $p + p$ collisions because of a small suppression.

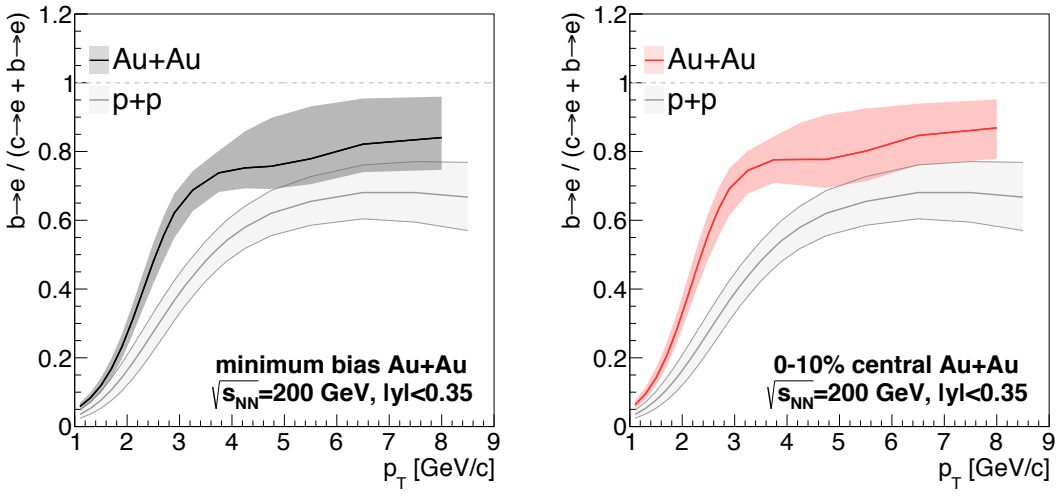

Figure 6.1: The bottom electron fractions, $b \rightarrow e/\,(c \rightarrow e + b \rightarrow e)$, in minimum bias (left) and 0-10% centrality (right).

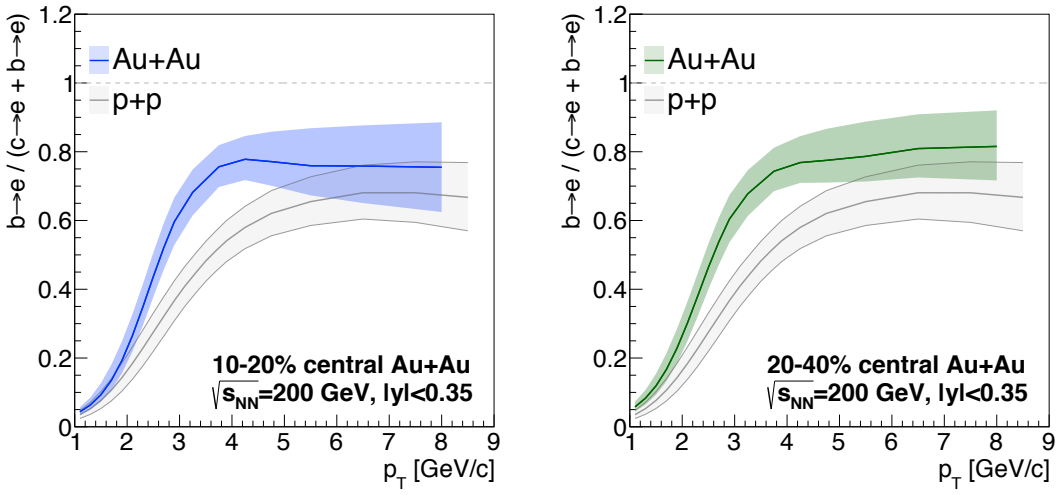

Figure 6.2: The bottom electron fractions, $b \rightarrow e/\left(c \rightarrow e + b \rightarrow e\right)$, in 10-20% centrality (left) and 20-40% centrality (right).

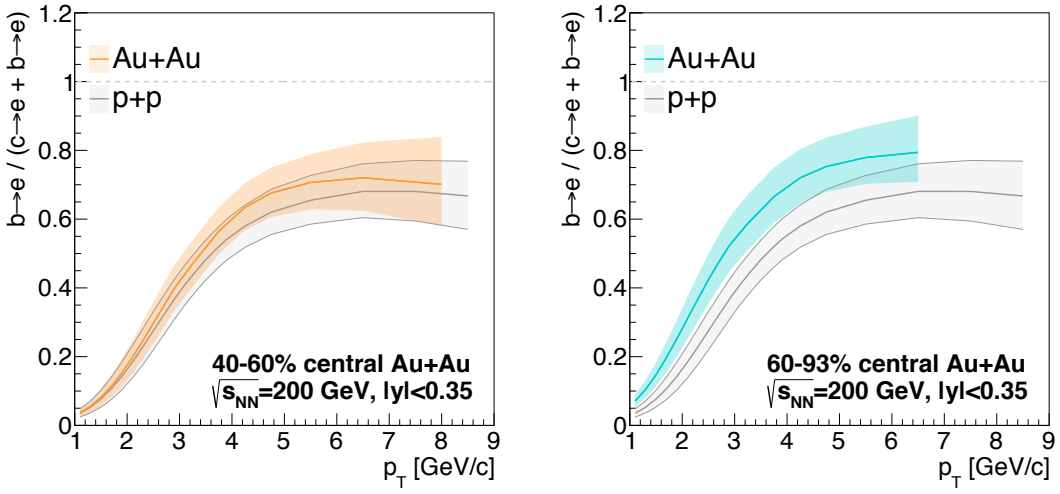

Figure 6.3: The bottom electron fractions, $b \rightarrow e/\left(c \rightarrow e + b \rightarrow e\right)$, in 40-60% centrality (left) and 60-93% centrality (right).

6.2 Invariant Yield of Electrons from Charm and Bottom Hadron Decays

The refold invariant yields of $c + b \rightarrow e$ with full-uncertainty are compared with the measured data as shown in Fig. 6.4. The refold spectra are in a reasonable agreement with the measured data.

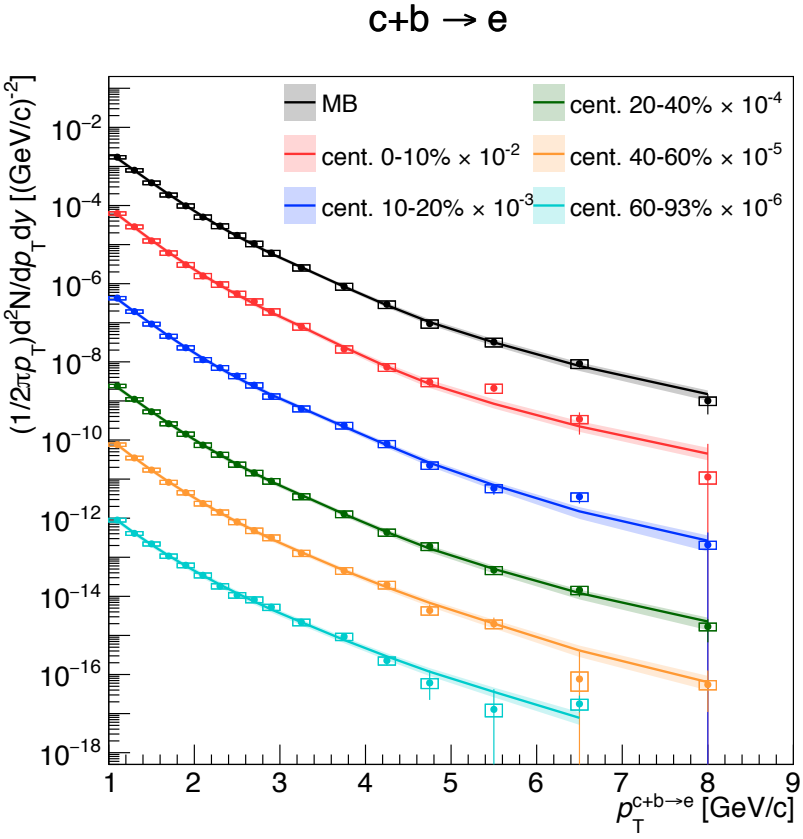

Figure 6.4: The invariant yield of electrons from charm and bottom hadron decays as a function of p_{T} from the measured data compared to refolded yields for each centrality.

The refolded invariant yields of $c \rightarrow e$ and $b \rightarrow e$ are shown in Fig. 6.5 and Fig. 6.6 and compared with the invariant yields in $p+p$ collisions [72] scaled by T_{AA} factors, where T_{AA} is the nuclear thickens function calculated by N_{coll} and the luminosity of $p+p$ collisions ($\mathcal{L}^{pp}$). The solid-line represents the most likely value about given p_{T} and the band represents the 1σ limits on the point-to-point correlated uncertainty. Both comparisons of the invariant yield of $c \rightarrow e$ and $b \rightarrow e$ show the yield suppression as a function of centrality and increasing suppression with increasing p_{T}. The invariant yield as a function of N_{coll} for integrated p_{T} is also calculated as shown in Fig. 6.7. The solid line denotes T_{AA} scaled yield in $p+p$ collisions. Both integrated yield of $c \rightarrow e$ and $b \rightarrow e$ in p_{T} range from 1.0-1.4 GeV/c show N_{coll} scaled the integrated yield because of no suppression at low p_{T} in Au+Au collisions. On the other hand, the integrated yield in high p_{T} range shows the yield suppression as a function of N_{coll}. This suppression pattern will be discussed in Sec. 7.1.

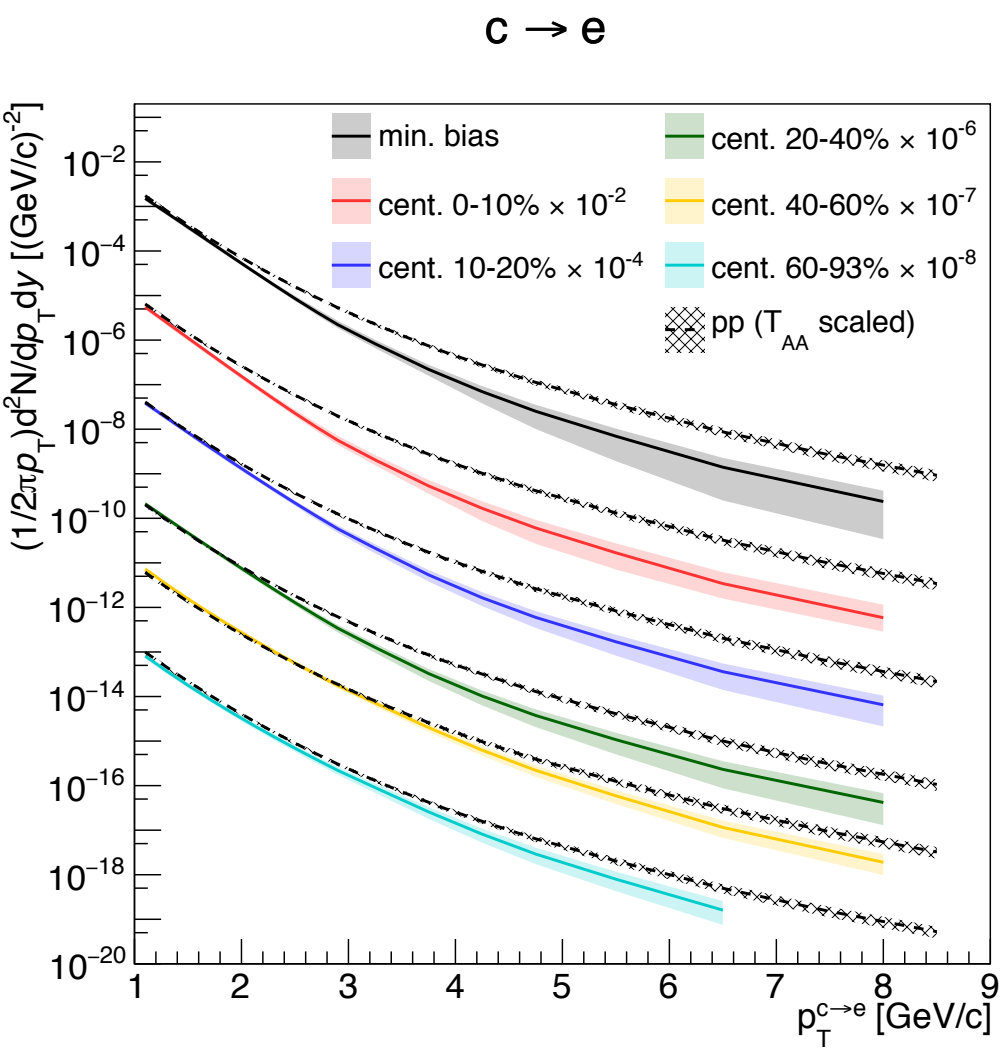

Figure 6.5: The invariant yield of electrons from charm hadron decays as a function of p_{T} in Au+Au collisions for each centrality, compared to T_{AA} scaled $p + p$ yield.

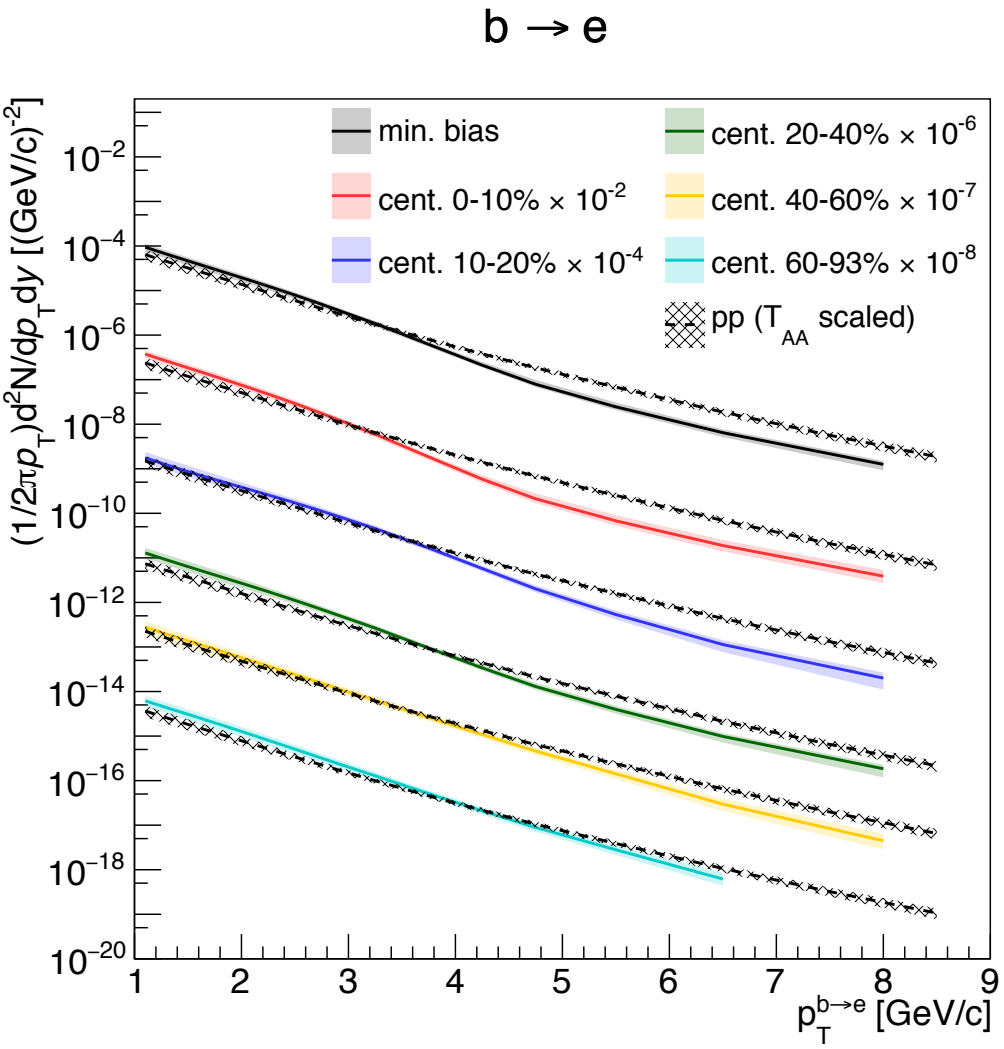

Figure 6.6: The invariant yield of electrons from bottom hadron decays as a function of p_{T} in Au+Au collisions for each centrality, compared to T_{AA} scaled $p + p$ yield.

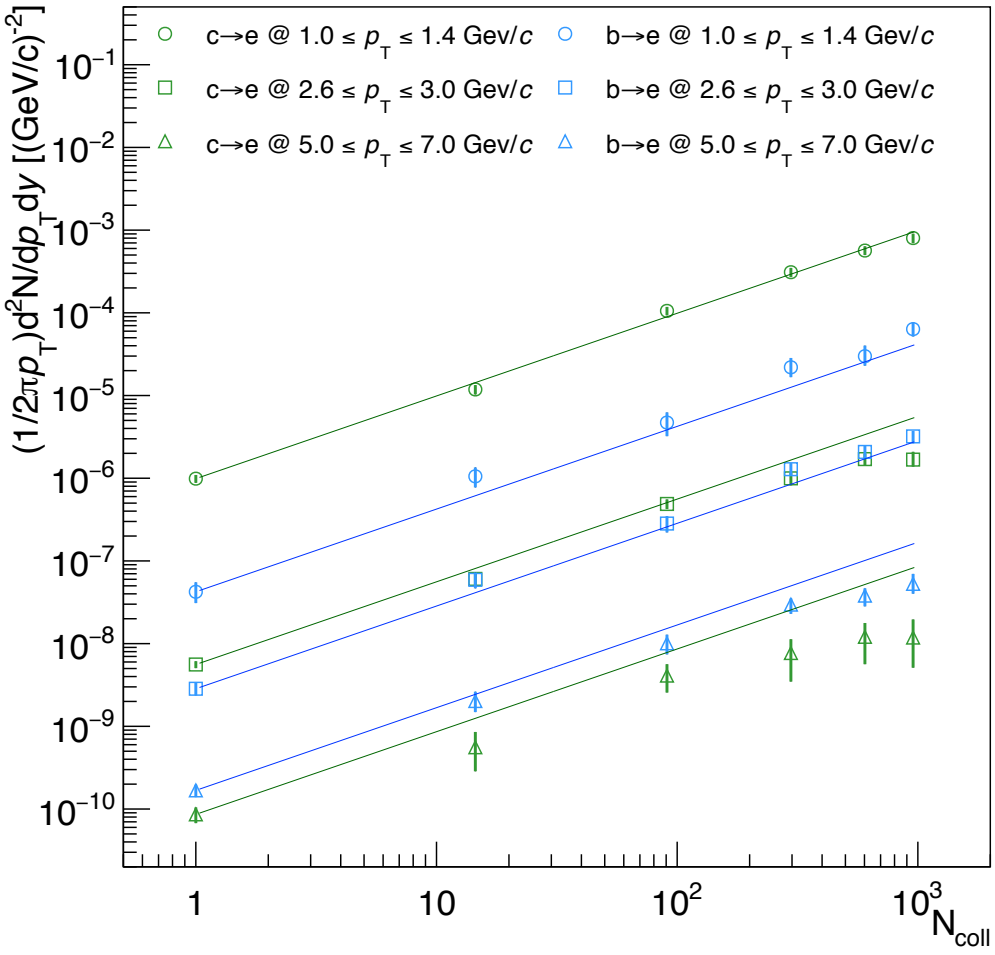

Figure 6.7: The integrated yield of $c \rightarrow e$ and $b \rightarrow e$ as a function of $N_{\rm part}$ in Au+Au collisions, compared to $T_{\rm AA}$ scaled $p + p$ yield.

6.2.1 Invariant Yields of Charm and Bottom Hadrons

The invariant yields of charm and bottom hadrons are unfolded point by point in 17 $p_{\rm T}$ bins and compared with $N_{\rm coll}$ scaled yields in $p + p$ collisions. The points represent the most likely value about given $p_{\rm T}$ and the box represents the 1σ limits on the point-to-point correlated uncertainty. A suppression pattern similar to the decay electron yields is shown in Fig. 6.8.

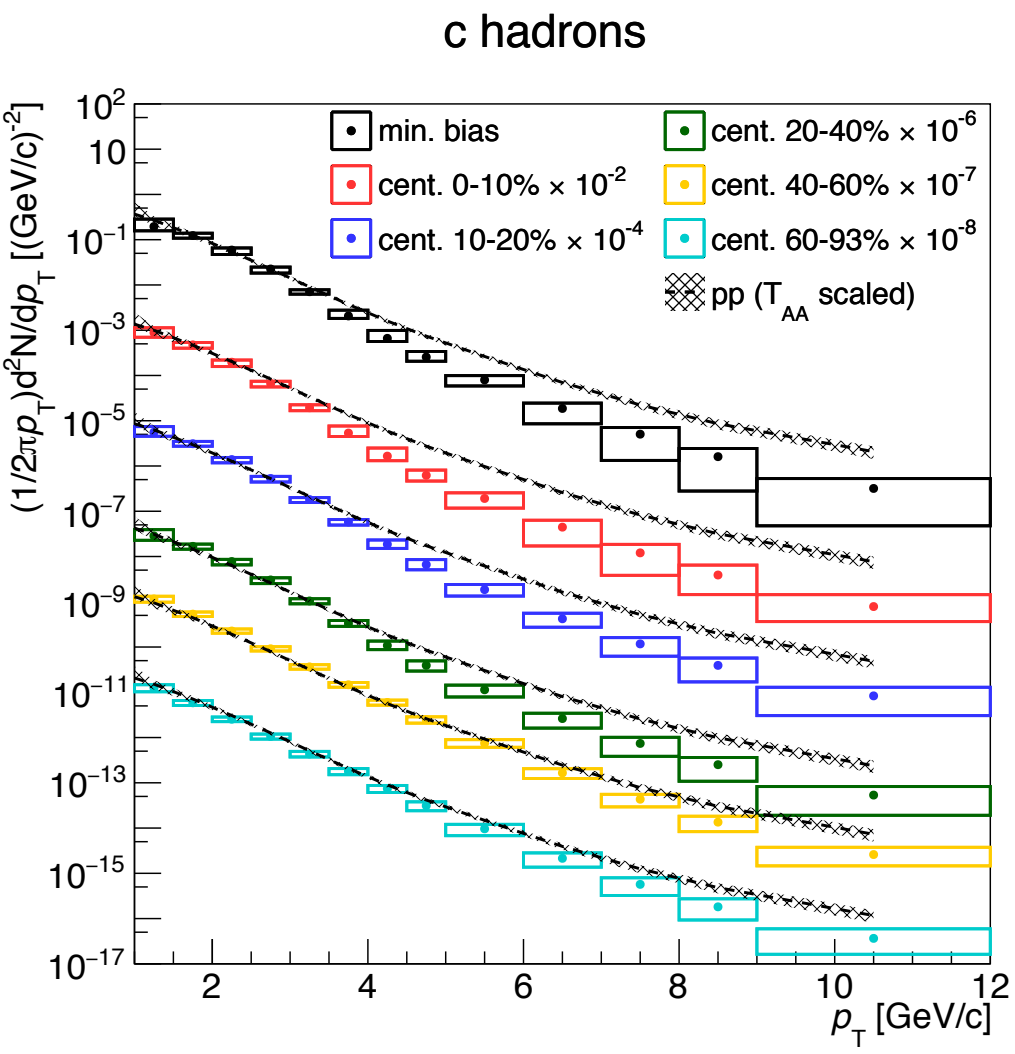

Figure 6.8: The invariant yield of charm hadrons as a function of p_{T} in Au+Au collisions for each centrality, compared to T_{AA} scaled $p + p$ yield.

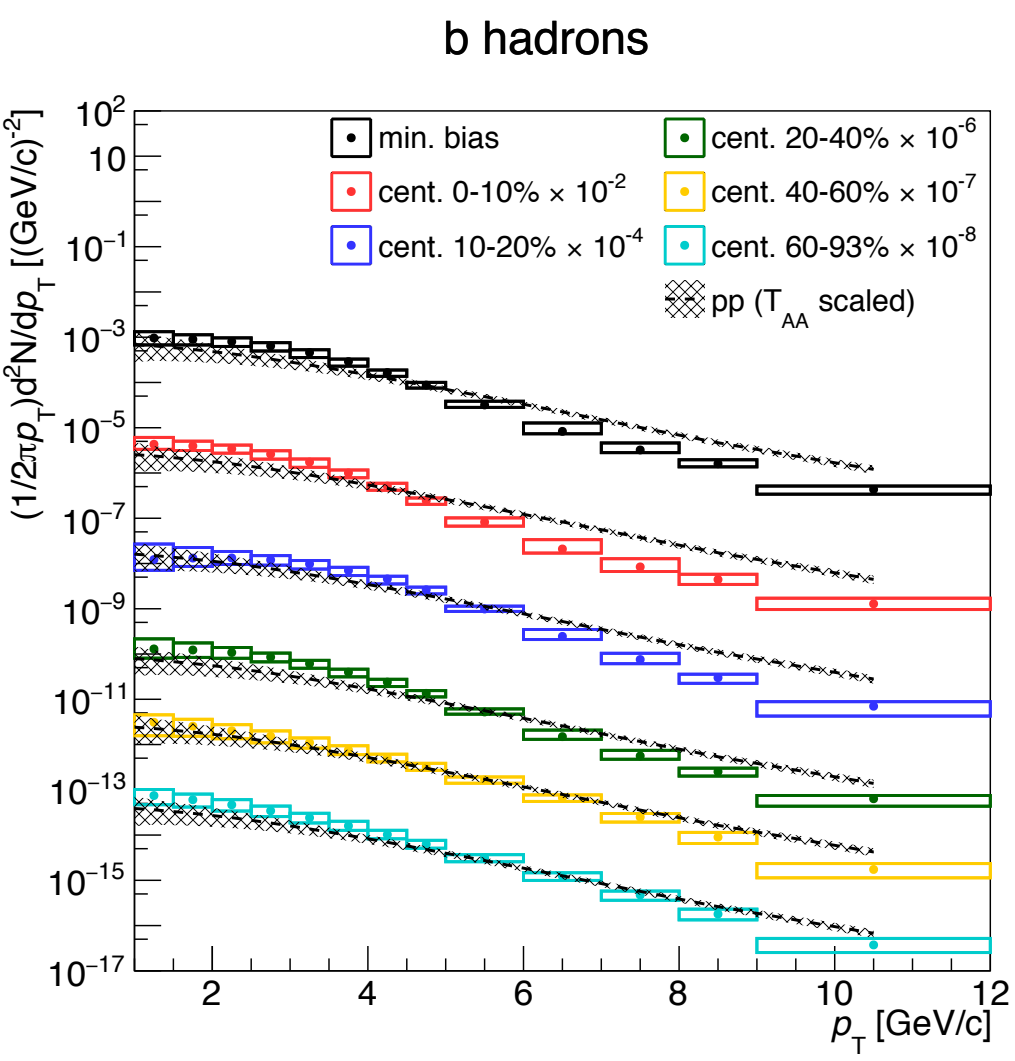

Figure 6.9: The invariant yield of bottom hadrons as a function of p_{T} in Au+Au collisions for each centrality, compared to T_{AA} scaled $p + p$ yield.

Chapter 7

Discussion

7.1 Nuclear modification factor

In order to better understand the yield suppression petters in Au+Au collisions, the nuclear modification factor $R_{\rm AA}$, a ratio of the invariant yield in Au+Au to $N_{\rm coll}$ scaled yield in $p + p$, is calculated as

$$R_{\rm AA} = \frac{dN_{\rm AA}/dp_{\rm T}}{T_{\rm AA} \times \sigma_{pp}/dp_{\rm T}} = \frac{dN_{\rm AA}/dp_{\rm T}}{< N_{\rm coll} > \times dN_{pp}/dp_{\rm T}}, \tag{7.1}$$

where dN_{AA} is the yield in Au+Au and $< N_{coll} > \times dN_{pp}$ is the yield scaled by the number of nuclear collisions in $p + p$. If there is no nuclear modification such as the energy loss in the QGP and Cold-Nuclear-Matter effect, $R_{\rm AA}$ should be unity. In short, $N_{\rm coll}$ scaled yield in $p + p$ collisions can describe a yield in Au+Au collisions except for the nuclear modification. Fig. 7.3 (top panel) shows $R_{\rm AA}$ of $c \rightarrow e$ and $b \rightarrow e$ as a function of $p_{\rm T}$ and indicates the $p_{\rm T}$ dependent yield suppression for both charm and bottom quark. It shows that $R_{\rm AA}$ of $b \rightarrow e$ is systematically higher than $R_{\rm AA}$ of $c \rightarrow e$ for high $p_{\rm T}$. Therefore, the strength of yield suppression shows quark mass dependence, ${R_{\rm AA}}^{b\rightarrow e} > {R_{\rm AA}}^{c\rightarrow e}$. $c \rightarrow e$ starts to be suppressed for $p_{\rm T} > 1$ GeV/c, on the other hand, $b \rightarrow e$ starts to be suppressed for $p_{\rm T} > 4$ GeV/c. It suggests that quarks hardly lose energy in case of $p_{\rm T} < m_q$. To calculate the significance of the difference between $R_{\rm AA}$ of $b \rightarrow e$ and $R_{\rm AA}$ of $c \rightarrow e$, the double ratio of $R_{\rm AA}$ is calculated with cancelation of the correlated uncertainty between $c \rightarrow e$ and $b \rightarrow e$ yields as shown in Fig. 7.3 (bottom panel). The double ratio shows that 1σ significance and over for ${R_{\rm AA}}^{b\rightarrow e} > {R_{\rm AA}}^{c\rightarrow e}$ in central Au+Au collisions. It indicates that the quark mass dependence of the energy loss in the QGP.

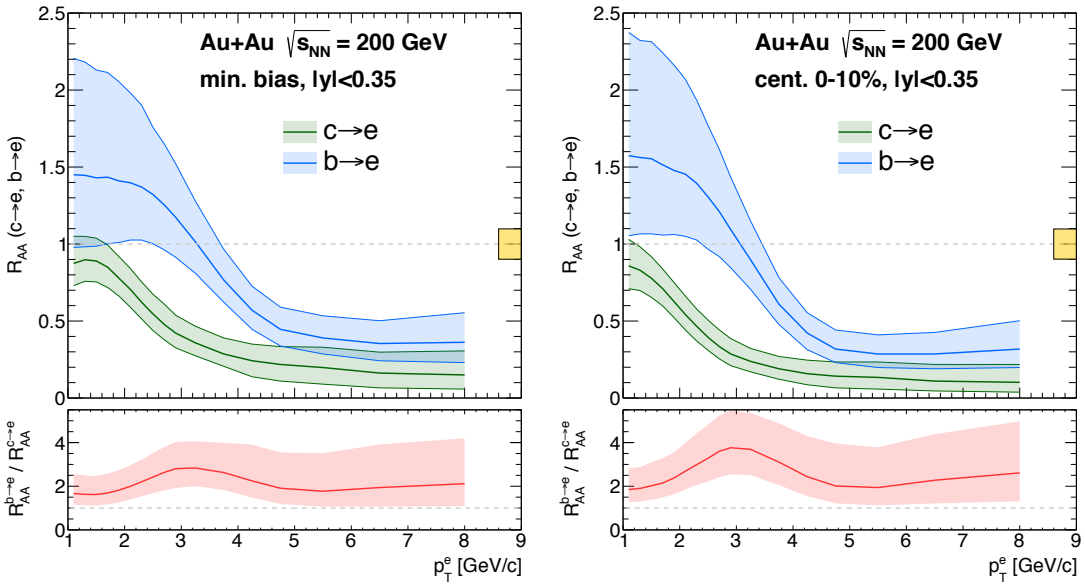

Figure 7.1: Nuclear modification factor of charm and bottom hadron decay electrons as a function of p_{T} in minimum bias (left) and 0-10% centrality (right).

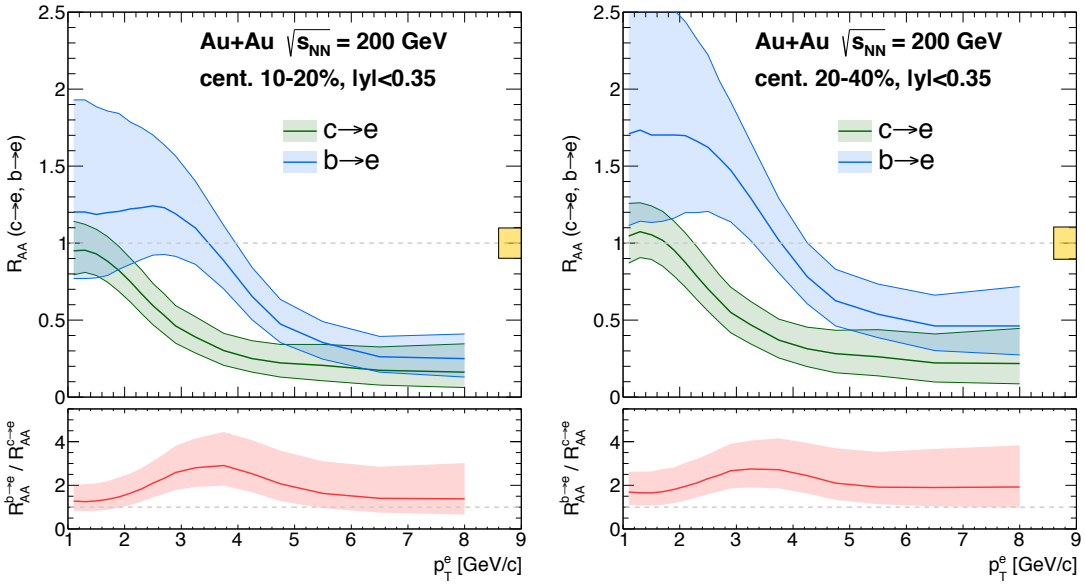

Figure 7.2: Nuclear modification factor of charm and bottom hadron decay electrons as a function of p_{T} in 10-20% centrality (left) and 20-40% centrality (right).

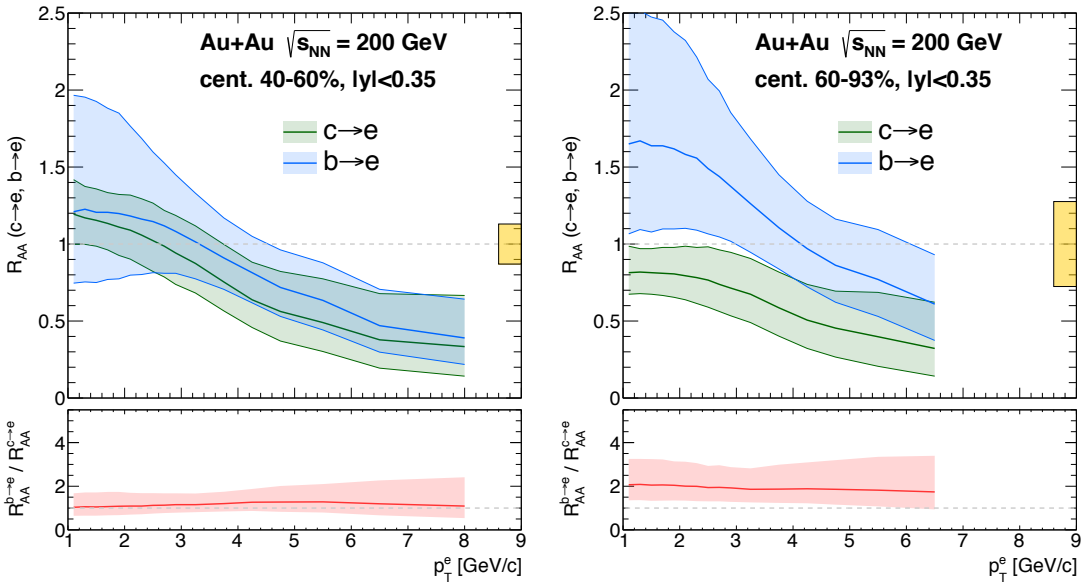

Figure 7.3: Nuclear modification factor of charm and bottom hadron decay electrons as a function of p_{T} in 40-60% centrality (left) and 60-93% centrality (right).

However, R_{AA} of $c \rightarrow e$ and $b \rightarrow e$ is smeared due to the decay kinematics and the parent hadron momentum cannot be known. Therefore, R_{AA} of parent charm and bottom hadrons are also calculated with the unfolded yield of charm and bottom hadrons as shown in Fig. 7.6. It shows the obvious difference of the suppression pattern between charm and bottom hadrons similar to that in the decay electron space, namely $R_{\mathrm{AA}}{}^{\mathrm{b}} > R_{\mathrm{AA}}{}^{\mathrm{c}}$ for $2 < p_{\mathrm{T}} < 7$ GeV/c. These results indicate that R_{AA} of bottom quark is higher than R_{AA} of charm quark in central collisions, strongly indicating the quark mass dependent energy loss in the QGP, $\Delta E_{\mathrm{c}} > \Delta E_{\mathrm{b}}$.

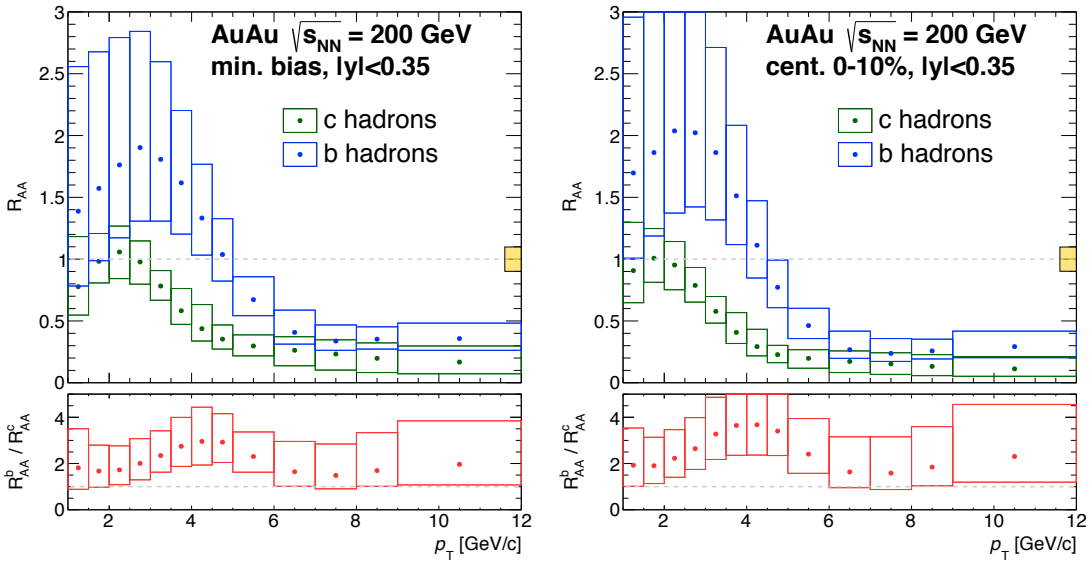

Figure 7.4: Nuclear modification factor of charm and bottom hadron decay electrons as a function of p_{T} in minimum bias (left) and 0-10% centrality (right).

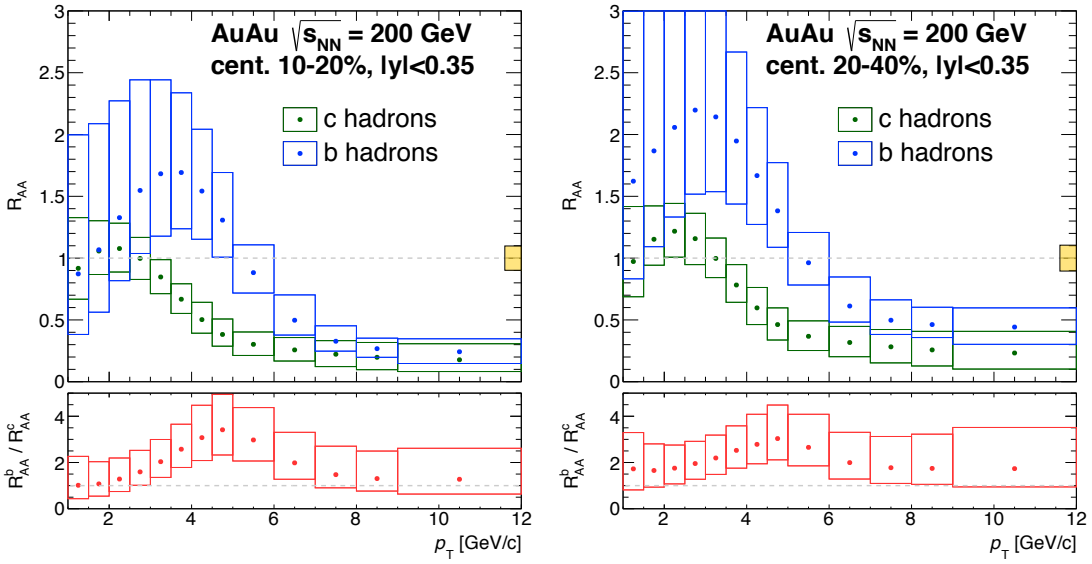

Figure 7.5: Nuclear modification factor of charm and bottom hadron decay electrons as a function of p_{T} in 10-20% centrality (left) and 20-40% centrality (right).

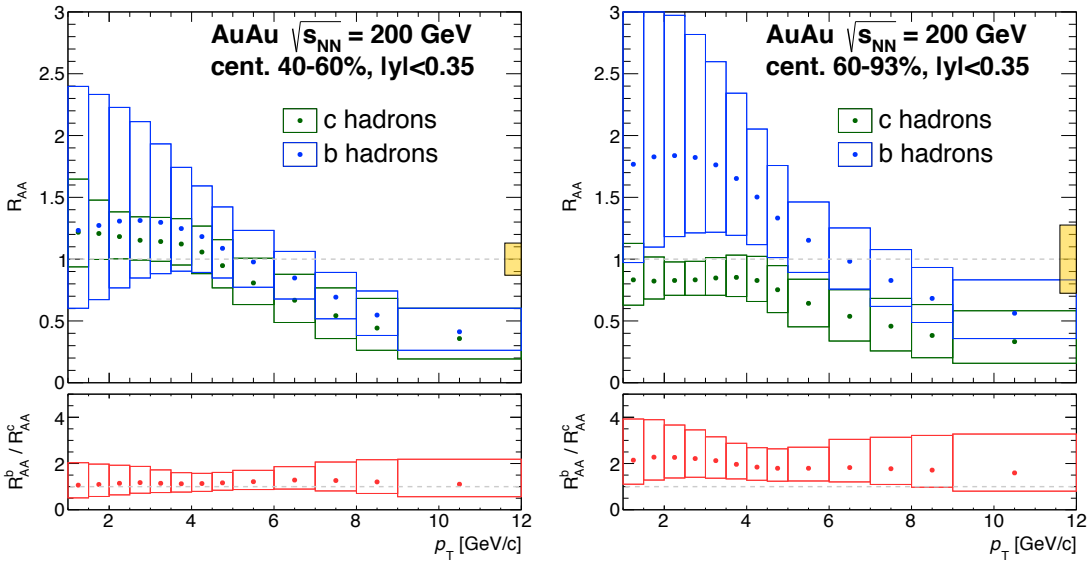

Figure 7.6: Nuclear modification factor of charm and bottom hadron decay electrons as a function of p_{T} in 40-60% centrality (left) and 60-93% centrality (right).

For the systematic study of the yield suppression, R_{AA} of $c \rightarrow e$ and $b \rightarrow e$ as a function of number of nuclear participant, N_{part} ($\sim$ the QGP medium size) is also calculated as shown in Fig. 7.7. R_{AA} of $c \rightarrow e$ and $b \rightarrow e$ is divided to 3 p_{T} ranges, 1-1.4 GeV/c, 2.6-3 GeV/c, and 5-7 GeV/c. In low p_{T} region (1-1.4 GeV/c), there is no N_{part} dependence and no suppression for both $c \rightarrow e$ and $b \rightarrow e$. In mid p_{T} region (2.6-3 GeV/c), the obvious difference of the suppression pattern between $c \rightarrow e$ and $b \rightarrow e$ can be seen, namely no suppression for $b \rightarrow e$ and the N_{part} dependent suppression for $c \rightarrow e$. In high p_{T} region (5-7 GeV/c), both R_{AA} of $c \rightarrow e$ and $b \rightarrow e$ show the similar N_{part} dependent suppression. But it show systematically smaller suppression of $b \rightarrow e$ than $c \rightarrow e$. The N_{part} dependent suppression suggests that the energy loss depends on the path length in the QGP.

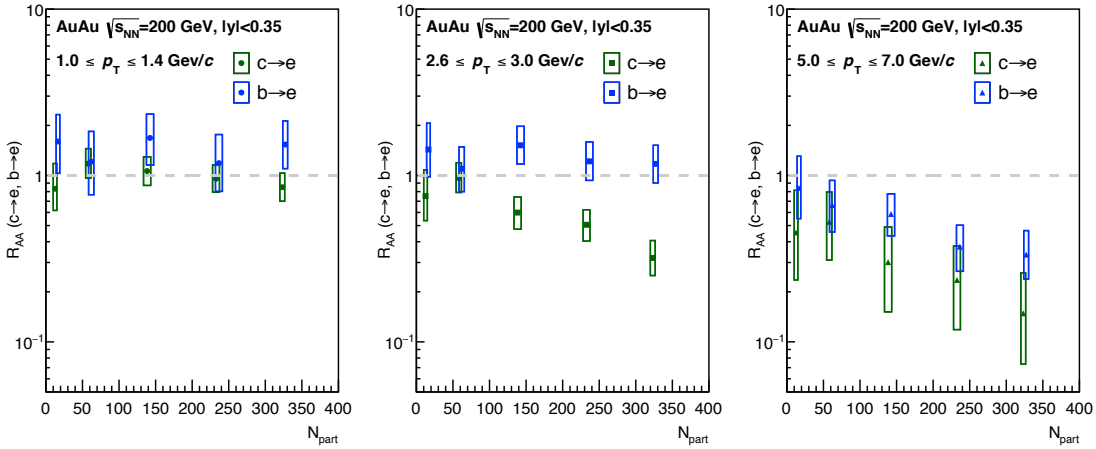

Figure 7.7: Nuclear modification factor of charm and bottom hadron decay electrons as a function of $N_{\rm part}$.

7.2 Fraction of Momentum Loss

The nuclear modification factor $R_{\rm AA}$ is the famous measured variable in high-energy heavy ion collisions. However, it indicates only the yield suppression which depends on not only the energy loss but also a shape of $p_{\rm T}$ spectrum for each hadron species. In order to directly understand the average fractional energy loss, we calculate the fractional momentum loss $\rm S_{loss}$ by

$$S_{loss} = \delta p_T / p_T = \frac{p_T^{pp} - p_T^{AuAu}}{p_T^{pp}}, \tag{7.2}$$

where $p_T^{\rm AuAu}$ is the $p_{\rm T}$ in Au+Au measurement and p_T^{pp} is that in $p+p$ measurement scaled by $T_{\rm AA}$ $(N_{\rm coll}/\mathcal{L}^{pp})$ at the same yield in Au+Au measurement. Fig. 7.8 shows an illustration of $\delta p_{\rm T}$ calculation.

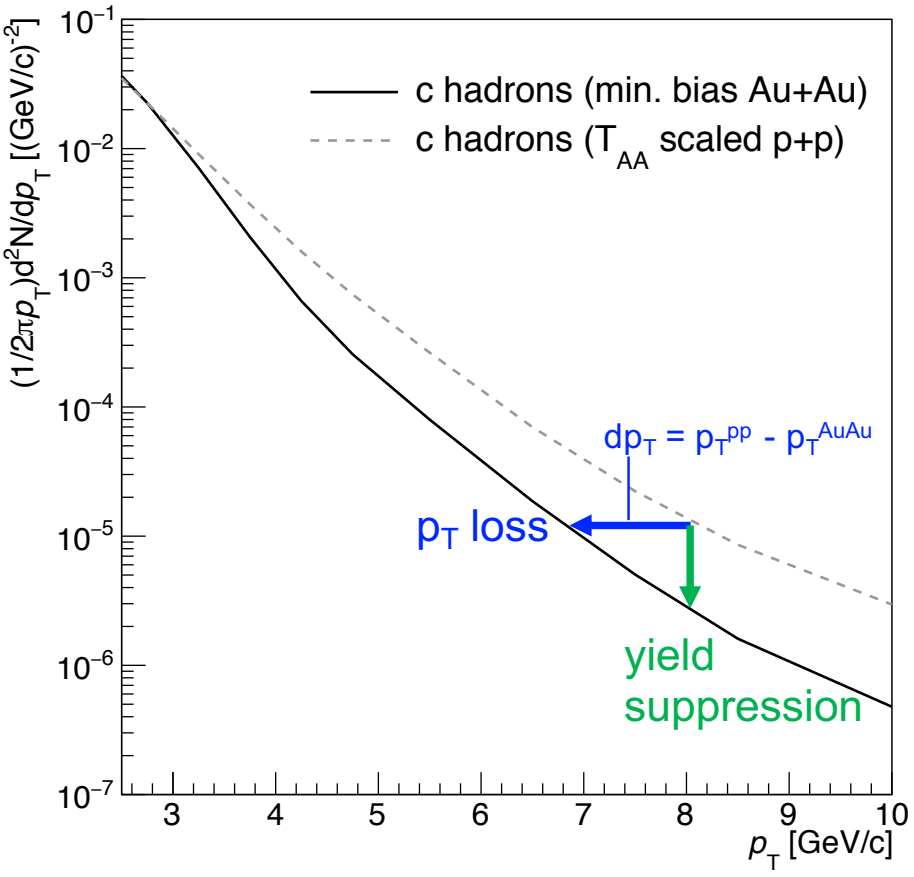

Figure 7.8: The illustration of δp_{T} calculation between yields in Au+Au and T_{AA} scaled yields in $p + p$.

$\mathrm{S_{loss}}$ is calculated as a function of the initial momentum of heavy-quark, p_T^{pp} [66]. In this analysis, we assume that the p_{T} spectrum in Au+Au is modified by only the energy loss. However, we have measured other modification effects, such as the radial flow of the QGP [6] and the baryon enhancement [60]. $\mathrm{S_{loss}}$ calculation performs for 6 GeV/c < p_{T} because their effects are considered to be very small at high p_{T}. Fig. 7.11 shows $\mathrm{S_{loss}}$ of charm and bottom hadrons as a function of the initial heavy-quark p_{T}.

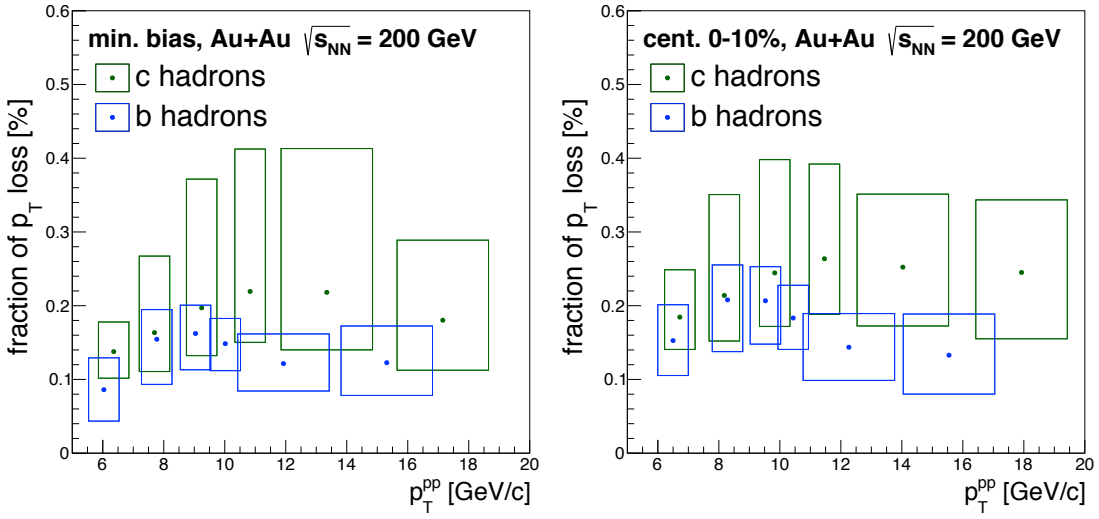

Figure 7.9: S_{loss} of charm and bottom hadrons as a function of the initial hadron p_T in minimum bias (left) and 0-10% centrality (right).

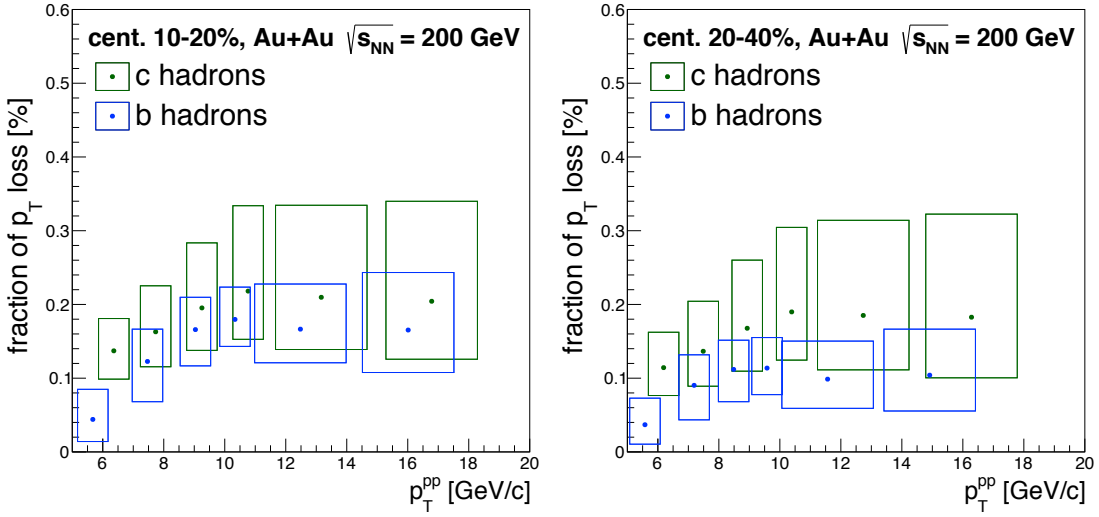

Figure 7.10: S_{loss} of charm and bottom hadrons as a function of the initial hadron p_T in 10-20% centrality (left) and 20-40% centrality (right).

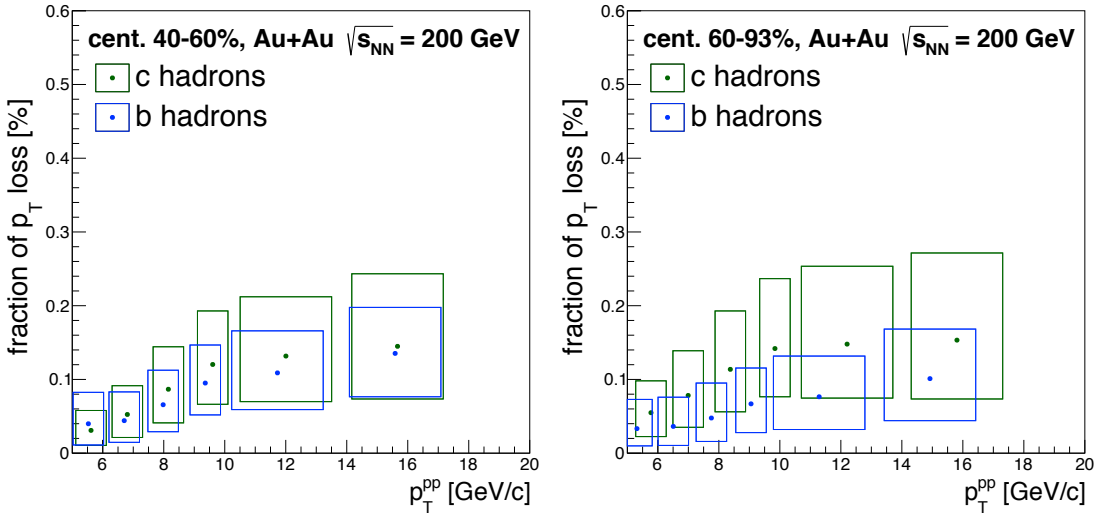

Figure 7.11: S_{loss} of charm and bottom hadrons as a function of the initial hadron p_T in 40-60% centrality (left) and 60-93% centrality (right).

In minimum bias Au+Au collisions, charm (bottom) quark loses ∼20% (∼15%) momentum in the QGP. The fractional momentum loss S_{loss} can be regarded as the fractional energy loss $\delta E/E$, if momentum is sufficiently larger than a quark mass. Measured S_{loss} factors of charm and bottom hadrons are consistent within the large uncertainty at high p_T. However, the measured S_{loss} of bottom hadrons is systematically smaller than that of charm hadrons in central Au+Au collisions, implying the quark mass dependent energy loss in the QGP, $\Delta E_c > \Delta E_b$. Both S_{loss} value decrease with increasing the centrality, indicating the dependence of path length in the QGP of the energy loss.

7.3 Comparison of charm hadrons R_{AA} to D^0 R_{AA}

The STAR experiment has measured the R_{AA} for D^0 meson as a function of p_T in Au+Au collisions at $\sqrt{s_{NN}}$ = 200 GeV [75] which is expected to be similar suppression pattern as our charm hadrons R_{AA}. We compare these measured R_{AA} in 3 centrality classes as shown in Fig. 7.12.

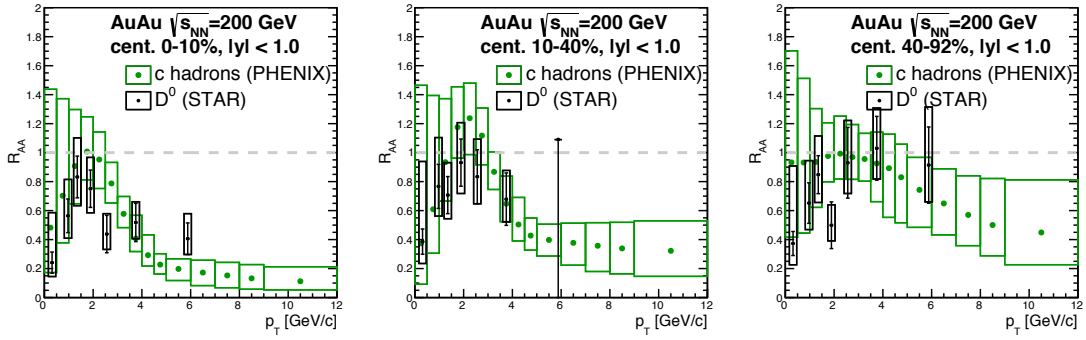

Figure 7.12: The comparison of $R_{\rm AA}$ between PHENIX charm hadrons measurement and STAR $\rm D^0$ measurement [75] as a function of $p_{\rm T}$ for each centrality class.

It should be noted that our unfolding procedure generates charm and bottom hadrons in all rapidity range and selects decay electrons in $|y| < 0.35$ to compare measured the data in the same rapidity region. On the other words, PHENIX D meson measurement performs for all rapidity region. On the other hand, the STAR measurement is the direct reconstruction of $\rm D^0$ meson and performs for $|\eta| < 1.0$. These measured $R_{\rm AA}$ are consistent within the large uncertainty and the similar suppression pattern can be seen in all centrality classes, but the PHENIX charm hadrons $R_{\rm AA}$ is likely systematically higher than the STAR $\rm D^0$ $R_{\rm AA}$ at low $p_{\rm T}$ (< 3 GeV/c). It may indicate a small suppression at forward rapidity and the baryon enhancement. Since ultra forward rapidity region ($|\eta| > 4.0$) is not Bjorken expansion region, the energy loss effect from the QGP medium is smaller than that in mid-rapidity regions. In addition, baryon to meson ratio increases in Au+Au collisions because a baryon composed of 3 quarks is easer produced in the QGP. These effects may increase $R_{\rm AA}$ at low $p_{\rm T}$.

7.4 Comparison of $R_{\rm AA}$ and $\rm S_{loss}$ to theoretical models

In order to consider the quark mass dependence of the energy loss in the QGP, we compare the measured $R_{\rm AA}$ in 0-10% centrality with the model predictions as shown in Fig. 7.13. Theoretical models are described as the following.

T-Matrix This model based on Lattice QCD calculations assumes that hadronic resonance of heavy quark survives in high-temperature QGP ($> 2\ T_c$). A heavy quark propagates the QGP medium as a hadron resonance (heavy-light quarks) and loses energy with elastic and inelastic scatterings. Since the formation of the hadron resonance state is non-pertavative process, a Brueckner-type in-medium T-matrix approach is employed for heavy-light quark scatterings [67].

SUBATECH: This model describes collisional energy loss by the linearized Boltzmann transport [68]. A running coupling constant is employed. The Debye

mass is replaced by a more realistic hard thermal loop (HTL) calculation.

DGLV: This model describes the radiative energy loss via gluon emission, which is based on the GLV model [70, 71], the radiative energy loss model of a light quark [69]. This model assumes an effectively static medium and calculates only the radiative energy loss. The effectively static medium is characterized by the gluon density, $dN_g/d\eta = 1000$, and the Debye mass to magnetic mass ratio, $0.4 < \mu_M/\mu_E < 0.6$.

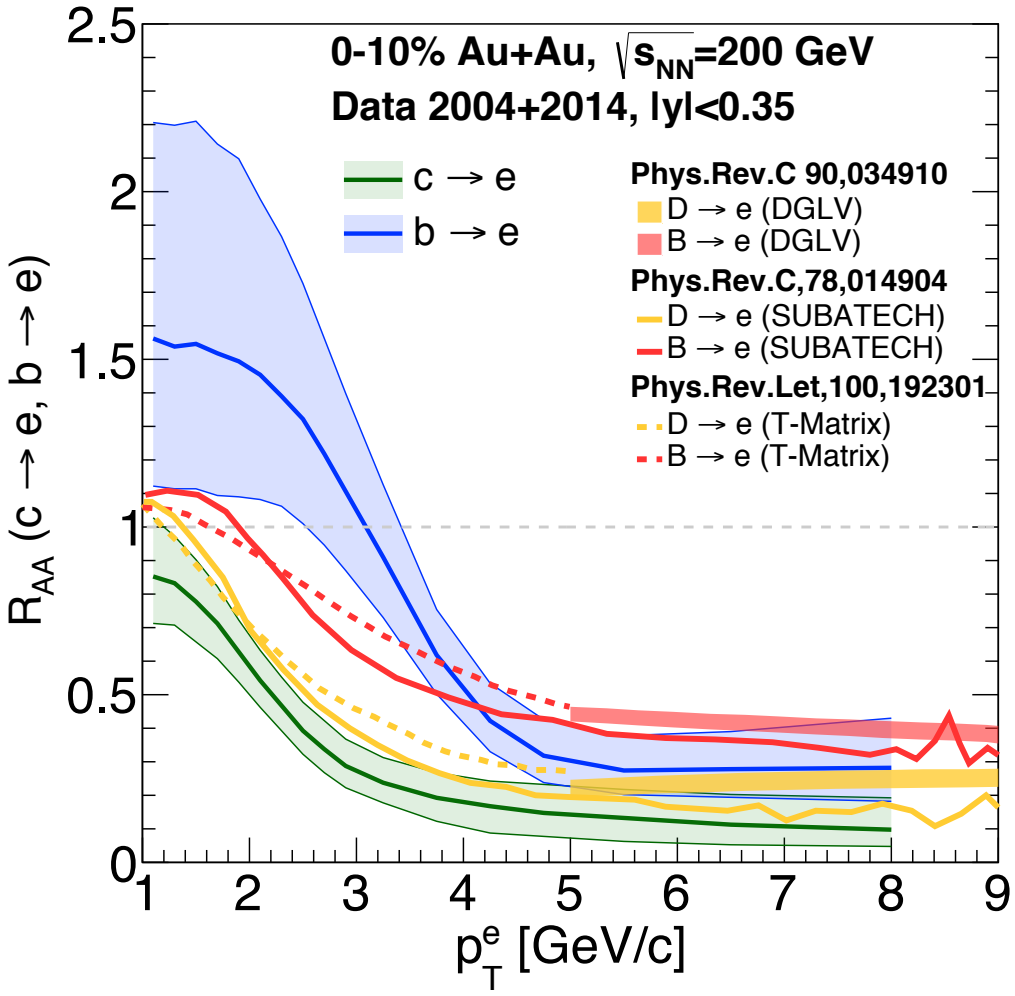

Figure 7.13: The comparison of $R_{\rm AA}$ between PHENIX measurement and theoretical models in 0-10% centrality.

The predicted $R_{\rm AA}$ of $c \rightarrow e$ assuming the initial temperature $T = 350$ MeV and $dN_g/dy = 1000$ is reasonable agreement with the measured $R_{\rm AA}$ of $c \rightarrow e$ for $1.0 < p_{\rm T} < 9$ GeV/c. It indicates that the initial $p_{\rm T}$ spectrum of $c \rightarrow e$ is well described and the energy loss model is reasonable. On the other hand,

the predicted $R_{\rm AA}$ of $b \rightarrow e$ cannot describe well the measured $R_{\rm AA}$ in low $p_{\rm T}$ region (< 4.0 GeV). The initial $p_{\rm T}$ spectrum of $b \rightarrow e$ in theories seems to be not reasonable. Actually, we have found FONLL calculation underestimates the invariant yield of $b \rightarrow e$ by a factor of 2 [72]. Theoretical models need a fine tune for the initial spectrum to understand the physical property of the QGP. In addition, the predicted fractional energy loss as shown in Fig. 1.13 [19] is compared with the measured $\rm S_{loss}$. The predicted fractional energy loss is converted to the fractional momentum loss $\rm S_{loss}$ with $m_c = 1.2$ GeV/c^2 and $m_b = 4.75$ GeV/c^2 ($\alpha_s = 0.3$). Fig. 7.14 shows the comparison of $\rm S_{loss}$ for charm hadrons between the measured data and theoretical models including the collisional and radiative energy loss. The radiative energy loss models describe well for high $p_{\rm T}$. This comparison suggests that the radiative energy loss dominates for $p_{\rm T} > 8$ GeV/c in case of the charm quark energy loss. On the other hand, both collisional and radiative energy loss model for bottom quark underestimates the measured $\rm S_{loss}$ for bottom hadrons as shown in Fig. 7.15. It indicates that both contributions in the bottom quark energy loss are dominated in the measured $p_{\rm T}$ region. Even if the collisional and radiative energy loss is added together, it seems to be slightly less than the measured $\rm S_{loss}$. It suggests that theory needs improvement for the bottom quark sector. Although the measured $R_{\rm AA}$ and $\rm S_{loss}$ agree with the quark mass dependence of the energy loss in the QGP, $\Delta E_{\rm c} > \Delta E_{\rm b}$, it suggests that the difference is smaller than the theoretical prediction.

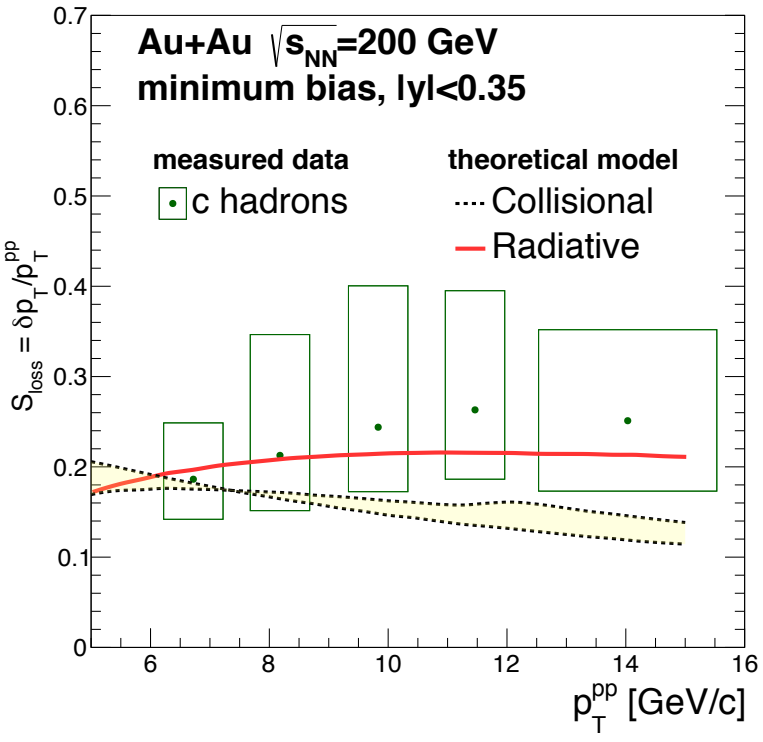

Figure 7.14: The comparison of measured $\rm S_{loss}$ for charm hadrons to models as a function of $p_{\rm T}$.

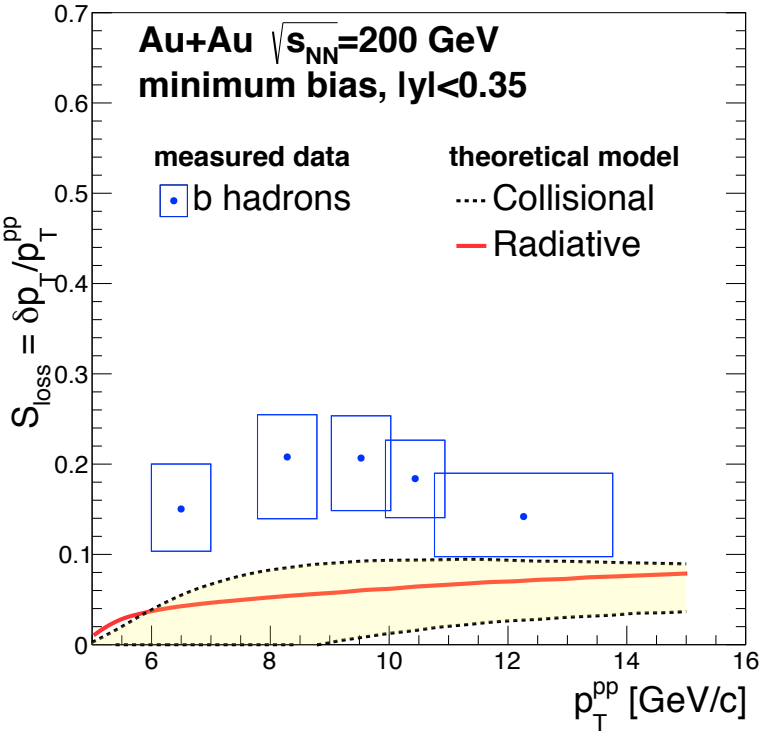

Figure 7.15: The comparison of measured S_{loss} for bottom hadrons to models as a function of p_T.

Chapter 8

Summary and Conclusions

The emergent phenomenon of the strongly coupled QGP has been studied by heavy ion collisions at RHIC and LHC. The energy loss of heavy quarks is the sensitive probe of the QGP dynamics such as a shear viscosity to entropy density ratio η/s. In order to understand the QGP dynamics from the measured data, it is necessary to understand the energy loss mechanism in the QGP and its quark mass dependence. The measurement of separated electrons from charm and bottom hadron decays in Au+Au and $p + p$ collisions at $\sqrt{s_{NN}} = 200$ GeV has been performed for p_{T} range 1-9 GeV/c at mid-rapidity ($|\eta| <0.35$) to understand the quark mass dependence of energy loss in the QGP. The PHENIX silicon vertex (VTX) detector installed in 2011 provides the capability of separation of charm and bottom hadron decay electrons with displaced vertex information, $\mathrm{DCA_T}$ distribution. In 2014, RHIC run Au+Au collisions at $\sqrt{s_{NN}} = 200$ GeV for 13.3 weeks and PHENIX has collected the collision data corresponding to 23.1 nb^{-1} integrated luminosity ($\sim$20 billion events) for the heavy flavor analysis.

PHENIX detectors have the powerful capability of electron identification and thus provides high signal to background ratio on heavy flavor analysis with decay electrons. In addition, the decay electron channel is the high-branching ratio, D$\rightarrow$e and B$\rightarrow$e = $\sim$10%. Therefore, heavy quark decay electrons dominate in electron tracks. The main background, photonic electrons, is tagged by the isolation method with VTX. The relative ratio of other backgrounds are estimated by the PHENIX electron cocktail and non-electrons are subtracted by the track swapping method. The invariant yield of $c + b \rightarrow e$ is calculated by the relative ratio and estimated invariant yield of photonic electrons by the PHENIX electron cocktail.

In order to separate charm and bottom hadron decay electrons, the displaced vertex analysis using $\mathrm{DCA_T}$ distributions of decay electrons has been performed. However, $\mathrm{DCA_T}$ distributions of $c \rightarrow e$ and $b \rightarrow e$ depend on unmeasured p_{T} distributions of parent charm and bottom hadrons, which is an unfolding problem. Bayesian inference technique has been employed to solve this unfolding problem. Our unfolding procedure samples the invariant yield of parent charm and bottom hadrons while fitting expected decay electron p_{T} and $\mathrm{DCA_T}$ distributions to the measured distributions. In this analysis, Markov chain Monte-Carlo (MCMC) is employed to obtain the probability distribution of parent charm and bottom hadron yields. Finally, the invariant yield of charm and bottom hadron and also

decay electrons ($c \rightarrow e$ and $b \rightarrow e$) have been measured in Au+Au collisions for each centrality and $p + p$ collisions.

The nuclear modification factors $R_{\rm AA}$ of separated electrons from charm and bottom hadron decays have been calculated by the invariant yield in Au+Au and the $N_{\rm coll}$ scaled yield in $p + p$. The measured $R_{\rm AA}$ shows the centrality dependence of the yield suppression for both $c \rightarrow e$ and $b \rightarrow e$, which indicates the QGP medium size dependence of the energy loss. The comparison between $R_{\rm AA}$ of $c \rightarrow e$ and $b \rightarrow e$ indicates that yield suppression of bottom quarks is less than that of charm quarks. This suppression order is also seen in $R_{\rm AA}$ of parent charm and bottom hadrons. These results indirectly indicate that energy loss of bottom quark is less than that of charm quark. In addition, the fractional momentum loss $\rm S_{loss}$ has been also calculated in order to directly understand the fractional energy loss of charm and bottom quarks. $\rm S_{loss}$ measurement has been performed in parent hadron space because momentum loss of charm and bottom hadrons can be regarded as energy loss of charm and bottom quark in case of high-$p_{\rm T}$ region, $m << p_{\rm T}$. Measured $\rm S_{loss}$ factors of charm and bottom hadrons are consistent within the large uncertainty, but $\rm S_{loss}$ of bottom hadron is systematically smaller than that of charm hadron in all centralities. Note that our unfolding procedure independently performs for each centrality. The difference of $\rm S_{loss}$ between charm and bottom hadrons more directly suggests the quark mass dependence of the energy loss in the QGP, $\Delta E_{\rm c} > \Delta E_{\rm b}$.

The model comparison provides the understanding of the heavy-quark dynamics in the QGP. The measured $R_{\rm AA}$ and $\rm S_{loss}$ were compared with several theoretical models. One model, DGLV, assuming $T = 350$ MeV and $\rm dN_{\it g}/d\eta = 1000$ describe well the measured $R_{\rm AA}$ of $c \rightarrow e$ and $\rm S_{loss}$ of charm hadrons. In addition, the radiative energy loss model well describes the measured $\rm S_{loss}$ of charm hadrons, which indicates the dominant contribution of the radiative energy loss at high $p_{\rm T}$ (> 8 GeV/c). However, DGLV model does not describe $R_{\rm AA}$ and $\rm S_{loss}$ for $b \rightarrow e$ and bottom hadrons. Models may need fine-tuning to reproduce the measured data. After the improvement of models, the measured $R_{\rm AA}$ and $\rm S_{loss}$ will be compared for each centrality to better understand the energy loss mechanism and the QGP dynamics finally.

Bibliography

[1] David J. Gross and Frank Wilczek, Phys. Rev. Lett. **30**, 1343-1346 (1973).

[2] H. David Politzer, Phys. Rev. Lett. **30**, 1346-1349 (1973).

[3] J. C. Collins and M. J. Perry, Phys. Rev. Lett. **34**, 1353 (1975).

[4] Cabibbo, Nicola, Parisi, Giorgio, Phys. Lett. **B**, 59 (1975).

[5] K. Adcox, *et al.* (PHENIX Collaboration), Nucl. Phys. **A757**, 184 (2005).

[6] I. Arsene, *et al.* (STAR Collaboration), Nucl. Phys. **A757**, 1 (2005).

[7] B. B. Back, *et al.*, Nucl. Phys. **A757**, 28 (2005).

[8] J. Adams, *et al.*, Nucl. Phys. **A757**, 102 (2005).

[9] Y. L. Dokshitzer and D. E. Kharzeev, Phys. Lett. B **519**, 199 (2001).

[10] A. Adare *et al.* (PHENIX Collaboration), Phys. Rev. Lett. **98**, 172301 (2007).

[11] A. Adare *et al.* (PHENIX Collaboration), Phys. Rev. C **93**, 034904 (2016).

[12] K. Nagashima, for the PHENIX Collaboration, Nucl. Phys. A **967**, 644 (2017).

[13] (Particle Data Group), Phys. Rev. D45, 1 (1992).

[14] The evidence of three colors for quarks, http://hyperphysics.phy-astr.gsu.edu/hbase/Particles/qevid.html.

[15] L3 Collaboration, Phys. Lett. B **623**, 26-36 (2005).

[16] K. Hagiwara *et al.* (Particle Data Group), Phys. Rev. D **66**, 010001 (2018).

[17] Gunnar S. Bali, Phys. Rept. **343**, 1-136 (2001).

[18] Szabolcs Borsanyi, *et al.*, JHEP **1011**, (2010) 077.

[19] Simon Wicks, *et al.*, Nucl. Phys. **A784** (2007) 426-442.

[20] J.D. Bjorken, Phys. Rev. **D27**, 140-151 (1983).

[21] M.H. Thoma, M. Gyulassy, Nucl. Phys. **B** 351 (1991) 491.

[22] E. Braaten, M.H. Thoma, Phys. Rev. **D** 44 (1991) 1298.

[23] Magdalena Djordjevic, Miklos Gyulassy, Nucl. Phys. **A733** (2004) 265-298.

[24] (Particle Data Group), Chin. Phys. C, **38**, 090001 (2014).

[25] P. W. Higgs, "Broken symmetries, massless particles and gauge fields", Phys. Lett. **12** (1964) 132.

[26] P. W. Higgs, "Broken Symmetries and the Masses of Gauge Bosons", Phys. Rev. Lett. **13** (1964) 508.

[27] F. Englert and R. Brout, "Broken Symmetry and the Mass of Gauge Vector Mesons", Phys. Rev. Lett. **13** (1964) 321.

[28] ATLAS Collaboration, "Observation of a new particle in the search for the Standard Model Higgs boson with the ATLAS detector at the LHC", Phys. Lett. **B716** (2012) 1-29.

[29] CMS Collaboration, "Observation of a new boson at a mass of 125 GeV with the CMS experiment at the LHC", Phys. Lett. **B716** (2012) 30-61.

[30] Y. Nambu and G. Jona-Lasinio, Phys. Rev. **122** (1961) 345.

[31] Y. Nambu and G. Jona-Lasinio, Phys. Rev. **124** (1961) 246.

[32] T. Hatsuda and T. Kunihiro, "QCD Phenomenology based on a Chiral Effective Lagrangian", Phys. Rept. **247** (1994) 221-367.

[33] P. Kovtun, D. T. Son and A. O. Starinets, "Viscosity in Strongly Interacting Quantum Field Theories from Black Hole Physics", Phys. Rev. Lett. **94** (2005) 111601.

[34] Tribble R (chair), Burrows A, *et al.*, 2013 Implementing the 2007 Long Range Plan, Report to the Nuclear Science Advisory Committee, (http://science.energy.gov/np/nsac/reports/).

[35] M. Asakawa and K. Yazaki, "Chiral Restoration at Finite Density and Temperature", Nucl. Phys. **A504** (1989) 668-684.

[36] Edmond Iancu, Andrei Leonidov and Larry D. McLerran, "Nonlinear gluon evolution in the color glass condensate. 1.", Nucl. Phys. **A692** (2001) 583-645.

[37] Barbara V. Jacak, Berndt Muller, "The Exploration of Hot Nuclear Matter", Science **337** 6092 (2012) 310-314.

[38] https://www.bnl.gov/rhic/physics.asp

[39] https://www.phenix.bnl.gov

[40] http://www.hepl.hiroshima-u.ac.jp/phx/bnl/bnl.html

[41] A. Adare *et al.* (PHENIX Collaboration), Phys. Rev. Lett. **109**, 242301 (2012) .

[42] M. Aggarwal *et al.* (STAR Collaboration), Measurement of the Bottom contribution to non-photonic electron production in $p + p$ collisions at $\sqrt{s_{NN}}$ =200 GeV, Phys. Rev. Lett. **105** (2010) 202301.

[43] K. Adocox *et al.* (PHENIX Collaboration), Nucl. Instr. Method A **499**, (2003) 469-479.

[44] S.H. Aronson *et al.* (PHENIX Collaboration), Nucl. Instr. Method A **499**, (2003) 480-488.

[45] K. Adocox *et al.* (PHENIX Collaboration), Nucl. Instr. Method A **499**, (2003) 489-507.

[46] M. Aizawa *et al.* (PHENIX Collaboration), Nucl. Instr. Method A **499**, (2003) 508-520.

[47] L. Aphecetche *et al.* (PHENIX Collaboration), Nucl. Instr. Method A **499**, (2003) 521-536.

[48] M. Allen *et al.* (PHENIX Collaboration), Nucl. Instr. Method A **499**, (2003) 549-559.

[49] Y. Akiba *et al.* (PHENIX Collaboration), Nucl. Instr. Methods A **433**, 143 (1999).

[50] M. Baker *et al.* Proposal for a Silicon Vertex Tracker (VTX) for the PHENIX Experiment. BNL internal report 72204.

[51] Y. Onuki *et al.*, Assembly procedure for the silicon pixel ladder for PHENIX silicon vertex tracker. Nucl. Instrum. Meth. A **606**, 395-403 (2009).

[52] W. Snoeys *et al.*, Pixel readout chips in deep submicron CMOS for ALICE and LHCb tolerant to 10 Mrad and beyond, Nucl. Instrum. Methods Phys. Res. Sec. A **466**, 366 (2001).

[53] R. Ichimiya *et al.* (PHENIX Collaboration), Status and overview of development of the Silicon Pixel Detector for the PHENIX experiment at the BNL RHIC, J. Inst. **4**, P05001 (2009).

[54] Ernest D. Courant, M. Stanley Livingston, and Hartland S. Snyder, "The Strong-Focusing Synchroton - A New High Energy Accelerator", Phys. Rev. **88**, 1190 (1952)

[55] S.S. Adler *et al.* (PHENIX Collaboration), Nucl. Instr. Method A **499**, (2003) 560-592.

[56] H. Hahn *et al.*, Nucl. Instr. Method A **499**, (2003) 245-263.

[57] G. Robert-Demolaize *et al.*, "RHIC performance for FY2014 heavy ion run", Proceedigns of the International Particle Accelerator Conference 2014, Dresden, Germany, pp. 1090-1093.

[58] J. T. Michell, PHENIX Technical Notes, **384**.

[59] P. Staszel for the BRAHMS Collaboration, Recent results from the BRAHMS experiment, Nucl. Phys. A **774**, 77 (2006).

[60] Guannan Xie for the STAR Collaboration, Nucl. Phys. A **967**, 928 (2017).

[61] P. R. Sorensen and X. Dong, Suppression of nonphotonic electrons from enhancement of charm baryons in heavy ion collisions, Phys. Rev. C **74**, 024902 (2006).

[62] J. Goodman and J. Weare, Ensemble samplers with affine invariance, Commun. Appl. Math. Comp. Sci. **5**, 65 (2010).

[63] D. Foreman-Mackey, D. W. Hogg, D. Lang, and J. Goodman, emcee: The MCMC Hammer, Publ. Astron. Soc. Pac. **125**, 306 (2013).

[64] A. M. Adare, M. P. McCumber, James L. Nagle, and P. Ro- matschke, Phys. Rev. C **90**, 024911 (2014).

[65] PYTHIA-6.2 with CTEQ5L, MSEL = 5, MSTP(91) = 1, PARP(91) = 1.5, MSTP(33) = 1, PARP(31) = 2.5. For bottom (charm) hadron studies, PARJ(13) = 0.75 (0.63), PARJ(2) = 0.29 (0.2), PARJ(1) = 0.35 (0.15).

[66] A. Adare *et al.* (PHENIX Collaboration), Phys. Rev. C **93**, 024911 (2016).

[67] H. van Hees, M. Mannarelli, V. Greco, and R. Rapp, Phys. Rev. Lett **100**, 192301.

[68] P. B. Gossiaux and J. Aichelin, Phys. Rev. C **78**, 014904.

[69] Magdalena Djordjevic and Marko Djordjevic, Phys. Rev. C **90**, 034910.

[70] M. Gyulassy, P. Levai and I. Vitev, Nucl. Phys. B **594**, 371 (2001).

[71] A. Buzzatti and M. Gyulassy, Phys. Rev. Lett. **108**, 022301 (2012).

[72] C. Aidala, arXiv: **1901.08405**.

[73] A. Adare *et al.* (PHENIX collaboration), Phys. Rev. C **92**, 034913 (2015).

[74] V. Khachatryan *et al.* (CMS collaboration), Eur. Phys. J. **C77**, 252 (2017).

[75] L. Adamczyk *et al.* (STAR Collaboration), Phys. Rev. Lett. **121**, 229901 (2018).

Acknowledgement

First and foremost, I would like to thank my supervisor Prof. K. Shigaki who led me to complete the doctoral program and taught me how to enjoy study and life. I would like to give heartful thanks to Dr. Y. Akiba who introduced me to the heavy flavor analysis and provided carefully considered feedback and valuable comments. I learned from him the importance of finding essence and the significance of experimental science. I think that these will be my wealth for the future. I would also like to thank Assistant Prof. T. Hachiya whose opinions and information have helped me very much throughout the production of this study.

My heartfelt appreciation goes to Dr. H. En'yo. Without his financial support, this work would not have been completed. This work was also supported by JSPS KAKENHI 16J04004. Many thanks to Prof. S. Esumi who managed U.S.-Japan Science and Technology Cooperation Program in High Energy Physics and supported my BNL stays.

Thanks to Prof. T. Sugitate for valuable comments and preparing a comfortable research environment. Many thanks to Dr. K. Homma for the guidance on experiment method and detector operation. Through discussions on physical phenomena with him, I became able to survey science in a wide perspective. Thanks to Quark Physics Laboratory group at Hiroshima University. Especially, I would like to express Dr. S. Yano, Dr. D. Sekihata, Ms. R. Tanizaki, Mr. Y. Ueda, Mr. K. Yamakawa for valuable discussions, corporations and a fun research environment.

I must acknowledge PHENIX collaborators. Thanks to Dr. M. Chiu, Dr. C. Pinkenburg, Dr. D. McGlinchey, Prof. J. Nagle, Dr. T. Sakaguchi, Dr. T. Rinn, Dr. J. D. Orjuela Koop, Dr. B. Johnson, Dr. D. Jouan, Prof. R. Nouicer, Prof. M. Rosati, Prof. S. Bathe for your guidance and corporation in the experiment and analysis.

Lastly, I am sincerely thankful to my family for continuing to send us a warm encouragement.

Appendix A

Selected Run Number

407178, 407197, 407198, 407199, 407200, 407270, 407271, 407272, 407369, 407370, 407371, 407372, 407376, 407377, 407378, 407379, 407380, 407381, 407454, 407455, 407456, 407457, 407526, 407608, 407610, 407611, 407614, 407618, 407620, 407621, 407661, 407662, 407664, 407666, 407669, 407670, 407671, 407672, 407673, 407676, 407786, 407792, 407796, 407797, 407798, 407799, 407800, 407802, 407842, 407945, 407946, 407947, 407948, 407950, 407951, 407953, 407959, 407960, 407963, 407964, 407965, 407966, 408070, 408071, 408073, 408074, 408075, 408076, 408077, 408078, 408175, 408176, 408177, 408181, 408182, 408183, 408184, 408218, 408219, 408220, 408224, 408225, 408227, 408321, 408322, 408323, 408324, 408325, 408328, 408329, 408330, 408332, 408333, 408334, 408335, 408336, 408404, 408405, 408406, 408408, 408409, 408432, 408433, 408435, 408436, 408437, 408438, 408439, 408440, 408572, 408573, 408574, 408575, 408577, 408578, 408579, 408580, 408582, 408583, 408584, 408585, 408586, 408587, 408588, 408589, 408642, 408643, 408644, 408645, 408646, 408648, 408649, 408650, 408673, 408674, 408675, 408798, 408799, 408801, 408802, 408803, 408805, 408857, 408858, 408859, 408860, 408881, 408882, 408883, 408885, 408886, 408887, 408888, 408889, 408920, 408921, 408923, 408924, 408925, 408994, 408995, 408996, 408997, 408998, 408999, 409006, 409010, 409011, 409012, 409082, 409611, 409612, 409613, 409614, 409616, 409617, 409619, 409620, 409622, 409637, 409638, 409639, 409640, 409641, 409642, 409643, 409644, 409647, 409678, 409680, 409681, 409682, 409683, 409684, 409687, 409688, 409694, 409695, 409696, 409697, 409698, 409699, 409700, 409702, 409703, 409705, 409706, 409707, 409709, 409714, 409716, 409718, 409720, 409723, 409825, 409826, 409827, 409829, 409830, 409831, 409832, 409833, 409836, 409837, 409838, 409839, 409840, 409841, 409842, 409887, 409889, 409890, 409891, 409892, 409893, 409894, 409897, 409900, 409902, 409967, 409968, 409971, 409972, 409973, 409974, 409975, 409977, 410009, 410010, 410011, 410012, 410013, 410014, 410015, 410066, 410105, 410106, 410107, 410108, 410110, 410111, 410112, 410114, 410118, 410119, 410120, 410122, 410156, 410158, 410166, 410167, 410168, 410169, 410221, 410222, 410224, 410226, 410227, 410228, 410230, 410231, 410261, 410262, 410263, 410265, 410266, 410267, 410653, 410654, 410655, 410656, 410659, 410670, 410675, 410677, 410679, 410680, 410681, 410682, 410685, 410720, 410721, 410722, 410723, 410724, 410725, 410726, 410728, 410729, 410748, 410749, 410750, 410752, 410753, 410754, 410759, 410796, 410797, 410800, 410802, 410803, 410810, 410836, 410837, 410838, 410839, 410840, 410841, 410842, 410843,

410920, 410921, 410922, 410923, 410924, 410937, 410938, 410939, 410940, 410941, 410942, 410943, 410944, 411009, 411010, 411011, 411012, 411013, 411014, 411015, 411019, 411020, 411022, 411024, 411025, 411154, 411155, 411156, 411158, 411159, 411173, 411267, 411270, 411271, 411272, 411273, 411274, 411275, 411276, 411277, 411350, 411351, 411352, 411353, 411354, 411356, 411404, 411408, 411411, 411419, 411422, 411423, 411425, 411456, 411458, 411459, 411460, 411501, 411502, 411503, 411554, 411555, 411556, 411557, 411558, 411559, 411561, 411596, 411597, 411598, 411599, 411601, 411602, 411635, 411636, 411638, 411640, 411649, 411652, 411767, 411817, 411818, 411819, 411823, 411825, 411826, 411912, 411913, 411914, 411915, 411916, 411921, 411922, 411924, 411925, 411926, 411991, 411992, 411993, 411994, 411995, 412065, 412067, 412068, 412069, 412092, 412093, 412094, 412097, 412098, 412099, 412101, 412102, 412149, 412150, 412215, 412216, 412317, 412318, 412319, 412320, 412321, 412322, 412324, 412326, 412328, 412329, 412410, 412411, 412412, 412413, 412414, 412416, 412417, 412419, 412424, 412426, 412427, 412428, 412429, 412430, 412431, 412433, 412484, 412485, 412486, 412487, 412488, 412489, 412490, 412491, 412512, 412514, 412515, 412516, 412517, 412519, 412520, 412521, 412523, 412647, 412648, 412706, 412707, 412708, 412709, 412742, 412743, 412745, 412805, 412806, 412807, 412808, 412841, 412842, 412847, 412848, 413265, 413267, 413384, 413392, 413436, 413439, 413440, 413539, 413541, 413542, 413543, 413545, 413546, 413551, 413552, 413553, 413555, 413556, 413557, 413560, 413561, 413562, 413563, 413564, 413604, 413605, 413607, 413609, 413610, 413611, 413631, 413634, 413636, 413638, 413639, 413642, 413643, 413662, 413663, 413665, 413666, 413667, 413669, 413672, 413709, 413710, 413715, 413716, 413717, 413721, 413722, 413723, 413724, 413747, 413748, 413749, 413750, 413751, 413752, 413753, 413755, 413756, 413843, 413844, 413924, 413925, 413926, 413927, 413931, 413932, 413933, 413934, 413936, 413940, 414049, 414050, 414051, 414052, 414053, 414059, 414060, 414061, 414071, 414072, 414073, 414074, 414075, 414076, 414077, 414078, 414079, 414132, 414133, 414134, 414135, 414136, 414138, 414140, 414148, 414149, 414150, 414151, 414152, 414153, 414154, 414156, 414157, 414158, 414186, 414187, 414191, 414195, 414196, 414197, 414198, 414200, 414201, 414202, 414203, 414204, 414205, 414206, 414207, 414284, 414285, 414425, 414427, 414428, 414430, 414431, 414432, 414434, 414499, 414505, 414507, 414512, 414515, 414517, 414519, 414520, 414557, 414560, 414562, 414563, 414565, 414604, 414605, 414606, 414607, 414610, 414626, 414627, 414631, 414632, 414633, 414634, 414635, 414702, 414703, 414704, 414705, 414706, 414728, 414729, 414731, 414732, 414824, 414827, 414828, 414829, 414830, 414832, 414847, 414848, 414851, 414852, 414853, 414854, 414856, 414885, 414886, 414887, 414888, 414889, 414890, 414892, 414893, 414899, 414978, 414979, 414982, 414985, 414986, 414987,

Appendix B

Invariant yield of $c + b \rightarrow e$

Table B.1: Invariant differential yield of $c + b \rightarrow e$ in minimum bias Au+Au collisions.

p_{T} [GeV/c]	inv. yield	stat. error (-)	stat. error (+)	sys. error (-)	sys. error (+)
0.7	8.07e-03	9.93e-04	7.94e-04	8.07e-04	8.07e-04
0.9	4.15e-03	2.10e-04	2.10e-04	3.94e-04	3.94e-04
1.1	1.70e-03	7.07e-05	5.30e-05	1.63e-04	1.63e-04
1.3	7.98e-04	2.68e-05	2.68e-05	7.98e-05	7.98e-05
1.5	3.90e-04	8.42e-06	1.12e-05	4.15e-05	4.15e-05
1.7	2.02e-04	3.85e-06	3.85e-06	2.31e-05	2.31e-05
1.9	9.06e-05	2.35e-06	1.77e-06	1.09e-05	1.09e-05
2.1	5.06e-05	1.20e-06	9.03e-07	6.57e-06	6.57e-06
2.3	2.83e-05	4.78e-07	6.37e-07	3.92e-06	3.92e-06
2.5	1.78e-05	3.65e-07	3.65e-07	2.65e-06	2.65e-06
2.7	9.87e-06	2.54e-07	2.03e-07	1.54e-06	1.54e-06
2.9	6.34e-06	1.24e-07	1.54e-07	1.06e-06	1.06e-06
3.25	2.71e-06	6.52e-08	5.22e-08	4.87e-07	4.87e-07
3.75	8.38e-07	2.58e-08	2.15e-08	1.66e-07	1.66e-07
4.25	3.04e-07	1.19e-08	1.19e-08	6.60e-08	6.60e-08
4.75	9.22e-08	8.59e-09	7.93e-09	2.20e-08	2.20e-08
5.5	3.31e-08	3.72e-09	3.72e-09	8.22e-09	8.22e-09
6.5	9.06e-09	1.93e-09	1.78e-09	2.28e-09	2.28e-09
8	1.02e-09	5.65e-10	4.88e-10	2.48e-10	2.48e-10

Table B.2: Invariant differential yield of $c + b \rightarrow e$ in centrality 0-10% Au+Au collisions.

p_{T} [GeV/c]	inv. yield	stat. error (-)	stat. error (+)	sys. error (-)	sys. error (+)
0.7	3.11e-02	2.72e-03	2.72e-03	2.95e-03	2.95e-03
0.9	1.57e-02	5.37e-04	7.15e-04	1.51e-03	1.51e-03
1.1	6.13e-03	2.36e-04	2.36e-04	6.24e-04	6.24e-04
1.3	2.85e-03	8.87e-05	8.87e-05	3.14e-04	3.14e-04
1.5	1.27e-03	3.60e-05	3.60e-05	1.52e-04	1.52e-04
1.7	6.54e-04	1.62e-05	1.62e-05	8.48e-05	8.48e-05
1.9	2.83e-04	9.01e-06	7.21e-06	3.91e-05	3.91e-05
2.1	1.59e-04	4.62e-06	4.62e-06	2.36e-05	2.36e-05
2.3	9.11e-05	2.44e-06	2.93e-06	1.44e-05	1.44e-05
2.5	5.66e-05	1.68e-06	1.68e-06	9.49e-06	9.49e-06
2.7	3.26e-05	1.11e-06	1.27e-06	5.72e-06	5.72e-06
2.9	2.01e-05	8.47e-07	7.53e-07	3.71e-06	3.71e-06
3.25	8.36e-06	3.14e-07	2.75e-07	1.63e-06	1.63e-06
3.75	2.07e-06	1.40e-07	1.40e-07	4.33e-07	4.33e-07
4.25	7.46e-07	7.77e-08	7.77e-08	1.68e-07	1.68e-07
4.75	3.00e-07	6.50e-08	5.89e-08	7.21e-08	7.21e-08
5.5	2.15e-07	3.95e-08	3.63e-08	5.66e-08	5.66e-08
6.5	3.43e-08	2.05e-08	1.66e-08	8.13e-09	8.13e-09
8	1.14e-09	9.65e-09	6.92e-09	3.91e-10	3.91e-10

Table B.3: Invariant differential yield of $c + b \rightarrow e$ in centrality 10-20% Au+Au collisions.

p_{T} [GeV/c]	inv. yield	stat. error (-)	stat. error (+)	sys. error (-)	sys. error (+)
0.7	1.90e-02	2.41e-03	1.93e-03	1.92e-03	1.92e-03
0.9	1.03e-02	5.07e-04	5.07e-04	9.90e-04	9.90e-04
1.1	4.18e-03	1.70e-04	1.70e-04	4.09e-04	4.09e-04
1.3	1.94e-03	6.41e-05	4.81e-05	1.99e-04	1.99e-04
1.5	9.51e-04	2.68e-05	2.01e-05	1.03e-04	1.03e-04
1.7	4.92e-04	1.22e-05	9.18e-06	5.71e-05	5.71e-05
1.9	2.11e-04	6.98e-06	6.98e-06	2.55e-05	2.55e-05
2.1	1.13e-04	3.45e-06	2.76e-06	1.45e-05	1.45e-05
2.3	6.69e-05	1.86e-06	1.86e-06	9.14e-06	9.14e-06
2.5	4.51e-05	1.32e-06	1.10e-06	6.67e-06	6.67e-06
2.7	2.37e-05	8.32e-07	8.32e-07	3.61e-06	3.61e-06
2.9	1.37e-05	5.49e-07	5.49e-07	2.17e-06	2.17e-06
3.25	6.64e-06	2.16e-07	2.16e-07	1.15e-06	1.15e-06
3.75	2.33e-06	1.09e-07	1.09e-07	4.44e-07	4.44e-07
4.25	8.19e-07	5.03e-08	5.45e-08	1.68e-07	1.68e-07
4.75	2.17e-07	4.25e-08	3.95e-08	4.65e-08	4.65e-08
5.5	6.05e-08	1.87e-08	1.73e-08	1.37e-08	1.37e-08
6.5	3.51e-08	1.15e-08	9.75e-09	8.62e-09	8.62e-09
8	2.09e-09	2.77e-09	2.25e-09	4.81e-10	4.81e-10

Table B.4: Invariant differential yield of $c + b \rightarrow e$ in centrality 20-40% Au+Au collisions.

p_{T} [GeV/c]	inv. yield	stat. error (-)	stat. error (+)	sys. error (-)	sys. error (+)
0.7	1.18e-02	9.98e-04	1.25e-03	1.16e-03	1.16e-03
0.9	5.76e-03	2.78e-04	2.78e-04	5.43e-04	5.43e-04
1.1	2.37e-03	9.66e-05	7.24e-05	2.28e-04	2.28e-04
1.3	1.10e-03	3.75e-05	2.82e-05	1.11e-04	1.11e-04
1.5	5.44e-04	1.19e-05	1.59e-05	5.87e-05	5.87e-05
1.7	2.83e-04	7.35e-06	7.35e-06	3.29e-05	3.29e-05
1.9	1.31e-04	3.42e-06	3.42e-06	1.60e-05	1.60e-05
2.1	7.42e-05	2.22e-06	1.77e-06	9.72e-06	9.72e-06
2.3	4.03e-05	1.16e-06	1.16e-06	5.59e-06	5.59e-06
2.5	2.45e-05	6.54e-07	6.54e-07	3.63e-06	3.63e-06
2.7	1.35e-05	5.07e-07	4.35e-07	2.09e-06	2.09e-06
2.9	9.29e-06	3.17e-07	2.72e-07	1.53e-06	1.53e-06
3.25	3.78e-06	1.12e-07	1.12e-07	6.59e-07	6.59e-07
3.75	1.25e-06	5.07e-08	5.07e-08	2.39e-07	2.39e-07
4.25	4.45e-07	2.46e-08	2.71e-08	9.18e-08	9.18e-08
4.75	1.85e-07	2.10e-08	1.99e-08	4.12e-08	4.12e-08
5.5	4.87e-08	8.67e-09	8.33e-09	1.12e-08	1.12e-08
6.5	1.44e-08	4.55e-09	4.02e-09	3.40e-09	3.40e-09
8	1.69e-09	1.02e-09	9.25e-10	3.74e-10	3.74e-10

Table B.5: Invariant differential yield of $c + b \rightarrow e$ in centrality 40-60% Au+Au collisions.

p_{T} [GeV/c]	inv. yield	stat. error (-)	stat. error (+)	sys. error (-)	sys. error (+)
0.7	4.66e-03	3.31e-04	2.48e-04	4.79e-04	4.79e-04
0.9	1.95e-03	9.47e-05	9.47e-05	1.94e-04	1.94e-04
1.1	7.46e-04	3.25e-05	3.25e-05	7.52e-05	7.52e-05
1.3	3.49e-04	1.26e-05	1.26e-05	3.65e-05	3.65e-05
1.5	1.73e-04	5.38e-06	5.38e-06	1.91e-05	1.91e-05
1.7	8.94e-05	2.49e-06	3.11e-06	1.05e-05	1.05e-05
1.9	4.23e-05	1.78e-06	1.48e-06	5.27e-06	5.27e-06
2.1	2.36e-05	7.54e-07	7.54e-07	3.14e-06	3.14e-06
2.3	1.35e-05	5.73e-07	4.91e-07	1.90e-06	1.90e-06
2.5	8.26e-06	3.24e-07	3.24e-07	1.24e-06	1.24e-06
2.7	4.51e-06	2.06e-07	2.32e-07	7.07e-07	7.07e-07
2.9	3.32e-06	1.66e-07	1.50e-07	5.57e-07	5.57e-07
3.25	1.36e-06	6.21e-08	5.52e-08	2.42e-07	2.42e-07
3.75	4.52e-07	2.83e-08	2.59e-08	8.84e-08	8.84e-08
4.25	2.01e-07	1.54e-08	1.54e-08	4.42e-08	4.42e-08
4.75	4.14e-08	1.02e-08	1.91e-08	1.00e-08	1.00e-08
5.5	2.06e-08	4.65e-09	8.76e-09	5.16e-09	5.16e-09
6.5	7.57e-10	1.80e-09	3.04e-09	3.91e-10	3.91e-10
8	5.56e-10	4.45e-10	7.21e-10	1.47e-10	1.47e-10

Table B.6: Invariant differential yield of $c + b \rightarrow e$ in centrality 60-93% Au+Au collisions.

p_{T} [GeV/c]	inv. yield	stat. error (-)	stat. error (+)	sys. error (-)	sys. error (+)
0.7	4.59e-04	8.46e-05	8.46e-05	5.34e-05	5.34e-05
0.9	2.15e-04	2.10e-05	2.10e-05	2.30e-05	2.30e-05
1.1	8.68e-05	7.02e-06	8.42e-06	9.31e-06	9.31e-06
1.3	4.12e-05	3.14e-06	3.14e-06	4.56e-06	4.56e-06
1.5	2.26e-05	1.55e-06	1.33e-06	2.64e-06	2.64e-06
1.7	1.17e-05	7.15e-07	8.18e-07	1.47e-06	1.47e-06
1.9	5.75e-06	4.46e-07	4.46e-07	7.70e-07	7.70e-07
2.1	3.43e-06	2.60e-07	2.60e-07	4.91e-07	4.91e-07
2.3	1.72e-06	1.78e-07	1.78e-07	2.63e-07	2.63e-07
2.5	1.11e-06	1.18e-07	1.18e-07	1.80e-07	1.80e-07
2.7	7.69e-07	7.66e-08	7.66e-08	1.31e-07	1.31e-07
2.9	5.55e-07	5.23e-08	5.23e-08	9.95e-08	9.95e-08
3.25	2.34e-07	2.10e-08	1.84e-08	4.47e-08	4.47e-08
3.75	9.30e-08	9.86e-09	8.87e-09	1.95e-08	1.95e-08
4.25	2.34e-08	5.80e-09	5.14e-09	5.43e-09	5.43e-09
4.75	5.66e-09	3.91e-09	6.70e-09	1.63e-09	1.63e-09
5.5	1.41e-09	1.71e-09	2.89e-09	4.77e-10	4.77e-10
6.5	1.78e-09	7.09e-10	1.13e-09	5.42e-10	5.42e-10

Appendix C

Invariant yield of $c \rightarrow e$

Table C.1: Invariant differential yield of $c \rightarrow e$ in minimum bias Au+Au collisions.

p_{T} [GeV/c]	inv. yield	total error (-)	total error (+)
1.1	1.52e-03	1.86e-04	2.09e-04
1.3	7.22e-04	8.34e-05	8.20e-05
1.5	3.42e-04	4.17e-05	3.69e-05
1.7	1.62e-04	1.97e-05	1.68e-05
1.9	7.68e-05	8.71e-06	7.73e-06
2.1	3.65e-05	4.01e-06	3.64e-06
2.3	1.75e-05	1.97e-06	2.02e-06
2.5	8.57e-06	1.03e-06	1.30e-06
2.7	4.30e-06	6.07e-07	8.32e-07
2.9	2.22e-06	3.63e-07	4.84e-07
3.25	8.26e-07	1.64e-07	1.83e-07
3.75	2.20e-07	6.18e-08	5.94e-08
4.25	6.96e-08	3.17e-08	2.32e-08
4.75	2.53e-08	1.51e-08	1.00e-08
5.5	6.96e-09	5.04e-09	3.38e-09
6.5	1.40e-09	1.15e-09	8.70e-10
8	2.38e-10	2.04e-10	1.79e-10

Table C.2: Invariant differential yield of $c \rightarrow e$ in centrality 0-10% Au+Au collisions.

p_{T} [GeV/c]	inv. yield	total error (-)	total error (+)
1.1	5.53e-03	7.58e-04	7.46e-04
1.3	2.48e-03	3.31e-04	3.06e-04
1.5	1.12e-03	1.52e-04	1.31e-04
1.7	5.03e-04	6.71e-05	5.88e-05
1.9	2.28e-04	2.94e-05	2.73e-05
2.1	1.04e-04	1.39e-05	1.34e-05
2.3	4.82e-05	6.88e-06	7.61e-06
2.5	2.28e-05	3.57e-06	4.53e-06
2.7	1.12e-05	2.02e-06	2.69e-06
2.9	5.63e-06	1.16e-06	1.50e-06
3.25	2.04e-06	4.91e-07	5.77e-07
3.75	5.32e-07	1.78e-07	1.93e-07
4.25	1.67e-07	8.06e-08	7.44e-08
4.75	6.08e-08	3.40e-08	3.19e-08
5.5	1.68e-08	9.72e-09	1.07e-08
6.5	3.43e-09	1.85e-09	2.74e-09
8	5.87e-10	3.01e-10	5.67e-10

Table C.3: Invariant differential yield of $c \rightarrow e$ in centrality 10-20% Au+Au collisions.

p_{T} [GeV/c]	inv. yield	total error (-)	total error (+)
1.1	5.53e-03	7.58e-04	7.46e-04
1.3	2.48e-03	3.31e-04	3.06e-04
1.5	1.12e-03	1.52e-04	1.31e-04
1.7	5.03e-04	6.71e-05	5.88e-05
1.9	2.28e-04	2.94e-05	2.73e-05
2.1	1.04e-04	1.39e-05	1.34e-05
2.3	4.82e-05	6.88e-06	7.61e-06
2.5	2.28e-05	3.57e-06	4.53e-06
2.7	1.12e-05	2.02e-06	2.69e-06
2.9	5.63e-06	1.16e-06	1.50e-06
3.25	2.04e-06	4.91e-07	5.77e-07
3.75	5.32e-07	1.78e-07	1.93e-07
4.25	1.67e-07	8.06e-08	7.44e-08
4.75	6.08e-08	3.40e-08	3.19e-08
5.5	1.68e-08	9.72e-09	1.07e-08
6.5	3.43e-09	1.85e-09	2.74e-09
8	5.87e-10	3.01e-10	5.67e-10

Table C.4: Invariant differential yield of $c \rightarrow e$ in centrality 20-40% Au+Au collisions.

p_{T} [GeV/c]	inv. yield	total error (-)	total error (+)
1.1	3.86e-03	4.72e-04	5.28e-04
1.3	1.80e-03	2.07e-04	2.12e-04
1.5	8.40e-04	1.01e-04	9.51e-05
1.7	3.97e-04	5.02e-05	4.41e-05
1.9	1.89e-04	2.41e-05	2.10e-05
2.1	9.13e-05	1.16e-05	1.03e-05
2.3	4.46e-05	5.80e-06	5.29e-06
2.5	2.21e-05	3.14e-06	2.83e-06
2.7	1.12e-05	1.87e-06	1.74e-06
2.9	5.81e-06	1.11e-06	1.08e-06
3.25	2.12e-06	4.89e-07	4.87e-07
3.75	5.37e-07	1.57e-07	1.52e-07
4.25	1.65e-07	5.77e-08	5.50e-08
4.75	5.98e-08	2.52e-08	2.27e-08
5.5	1.69e-08	8.65e-09	7.44e-09
6.5	3.61e-09	2.21e-09	1.90e-09
8	6.50e-10	4.38e-10	3.96e-10

Table C.5: Invariant differential yield of $c \rightarrow e$ in centrality 40-60% Au+Au collisions.

p_{T} [GeV/c]	inv. yield	total error (-)	total error (+)
1.1	2.11e-03	2.76e-04	2.91e-04
1.3	9.93e-04	1.21e-04	1.18e-04
1.5	4.71e-04	5.94e-05	5.42e-05
1.7	2.25e-04	2.95e-05	2.57e-05
1.9	1.08e-04	1.42e-05	1.25e-05
2.1	5.24e-05	6.86e-06	6.21e-06
2.3	2.57e-05	3.44e-06	3.18e-06
2.5	1.28e-05	1.87e-06	1.78e-06
2.7	6.55e-06	1.13e-06	1.08e-06
2.9	3.41e-06	6.82e-07	6.55e-07
3.25	1.26e-06	3.09e-07	2.85e-07
3.75	3.27e-07	1.03e-07	9.00e-08
4.25	1.02e-07	3.91e-08	3.32e-08
4.75	3.76e-08	1.70e-08	1.39e-08
5.5	1.08e-08	5.71e-09	4.65e-09
6.5	2.32e-09	1.44e-09	1.21e-09
8	4.19e-10	2.89e-10	2.56e-10

Table C.6: Invariant differential yield of $c \rightarrow e$ in centrality 60-93% Au+Au collisions.

p_{T} [GeV/c]	inv. yield	total error (-)	total error (+)
1.1	8.11e-05	1.08e-05	1.08e-05
1.3	3.73e-05	4.72e-06	4.74e-06
1.5	1.78e-05	2.26e-06	2.26e-06
1.7	8.83e-06	1.15e-06	1.15e-06
1.9	4.50e-06	6.16e-07	6.13e-07
2.1	2.35e-06	3.42e-07	3.40e-07
2.3	1.26e-06	1.96e-07	1.94e-07
2.5	6.90e-07	1.15e-07	1.14e-07
2.7	3.87e-07	7.02e-08	6.89e-08
2.9	2.19e-07	4.50e-08	4.36e-08
3.25	9.02e-08	2.18e-08	2.08e-08
3.75	2.57e-08	7.76e-09	7.24e-09
4.25	8.14e-09	2.91e-09	2.73e-09
4.75	2.91e-09	1.18e-09	1.14e-09
5.5	7.95e-10	3.68e-10	3.78e-10
6.5	1.60e-10	8.55e-11	9.65e-11

Appendix D

Invariant yield of $b \rightarrow e$

Table D.1: Invariant differential yield of $b \rightarrow e$ in minimum bias Au+Au collisions.

p_{T} [GeV/c]	inv. yield	total error (-)	total error (+)
1.1	9.41e-05	1.93e-05	1.84e-05
1.3	6.57e-05	1.36e-05	1.30e-05
1.5	4.63e-05	9.56e-06	9.17e-06
1.7	3.28e-05	6.64e-06	6.35e-06
1.9	2.32e-05	4.53e-06	4.32e-06
2.1	1.63e-05	3.05e-06	2.91e-06
2.3	1.14e-05	2.04e-06	1.94e-06
2.5	7.91e-06	1.38e-06	1.29e-06
2.7	5.41e-06	9.16e-07	8.44e-07
2.9	3.65e-06	5.91e-07	5.46e-07
3.25	1.82e-06	2.65e-07	2.57e-07
3.75	6.19e-07	7.67e-08	8.44e-08
4.25	2.12e-07	2.42e-08	3.91e-08
4.75	7.87e-08	1.04e-08	2.00e-08
5.5	2.45e-08	3.88e-09	6.07e-09
6.5	6.45e-09	1.30e-09	1.24e-09
8	1.25e-09	3.37e-10	2.49e-10

Table D.2: Invariant differential yield of $b \rightarrow e$ in centrality 0-10% Au+Au collisions.

p_{T} [GeV/c]	inv. yield	total error (-)	total error (+)
1.1	3.74e-04	7.07e-05	8.08e-05
1.3	2.62e-04	4.97e-05	5.75e-05
1.5	1.84e-04	3.50e-05	4.06e-05
1.7	1.29e-04	2.44e-05	2.78e-05
1.9	9.03e-05	1.67e-05	1.86e-05
2.1	6.27e-05	1.14e-05	1.23e-05
2.3	4.30e-05	7.67e-06	8.06e-06
2.5	2.91e-05	5.20e-06	5.24e-06
2.7	1.94e-05	3.48e-06	3.34e-06
2.9	1.27e-05	2.25e-06	2.10e-06
3.25	5.97e-06	9.98e-07	9.33e-07
3.75	1.84e-06	2.87e-07	2.78e-07
4.25	5.83e-07	1.02e-07	1.33e-07
4.75	2.12e-07	4.21e-08	6.76e-08
5.5	6.78e-08	1.52e-08	2.31e-08
6.5	1.89e-08	4.87e-09	6.19e-09
8	3.88e-09	1.17e-09	1.45e-09

Table D.3: Invariant differential yield of $b \rightarrow e$ in centrality 10-20% Au+Au collisions.

p_{T} [GeV/c]	inv. yield	total error (-)	total error (+)
1.1	1.77e-04	4.16e-05	6.12e-05
1.3	1.22e-04	2.91e-05	4.40e-05
1.5	8.64e-05	2.05e-05	3.10e-05
1.7	6.21e-05	1.44e-05	2.10e-05
1.9	4.51e-05	1.01e-05	1.37e-05
2.1	3.28e-05	6.97e-06	8.73e-06
2.3	2.38e-05	4.78e-06	5.53e-06
2.5	1.72e-05	3.24e-06	3.57e-06
2.7	1.22e-05	2.19e-06	2.35e-06
2.9	8.57e-06	1.49e-06	1.53e-06
3.25	4.54e-06	7.44e-07	7.32e-07
3.75	1.66e-06	2.30e-07	2.39e-07
4.25	5.77e-07	7.97e-08	8.77e-08
4.75	2.01e-07	3.39e-08	4.04e-08
5.5	5.34e-08	1.20e-08	1.20e-08
6.5	1.13e-08	3.68e-09	2.83e-09
8	2.00e-09	9.00e-10	6.64e-10

Table D.4: Invariant differential yield of $b \rightarrow e$ in centrality 20-40% Au+Au collisions.

p_{T} [GeV/c]	inv. yield	total error (-)	total error (+)
1.1	1.29e-04	3.10e-05	3.86e-05
1.3	9.02e-05	2.19e-05	2.77e-05
1.5	6.36e-05	1.54e-05	1.95e-05
1.7	4.51e-05	1.07e-05	1.33e-05
1.9	3.20e-05	7.26e-06	8.70e-06
2.1	2.27e-05	4.84e-06	5.56e-06
2.3	1.59e-05	3.18e-06	3.53e-06
2.5	1.11e-05	2.06e-06	2.26e-06
2.7	7.65e-06	1.34e-06	1.44e-06
2.9	5.21e-06	8.78e-07	9.11e-07
3.25	2.65e-06	4.14e-07	4.23e-07
3.75	9.47e-07	1.27e-07	1.36e-07
4.25	3.39e-07	4.43e-08	5.43e-08
4.75	1.29e-07	2.01e-08	2.64e-08
5.5	3.96e-08	7.98e-09	8.05e-09
6.5	9.82e-09	2.69e-09	1.86e-09
8	1.85e-09	6.72e-10	4.12e-10

Table D.5: Invariant differential yield of $b \rightarrow e$ in centrality 40-60% Au+Au collisions.

p_{T} [GeV/c]	inv. yield	total error (-)	total error (+)
1.1	2.77e-05	8.72e-06	9.13e-06
1.3	1.94e-05	6.20e-06	6.47e-06
1.5	1.38e-05	4.38e-06	4.56e-06
1.7	9.74e-06	3.02e-06	3.16e-06
1.9	6.88e-06	2.04e-06	2.14e-06
2.1	4.85e-06	1.35e-06	1.43e-06
2.3	3.40e-06	8.79e-07	9.37e-07
2.5	2.38e-06	5.75e-07	6.11e-07
2.7	1.67e-06	3.77e-07	3.97e-07
2.9	1.16e-06	2.48e-07	2.57e-07
3.25	6.34e-07	1.24e-07	1.26e-07
3.75	2.60e-07	4.60e-08	4.50e-08
4.25	1.08e-07	1.89e-08	1.80e-08
4.75	4.60e-08	9.01e-09	8.80e-09
5.5	1.42e-08	3.37e-09	3.37e-09
6.5	2.97e-09	8.97e-10	9.60e-10
8	4.47e-10	1.62e-10	1.95e-10

Table D.6: Invariant differential yield of $b \rightarrow e$ in centrality 60-93% Au+Au collisions.

p_{T} [GeV/c]	inv. yield	total error (-)	total error (+)
1.1	6.19e-06	1.64e-06	1.75e-06
1.3	4.35e-06	1.16e-06	1.24e-06
1.5	3.08e-06	8.22e-07	8.74e-07
1.7	2.17e-06	5.70e-07	6.08e-07
1.9	1.52e-06	3.87e-07	4.14e-07
2.1	1.06e-06	2.59e-07	2.78e-07
2.3	7.34e-07	1.72e-07	1.85e-07
2.5	5.08e-07	1.14e-07	1.23e-07
2.7	3.50e-07	7.55e-08	8.12e-08
2.9	2.41e-07	4.99e-08	5.38e-08
3.25	1.28e-07	2.49e-08	2.68e-08
3.75	5.11e-08	9.28e-09	9.67e-09
4.25	2.09e-08	3.78e-09	4.12e-09
4.75	8.89e-09	1.79e-09	1.96e-09
5.5	2.80e-09	6.68e-10	7.37e-10
6.5	6.19e-10	1.84e-10	2.24e-10

Appendix E

Integrated yield of $c \rightarrow e$ and $b \rightarrow e$

Table E.1: Integrated yields of $c \rightarrow e$

p_{T} [GeV/c]	0-10%	10-20%	20-40%	40-60%	60-92%	p+p
$1 < p_T < 3$	1.01e-03	7.27e-04	4.06e-04	1.37e-04	1.55e-05	1.29e-06
$3 < p_T < 5$	7.01e-07	7.48e-07	4.66e-07	2.54e-07	3.47e-08	3.43e-09
$5 < p_T < 9$	1.18e-08	1.73e-08	1.16e-08	4.35e-09	7.37e-10	6.93e-11

Table E.2: Integrated yields of $b \rightarrow e$

p_{T} [GeV/c]	0-10%	10-20%	20-40%	40-60%	60-92%	p+p
$1 < p_T < 3$	1.21e-04	6.65e-05	4.24e-05	9.05e-06	2.00e-06	8.32e-08
$3 < p_T < 5$	2.15e-06	1.71e-06	9.99e-07	2.59e-07	4.94e-08	3.07e-09
$5 < p_T < 9$	5.28e-08	3.78e-08	2.60e-08	1.00e-08	1.74e-09	1.31e-10

Appendix F

Nuclear Modification Factor R_{AA} of $c \rightarrow e$

Table F.1: R_{AA} of $c \rightarrow e$ in minimum bias Au+Au collisions.

p_{T} [GeV/c]	R_{AA}	total error (-)	total error (+)
1.1	8.74e-01	1.44e-01	1.76e-01
1.3	8.98e-01	1.40e-01	1.52e-01
1.5	8.90e-01	1.36e-01	1.48e-01
1.7	8.50e-01	1.32e-01	1.44e-01
1.9	7.78e-01	1.16e-01	1.40e-01
2.1	7.06e-01	1.16e-01	1.36e-01
2.3	6.22e-01	1.08e-01	1.32e-01
2.5	5.46e-01	1.08e-01	1.28e-01
2.7	4.78e-01	1.00e-01	1.32e-01
2.9	4.22e-01	9.60e-02	1.16e-01
3.25	3.58e-01	8.40e-02	1.08e-01
3.75	2.90e-01	8.40e-02	1.00e-01
4.25	2.42e-01	1.04e-01	1.04e-01
4.75	2.14e-01	1.04e-01	1.16e-01
5.5	1.86e-01	1.00e-01	1.24e-01
6.5	1.58e-01	9.20e-02	1.28e-01
8	1.30e-01	8.00e-02	1.40e-01

Table F.2: R_{AA} of $c \rightarrow e$ in centrality 0-10% Au+Au collisions.

p_{T} [GeV/c]	R_{AA}	total error (-)	total error (+)
1.1	8.58e-01	1.48e-01	1.72e-01
1.3	8.30e-01	1.32e-01	1.52e-01
1.5	7.78e-01	1.24e-01	1.40e-01
1.7	7.10e-01	1.12e-01	1.28e-01
1.9	6.26e-01	1.04e-01	1.24e-01
2.1	5.42e-01	1.00e-01	1.20e-01
2.3	4.66e-01	9.60e-02	1.12e-01
2.5	3.94e-01	8.40e-02	1.12e-01
2.7	3.34e-01	8.00e-02	1.08e-01
2.9	2.86e-01	7.60e-02	1.00e-01
3.25	2.38e-01	6.80e-02	8.40e-02
3.75	1.90e-01	6.40e-02	8.40e-02
4.25	1.58e-01	7.60e-02	8.40e-02
4.75	1.38e-01	7.20e-02	9.20e-02
5.5	1.26e-01	7.20e-02	9.60e-02
6.5	1.06e-01	6.00e-02	1.04e-01
8	9.00e-02	5.60e-02	1.04e-01

Table F.3: R_{AA} of $c \rightarrow e$ in centrality 10-20% Au+Au collisions.

p_{T} [GeV/c]	R_{AA}	total error (-)	total error (+)
1.1	9.50e-01	1.56e-01	1.92e-01
1.3	9.54e-01	1.44e-01	1.68e-01
1.5	9.30e-01	1.40e-01	1.60e-01
1.7	8.82e-01	1.36e-01	1.60e-01
1.9	8.22e-01	1.36e-01	1.56e-01
2.1	7.50e-01	1.32e-01	1.52e-01
2.3	6.70e-01	1.28e-01	1.56e-01
2.5	5.94e-01	1.24e-01	1.44e-01
2.7	5.30e-01	1.20e-01	1.40e-01
2.9	4.62e-01	1.12e-01	1.32e-01
3.25	3.90e-01	1.04e-01	1.32e-01
3.75	3.02e-01	9.20e-02	1.16e-01
4.25	2.50e-01	8.80e-02	1.12e-01
4.75	2.22e-01	9.20e-02	1.16e-01
5.5	1.94e-01	9.60e-02	1.24e-01
6.5	1.66e-01	9.20e-02	1.48e-01
8	1.46e-01	9.20e-02	1.60e-01

Table F.4: R_{AA} of $c \rightarrow e$ in centrality 20-40% Au+Au collisions.

p_{T} [GeV/c]	R_{AA}	total error (-)	total error (+)
1.1	1.05e+00	1.76e-01	2.12e-01
1.3	1.07e+00	1.68e-01	1.88e-01
1.5	1.05e+00	1.60e-01	1.88e-01
1.7	1.02e+00	1.68e-01	1.88e-01
1.9	9.54e-01	1.68e-01	1.88e-01
2.1	8.74e-01	1.60e-01	1.92e-01
2.3	7.86e-01	1.52e-01	1.92e-01
2.5	7.02e-01	1.44e-01	1.84e-01
2.7	6.26e-01	1.40e-01	1.68e-01
2.9	5.50e-01	1.32e-01	1.64e-01
3.25	4.70e-01	1.24e-01	1.56e-01
3.75	3.70e-01	1.12e-01	1.40e-01
4.25	3.10e-01	1.12e-01	1.40e-01
4.75	2.78e-01	1.20e-01	1.48e-01
5.5	2.46e-01	1.16e-01	1.64e-01
6.5	2.14e-01	1.16e-01	1.80e-01
8	1.90e-01	1.16e-01	2.04e-01

Table F.5: R_{AA} of $c \rightarrow e$ in centrality 40-60% Au+Au collisions.

p_{T} [GeV/c]	R_{AA}	total error (-)	total error (+)
1.1	1.05e+00	1.76e-01	2.12e-01
1.3	1.07e+00	1.68e-01	1.88e-01
1.5	1.05e+00	1.60e-01	1.88e-01
1.7	1.02e+00	1.68e-01	1.88e-01
1.9	9.54e-01	1.68e-01	1.88e-01
2.1	8.74e-01	1.60e-01	1.92e-01
2.3	7.86e-01	1.52e-01	1.92e-01
2.5	7.02e-01	1.44e-01	1.84e-01
2.7	6.26e-01	1.40e-01	1.68e-01
2.9	5.50e-01	1.32e-01	1.64e-01
3.25	4.70e-01	1.24e-01	1.56e-01
3.75	3.70e-01	1.12e-01	1.40e-01
4.25	3.10e-01	1.12e-01	1.40e-01
4.75	2.78e-01	1.20e-01	1.48e-01
5.5	2.46e-01	1.16e-01	1.64e-01
6.5	2.14e-01	1.16e-01	1.80e-01
8	1.90e-01	1.16e-01	2.04e-01

Table F.6: R_{AA} of $c \rightarrow e$ in centrality 60-93% Au+Au collisions.

p_{T} [GeV/c]	R_{AA}	total error (-)	total error (+)
1.1	1.19e+00	1.96e-01	2.24e-01
1.3	1.17e+00	1.72e-01	2.04e-01
1.5	1.15e+00	1.68e-01	2.04e-01
1.7	1.13e+00	1.72e-01	2.00e-01
1.9	1.11e+00	1.84e-01	2.12e-01
2.1	1.09e+00	1.88e-01	2.28e-01
2.3	1.06e+00	1.96e-01	2.36e-01
2.5	1.02e+00	2.00e-01	2.44e-01
2.7	9.86e-01	2.00e-01	2.32e-01
2.9	9.42e-01	2.04e-01	2.44e-01
3.25	8.74e-01	1.92e-01	2.48e-01
3.75	7.58e-01	1.84e-01	2.48e-01
4.25	6.34e-01	1.76e-01	2.40e-01
4.75	5.54e-01	1.84e-01	2.56e-01
5.5	4.62e-01	1.80e-01	2.64e-01
6.5	3.66e-01	1.76e-01	2.84e-01
8	2.94e-01	1.68e-01	2.96e-01

Appendix G

Nuclear Modification Factor R_{AA} of $b \rightarrow e$

Table G.1: R_{AA} of $b \rightarrow e$ in minimum bias Au+Au collisions.

p_{T} [GeV/c]	R_{AA}	total error (-)	total error (+)
1.1	1.45e+00	4.72e-01	7.56e-01
1.3	1.45e+00	4.64e-01	7.36e-01
1.5	1.43e+00	4.44e-01	7.00e-01
1.7	1.43e+00	4.32e-01	6.80e-01
1.9	1.41e+00	4.00e-01	6.44e-01
2.1	1.40e+00	3.72e-01	5.84e-01
2.3	1.37e+00	3.44e-01	5.32e-01
2.5	1.32e+00	3.20e-01	4.36e-01
2.7	1.25e+00	2.92e-01	3.96e-01
2.9	1.17e+00	2.60e-01	3.48e-01
3.25	1.01e+00	2.04e-01	2.64e-01
3.75	7.70e-01	1.44e-01	2.00e-01
4.25	5.70e-01	1.24e-01	1.56e-01
4.75	4.42e-01	1.04e-01	1.40e-01
5.5	3.66e-01	9.60e-02	1.36e-01
6.5	3.42e-01	1.08e-01	1.40e-01
8	3.22e-01	1.20e-01	1.68e-01

Table G.2: R_{AA} of $b \rightarrow e$ in centrality 0-10% Au+Au collisions.

p_{T} [GeV/c]	R_{AA}	total error (-)	total error (+)
1.1	1.57e+00	5.20e-01	8.00e-01
1.3	1.56e+00	4.96e-01	7.60e-01
1.5	1.55e+00	4.88e-01	7.60e-01
1.7	1.51e+00	4.56e-01	7.28e-01
1.9	1.48e+00	4.16e-01	6.84e-01
2.1	1.45e+00	4.04e-01	6.16e-01
2.3	1.39e+00	3.68e-01	5.40e-01
2.5	1.31e+00	3.40e-01	4.64e-01
2.7	1.21e+00	2.92e-01	4.04e-01
2.9	1.09e+00	2.48e-01	3.40e-01
3.25	8.98e-01	1.92e-01	2.52e-01
3.75	6.14e-01	1.32e-01	1.72e-01
4.25	4.18e-01	1.04e-01	1.32e-01
4.75	3.18e-01	8.80e-02	1.16e-01
5.5	2.70e-01	8.40e-02	1.16e-01
6.5	2.78e-01	9.60e-02	1.32e-01
8	2.82e-01	1.08e-01	1.60e-01

Table G.3: R_{AA} of $b \rightarrow e$ in centrality 10-20% Au+Au collisions.

p_{T} [GeV/c]	R_{AA}	total error (-)	total error (+)
1.1	1.20e+00	4.32e-01	7.28e-01
1.3	1.20e+00	4.32e-01	7.28e-01
1.5	1.19e+00	4.12e-01	7.00e-01
1.7	1.20e+00	4.08e-01	6.60e-01
1.9	1.21e+00	3.76e-01	6.36e-01
2.1	1.22e+00	3.60e-01	5.64e-01
2.3	1.23e+00	3.36e-01	5.20e-01
2.5	1.24e+00	3.20e-01	4.60e-01
2.7	1.23e+00	3.04e-01	4.08e-01
2.9	1.19e+00	2.76e-01	3.76e-01
3.25	1.10e+00	2.36e-01	3.04e-01
3.75	8.90e-01	1.84e-01	2.32e-01
4.25	6.50e-01	1.48e-01	1.88e-01
4.75	4.70e-01	1.16e-01	1.56e-01
5.5	3.34e-01	1.00e-01	1.24e-01
6.5	2.54e-01	9.60e-02	1.24e-01
8	2.22e-01	1.08e-01	1.40e-01

Table G.4: R_{AA} of $b \rightarrow e$ in centrality 20-40% Au+Au collisions.

p_{T} [GeV/c]	R_{AA}	total error (-)	total error (+)
1.1	1.71e+00	5.96e-01	9.04e-01
1.3	1.73e+00	5.92e-01	8.68e-01
1.5	1.70e+00	5.68e-01	8.56e-01
1.7	1.70e+00	5.60e-01	8.44e-01
1.9	1.70e+00	5.40e-01	8.12e-01
2.1	1.70e+00	5.00e-01	7.40e-01
2.3	1.66e+00	4.64e-01	6.64e-01
2.5	1.62e+00	4.16e-01	6.00e-01
2.7	1.55e+00	3.80e-01	5.04e-01
2.9	1.47e+00	3.36e-01	4.44e-01
3.25	1.29e+00	2.72e-01	3.68e-01
3.75	1.03e+00	2.12e-01	2.72e-01
4.25	7.82e-01	1.76e-01	2.16e-01
4.75	6.18e-01	1.56e-01	2.00e-01
5.5	5.06e-01	1.40e-01	1.80e-01
6.5	4.46e-01	1.56e-01	1.92e-01
8	4.06e-01	1.64e-01	2.32e-01

Table G.5: R_{AA} of $b \rightarrow e$ in centrality 40-60% Au+Au collisions.

p_{T} [GeV/c]	R_{AA}	total error (-)	total error (+)
1.1	1.21e+00	4.64e-01	7.56e-01
1.3	1.23e+00	4.72e-01	7.28e-01
1.5	1.21e+00	4.56e-01	7.20e-01
1.7	1.21e+00	4.36e-01	6.76e-01
1.9	1.20e+00	4.24e-01	6.52e-01
2.1	1.18e+00	3.84e-01	5.84e-01
2.3	1.16e+00	3.60e-01	5.24e-01
2.5	1.15e+00	3.32e-01	4.52e-01
2.7	1.12e+00	3.08e-01	4.08e-01
2.9	1.08e+00	2.72e-01	3.68e-01
3.25	1.01e+00	2.44e-01	3.16e-01
3.75	9.14e-01	2.00e-01	2.64e-01
4.25	8.10e-01	1.92e-01	2.36e-01
4.75	7.10e-01	1.84e-01	2.40e-01
5.5	5.98e-01	1.84e-01	2.28e-01
6.5	4.54e-01	1.68e-01	2.24e-01
8	3.42e-01	1.52e-01	2.28e-01

Table G.6: R_{AA} of $b \rightarrow e$ in centrality 60-93% Au+Au collisions.

p_{T} [GeV/c]	R_{AA}	total error (-)	total error (+)
1.1	1.65e+00	5.84e-01	8.96e-01
1.3	1.67e+00	5.76e-01	8.44e-01
1.5	1.64e+00	5.60e-01	8.36e-01
1.7	1.64e+00	5.40e-01	8.16e-01
1.9	1.62e+00	5.20e-01	7.60e-01
2.1	1.58e+00	4.80e-01	7.40e-01
2.3	1.56e+00	4.68e-01	6.56e-01
2.5	1.49e+00	4.24e-01	5.80e-01
2.7	1.44e+00	3.92e-01	5.56e-01
2.9	1.37e+00	3.56e-01	4.80e-01
3.25	1.26e+00	3.12e-01	4.24e-01
3.75	1.11e+00	2.68e-01	3.44e-01
4.25	9.66e-01	2.44e-01	3.08e-01
4.75	8.54e-01	2.36e-01	2.92e-01
5.5	7.26e-01	2.28e-01	2.96e-01
6.5	5.90e-01	2.28e-01	3.04e-01

Appendix H

Nuclear Modification Factor R_{AA} of c hadrons

Table H.1: R_{AA} of c hadrons in minimum bias Au+Au collisions.

p_{T} [GeV/c]	R_{AA}	total error (-)	total error (+)
1.25	0.78	0.23	0.41
1.75	0.98	0.18	0.22
2.25	1.06	0.22	0.21
2.75	0.98	0.18	0.17
3.25	0.78	0.12	0.12
3.75	0.58	0.11	0.18
4.25	0.44	0.10	0.19
4.75	0.35	0.08	0.12
5.5	0.30	0.08	0.09
6.5	0.26	0.12	0.11
7.5	0.23	0.13	0.11
8.5	0.20	0.12	0.12
10.5	0.17	0.10	0.13

Table H.2: R_{AA} of c hadrons in centrality 0-10% Au+Au collisions.

p_{T} [GeV/c]	R_{AA}	total error (-)	total error (+)
1.25	0.91	0.26	0.39
1.75	1.01	0.20	0.24
2.25	0.95	0.20	0.19
2.75	0.79	0.14	0.14
3.25	0.58	0.09	0.12
3.75	0.41	0.09	0.16
4.25	0.29	0.07	0.14
4.75	0.23	0.07	0.08
5.5	0.20	0.08	0.07
6.5	0.17	0.09	0.08
7.5	0.15	0.09	0.09
8.5	0.13	0.07	0.10
10.5	0.11	0.06	0.10

Table H.3: R_{AA} of c hadrons in centrality 10-20% Au+Au collisions.

p_{T} [GeV/c]	R_{AA}	total error (-)	total error (+)
1.25	0.92	0.25	0.41
1.75	1.06	0.19	0.25
2.25	1.08	0.19	0.21
2.75	1.00	0.17	0.17
3.25	0.85	0.14	0.14
3.75	0.67	0.12	0.12
4.25	0.50	0.11	0.14
4.75	0.38	0.09	0.12
5.5	0.30	0.09	0.10
6.5	0.26	0.09	0.10
7.5	0.22	0.10	0.11
8.5	0.20	0.10	0.12
10.5	0.18	0.09	0.13

Table H.4: R_{AA} of c hadrons in centrality 20-40% Au+Au collisions.

p_{T} [GeV/c]	R_{AA}	total error (-)	total error (+)
1.25	0.97	0.29	0.44
1.75	1.15	0.21	0.27
2.25	1.22	0.21	0.23
2.75	1.16	0.21	0.20
3.25	1.00	0.16	0.17
3.75	0.78	0.14	0.16
4.25	0.60	0.14	0.16
4.75	0.46	0.12	0.14
5.5	0.37	0.12	0.12
6.5	0.32	0.11	0.13
7.5	0.28	0.13	0.14
8.5	0.26	0.13	0.15
10.5	0.23	0.13	0.17

Table H.5: R_{AA} of c hadrons in centrality 40-60% Au+Au collisions.

p_{T} [GeV/c]	R_{AA}	total error (-)	total error (+)
1.25	1.22	0.28	0.43
1.75	1.21	0.21	0.27
2.25	1.18	0.18	0.20
2.75	1.15	0.16	0.19
3.25	1.14	0.16	0.19
3.75	1.12	0.17	0.21
4.25	1.06	0.18	0.21
4.75	0.95	0.18	0.21
5.5	0.81	0.18	0.20
6.5	0.67	0.18	0.21
7.5	0.54	0.19	0.22
8.5	0.44	0.18	0.24
10.5	0.36	0.16	0.25

Table H.6: R_{AA} of c hadrons in centrality 60-93% Au+Au collisions.

p_{T} [GeV/c]	R_{AA}	total error (-)	total error (+)
1.25	0.83	0.20	0.30
1.75	0.82	0.14	0.20
2.25	0.83	0.12	0.15
2.75	0.83	0.12	0.15
3.25	0.85	0.14	0.17
3.75	0.85	0.16	0.18
4.25	0.83	0.17	0.20
4.75	0.75	0.19	0.19
5.5	0.64	0.19	0.19
6.5	0.54	0.20	0.21
7.5	0.46	0.20	0.22
8.5	0.38	0.18	0.25
10.5	0.33	0.18	0.25

Appendix I

Nuclear Modification Factor R_{AA} of b hadrons

Table I.1: R_{AA} of b hadrons in minimum bias Au+Au collisions.

p_{T} [GeV/c]	R_{AA}	total error (-)	total error (+)
1.25	1.39	0.61	1.17
1.75	1.57	0.58	1.11
2.25	1.76	0.59	1.03
2.75	1.90	0.60	0.94
3.25	1.81	0.50	0.79
3.75	1.62	0.41	0.59
4.25	1.33	0.30	0.44
4.75	1.04	0.22	0.29
5.5	0.67	0.13	0.19
6.5	0.41	0.09	0.18
7.5	0.34	0.08	0.13
8.5	0.35	0.08	0.10
10.5	0.36	0.09	0.12

Table I.2: R_{AA} of b hadrons in centrality 0-10% Au+Au collisions.

p_{T} [GeV/c]	R_{AA}	total error (-)	total error (+)
1.25	1.70	0.69	1.26
1.75	1.86	0.67	1.16
2.25	2.04	0.66	1.09
2.75	2.02	0.60	1.00
3.25	1.86	0.54	0.85
3.75	1.51	0.40	0.57
4.25	1.11	0.26	0.36
4.75	0.77	0.16	0.22
5.5	0.46	0.11	0.14
6.5	0.27	0.07	0.15
7.5	0.24	0.06	0.12
8.5	0.26	0.06	0.09
10.5	0.29	0.09	0.12

Table I.3: R_{AA} of b hadrons in centrality 10-20% Au+Au collisions.

p_{T} [GeV/c]	R_{AA}	total error (-)	total error (+)
1.25	0.87	0.49	1.12
1.75	1.07	0.50	1.02
2.25	1.33	0.51	0.95
2.75	1.55	0.51	0.90
3.25	1.68	0.50	0.76
3.75	1.69	0.46	0.65
4.25	1.54	0.39	0.50
4.75	1.31	0.30	0.38
5.5	0.88	0.17	0.22
6.5	0.50	0.12	0.20
7.5	0.33	0.08	0.12
8.5	0.27	0.07	0.08
10.5	0.24	0.10	0.10

Table I.4: R_{AA} of b hadrons in centrality 20-40% Au+Au collisions.

p_{T} [GeV/c]	R_{AA}	total error (-)	total error (+)
1.25	1.62	0.79	1.38
1.75	1.87	0.77	1.29
2.25	2.06	0.72	1.16
2.75	2.20	0.68	1.04
3.25	2.14	0.60	0.93
3.75	1.95	0.51	0.72
4.25	1.67	0.39	0.55
4.75	1.38	0.30	0.39
5.5	0.96	0.18	0.25
6.5	0.61	0.13	0.24
7.5	0.50	0.12	0.17
8.5	0.46	0.11	0.14
10.5	0.44	0.14	0.16

Table I.5: R_{AA} of b hadrons in centrality 40-60% Au+Au collisions.

p_{T} [GeV/c]	R_{AA}	total error (-)	total error (+)
1.25	1.23	0.63	1.17
1.75	1.27	0.60	1.06
2.25	1.31	0.54	0.92
2.75	1.31	0.46	0.80
3.25	1.30	0.42	0.63
3.75	1.25	0.34	0.50
4.25	1.18	0.29	0.41
4.75	1.09	0.24	0.34
5.5	0.98	0.21	0.25
6.5	0.85	0.17	0.21
7.5	0.69	0.18	0.20
8.5	0.55	0.17	0.19
10.5	0.41	0.15	0.19

Table I.6: R_{AA} of b hadrons in centrality 60-93% Au+Au collisions.

p_{T} [GeV/c]	R_{AA}	total error (-)	total error (+)
1.25	1.77	0.80	1.34
1.75	1.83	0.73	1.29
2.25	1.84	0.65	1.14
2.75	1.82	0.61	1.00
3.25	1.76	0.55	0.84
3.75	1.65	0.46	0.69
4.25	1.50	0.39	0.55
4.75	1.33	0.32	0.43
5.5	1.15	0.26	0.31
6.5	0.98	0.23	0.27
7.5	0.83	0.21	0.25
8.5	0.68	0.19	0.25
10.5	0.56	0.21	0.27

Appendix J

Heavy Flavor Flow

Heavy quark provides an important information on the properties of the Quark-Gluon Plasma (QGP). They are mainly produced in the initial stage of the heavy-ion collisions and propagates the QGP. Since heavy quark propagate thorough the QGP with a strong coupling, the modification of their phase space distribution strongly reflects the QGP dynamics.

Ten years ago, we have measured the nuclear modification factor $R_{\rm AA}$ of $c + b \rightarrow e$ in Au+Au and d +Au collisions which reflects the modification of a momentum distribution as shown in Fig. J.1 (left) [10]. $R_{\rm AA}$ of $c + b \rightarrow e$ in Au+Au collisions indicates a strong yield suppression at high $p_{\rm T}$ compared with that in d +Au collisions. It was not expected and we need to reconsider the energy loss mechanism and understand its quark-mass dependence. Recently, we have measured $R_{\rm AA}$ of $c \rightarrow e$ and $b \rightarrow e$ and observed a quark-mass dependence of the suppression, namely a suppression less pronounced for bottom quarks than for charm quarks [10, 11, 12].

On the other hand, we have also found a large azimuthal anisotropy v_2 of $c + b \rightarrow e$ in Au+Au collisions ten years ago as shown in Fig. J.1 (right) [10]. It indicates that heavy flavors are strongly coupled in the QGP which was also not expected. We now are interested in the quark-mass dependence of the elliptic flow in the QGP. Especially, whether a very heavy bottom quark can be strongly coupled with the QGP is an object of interest.

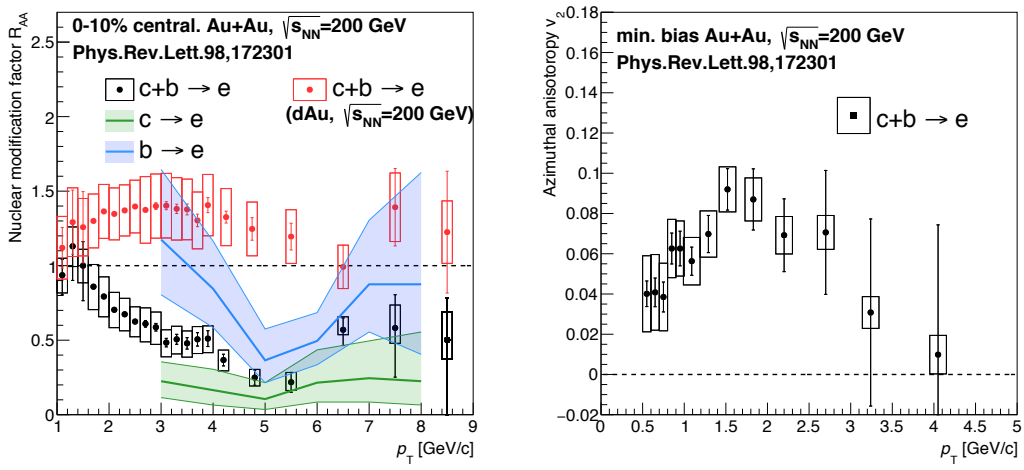

Figure J.1: Left: The nuclear modification factor for $c + b \rightarrow e$, $c \rightarrow e$ and $b \rightarrow e$ in d +Au and Au+Au collisions at $\sqrt{s_{NN}} = 200$ GeV. Right: The azimuthal anisotropy of $c + b \rightarrow e$ in Au+Au collisions at $\sqrt{s_{NN}} = 200$ GeV.

We have measured the azimuthal anisotropy v_2 of $c \rightarrow e$ and $b \rightarrow e$ via a displaced vertex analysis in Au+Au collisions at $\sqrt{s_{NN}} = 200$ GeV. Firstly, we measure the p_{T} spectrum and $\mathrm{DCA_T}$ distributions of single electrons and estimate background contributions which include non-electrons, internal and external conversion electrons, J/ψ decay electrons, Kaon decay electrons, and electron tracks mis-associated with uncorrelated inner tracker hits. These background components and $\mathrm{DCA_T}$ shapes are estimated by the data-driven method and the PHENIX detector full-simulation. Secondly, each component of $c \rightarrow e$ and $b \rightarrow e$ are extracted in $\mathrm{DCA_T}$ distributions. In this analysis, we employ our Bayesian inference technique [11, 12] and unfold the p_{T} spectrum of parent charm and bottom hadrons because $\mathrm{DCA_T}$ shapes depend on parent hadron p_{T} spectrum shape. The refold $\mathrm{DCA_T}$ shape from unfolded p_{T} spectrum of parent charm and bottom hadrons describes well the measured $\mathrm{DCA_T}$ distribution of electrons as shown in Fig. J.2 (left). Thirdly, the $\mathrm{DCA_T}$ distribution is divided to charm enriched region ($|\mathrm{DCA_T}| < 200$ μm) and bottom enriched region ($300 < |\mathrm{DCA_T}| < 1000$ μm) as shown in Fig. J.2 to extract the azimuthal anisotropy of $c \rightarrow e$ and $b \rightarrow e$.

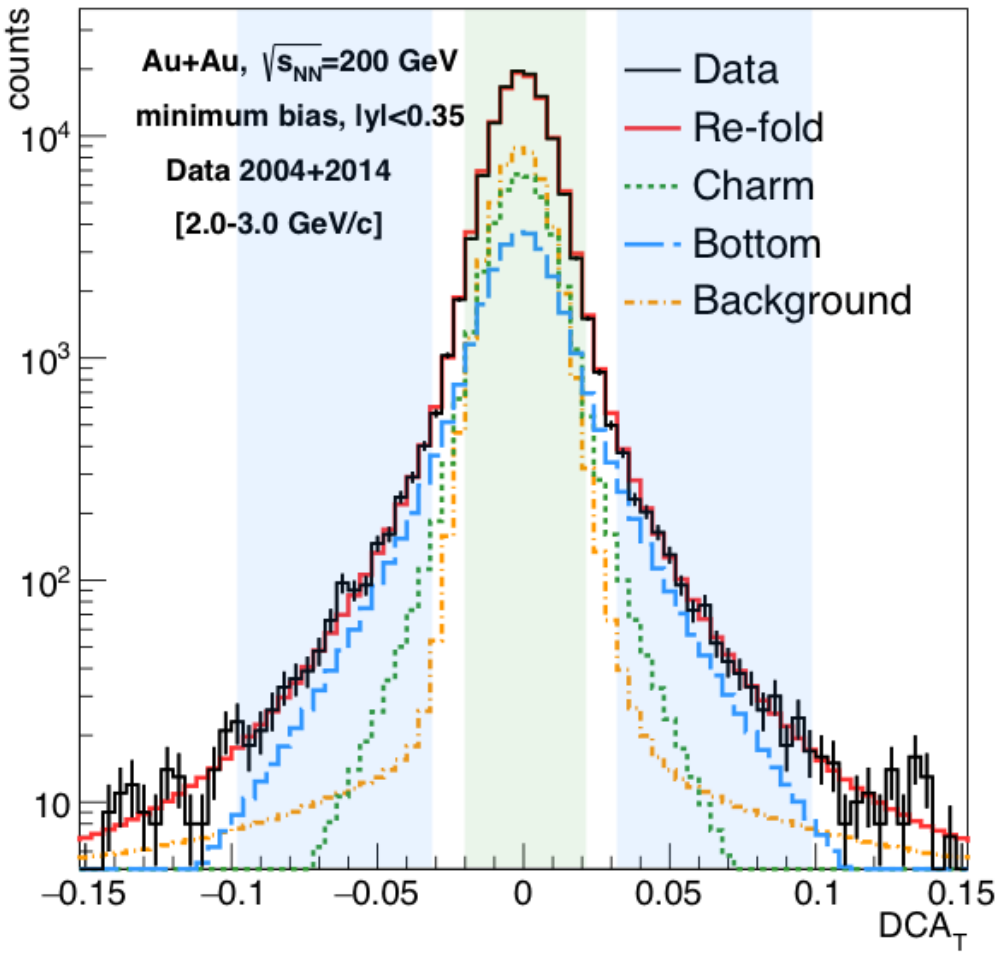

Figure J.2: The DCA_T distribution for measured electrons compared to the decomposed DCA_T distributions for background components, electrons from charm and bottom hadron decays in minimum bias Au+Au collisions at $\sqrt{s_{NN}} = 200$ GeV. The green (blue) band indicates the charm (bottom) enriched region in DCA_T.

For both charm and bottom enriched region, the azimuthal anisotropy of $c + b \rightarrow e$ as a function of p_T is measured with the background v_2 subtraction as shown in Fig. J.3.

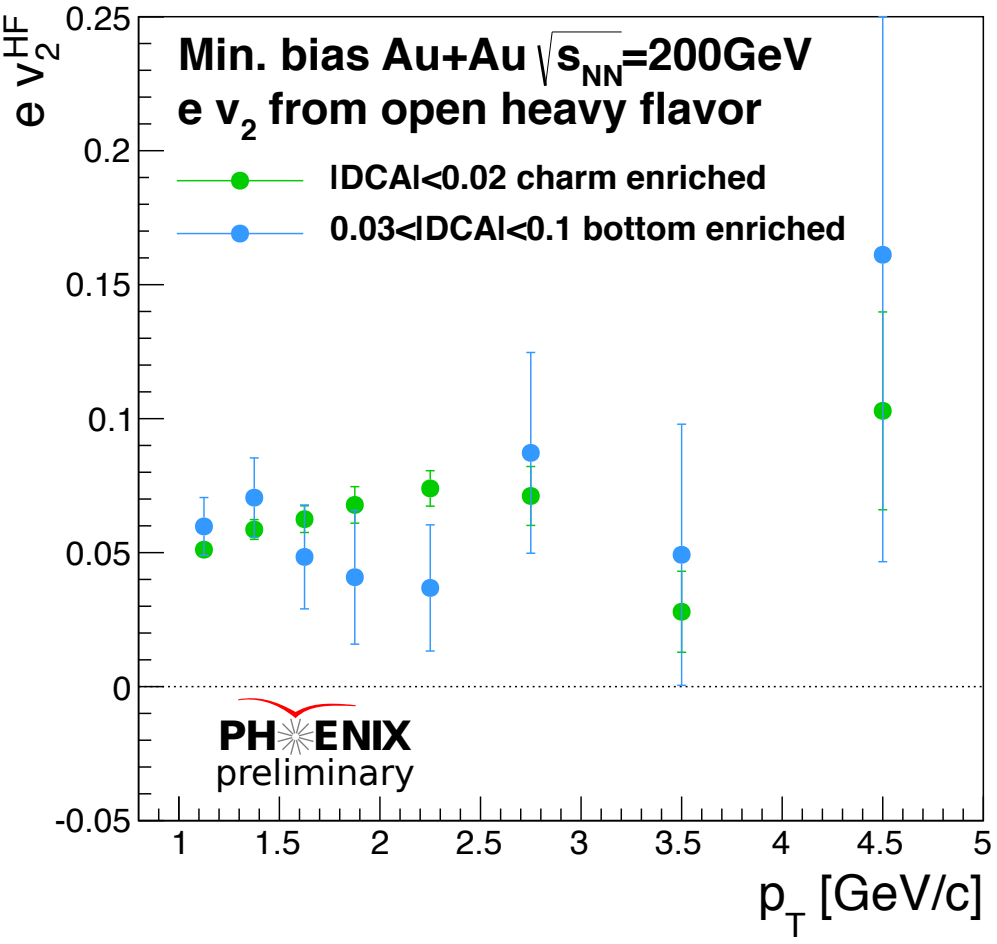

Figure J.3: The azimuthal anisotropy v_2 of $c + b \rightarrow e$ as a function of p_{T} for both charm and bottom enriched region.

These v_2 of $c + b \rightarrow e$ in charm and bottom enriched regions are expressed as

$$v_2^{c\ rich} = F_c^{c\ rich} \times v_2^c + F_b^{c\ rich} \times v_2^b \quad \text{(J.1)}$$

$$v_2^{b\ rich} = F_c^{b\ rich} \times v_2^c + F_b^{b\ rich} \times v_2^b \quad \text{(J.2)}$$

where F_c (F_b) is the fraction of $c \rightarrow e$ ($b \rightarrow e$) in each $\mathrm{DCA_T}$ regions, v_2^c (v_2^b) is true azimuthal anisotropy of $c \rightarrow e$ ($b \rightarrow e$). Simultaneous equations can be solved with each fraction and inclusive v_2 values to extract v_2 of $c \rightarrow e$ and $b \rightarrow e$. Fig. J.4 and J.5 shows extracted v_2 of $c \rightarrow e$ and $b \rightarrow e$ as a function of p_{T} which is the first measurement at RHIC energy. v_2 of $c \rightarrow e$ increases with increasing p_{T} and indicates the large elliptic flow of charm quarks in the QGP. The order of magnitude is less than the charged hadron v_2 [73]. To a direct comparison, an unfolding of parent hadron v_2 and Quark-Constituent-Number scaling are

needed. On the other hand, v_2 of $b \rightarrow e$ indicates no strong p_{T} dependence and non-zero flow of bottom quarks which is consistent with LHC result [74]. Measured v_2 of $b \rightarrow e$ is likely smaller than v_2 for $c \rightarrow e$, indicating the quark-mass dependence of flow in the QGP. However, v_2 of $b \rightarrow e$ is consistent with zero and v_2 of $c \rightarrow e$ within the large uncertainty. The analysis method will be improved to reduce the uncertainty and better understand the quark-mass dependence of flow.

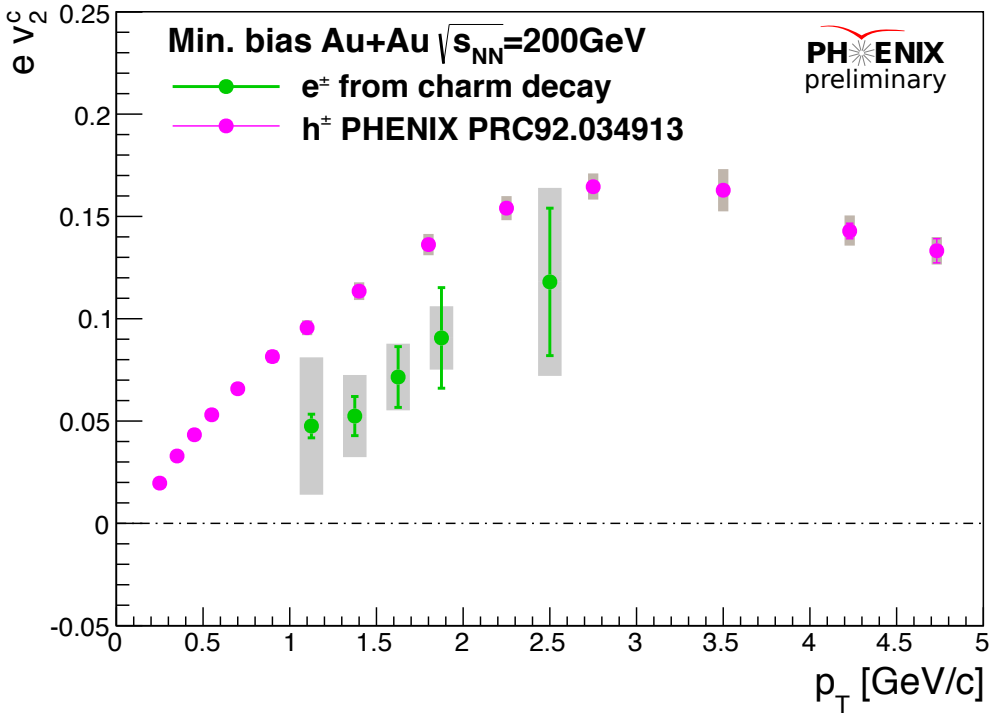

Figure J.4: The azimuthal anisotropy v_2 of $c \rightarrow e$ as a function of p_{T} compared with charged hadron v_2.

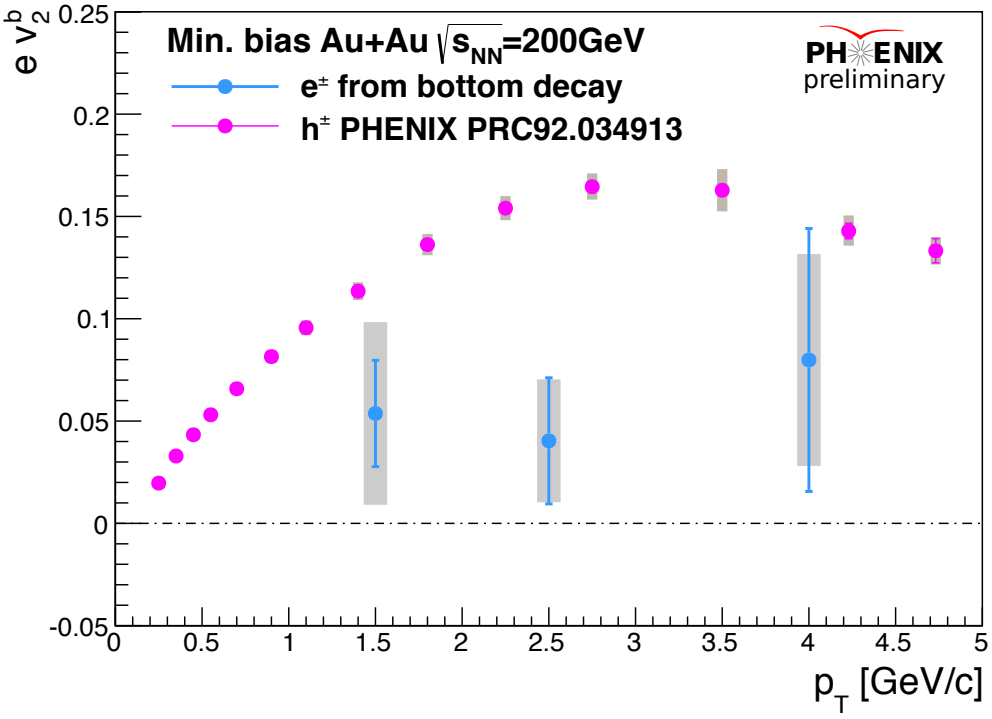

Figure J.5: The azimuthal anisotropy v_2 of $b \rightarrow e$ as a function of p_T compared with charged hadron v_2.

公表論文

公表論文

PHENIX measurements of single electrons from charm and bottom decays at midrapidity in Au+Au collisions.
K. Nagashima for the PHENIX collaboration.
Nuclear Physics A, **967**, 644-647 (2017).

参考論文

参考論文

Single electron yields from semileptonic charm and bottom hadron decays in Au+Au collisions at $\sqrt{s_{NN}} = 200$ GeV.
A. Adare, K. Nagashima, *et al.*
Physical Review C, **93**, 034904 (2016).